I. Tin Silsesquioxanes as Analogs for the Open and Closed Sites in Tin-Containing Zeotype Beta
and
II. Enantiomerically Enriched, Polycrystalline Molecular Sieves

Thesis by
Stephen Kramer Brand

In Partial Fulfillment of the Requirements for the
degree of
Doctor of Philosophy

CALIFORNIA INSTITUTE OF TECHNOLOGY
Pasadena, California

2017
Defended 17 April 2017

Stephen Kramer Brand
ORCID: 0000-0002-0894-401X

ACKNOWLEDGMENTS

The incredible opportunity to pursue a PhD from Caltech and complete the work presented here would not have been possible without the selfless support and innumerable contributions of my family, outstanding mentors (both past and present), sensational collaborators, and amazing friends.

First and foremost, I would like to thank my parents, Stephen and Karen, for their undying encouragement and love throughout all of my life. You have consistently provided me with tremendous opportunities that ultimately positioned me to pursue and complete the PhD program at Caltech.

I also thank my undergraduate advisors at Northwestern University, Professors Randall Q. Snurr and Justin M. Notestein. You both provided me with the resources to find and foster my love for research, and were invaluable in assisting me become the person I am today.

I would like to express my deepest gratitude to my advisor, Professor Mark E. Davis, for the opportunity and privilege to work in his laboratory. Your tutelage has helped me to grow professionally and personally. Most importantly, you have taught me that the toughest challenges in life should be met with a smile.

Additionally, I would like thank the members of my thesis committee: Dr. Jay A. Labinger, Professor Richard C. Flagan, and Professor Theodor Agapie. Jay, your insight and input throughout our collaborations has compelled me be a better scientist and problem-solver. Your guidance over the years has been remarkable, and will stick with me well beyond Caltech.

I am forever thankful and indebted to the scientific support staff that have assisted me in learning new analytical techniques and interpreting data: Dr. Sonjong Hwang for Solid State NMR, Dr. David VanderVelde for liquid NMR, Dr. Chi Ma for SEM, and Dr. Jay Winkler for CD. Additionally, I would like to thank the support staff within the Division of Chemistry and Chemical Engineering: Martha, Kathy, Suresh, and Joe.

Furthermore, I would like to thank my collaborators outside of Caltech for helping to enrich my graduate student experience. Specifically, Professors Dion Vlachos and Stavros Caratzoulas as well as Dr. Tyler R. Josephson from the University of Delaware, Dr. Stacey I. Zones from Chevron, and Professor Michael W. Deem from Rice University. Stacey, your advice regarding zeolites and life was invaluable and unforgettable.

Last, but certainly not least, I thank all members of the Davis lab I interacted with during my time at Caltech. Yasho, Ricardo, Raj and Bingjun, I sincerely appreciate your mentorship, particularly as I began my career as a graduate student. Collectively, you taught me the fundamentals of zeolite synthesis, material characterization, reaction testing, and helped me adapt and seamlessly become a part of the Davis lab. Ben, your organic chemistry lessons are irreplaceable. A special thanks goes to Marat, for his willingness to discuss and develop experiments throughout our time in the Davis lab together and for being a great friend. Joel, Mark, Josh, Viktor and Michiel, you each played an instrumental part in shaping how I think and act as an engineer, researcher, and human being. I look forward to continuing to grow our relationships in the years to come. Finally, I would like to extend an enormous thank you to all aforementioned and remaining group members for their kind and ceaseless comradery and friendship, and for all the great times we shared together. You all shaped my Caltech experience into one I will cherish for the rest of my life.

ABSTRACT

The use of biomass as a resource to produce value-added products has garnered significant interest as a means of reducing reliance on fossil fuels. This task is complicated by the complex, highly functionalized nature of abundant biomass derivatives, such as glucose. Tin-containing zeolite Beta (Sn-Beta) has been investigated as a catalyst for isomerizing aldohexoses into ketohexoses through a Lewis acid mediated hydride shift (1,2-intramolecular hydride shift, 1,2-HS). Recent studies on the reactivities of Lewis base-doped and alkali-exchanged Sn-Beta samples have conclusively demonstrated that the open tin site performs the glucose isomerization reaction. With Lewis base doped Sn-Beta, glucose conversion is almost completely eliminated and product selectivity is shifted predominantly to mannose, formed through a 1,2-intramolecular carbon shift (1,2-CS). To understand the structure-activity relationships between the conditions of the active sites in the zeolite, three molecular models (tin silsesquioxanes) of the tin sites in the zeolite are synthesized. Two tin silsesquioxanes that contain an octahedral tin site with and without an adjacent silanol group are prepared and used as catalysts for the reaction of glucose. The catalyst that contains the adjacent silanol group selectively forms fructose through a 1,2-HS while the catalyst without the silanol group yields mannose through a 1,2-CS. These results provide further evidence for the nature of the active sites in Sn-Beta. A methyl-ligated tin silsesquioxane is experimentally and theoretically examined to examine possible reactivities at the closed site. This compound is an active glucose conversion catalyst that selectively produces mannose, although the rates of reaction are far below those obtained from Sn-Beta. Additionally, a hybrid quantum mechanical/molecular mechanics model is constructed, and the complete

catalytic cycle is computationally examined *via* considering ring-opening, three distinct pathways for each hydride- and carbon-shift reaction, and ring-closing. The combined experimental and computational results suggest that there could be reaction pathways that involve Si-O-Sn cleavage that give much slower reaction rates than the open tin site in Sn-Beta.

Zeolite and zeolite-like molecular sieves are being used in a large number of applications such as adsorption and catalysis. Achievement of the long-standing goal of creating a chiral, polycrystalline molecular sieve with bulk enantioenrichment would enable these materials to perform enantioselective functions. In part II of this thesis, the synthesis of enantiomerically enriched samples of a molecular sieve is reported. Enantiopure organic structure directing agents (OSDAs) are designed with the assistance of computational methods, and used to synthesize enantioenriched, polycrystalline molecular sieve samples of either enantiomer. Computational results correctly predicted which enantiomer is obtained, and enantiomeric enrichment is proven by high-resolution transmission electron microscopy. The enantioenriched and racemic samples of the molecular sieves are tested as adsorbents and heterogeneous catalysts. The enantioenriched molecular sieves show enantioselectivity for the ring opening reaction of epoxides and enantioselective adsorption of 2-butanol (*R* enantiomer of the molecular sieve shows opposite and approximately equal enantioselectivity from the *S* enantiomer of the molecular sieve, while the racemic sample of the molecular sieve shows no enantioselectivity).

PUBLISHED CONTENT AND CONTRIBUTIONS

(1) Brand, S. K.; Schmidt, J. E.; Deem, M. W.; Daeyaert, F.; Ma, Y.; Terasaki, O.; Orazov, M.; Davis, M. E. Enantiomerically Enriched, Polycrystalline Molecular Sieves. *Proceedings of the National Academy of Sciences* **2017**, DOI: 10.1073/pnas.1704638114,
All authors designed research; M.W.D. and F.D. performed the computational work; S.K.B., J.E.S., M.O. and Y.M. performed the experimental research; all authors analyzed the data; S.K.B., J.E.S. and M.E.D. wrote the paper.

(2) Josephson, T. R.; Brand, S. K.; Caratzoulas, S.; Vlachos, D. G. 1,2-H- versus 1,2-C-Shift on Sn-Silsesquioxanes. *ACS Catalysis* **2017**, *7*, 25–33, DOI: 10.1021/acscatal.6b03128,
S.K.B, T.R.J., S.C., and D.G.V. designed research; T.R.J. and S.K.B. performed research; S.K.B., T.R.J., S.C. and D.G.V. analyzed data; and S.K.B., T.R.J., S.C. and D.G.V. wrote the manuscript.

(3) Brand, S. K.; Josephson, T. R.; Labinger, J. A.; Caratzoulas, S.; Vlachos, D. G.; Davis, M. E. Methyl-Ligated Tin Silsesquioxane Catalyzed Reactions of Glucose. *Journal of Catalysis* **2016**, *341*, 62–71, DOI: 10.1016/j.jcat.2016.06.013,
S.K.B, J.A.L, and M.E.D. designed experimental research; T.R.J., S.C., and D.G.V. designed computational research; S.K.B. and T.R.J. performed research; S.K.B., T.R.J., J.A.L., S.C., D.G.V. and M.E.D. analyzed data; and S.K.B., T.R.J., J.A.L., S.C. D.G.V. and M.E.D. wrote the manuscript.

(4) Brand, S. K.; Labinger, J. A.; Davis, M. E. Tin Silsesquioxanes as Models for the "Open" Site in Tin-Containing Zeolite Beta. *ChemCatChem* **2016**, *8*, 121–124, DOI: 10.1002/cctc.201501067,
S.K.B., J.A.L. and M.E.D. designed research; S.K.B. performed research; S.K.B., J.A.L. and M.E.D. analyzed data; and S.K.B., J.A.L. and M.E.D. wrote the manuscript.

TABLE OF CONTENTS

LIST OF ILLUSTRATIONS

LIST OF TABLES

Number *Page*

Part I

Tin Silsesquioxanes as Analogs for the Open and Closed Sites in Tin-Containing Zeotype Beta

Chapter 1

INTRODUCTION TO PART I: UNLOCKING AND UNDERSTANDING THE KEY CATALYTIC PATHWAYS OF BIOMASS CONVERSION

This beginning of this chapter serves to introduce the motivation, obstacles, and current progress in the quest to produce value-added chemicals from biomass feedstocks. A discussion of molecular sieves and the current possibilities and future goals for biomass conversion catalysis utilizing these materials is also presented. Additionally, the implementation of silsesquioxanes as homogeneous complexes to mimic and study the active site in heterogeneous catalysts is introduced. Finally, a broad overview of Part I of this thesis is given.

1.1 Motivation for Using Biomass Feedstocks in the Chemical Industry

Since the Industrial Revolution of the 18^{th} century, humanity has globally experienced remarkable growth economically and technologically.[1] The beginnings of this revolution coincided with the design and utilization of devices (like the steam engine) that were dependent on fossil fuels (namely coal, natural gas, and oil), leading to the facile introduction of machines to manufacturing processes.[1] 150 years later, fossil fuel resources remain the dominant sources of energy and chemicals.[2] Despite ongoing advances in the oil and gas sector that have allowed for dramatically greater quantities of crude to be extracted from existing (and future) reserves, growing concerns associated with extraction and consumption of fossil fuels has motivated substantial efforts from academia and industry to pursue and transition to sustainable, renewable, and clean sources for the production of energy and chemicals. The U.S. Energy Information Administration, however, reports that in

2015 coal, natural gas, and oil provided 16%, 29%, and 36% of the energy consumed in the United States, respectively.[2,3] In the same year, only 9% over the energy consumed was produced from renewable resources, half of which was derived from biomass-related sources.[3] Moreover, despite growth in the renewable energy sector, particularly amongst solar-derived sources, fossil fuels are expected to remain the dominant, primary sources of energy — likely due to the capital expenses associated with adapting and implementing new technologies, as well as current issues regarding energy storage.[2]

Beyond the production of energy, fossil fuels are crucial feedstocks for the production of commodity goods. Specifically, 3% of natural gas and 7% of oil consumed in the United States is used in the chemical industry.[2] Biomass (matter that has been produced from biological photosynthesis) presents itself as an intriguing feedstock replacement for some chemical processes.[4–6] However, the oxygenated nature of biomass (relative to fossil fuel derived hydrocarbons) complicates traditional industrial reactions and potentially compromises the economic viability of it as a feedstock. Therefore, it is critical to produce compounds from biomass that have value above the original energy content of the biomass itself, and, preferably, are easier to synthesize than from conventional methods.[7–9] The first part of this thesis focuses on examining a crucial transformation of glucose, a monomer obtained from lignocellulosic biomass, into fructose — from which numerous interesting value-added chemicals can be directly obtained.

Despite the significant political, economic, and scientific challenges that persist in developing and encouraging the adaptation of biomass-derived energy and chemicals, academia and industry must remain focused on developing processes that are net green.

1.2 Molecular Sieves and their Application for Biomass Catalysis

Molecular sieves are microporous, crystalline materials with pores of less than 2 nm that are formed from three-dimensional networks of oxide tetrahedra.[10,11] Currently, these materials have found applications in catalysis, separations, ion exchange, and adsorption.[11,12] Molecular sieves provide inherent shape-selectivity properties and, coupled with the inclusion of catalytic metal centers, are capable of innumerable, highly selective chemical reactions.[10,11] While theory demonstrates that there are millions of distinct hypothetical framework structures, currently only around 230 framework have been successfully synthesized.[13–16] However, due to the numerous economic and scientific benefits of utilizing molecular sieves, motivation to develop new structures remains high.

The composition of molecular sieves can vary drastically, imparting distinct properties - even among equivalent frameworks.[10] A typical framework consists of tetrahedrally coordinated atomic centers (referred to as T-atoms) connected to one another *via* oxygen atoms to form a complex crystalline structure.[10] In many instances, it is possible to incorporate tetravalent or non-tetravalent elements into the T-atom position, such as tin (IV).[10,17] In general, microporous materials with framework compositions limited to silicon, aluminum, and oxygen (*i.e.*, aluminosilicate) are known as zeolites.[10,11] Zeotypes are materials that retain equivalent framework structures to zeolites, but the compositional range of the structure is unconstrained.[11]

One particular framework of particular interest is Beta, due in part to its stability and ease of synthesis that does not require expensive starting materials. Most commonly, zeolites with *BEA topology consist of an intergrowth of polymorphs A and B of the BEA

structure.[18] As shown in Figure 1.1, this structure consists of a three-dimensional network of intersecting 12-membered ring channels (*i.e.*, 12 T-atoms).[15] Such large channels (*ca.* 0.8 nm pore diameter) render *BEA a promising platform to perform catalysis on bulky molecules, such as glucose.[19]

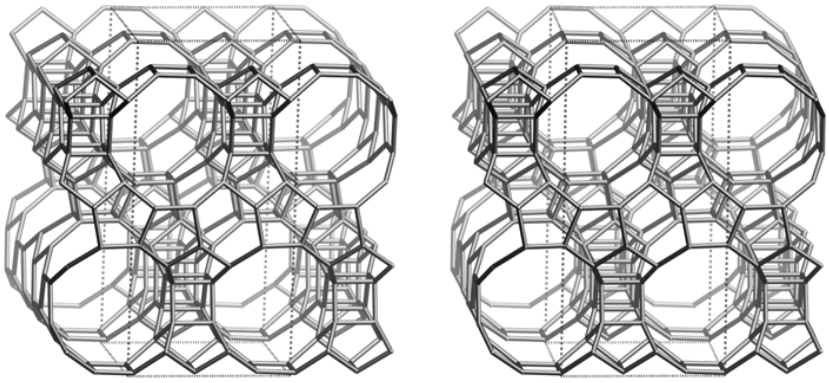

Figure 1.1: Framework structure of zeolite Beta.

In molecular sieves, depending upon the conditions under which the material was synthesized, defects may arise throughout the structure.[20] For a pure-silica molecular sieve, these defects transpire as silanol "nests" within the framework, whereby a given silicon is incompletely coordinated to the broader network of atoms (*e.g.*, only two or three silicon-oxygen-silicon bonds are made). A similar principal exists for metal-containing frameworks that have been isomorphously substituted. For tin-containing zeotype Beta, a known and highly-selective glucose conversion catalyst that will be discussed at length in Part I of this thesis, there exist two possible active sites: the closed site and open site.[21] The closed site is classified as a metal center bound to the framework *via* four –OSi bonds. On the other hand, the open site is characterized by the presence of a stannanol and three –OSi bonds to the molecular sieve framework. As open sites are formed by the hydrolysis of a single closed site bond, a silanol group is expected to be present adjacent to the metal site. Depictions of

these sites are given in Figure 1.2. Part II of this thesis presents a more rigorous discussion of molecular sieves and their synthesis.

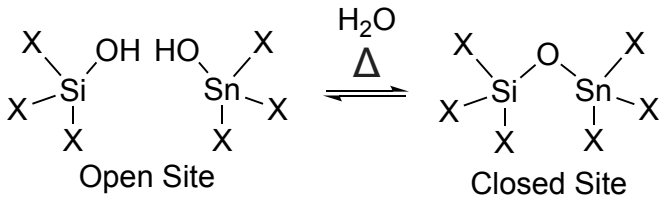

Figure 1.2: Open (left) and closed (right) sites present in tin-containing Beta.

Moliner *et al*. first reported that tin-containing zeotypes are active in performing the isomerization of glucose in water.[19] Bermejo-Deval and coworkers demonstrated that Sn-Beta is also active in methanol solutions.[22,23] Utilizing Sn-Beta for a reaction performed in 10 wt% aqueous glucose solution at 383 K for 30 minutes yields of 45%, 32%, and 9% for glucose, fructose, and mannose are obtained, respectively. Work in the Davis lab has determined it is also possible to manipulate the active site of Sn-Beta to solely produce mannose through a 1,2-intramolecular carbon shift (1,2-CS). This highlights the tunability of the active site and the necessity to develop a fundamental understanding of how the structure of a given catalytic site influences subsequent product formation.

In an attempt to understand the glucose isomerization mechanism in Sn-Beta, Román-Leshkov and workers utilized isotopic tracer studies to demonstrate that Sn-Beta catalyzed glucose isomerization proceeds *via* a $C_1 - C_2$ intramolecular hydride shift (1,2-HS), as depicted by Figure 1.3. This proposed mechanism stipulated that the active site of Sn-Beta is the partially hydrolyzed framework tin species. To confirm this hypothesis and gain further insight as to how glucose catalysis occurs, Bermejo-Deval *et al*. prepared Sn-Beta with CH_3SnCl_3, ensuring that all framework tin was of the open site form (with the typical

hydroxyl group replaced with a methyl group); however, results obtained from this material were inconclusive.[22]

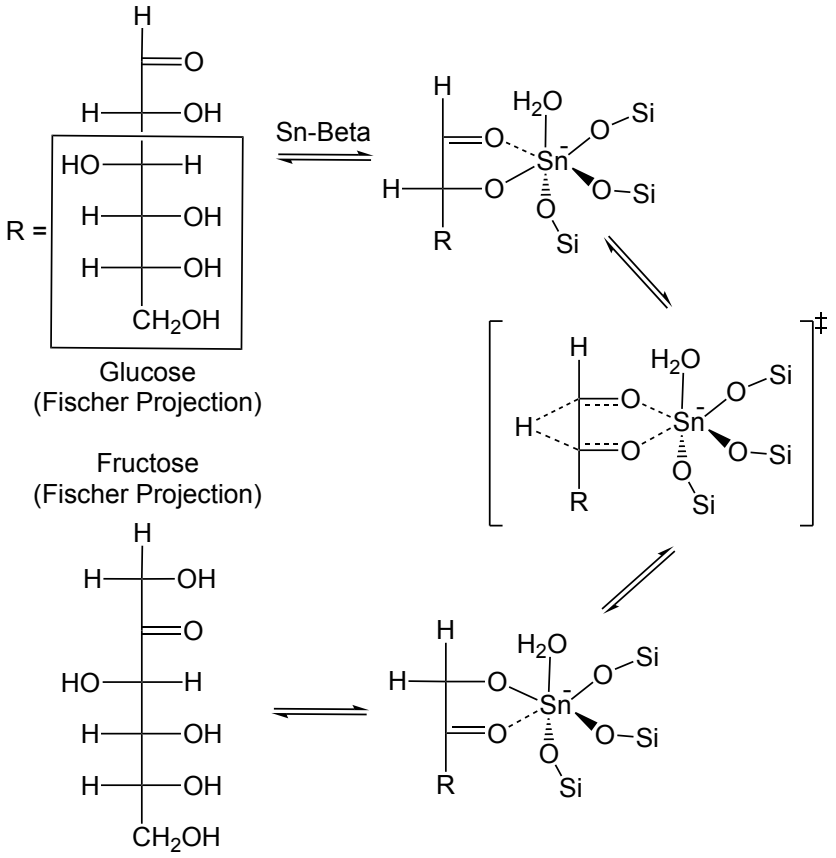

Figure 1.3: Initial mechanism proposed for the Sn-Beta Lewis acid catalyzed C_1 – C_2 intramolecular hydride shift isomerization of glucose to fructose.

Subsequent experimental work, in addition to computational studies, strongly indicates that the active site in Sn-Beta is indeed the open site.[21,24–26] Initially, Bermejo-Deval *et al.* titrated the silanol groups adjacent to the open tin site with sodium and observed a complete shift in selectivity from fructose to mannose. This provided the first experimental evidence that the open site was the most active tin site and emphasized the significance of the silanol moiety in the reaction mechanism.[24] This work also revealed that titration of the open site with NH_3 (Sn-Beta-NH_3) attenuated the activity of the catalyst indicating that the open and

closed sites do not interconvert under reaction conditions. Harris *et al.* subsequently have shown that the number of open and closed sites in Sn-Beta may be quantitatively determined utilizing Lewis bases as titrants.[26] In doing so, they are able to demonstrate an inverse linear correlation between the initial rate of glucose isomerization with the quantity of pyridine dosed. This provided the first true experimental demonstration that isomerization activity is fully suppressed when all open sites are titrated.

Numerous reaction mechanisms involving the open (and closed) site have been proposed. Work from Li *et al.* suggests that glucose first binds to the open site through coordination of the basic C_1 carbon hydroxyl, with subsequent transfer of the acidic proton to the framework lattice followed by a 1,2-intramolecular hydride shift.[27] This results in a monodentately bound fructose stabilized by the adjacent silanol group through the O_1 oxygen. Yang *et al.* consider a similar type of mechanism, but at the closed site.[28] Most significantly, Rai *et al.* and Christianson *et al.* propose similar pathways; however, their calculations involve the acidic C_2 hydroxyl proton transferring to the stannanol group, forming a water molecule.[25,29] Rai *et al.* also demonstrated that in the absence of a silanol group adjacent to the tin center the glucose binds to the tin bidentately and selectively produces mannose through a 1,2-CS, known as the Bílik reaction.[24,30]

In general, the mechanisms proposed by Rai *et al.* are the most consistent with those observed experimentally, and are shown in Figures 1.4 and 1.5. In general, it was demonstrated that glucose in a bidentate coordination to the Sn favored a C-shift reaction, while glucose coordinated to the Sn and neighboring SiOH favored the H-shift reaction, suggesting the neighboring SiOH promotes fructose selectivity by participating in a concerted reaction.

Although Sn-Beta demonstrates the highest conversion of glucose in water at 413 K, a

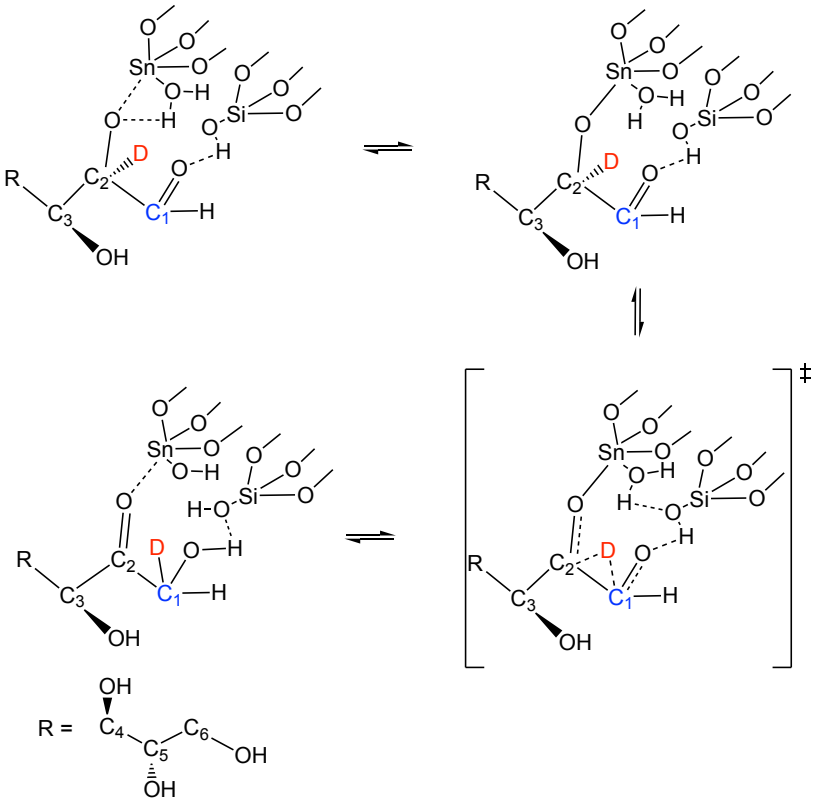

Figure 1.4: Mechanism proposed for the Sn-Beta Lewis acid catalyzed $C_1 - C_2$ intramolecular hydride shift isomerization of glucose to fructose.

number of other materials exhibit isomerization activity. Mesoporous MCM-41 materials synthesized with tin exhibit approximately 30% glucose conversion, respectively.[19] SnO_2 dispersed on silica also shows reactivity in methanol solutions.[23]

The majority of mechanistic studies have relied heavily upon the use of isotopic labeling studies to deduce the nature of a given reaction. Despite significant recent advances that have indicated that the open sites are indeed the active catalytic sites, a clear mechanistic picture of the glucose isomerization and epimerization processes has yet to be thoroughly developed.[24,26] This stems from the inherent characterization limitations of a heterogeneous

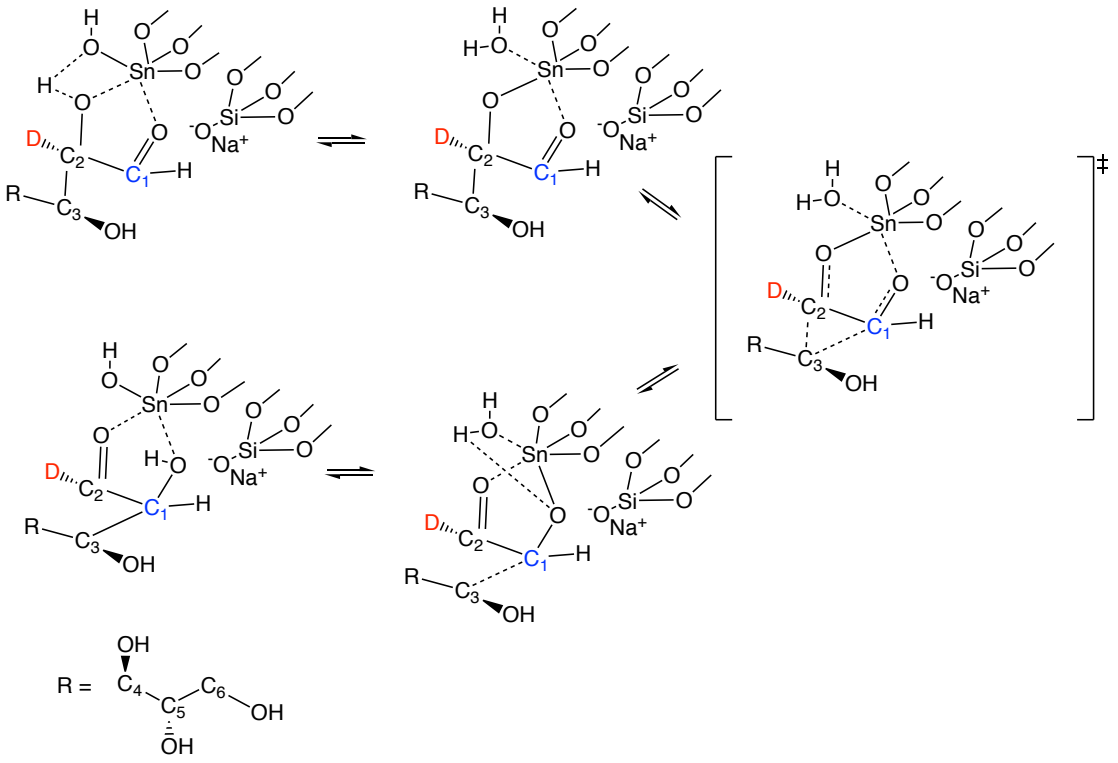

Figure 1.5: Mechanism proposed for the Sn-Beta Lewis acid catalyzed $C_1 - C_2$ intramolecular carbon shift epimerization of glucose to mannose.

catalyst and the multiplicity of sites that may exist within a given sample. It is clear that further studies are necessary in order to understand the nature of the interactions amongst the active sites Sn-Beta, the sugar complexes, as well as the solvent during the isomerization and epimerization reactions. Given the general observation that tin centers dispersed within or on siliceous matrices are active in the conversion of glucose, it follows naturally that soluble, homogeneous, well-defined complexes, like metallosilsesquioxanes, are ideal models for studying the reaction mechanism and active site structure in heterogeneous catalysts.

1.3 Introduction to Silsesquioxanes: Homogeneous Analogues of Heterogeneous Systems

Silsesquioxanes are organosilicon compounds that retain a cage-like structure, as demonstrated by Figure 1.6. Most commonly, silsesquioxane structures are cubic (T_8), while others may be trigonal prismatic (T_6) or pentahedral (T_{10}). The T_8 structure is most prevalent due to the geometric stability of the Si_4O_4 rings. Moreover, the silsesquioxane complex may either be fully condensed, implying that the most Si-O-Si bonds are attained in a given geometric arrangement, or incompletely condensed, whereby fewer Si-O-Si bonds comprise the structure than are possible. In this latter instance, silanol groups are imparted into the structure, invoking an inherent functionality to the complex, as shown in Figure 1.7. Most importantly, silsesquioxanes are soluble in non-polar solvents, and are therefore unique candidates to study siliceous heterogeneous catalysts.

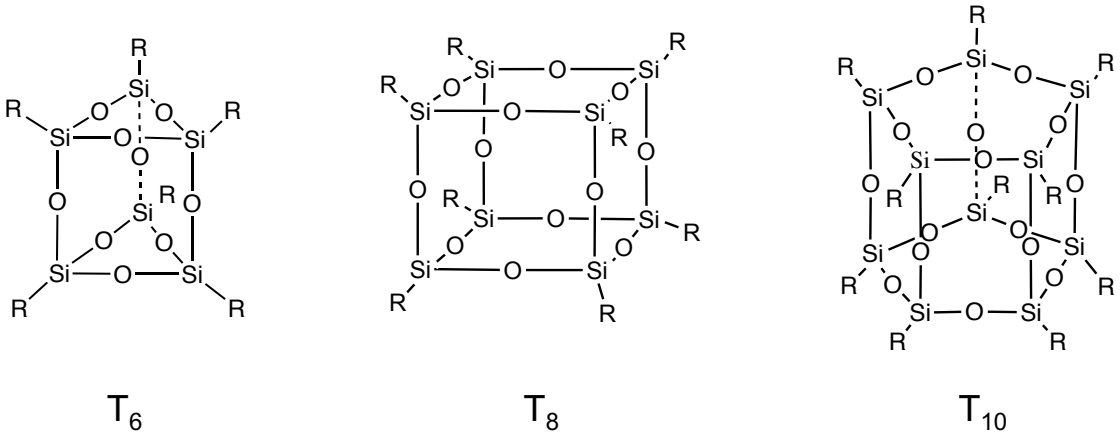

Figure 1.6: Examples of fully condensed silsesquioxanes, where R is an aliphatic or aryl group.

Incompletely condensed cubic silsesquioxanes are of particular interest as they are representative of D4R rings, fundamental molecular sieve building blocks, and provide great

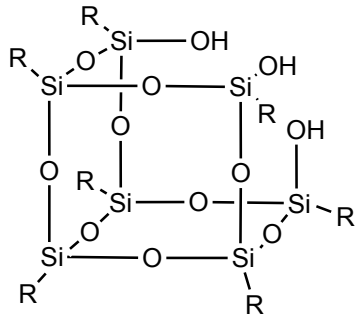

Figure 1.7: Incompletely condensed $T_7(OH)_3$ silsesquioxane.

structural similarity to the environment surrounding metal sites in the Beta topology. Moreover, incompletely condensed trisilanol T_7-derivatives ($T_7(OH)_3$) yield opportunities to introduce metals, such as tin and titanium into the material to mimic metal centers, depicted in Figure 1.8.

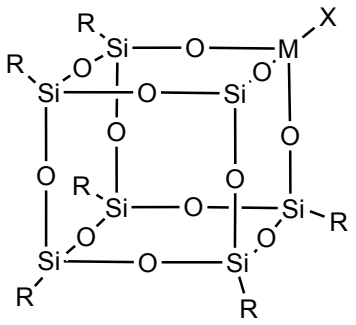

Figure 1.8: General structure of a metallosilsesquioxane, where M and X are a given metal and organic ligand, respectively.

Brown and Vogt first reported the synthesis of $T_7(OH)_3$ complexes in 1965 *via* the hydrolytic condensation of cyclohexyltrichlorosilane in hydrous acetone.[31] The product was allowed to precipitate from solution over a period of 36 months, and was collected intermittently. Fortunately, work performed by Feher through the 1990s drastically reduced required synthesis times.[32–36]

Feher's seminal work on silsesquioxanes also established a structural relationship be-

tween $T_7(OH)_3$ and that of the (111) octahedral face of β-cristobalite and the (0001) rhombohedral face of β-tridymite, both polymorphs of silica that are commonly observed in amorphous silica.[35] Moreover, there exists extensive spectroscopic similarities between isolated and geminal surface silanol groups on silica with their respective silsesquioxane complex analogues.[37] Lastly, pKa calculations indicate that the silsesquioxane cage provides an electronegative CF_3–like electron withdrawing effect similar to bulk silica on a silanol species.[37] There is also an observed increase in acidity for silsesquioxane complexes bearing multiple silanol groups, as is also the case with bulk silica.

Given the clear applicability of implementing silsesquioxanes as models for silica surfaces and the geometric similarities between silsesquioxane cages and zeolitic building blocks, researchers have turned toward utilizing them as analogues for zeolites.[38–41] In particular, aluminosilsesquioxanes as model compounds for acidic sites in zeolites have been obtained by reacting alkylaluminum compounds with $T_7(OH)_3$.[38,40] Using this procedure, both Lewis and Brønsted acidic silsesquioxane complexes were synthesized. It was shown that the aluminosilsesquioxane Brønsted acid model retained an intramolecular hydrogen bond comparable to that found in zeolite HY, although the relative acidity of the compound was reduced due to the inherent strength of the aforementioned bond.[41] Moreover, a number of studies have utilized titanosilsesquioxanes to probe the activity of titanosilicates, such as Ti-MCM-41, a mesoporous molecular sieve, as well as Ti-substituted MFI, also referred to as TS-1.[42–45]

It is interesting to note that despite the clear advantages of utilizing well-defined single-site compounds to directly analyze the nature of a catalytic site, there exists little discussion in the literature on studies where such experiments have been performed. In fact, some

workers have focused adsorbing metallosilsesquioxanes within MCM-41 structures for direct use as catalysts.[46–48] This is potentially a consequence of the promising performance that silsesquioxane-based catalysts demonstrate towards epoxidation of alkenes. Notably, Crocker *et al*. have reported that titanosilsesquioxanes are the most active titanium-based epoxidation catalysts reported to date.[43]

1.4 Overview of Part I

The collection of work presented in the first part of this thesis focuses on the synthesis and characterization of three tin silsesquioxanes that function as analogues to the open and closed sites within tin-containing Beta. Furthermore, these complexes are rigorously analyzed for their capacity to perform glucose conversion chemistries. Chapter 2 analyzes two such complexes, one that mimics the open site and one that mimics a sodium-exchanged open site. This work provides not only the first example of utilizing tin silsesquioxanes to perform carbohydrate-based chemistry, but also he first fundamental indication of the structure-activity relationship between catalyst geometries and reaction products for this system. It was demonstrated that the open site geometry does indeed selectively produce fructose from glucose through the 1,2-HS mechanism, while the sodium-exchanged open site analogue produced mannose by the 1,2-CS mechanism. These are in direct alignment with what has been demonstrated with the heterogeneous Sn-Beta system. Furthermore, as these compounds are fully characterizable utilizing a host of techniques, the precise structure of the active site is known. Chapter 3 focuses on a singular complex that mimics the closed site in tin-containing zeotype Beta. Despite this complex producing mannose (selectively) and fructose (less selectively), the rates are exceptionally below those found for

the complexes examined in Chapter 2. This indicates that it is possible to perform glucose conversion chemistries by breaking the framework Sn-O-Si bond, but it is not likely to be the primary mechanism by which products are formed using Sn-Beta. Thus, if closed sites are to participate in catalysis, it is at a rate significantly lower than at the open site. Finally, in Appendix C, a further examination of how reactions occur on materials studied in Chapter 2 is detailed.

1.5 References

(1) Wrigley, E. A. Energy and the English Industrial Revolution. *Philosophical Transactions of the Royal Society of London A: Mathematical, Physical and Engineering Sciences* **2013**, *371*, DOI: 10.1098/rsta.2011.0568.

(2) US. Energy Information Administration, Annual Energy Outlook 2017., http://www.eia.gov/outlooks/aeo/.

(3) US. Energy Information Administration, Monthly Energy Review, January 2017., http://www.eia.gov/totalenergy/data/monthly/#summary.

(4) McKendry, P. Energy production from biomass (part 1): overview of biomass. *Bioresource Technology* **2002**, *83*, Reviews Issue, 37–46, DOI: http://dx.doi.org/10.1016/S0960-8524(01)00118-3.

(5) McKendry, P. Energy production from biomass (part 2): conversion technologies. *Bioresource Technology* **2002**, *83*, Reviews Issue, 47–54, DOI: http://dx.doi.org/10.1016/S0960-8524(01)00119-5.

(6) McKendry, P. Energy production from biomass (part 3): gasification technologies. *Bioresource Technology* **2002**, *83*, Reviews Issue, 55–63, DOI: http://dx.doi.org/10.1016/S0960-8524(01)00120-1.

(7) Serrano-Ruiz, J. C.; Dumesic, J. A. Catalytic routes for the conversion of biomass into liquid hydrocarbon transportation fuels. *Energy & Environmental Science* **2011**, *4*, 83.

(8) Dusselier, M.; Van Wouwe, P.; Dewaele, A.; Makshina, E.; Sels, B. F. Lactic acid as a platform chemical in the biobased economy: the role of chemocatalysis. *Energy & Environmental Science* **2013**, *6*, 1415, DOI: 10.1039/c3ee00069a.

(9) Corma, A.; Iborra, S.; Velty, A. Chemical Routes for the Transformation of Biomass into Chemicals. *Chemical Reviews* **2007**, *107*, PMID: 17535020, 2411–2502, DOI: 10.1021/cr050989d.

(10) Davis, M. E.; Lobo, R. F. Zeolite and molecular sieve synthesis. *Chemistry of Materials* **1992**, *4*, 756–768, DOI: 10.1021/cm00022a005.

(11) Corma, A. State of the art and future challenges of zeolites as catalysts. *Journal of Catalysis* **2003**, *216*, 40th Anniversary Commemorative Issue, 298–312, DOI: http://dx.doi.org/10.1016/S0021-9517(02)00132-X.

(12) Čejka, J.; Corma, A.; Zones, S. I., *Zeolites and Catalysis: Synthesis, Reactions and Applications*; Wiley-VCH Verlag GmbH: 2010.

(13) Davis, M. E. Ordered porous materials for emerging applications. *Nature* **2002**, *417*, 813–821.

(14) Moliner, M.; Rey, F.; Corma, A. Towards the rational design of efficient organic structure-directing agents for zeolite synthesis., 2013, DOI: 10.1002/anie.201304713.

(15) McCuster, L. B.; Baerlocher, C. Database of Zeolite Structures., http://www.iza-structure.org/databases.

(16) Earl, D. J.; Deem, M. W. Toward a Database of Hypothetical Zeolite Structures. *Industrial & Engineering Chemistry Research* **2006**, *45*, 5449–5454, DOI: 10.1021/ie0510728.

(17) Li, J.; Corma, A.; Yu, J. Synthesis of new zeolite structures. *Chem. Soc. Rev.* **2015**, *44*, 7112–7127, DOI: 10.1039/C5CS00023H.

(18) Higgins, J. B.; LaPierre, R. B.; Schlenker, J. L.; Rohrman, A. C.; Wood, J. D.; Kerr, G. T.; Rohrbaugh, W. J. The framework topology of zeolite beta. *Zeolites* **1988**, *8*, 446–452, DOI: 10.1016/S0144-2449(88)80219-7.

(19) Moliner, M.; Román-Leshkov, Y.; Davis, M. E. Tin-containing zeolites are highly active catalysts for the isomerization of glucose in water. *Proceedings of the National Academy of Sciences of the United States of America* **2010**, *107*, 6164–6168.

(20) Chezeau, J.; Delmotte, L.; Guth, J.; Gabelica, Z. Influence of synthesis conditions and postsynthesis treatments on the nature and quantity of structural defects in highly siliceous {MFI} zeolites: A high-resolution solid-state 29Si n.m.r. study. *Zeolites* **1991**, *11*, 598–606, DOI: http://dx.doi.org/10.1016/S0144-2449(05)80011-9.

(21) Boronat, M.; Concepción, P.; Corma, A.; Renz, M.; Valencia, S. Determination of the catalytically active oxidation Lewis acid sites in Sn-beta zeolites, and their optimisation by the combination of theoretical and experimental studies. *Journal of Catalysis* **2005**, *234*, 111–118.

(22) Bermejo-Deval, R.; Assary, R. S.; Nikolla, E.; Moliner, M.; Román-Leshkov, Y.; Hwang, S.-J.; Palsdottir, A.; Silverman, D.; Lobo, R. F.; Curtiss, L. A.; Davis, M. E. Metalloenzyme-like catalyzed isomerizations of sugars by Lewis acid zeolites. *Proceedings of the National Academy of Sciences of the United States of America* **2012**, *109*, 9727–32.

(23) Bermejo-Deval, R.; Gounder, R.; Davis, M. E. Framework and Extraframework Tin Sites in Zeolite Beta React Glucose Differently. *ACS Catalysis* **2012**, *2*, 2705–2713.

(24) Bermejo-Deval, R.; Orazov, M.; Gounder, R.; Hwang, S. J.; Davis, M. E. Active sites in Sn-beta for glucose isomerization to fructose and epimerization to mannose. *ACS Catalysis* **2014**.

(25) Rai, N.; Caratzoulas, S.; Vlachos, D. G. Role of Silanol Group in Sn-Beta Zeolite for Glucose Isomerization and Epimerization Reactions. *ACS Catalysis* **2013**, *3*, 2294–2298.

(26) Harris, J. W.; Cordon, M. J.; Di Iorio, J. R.; Vega-Vila, J. C.; Ribeiro, F. H.; Gounder, R. Titration and quantification of open and closed Lewis acid sites in Sn-Beta zeolites that catalyze glucose isomerization. *Journal of Catalysis* **2016**, *335*, 141–154.

(27) Li, Y.-P.; Head-Gordon, M.; Bell, A. T. Analysis of the Reaction Mechanism and Catalytic Activity of Metal-Substituted Beta Zeolite for the Isomerization of Glucose to Fructose. *ACS Catalysis* **2014**, *4*, 1537–1545.

(28) Yang, G.; Pidko, E. A.; Hensen, E. J. M. The mechanism of glucose isomerization to fructose over Sn-BEA zeolite: A periodic density functional theory study. *ChemSusChem* **2013**, *6*, 1688–1696.

(29) Christianson, J. R.; Caratzoulas, S.; Vlachos, D. G. Computational Insight into the Effect of Sn-Beta Na Exchange and Solvent on Glucose Isomerization and Epimerization. *ACS Catalysis* **2015**, *1*.

(30) Bílik, V.; Petrus, L.; Farkas, V. Reactions of saccharides catalyzed by molybdate ions. XV.* Mechanism of the epimerization reaction. *Chem. Zvesti* **1975**, *685*, 690–693.

(31) Brown, J. F.; Vogt, L. H. The Polycondensation of Cyclohexylsilanetriol. *Journal of the American Chemical Society* **1965**, *87*, 4313–4317.

(32) Feher, F. J.; Soulivong, D.; Lewis, G. T. Facile Framework Cleavage Reactions of a Completely Condensed Silsesquioxane Framework. *Journal of the American Chemical Society* **1997**, *119*, 11323–11324.

(33) Feher, F. J. Controlled cleavage of $R_8Si_8O_{12}$ frameworks: a revolutionary new method for manufacturing precursors to hybrid inorganic–organic materials. *Chemical Communications* **1998**, 399–400.

(34) Feher, F. J.; Soulivong, D.; Nguyen, F. Practical methods for synthesizing four incompletely condensed silsesquioxanes from a single $R_8Si_8O_{12}$ framework. *Chemical Communications* **1998**, 1279–1280.

(35) Feher, F. J.; Newman, D. A.; Walzer, J. F. Silsesquioxanes as models for silica surfaces. *Journal of the American Chemical Society* **1989**, *111*, 1741–1748.

(36) Feher, F. J.; Nguyen, F.; Soulivong, D.; Ziller, J. W. A new route to incompletely condensed silsesquioxanes: acid-mediated cleavage and rearrangement of $(c\text{-}C_6H_{11})_6Si_6O_9$ to C_2-$[(c\text{-}C_6H_{11})_6Si_6O_8X_2]$. *Chemical Communications* **1999**, 1705–1706.

(37) Dijkstra, T. W.; Duchateau, R.; van Santen, R. A.; Meetsma, A.; Yap, G. P. A. Silsesquioxane Models for Geminal Silica Surface Silanol Sites. A Spectroscopic Investigation of Different Types of Silanols. *Journal of the American Chemical Society* **2002**, *124*, 9856–9864.

(38) Feher, F. J.; Budzichowski, T. A.; Weller, K. J. Polyhedral aluminosilsesquioxanes: soluble organic analogs of aluminosilicates. *Journal of the American Chemical Society* **1989**, *111*, 7288–7289.

(39) Feher, F. J.; Weller, K. J. Polyhedral Aluminosilsesquioxanes as Models for Aluminosilicates: Unique Synthesis of Anionic Al/Si/O Frameworks. *Organometallics* **1990**, *9*, 2638–2640.

(40) Duchateau, R.; Harmsen, R. J.; Abbenhuis, H. C. L.; van Santen, R. A.; Meetsma, A.; Thiele, S. K.-H.; Kranenburg, M. Modeling Acidic Sites in Zeolites and Aluminosilicates by Aluminosilsesquioxanes. *Chemistry - A European Journal* **1999**, *5*, 3130–3135.

(41) Edelmann, F. T.; Gun'ko, Y. K.; Giessmann, S.; Olbrich, F.; Jacob, K. Silsesquioxane Chemistry: Synthesis and Structure of the Novel Anionic Aluminosilsesquioxane $[HNEt_3][\{Cy_7Si_7O_9(OSiMe_3)O_2\}_2Al]\cdot C_6H_{14}$ (Cy = $c\text{-}C_6H_{11}$). *Inorganic Chemistry* **1999**, *38*, 210–211.

(42) Crocker, M.; Herold, R. H. M.; Guy Orpen, A. Synthesis and structural characterisation of tripodal titanium silsesquioxane complexes: a new class of highly active catalysts for liquid phase alkene epoxidation. *Chemical Communications* **1997**, 2411–2412.

(43) Crocker, M.; Herold, R. H. M.; Orpen, A. G.; Overgaag, M. T. A. Synthesis and characterisation of titanium silasesquioxane complexes: soluble models for the active site in titanium silicate epoxidation catalysts †. *Journal of the Chemical Society, Dalton Transactions* **1999**, 3791–3804.

(44) Maschmeyer, T.; C. Klunduk, M.; M. Martin, C.; S. Shephard, D.; F. G. Johnson, B.; Meurig Thomas, J. Modelling the active sites of heterogeneous titanium-centred

epoxidation catalysts with soluble silsesquioxane analogues. *Chemical Communications* **1997**, *004*, 1847.

(45) Fraile, J. M.; García, J. I.; Mayoral, J. A.; Vispe, E. Catalytic sites in silica-supported titanium catalysts: Silsesquioxane complexes as models. *Journal of Catalysis* **2005**, *233*, 90–99.

(46) Smet, P.; Riondato, J.; Pauwels, T.; Moens, L.; Verdonck, L. Preparation and characterization of a titanium(IV) silsesquioxane epoxidation catalyst anchored into mesoporous MCM-41. *Inorganic Chemistry Communications* **2000**, *3*, 557–562.

(47) Krijnen, S.; Mojet, B. L.; Abbenhuis, H. C. L.; Van Hooff, J. H. C.; Van Santen, R. A. MCM-41 heterogenised titanium silsesquioxane epoxidation catalysts: a spectroscopic investigation of the adsorption characteristics. *Physical Chemistry Chemical Physics* **1999**, *1*, 361–365.

(48) Krijnen, S.; Abbenhuis, H. C. L.; Hanssen, R. W. J. M.; van Hooff, J. H. C.; van Santen, R. A. Solid-Phase Immobilization of a New Epoxidation Catalyst. *Angewandte Chemie International Edition* **1998**, *37*, 356–358.

Chapter 2

TIN SILSESQUIOXANES AS MODELS FOR THE OPEN SITE IN TIN-CONTAINING ZEOLITE BETA

Information contained in Chapter 2 was originally published in:

(1) Brand, S. K.; Labinger, J. A.; Davis, M. E. Tin Silsesquioxanes as Models for the "Open" Site in Tin-Containing Zeolite Beta. *ChemCatChem* **2016**, *8*, 121–124, DOI: 10.1002/cctc.201501067,

2.1 Introduction

Zeolites containing framework Lewis acid sites have been demonstrated to be highly active and selective catalysts in the conversion of complex carbonyl-containing molecules.[1–3] Notably, tin-containing zeolite beta (Sn-Beta) has been shown to catalyze glucose to fructose in aqueous conditions with high yields.[4,5] The glucose isomerization pathway for this reaction had been shown to occur at the framework tin sites by 1) the ring-opening of glucose, 2) coordination of the glucose to the tin site, and 3) an intramolecular hydride shift from the C_2 to C_1 position on the open glucose chain.[6] Remarkably, this glucose isomerization pathway is analogous to what has been observed with metalloenzymes, such as D-xylose isomerase XI.[7,8]

To date, the catalytically active site of Sn-Beta has yet to be elucidated experimentally under reactions conditions. Corma *et al*. proposed that framework tin sites in Sn-Beta may exist in either an "open" (a $(SiO)_3SnOH$ center with an adjacent silanol group) or "closed" (a $(SiO)_4Sn$ center) state.[9] However, experimental results as well as theoretical calculations suggest that the open site is most active.[2,6,9–15] In work from the Davis lab, Bermejo-Deval

et al. sodium-exchanged the silanol groups adjacent to the open Sn site and observed a complete shift in selectivity from fructose to mannose, not only implying that the open site was likely the most active tin site, but also demonstrating the importance of the adjacent silanol group in the glucose isomerization pathway.[10] In this same study, the open site was selectively titrated with NH_3, which was discovered to render Sn-Beta effectively inactive, implying that the open site is most active, and that the closed sites do not convert to open sites under the conditions of the reaction. In a theoretical study, the effect of the adjacent silanol group at the open site was examined by Rai *et al*.[13] This work demonstrated that the activation energy to perform the 1,2-HS to form fructose was significantly lower when the adjacent silanol group participates in the reaction. However, when the silanol moiety acts as a spectator, the activation barrier to form mannose by the Bílik mechanism was found to be much lower than the isomerization reaction.

Here, we examine the reactivities and reaction pathways for homogeneous, readily-characterizable molecular analogues of the hypothesized active sites in Sn-Beta. The two tin silsesquioxanes studied are schematically shown in Figure 2.1.

Both materials retain octahedrally coordinated tin sites with an adjacent siloxy group capped by either a proton (**1a**), analogous to the open site in Sn-Beta, or a trimethylsilyl substituent (**1b**), representative of Na-Sn-Beta. These octahedral tin (IV) structures are stable in the presence of small amounts of water.[16]

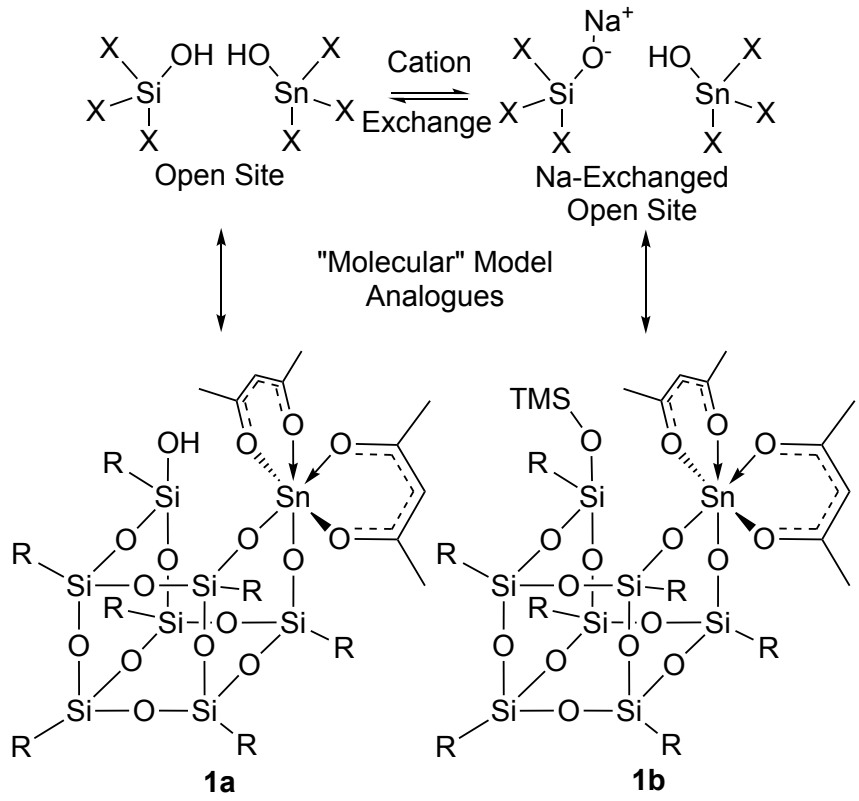

Figure 2.1: Schematic representation of the hypothesized active sites present in Sn-Beta, and the analogous tin silsesquioxanes synthesized. "R" denotes a cyclohexyl ligand, while and "X" signifies framework O-Si units. Two water molecules per Sn open site have been omitted for clarity in the top schematics.

2.2 Experimental Methods

General Air- and Water-Free Synthesis and Purification Procedures

All glassware was dried at 433 K prior to all syntheses, and purged with argon while cooling. All syntheses, purification procedures, and reaction tests were carried out under argon using standard air- and water-free techniques. Benzene (99.8%, anhydrous, Sigma-Aldrich), hexane (95%, anhydrous, Sigma-Aldrich), dimethyl sulfoxide (DMSO, ⩾99.9%, anhydrous, Sigma-Aldrich), toluene (99.8%, anhydrous, Sigma-Aldrich), and acetonitrile (99.8%, anhydrous, Sigma-Aldrich) were used as received. Triethylamine (99.5%, Sigma-Aldrich) was distilled from 3 Å molecular sieves. Tin bis(acetylacetonate) dichloride (98%,

Sigma-Aldrich) and chlorotrimethylsilane (⩾99%, Sigma-Aldrich) were both used without further purification.

The incompletely condensed cyclohexyl-ligated trisilanol silsesquioxane, **1**, was obtained from Hybrid Plastics. **1** was purified by recrystallization by slow diffusion of acetonitrile into a concentrated solution of THF. Purity of **1** was then confirmed using ^{1}H, ^{13}C, and ^{29}Si.

Synthesis of 1a and 1b

The methods of synthesis for **1a** and **1b** were adapted from Duchateau *et al* who alternatively used heptacyclopentyl trisilanol silsesquioxane as a starting material for their complexes.[16]

1a was synthesized by the addition of tin bis(acetylacetonate) dichloride ($Sn(acac)_2Cl_2$) and heptacyclohexyl trisilanol silsesquioxane, **1**, to a dried round bottom flask in stoichiometric quantities, and subsequently dissolved in toluene. A slight excess of triethylamine was then introduced as a scavenger base. The flask was placed in an oil bath at 353 K and allowed to react over night. Triethylamine hydrochloride slowly precipitated from solution, and after allowing the reaction to cool, was removed by filtration. The toluene was removed in vacuo. Hexane was then added, the solids were allowed to dissolve, and then the solvent was removed in vacuo yielding a white powder as a product in quantitative yields.

1b was synthesized by first reacting a stoichiometric quantity of chlorotrimethylsilane with **1** to produce a monosilylated intermediate compound, **1b-i**, as described by Feher *et al*.[17] The crude silylated product was purified by fractional recrystallization to remove any undesired di- or tri-silylated species. **1b-i** was then reacted with $Sn(acac)_2Cl_2$ using the method described for **1a** to yield **1b** in quantitative yields.

To ensure that all triethylamine (used as a scavenger base, and reported to be a highly selective catalyst in the conversion of glucose to fructose) and triethylamine hydrochloride were removed from both products, the purified solids were additionally heated to 343 K and held under vacuum for 12 hours to sublimate any residual triethylamine hydrochloride salt.[18] Characterization of the material demonstrated that neither the $Sn(acac)_2Cl_2$ nor triethylamine hydrochloride salt remained post-reaction.

Material Characterization

Nuclear magnetic resonance (NMR) spectra of **1a** and **1b** were collected either on a Varian Inova 500 (^{1}H, 499.7; ^{13}C, 125.7 MHz) equipped with a broadband probe or on a Varian Inova 400 (^{29}Si, 79.4; ^{119}Sn, 149.1 MHz). ^{29}Si and ^{119}Sn NMR were referenced to $SiMe_4$ and $SnMe_4$, respectively. Chromium(III) acetylacetonate ($Cr(acac)_3$) was added to samples for ^{29}Si and ^{119}Sn NMR characterization as a shiftless relaxation agent.

1a: ^{1}H NMR (500 MHz, $CDCl_3$, 298 K) δ = 5.57, 5.56 (s, 2 x C*H*, acac, 2H), 4.76 (s, SiO*H*, 1H), 2.18, 2.12, 2.04, 2.01 (s, 4 x CH_3, acac, 12 H), 1.82 – 1.60 (vbr m, CHH_2, cyclohexyl, 35 H), 1.35 – 1.05 (vbr m, CH_2, cyclohexyl, 35 H), 0.80 – 0.64 (vbr m, C*H*, cyclohexyl, 6 H), 0.58 (m, C*H*, cyclohexyl, 1 H). ^{13}C NMR (125.7 MHz, $CDCl_3$, 298 K) δ = 196.94, 196.10, 195.26, 194.76 (4 x *C*=O, acac), 102.39, 102.16 (2 x *C*H, acac), 28.30 – 26.50 (*C*H_2, cyclohexyl), 25.21, 25.18, 24.17, 24.03, 23.83, 23.56, 23.42 (*C*H, cyclohexyl, 1:1:1:1:1:1:1 ratio). ^{29}Si NMR (79.4 MHz, $CDCl_3$, 298 K, 0.02 M $Cr(acac)_3$) δ = -58.37 (*Si*OH), -64.31, -65.83, -67.47, -68.30, -69.14, -70.67 (O_3*Si*C_6H_{11}, 1:1:1:1:1:1:1 ratio). ^{119}Sn NMR (149.1 MHz, $CDCl_3$, 298 K, 0.02 M $Cr(acac)_3$) δ = -729.96.

1b: ^{1}H NMR (500 MHz, $CDCl_3$, 298 K) δ = 5.55, 5.53 (s, 2 x C*H*, acac, 2 H), 2.15, 2.12,

2.01, 2.00 (s, 4 x CH_3, acac, 12 H), 1.85 – 1.59 (vbr m, CH_2, cyclohexyl, 35 H), 1.32-1.10 (vbr m, CH_2, cyclohexyl, 35 H), 0.76 – 0.65 (vbr m, C*H*, cyclohexyl, 5 H), 0.60 (m, C*H*, cyclohexyl, 1 H), 0.45 (m, C*H*, cyclohexyl, 1 H), 0.13 (s, OSi(CH_3)$_3$, 9 H). ^{13}C NMR (125.7 MHz, $CDCl_3$, 298 K) δ = 196.52, 195.37, 194.87, 194.83 (4 x *C*=O, acac), 102.28, 102.10 (2 x *C*H, acac), 28.50 – 26.50 (*C*H_2, cyclohexyl), 25.67, 25.58, 25.43, 25.27, 24.49, 23.59, 23.45 (*C*H, cyclohexyl, 1:1:1:1:1:1:1 ratio), 2.13 (OSi(*C*H_3)$_3$. ^{29}Si NMR (79.4 MHz, $CDCl_3$, 298 K, 0.02 M Cr(acac)$_3$) δ = 8.84 (s, O*Si*(CH$_3$)$_3$, -65.69, -67.33, -67.60, -67.83, -68.31, -70.33, -71.87 (O_3*Si*C_6H_{11}, 1:1:1:1:1:1:1 ratio). ^{119}Sn NMR (149.1 MHz, $CDCl_3$, 298 K, 0.02 M Cr(acac)$_3$) δ = -738.01.

Variable-temperature (VT) NMR experiments were used to determine how the structures of the catalysts were affected under reaction conditions. In a typical experiment, a 2% (w/w) glucose solution (1:1 volumetric ratio of benzene and DMSO) was mixed with each catalyst (maintaining a 25:1 glucose to Sn molar ratio) in an NMR tube. Due to a number of overlapping peaks in the ^{1}H and ^{13}C NMR spectra amongst the catalysts, glucose, and reaction products, only ^{29}Si and ^{119}Sn spectra were collected to evaluate the structure of the catalyst. In conducting the VT NMR experiments, the system was allowed to equilibrate at a given temperature in the NMR for 10 minutes, and then a spectrum was obtained (256 scans for each nuclei). Due to line broadening effects, ^{29}Si spectra were only obtained at 278 and 353 K.

Glucose Reaction Procedures

Reactions with D-glucose (Sigma-Aldrich, anhydrous, ⩾99.5%) were conducted in 10 mL thick-walled glass reactors (VWR) that were heated in a temperature-controlled oil bath

placed on top of a digital stirring hot plate (Fisher Scientific). Glucose, **1a**, and **1b** were separately dried under vacuum (<50 mTorr) for at least 12 hours prior to the addition of the anhydrous DMSO and benzene solvents, respectively. Additionally, the glass reactors and stir bars were dried at 433 K for at least 3 hours in an oven, capped with a Teflon septum, and allowed to cool under an argon purge. In a typical reaction, the dried reactors were charged with equivalent volumetric quantities of glucose and catalyst stock solutions to obtain a 6 mL reactor volume. The resultant mixture yielded a 2% (w/w) initial glucose solution, with a Sn/glucose molar ratio of 1:75. Reactors were placed in the oil bath at 353 K, and approximately 125 mg aliquots were extracted every 15 minutes. These reaction aliquots were mixed with 125 mg of a 2% (w/w) aqueous D-mannitol (Sigma-Aldrich, ⩾98%) solution, which was used as an internal standard for quantification. To ensure thorough catalyst removal from the aliquot solution prior to quantification, 0.3 mL of H_2O was added, and the solution was filtered using a 0.2 μm PTFE syringe filter.

Reaction aliquots were analyzed by high performance liquid chromatography (HPLC) using an Agilent 1200 system (Agilent) equipped with refractive index (RI) and evaporative light scattering (ELS) detectors. The glucose, fructose, mannose, and mannitol fractions were separated with a Hi-Plex Ca column (6.5 x 300 mm, 8 μm particle size, Agilent) held at 353 K. Ultrapure water was used as the mobile phase at a flow rate of 0.6 mL min^{-1}.

Glucose conversion and product yields were calculated by:

$$X_{gluc} = \frac{n_{gluc}(t=0) - n_{gluc}(t)}{n_{gluc}(t=0)} x100[\%] \tag{2.1}$$

$$Y_i(t) = \frac{n_i(t)}{n_{gluc}(t=0)} x100[\%] \tag{2.2}$$

where $X_{gluc}(t)$ is the glucose conversion at time t; $Y_i(t)$ is the yield of product i at time t; $n_{gluc}(t = 0)$ is the initial moles of glucose in the reactor; and $n_i(t)$ is the moles of product i at time t.

Reactions performed using labeled ^{13}C glucose at the C_1 position (Cambridge Isotope Laboratories, 1-^{13}C D-glucose, 98-99%), glucose enriched with deuterium at the C_2 position of glucose (Omicron Biochemicals, D-[2-^{2}H]-glucose, 98% ^{2}H), and doubly labeled glucose with deuterium at the C_2 position and labeled ^{13}C glucose at the C_1 position (Omicron Biochemicals, D-[2-^{2}H;1-^{13}C;]-glucose, 99% ^{13}C, 98% ^{2}H) were performed utilizing the same procedures outlined for D-glucose. Generally, 10% (w/w) initial glucose solutions were used for isotopic labeling experiments. All other conditions remain equivalent as described for D-glucose. However, these reactions were quenched in cold water after a set duration. To separate the catalyst from the reaction solution, approximately 6 mL of ultrapure water was added and the resultant biphasic solution was filtered. The solvent of the catalyst-free fraction was then removed *in vacuo*. The recovered solids were then dissolved in deuterium oxide and analyzed using ^{1}H (64 scans) and ^{13}C (2048 scans) NMR. These NMR spectra were referenced to 3-(trimethylsilyl)-1-propanesulfonic acid sodium salt (DSS).

2.3 Results and Discussion

Reaction Testing

The catalytic activities of **1a** and **1b** were examined using batch reactions. Conversion and yield data for glucose reactions catalyzed by **1a** and **1b** are presented in Figure 2.2. For **1a**, fructose is formed as the major primary product. Initially, a small amount of mannose

is produced concomitantly, but it does not continue to increase after approximately 30 minutes. This behavior is in part likely due to a secondary mannose to fructose isomerization mechanism. After 120 minutes, the maximum yields obtained were 19.0% and 5.7% for fructose and mannose, respectively. Glucose reactions with **1b**, however, demonstrate a significant shift in product selectivity to yield 10.2% mannose and 2.2% fructose over the same reaction duration. These reaction data highlight the influence of the interaction between the open-chain glucose and the silanol group adjacent to the Lewis acidic tin site. It is clear that the presence of the silanol group results in the selective formation of fructose from glucose. However, removal of the silanol group produces predominantly mannose. Qualitatively, these reactivity results are in agreement with those obtained by Bermejo-Deval *et al.* and Rai *et al.*[10,13]

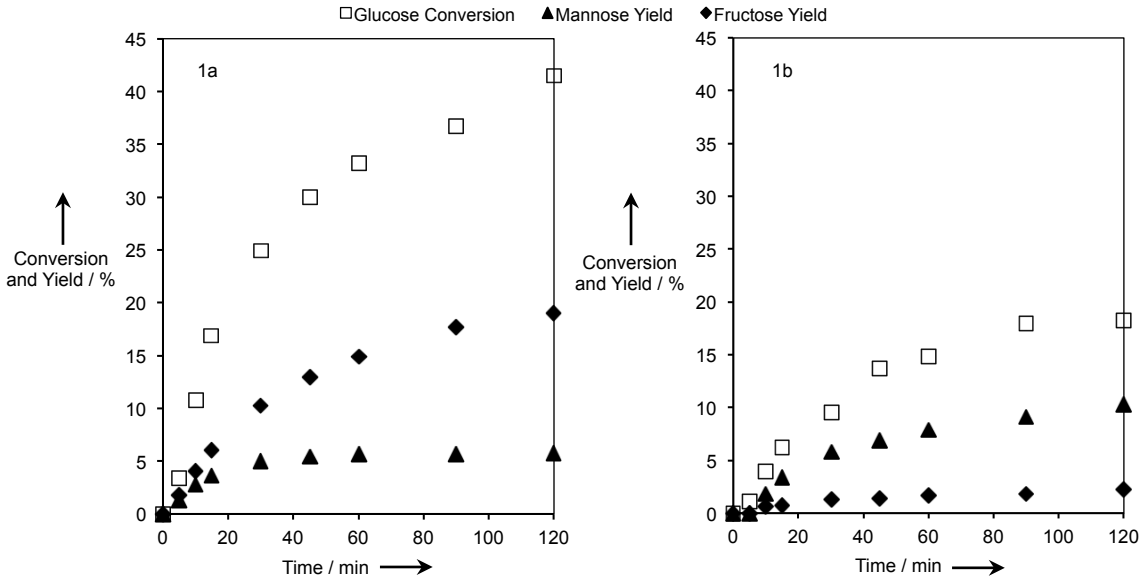

Figure 2.2: Conversion and yield profiles for reactions with unlabelled glucose: **1a** (left) and **1b** (right) at 353 K.

Examination of the structural integrity of 1a and 1b

Confirmation that **1a** and **1b** were the sole Sn species in solution was obtained by in situ NMR characterization while exposing the catalyst to reaction conditions. ^{29}Si and ^{119}Sn NMR spectra (Figures A.1 – A.3) of **1b** in the presence of glucose demonstrates that neither the geometry of the cluster, nor the electronic structure around the Sn changes. For **1a**, a change in the ^{29}Si and ^{119}Sn NMR spectra is observed (Figure A.4), however, this is most likely due to an interaction between the silanol group and Sn site inducing a geometric rearrangement of the catalyst under reaction conditions. Importantly, hydrolysis products for either catalyst are not observed at reaction temperatures in the presence of glucose. Therefore, these data suggest that the tin silsesquioxanes remain intact under reaction conditions and indicate that under the reaction conditions used the Sn-OSi bonds are not hydrolyzed to irreversibly form a free tin species and **1**.

The hydrogen bonding capacity of the silanol moiety on **1a** complicates the analysis demonstrated with **1b**, but generally leads to the same conclusion. The ^{119}Sn spectrum at 353 K is shown in Figure A.4. Compared to **1a** in $CDCl_3$, there is a noticeable shift upfield in the ^{119}Sn spectra (no such shift is observed with **1b**). This indicates that the Sn center has become more shielded, perhaps due to a small interaction between the electron rich silanol group and the Sn. This peak does not correspond to a free tin species. The ^{29}Si spectrum collected after cooling the sample is additionally shown in Figure A.4. This confirms that a shift in the geometry of the catalyst occurs; however, none of the peaks corresponding to the starting material are present. This strongly suggests that hydrolysis of the material has not occurred.[19] The implied geometry of this complex is not in agreement

with typical dimer formation due to the interaction between two silanol groups. Rather, the 3:1:1:2 relative peak ratio is suggestive of a complex of higher symmetry that may perhaps be induced by an interaction between the silanol group and Sn. The results obtained from the VT NMR experiments performed with **1b** indicate that the Sn-OSi bond are not broken under reaction conditions. Generally, the substitution of the TMS moiety with a hydroxyl group to form **1a** would not be expected to destabilize these bonds, further indicating that **1a** simply rearranges under reaction conditions.

Reaction Mechanism Elucidation

To examine the mechanism by which fructose and mannose are produced by **1a** and **1b**, ^{1}H and ^{13}C nuclear magnetic resonance (NMR) spectroscopy were used. Figure 2.3 summarizes the ^{13}C spectra of the product solutions obtained from reacting 10 %(w/w) solutions of glucose deuterated at the C_2 position (2-^{2}H glucose), glucose enriched with ^{13}C at the C_1 position (1-^{13}C glucose), or glucose consisting of a combination thereof (2-^{2}H; 1-^{13}C glucose). For reactions carried out using deuterium labeled glucose, low intensity triplets are observed for the starting reagent, as well as near the anticipated fructose resonances. This effect is a consequence of the nuclear Overhauser enhancement (NOE), a technique utilized to amplify ^{13}C resonances for directly bonded ^{1}H-^{13}C pairs. ^{2}H-^{13}C connectivity however, interrupts this effect, and results in substantial attenuation of the ^{13}C resonances and production of triplets from coupling to ^{2}H (spin 1). This effect allows for the simultaneous tracking of ^{2}H and ^{13}C labels using solely ^{13}C NMR.

The absence of a singlet in the product spectra from reactions run with 2-^{2}H glucose (Figures 2.3 a,c,d,f) at δ = 77.0 and 74.3 ppm (while simultaneously retaining low lying

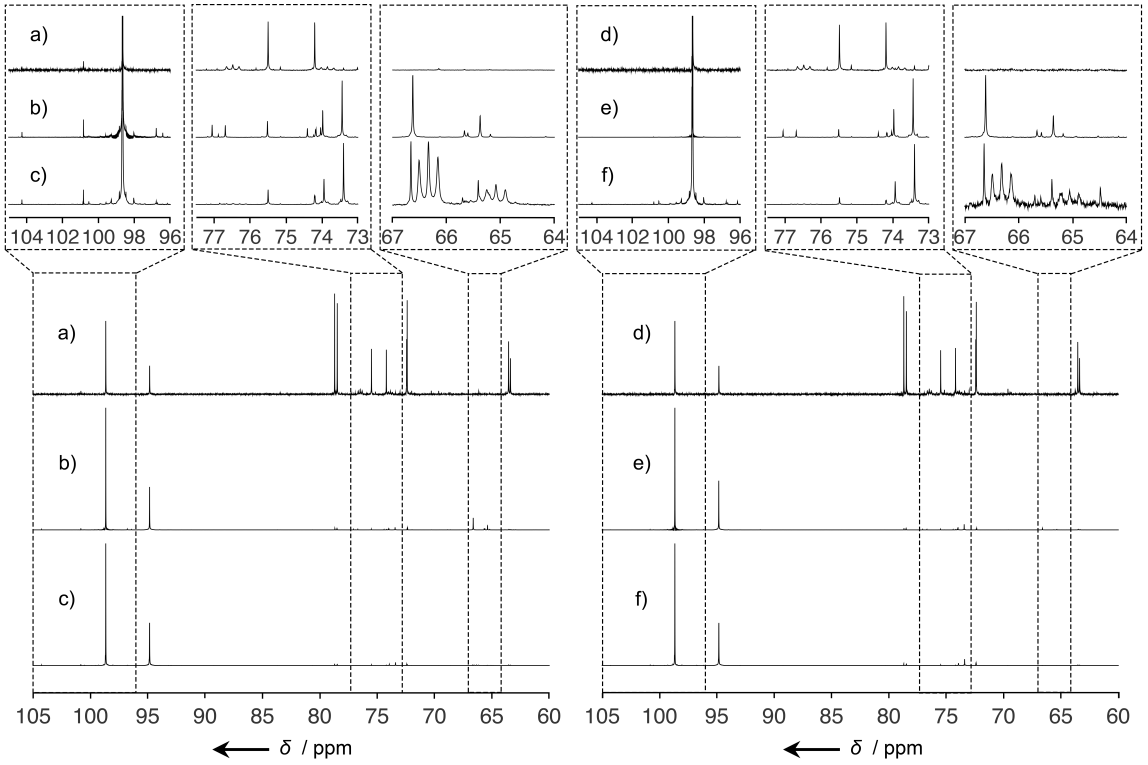

Figure 2.3: ^{13}C NMR spectra of the reactant and product solutions in D_2O obtained after reacting a) 2-^{2}H glucose, b) 1-^{13}C glucose, and c) 2-^{2}H; 1-^{13}C glucose with **1a**; d) 2-^{2}H glucose, e) 1-^{13}C glucose, and f) 2-^{2}H; 1-^{13}C glucose with **1b**. The inset spectra have been enlarged to different extents for clarity and do not represent measured intensities.

triplets) demonstrates that the glucose does not undergo isotopic scrambling. Additionally, ^{1}H NMR demonstrates (Figures A.5 a,c,d,f) that a peak at δ = 3.2 ppm corresponding to 2-^{2}H, does not arise post-reaction confirming that isotopic scrambling events do not occur.[2] Importantly, this demonstrates that any isotopic rearrangement that occurs throughout a reaction is solely an act of **1a** or **1b** and not due to the solvent system.

Reactions performed with 1-^{13}C glucose and **1a** (Figure 2.3 b,e) demonstrate intense peaks at δ = 66.7 and 65.5 ppm, that are representative of the β and α forms of 1-^{13}C fructofuranose, respectively. Additionally, less intense peaks are observed at δ = 74.0 and 73.5 ppm, assignable to the β and α forms of 2-^{13}C mannopyranose, respectively. This

result is also observed with reactions run with 2-^{2}H; 1-^{13}C glucose and **1a**, indicating that a 1,2-intramolecular carbon shift occurs corresponding to the Bílik mechanism.[20–22] For this reactant however, a different result is observed in the region associated with 2-^{13}C fructose. The data in Figure 2.3 c,f depict low intensity triplets at δ = 66.3 and 65.0 indicative of a deuterium bound to the labeled ^{13}C at that position. However, small singlets are also observed as when 1-^{13}C glucose was used as a starting material. Typically, this result would be suggestive of a base-catalyzed mechanism. In this instance it is likely a consequence of utilizing a compound with a small quantity of ^{1}H (*ca.* 2%) at the C_2 position. A similar phenomenon was observed when 2-^{2}H; 1-^{13}C glucose was reacted with Sn-Beta (Figure A.6 a,b).

These isotopic labeling experiments demonstrate that for both **1a** and **1b**, fructose and mannose are produced from glucose *via* a 1,2-HS and a 1,2-CS, respectively. **1a** appears to promote the 1,2-HS reaction, selectively producing fructose from glucose. A 1,2-HS also occurs to form fructose from mannose for reactions catalyzed by **1a** but is not observed with **1b** under the conditions examined, likely due to a low concentration of mannose. The 1,2-CS is shown to occur for both catalysts. However, the reaction data indicate that this pathway is significantly favored for **1b**. A summary of the reaction pathways is given in Figure 2.4.

2.4 Conclusion

In summary, we have shown that **1a** and **1b** catalyze glucose in qualitatively equivalent yields to the respective active sites hypothesized in Sn-Beta and Na-Sn-Beta. These reactions are also performed through equivalent mechanistic pathways. The use of well-defined, stable

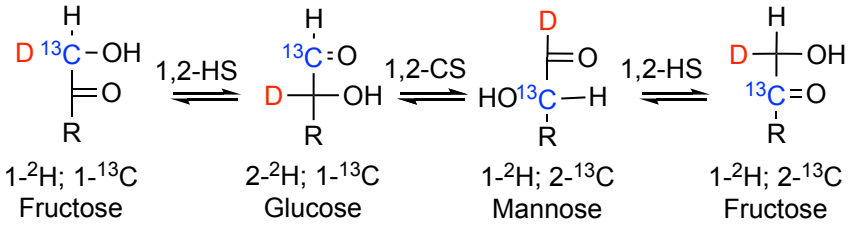

Figure 2.4: Schematic representation of the reaction network of glucose with **1a** and **1b** deduced from isotopic labelling experiments. R = $C_4O_4H_9$.

molecular analogues of framework tin sites conclusively demonstrates the structure-activity relationship of the open site present in Sn-Beta. These data indicate that an octahedral tin site adjacent to a silanol group results in the selective formation of fructose *via* a 1,2-HS. However, removing the silanol group results in a qualitative shift to the mannose producing 1,2-CS mechanism, as was first reported by Bermejo-Deval *et al*.[5] These results with our "molecular" models strongly suggest that the open site is the most active catalytic center in Sn-Beta, and that the silanol group is a crucial moiety affecting the distribution of products obtained from reacting glucose. Furthermore, our study indicates that the sodium cation present in sodium-exchanged Sn-Beta is likely most strongly associated with the siloxy group adjacent to the tin site.

2.5 Acknowledgments

Research was supported as part of the Catalysis Center for Energy Innovation, an Energy Frontier Research Center funded by the U.S. Department of Energy (DOE), Office of Science, Basic Energy Sciences (BES), under Award number DE-SC0001004. S.K.B. wishes to acknowledge funding from the National Science Foundation Graduate Research Fellowship Program under Grant No. DGE-1144469. Any opinions, findings, and conclusions or recommendations expressed in this material are those of the author(s) and do not necessarily

reflect the views of the National Science Foundation. The authors would like to thank Marat Orazov for numerous useful conversations.

2.6 References

(1) Román-Leshkov, Y.; Davis, M. E. Activation of Carbonyl-Containing Molecules with Solid Lewis Acids in Aqueous Media. *ACS Catalysis* **2011**, *1*, 1566–1580.

(2) Román-Leshkov, Y.; Moliner, M.; Labinger, J. A.; Davis, M. E. Mechanism of glucose isomerization using a solid Lewis acid catalyst in water. *Angewandte Chemie (International ed. in English)* **2010**, *49*, 8954–7.

(3) Corma, A.; García, H. Lewis Acids as Catalysts in Oxidation Reactions: From Homogeneous to Heterogeneous Systems. *Chemical reviews* **2002**, *102*, 3837–92.

(4) Moliner, M.; Román-Leshkov, Y.; Davis, M. E. Tin-containing zeolites are highly active catalysts for the isomerization of glucose in water. *Proceedings of the National Academy of Sciences of the United States of America* **2010**, *107*, 6164–6168.

(5) Bermejo-Deval, R.; Gounder, R.; Davis, M. E. Framework and Extraframework Tin Sites in Zeolite Beta React Glucose Differently. *ACS Catalysis* **2012**, *2*, 2705–2713.

(6) Bermejo-Deval, R.; Assary, R. S.; Nikolla, E.; Moliner, M.; Roman-Leshkov, Y.; Hwang, S.-J.; Palsdottir, A.; Silverman, D.; Lobo, R. F.; Curtiss, L. A.; Davis, M. E. Metalloenzyme-like catalyzed isomerizations of sugars by Lewis acid zeolites. *Proceedings of the National Academy of Sciences* **2012**, *109*, 9727–9732.

(7) Allen, K. N.; Lavie, A.; Farber, G. K.; Glasfeld, A.; Petsko, G. A.; Ringe, D. Isotopic exchange plus substrate and inhibition kinetics of D-xylose isomerase do not support a proton-transfer mechanism. *Biochemistry* **1994**, *33*, 1481–1487.

(8) Kovalevsky, A. Y.; Hanson, L.; Fisher, S. Z.; Mustyakimov, M.; Mason, S. A.; Forsyth, V. T.; Blakeley, M. P.; Keen, D. A.; Wagner, T.; Carrell, H. L.; Katz, A. K.; Glusker, J. P.; Langan, P. Metal Ion Roles and the Movement of Hydrogen during Reaction Catalyzed by D-Xylose Isomerase: A Joint X-Ray and Neutron Diffraction Study. *Structure* **2010**, *18*, 688–699.

(9) Boronat, M.; Concepción, P.; Corma, A.; Renz, M.; Valencia, S. Determination of the catalytically active oxidation Lewis acid sites in Sn-beta zeolites, and their optimisation by the combination of theoretical and experimental studies. *Journal of Catalysis* **2005**, *234*, 111–118.

(10) Bermejo-Deval, R.; Orazov, M.; Gounder, R.; Hwang, S. J.; Davis, M. E. Active sites in Sn-beta for glucose isomerization to fructose and epimerization to mannose. *ACS Catalysis* **2014**.

(11) Osmundsen, C. M.; Holm, M. S.; Dahl, S.; Taarning, E. Tin-containing silicates: structure-activity relations. *Proceedings of the Royal Society A: Mathematical, Physical and Engineering Sciences* **2012**, *468*, 2000–2016.

(12) Boronat, M.; Concepción, P.; Corma, A.; Navarro, M. T.; Renz, M.; Valencia, S. Reactivity in the confined spaces of zeolites: the interplay between spectroscopy and theory to develop structure-activity relationships for catalysis. *Physical chemistry chemical physics : PCCP* **2009**, *11*, 2876–2884.

(13) Rai, N.; Caratzoulas, S.; Vlachos, D. G. Role of Silanol Group in Sn-Beta Zeolite for Glucose Isomerization and Epimerization Reactions. *ACS Catalysis* **2013**, *3*, 2294–2298.

(14) Li, Y.-P.; Head-Gordon, M.; Bell, A. T. Analysis of the Reaction Mechanism and Catalytic Activity of Metal-Substituted Beta Zeolite for the Isomerization of Glucose to Fructose. *ACS Catalysis* **2014**, *4*, 1537–1545.

(15) Harris, J. W.; Cordon, M. J.; Di Iorio, J. R.; Vega-Vila, J. C.; Ribeiro, F. H.; Gounder, R. Titration and quantification of open and closed Lewis acid sites in Sn-Beta zeolites that catalyze glucose isomerization. *Journal of Catalysis* **2016**, *335*, 141–154.

(16) Duchateau, R.; Dijkstra, T. W.; Severn, J. R.; van Santen, R. A.; Korobkov, I. V. Synthesis and characterization of tin containing polyhedral oligometallasilsesquioxanes (POMSS). *Dalton transactions (Cambridge, England : 2003)* **2004**, 2677–82.

(17) Feher, F. J.; Newman, D. A.; Walzer, J. F. Silsesquioxanes as models for silica surfaces. *Journal of the American Chemical Society* **1989**, *111*, 1741–1748.

(18) Liu, C.; Carraher, J. M.; Swedberg, J. L.; Herndon, C. R.; Fleitman, C. N.; Tessonnier, J.-P. Selective Base-Catalyzed Isomerization of Glucose to Fructose. *ACS Catalysis* **2014**, *4*, 4295–4298.

(19) Feher, F. J.; Budzichowski, T. A.; Weller, K. J. Polyhedral aluminosilsesquioxanes: soluble organic analogs of aluminosilicates. *Journal of the American Chemical Society* **1989**, *111*, 7288–7289.

(20) Bílik, V. Reactions of Saccharides Catalyzed by Molybdate Ions. II.* Epimerization of D-Glucose and D-Mannose. *Chem. Zvesti* **1972**, *26*, 183–186.

(21) Bílik, V.; Petrus, L.; Farkas, V. Reactions of saccharides catalyzed by molybdate ions. XV.* Mechanism of the epimerization reaction. *Chem. Zvesti* **1975**, *685*, 690–693.

(22) Bílik, V.; Petrus, L.; Zemek, J. Reactions of saccharides catalyzed by molybdate ions. XIX.* Molybdate complexes and epimerization of aldoses as a function of pH. *Chem. Zvesti* **1978**, *32*, 242–251.

Chapter 3

METHYL-LIGATED TIN SILSESQUIOXANE CATALYZED REACTIONS OF GLUCOSE

Information contained in Chapter 3 was originally published in:

(1) Brand, S. K.; Josephson, T. R.; Labinger, J. A.; Caratzoulas, S.; Vlachos, D. G.; Davis, M. E. Methyl-Ligated Tin Silsesquioxane Catalyzed Reactions of Glucose. *Journal of Catalysis* **2016**, *341*, 62–71, DOI: 10.1016/j.jcat.2016.06.013,

T.R.J. provided computational data presented in this chapter.

3.1 Introduction

Microporous solids containing Lewis acid sites have garnered considerable interest for their ability to selectively convert highly functionalized, carbonyl-containing molecules such as glucose.[1–3] Interest in carbonyl-based chemistry has been driven by the attractiveness of producing transportation fuels and fine chemicals from biomass-derived sources.[4–6] A tin-containing molecular sieve with the zeolite beta topology (Sn-Beta) has emerged as a useful solid Lewis acid catalyst to perform highly selective reactions with carbohydrates, such as the isomerization of glucose to fructose.[7] Sn-Beta, initially synthesized by Corma *et al*., has been demonstrated to catalyze the Baeyer-Villiger oxidation of ketones to lactones, Meerwein-Ponndorf-Verley (MPV) reduction of aldehydes and ketones, isomerization and epimerization of glucose, carbon-carbon bond coupling reactions, and Diels-Alder reactions.[7–17]

The efficacy of Sn-Beta has stimulated research on resolving the active catalytic site and mechanism for the glucose isomerization reaction. Metal-containing zeolites like

Sn-Beta, contain a distribution of "closed" sites (a $(SiO)_4Sn$ center) and "open" sites (a $(SiO)_3SnOH$ center with an adjacent silanol group) that occur when the framework is partially hydrolyzed.[18] In a recent study, Harris *et al*. demonstrated that the number of open and closed sites in Sn-Beta may be quantitatively determined utilizing Lewis bases as titrants.[19] In the same report, an inverse linear correlation between the initial rate of glucose isomerization with the amount of pyridine dosed was demonstrated, implying that isomerization activity should be fully suppressed when all open sites are titrated. Bermejo-Deval *et al*. sodium-exchanged the silanol groups adjacent to the open tin site and observed a complete shift in selectivity from fructose to mannose, providing the first experimental evidence that the open site was the most active tin site, as well as emphasizing the significance of the silanol moiety in the reaction mechanism.[15] This work also revealed that titration of the open site with NH_3 (Sn-Beta-NH_3) attenuated the activity of the catalyst, indicating that the open and closed sites do not interconvert under reaction conditions.

Several different reaction mechanisms involving a catalytically active open site have been proposed. Work from Li *et al*. suggests that glucose first binds to the open site through coordination of the basic C_1 carbon hydroxyl, with subsequent transfer of the acidic proton to the framework lattice followed by a 1,2-intramolecular hydride shift.[20] This results in a monodentately bound fructose stabilized by the adjacent silanol group through the O_1 oxygen. Yang *et al*. consider a similar type of mechanism involving the closed site.[21] Rai *et al*. and Christianson *et al*. propose similar pathways, however, their calculations involve the acidic C_2 hydroxyl proton transferring to the stannanol group, forming a water molecule.[22,23] Rai *et al*. also demonstrated that in the absence of a silanol group adjacent to the tin center, the glucose binds to the tin bidentately and selectively produces mannose

through a 1,2-intramolecular carbon shift. Experimental results support this prediction.[15] The Davis lab has also shown the effect of the silanol moiety in directing the selectivity of glucose conversion to either fructose or mannose using a pair of silsesquioxanes retaining an octahedral tin site with and without an adjacent silanol substituent.[24]

The observation of some glucose activity despite poisoning (Sn-Beta-NH_3) implies that there may be other reaction pathways with rates slower than those catalyzed by the open site in Sn-Beta. One possible pathway could involve the protonation of a framework Sn-O-Si bond by glucose to facilitate binding to the Lewis acidic site. To test this case, we synthesized a methyl-ligated tin silsesquioxane (**2a**), and investigated its glucose reaction pathways, both experimentally and theoretically. Compound **2a** contains a tin atom terdentately bound to a silsesquioxane ligand through three Sn-O-Si bridging bonds, as schematically shown in Figure 3.1. Here, we demonstrate that **2a** is an active catalyst (but with low rates of reaction) for the conversion of glucose to mannose and fructose *via* 1,2-intramolecular carbon and hydride shifts, respectively. Additionally, a hybrid quantum mechanics/molecular mechanics (QM/MM) electronic structure model is used to compare pathways in the production of fructose and mannose. The catalytic cycle model consists of three distinct operations: 1) deprotonation and ring-opening of glucose, 2) hydride- or carbon-shift (Bílik) reactions, and 3) ring-closing and reprotonation of the mannose or fructose products.

3.2 Experimental Methods

General Air- and Water-Free Synthesis and Purification Procedures

All glassware was dried at 433 K prior to all syntheses, and purged with argon while cooling. All syntheses, purification procedures, and reaction tests were carried out under

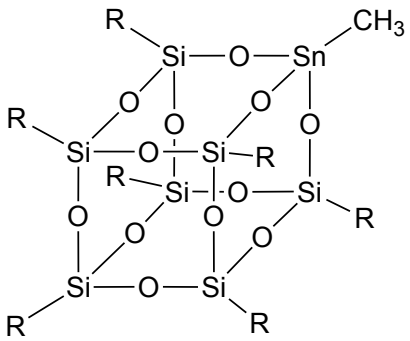

Figure 3.1: Schematic representation of the structure of **2a**. R = cyclohexyl.

argon using standard air- and water-free techniques. Benzene (99.8%, anhydrous, Sigma-Aldrich), hexane (95%, anhydrous, Sigma-Aldrich), tetrahydrofuran (THF, ⩾99.9%, anhydrous, Sigma-Aldrich), dimethyl sulfoxide (DMSO, ⩾99.9%, anhydrous, Sigma-Aldrich) and acetonitrile (99.8%, anhydrous, Sigma-Aldrich) were used as received. Triethylamine (99.5%, Sigma-Aldrich) was distilled from 3A molecular sieves. Methyltin trichloride (97%, Sigma-Aldrich) was used without further purification. Heptacyclohexyl trisilanol silsesquioxane (**1**) was obtained from Hybrid Plastics and recrystallized by slow diffusion of acetonitrile into a concentrated THF solution of; its purity was confirmed by ^{1}H, ^{13}C, and ^{29}Si NMR.

Synthesis of 2a

2a was synthesized by the reaction of methyltin trichloride with the incompletely condensed trisilanol silsesquioxane **1**, as reported by Feher *et al*.[25] To ensure that all triethylamine (used as a scavenger base, and reported to be a highly selective catalyst in the conversion of glucose to fructose) was removed from the product, acetonitrile was layered onto a concentrated solution of **2a** in benzene.[26] The resultant white powder was filtered and dried for 12 hours

under a dynamic vacuum of <50 mTorr.

Material Characterization

Nuclear magnetic resonance (NMR) spectra of **2a** were collected either on a Varian Inova 500 (^{1}H, 499.7 MHz; ^{13}C, 125.7 MHz) equipped with a broadband probe or on a Varian Inova 400 (^{29}Si, 79.4 MHz; ^{119}Sn, 149.1 MHz). ^{29}Si and ^{119}Sn NMR were referenced to $SiMe_4$ and $SnMe_4$, respectively. Chromium(III) acetylacetonate ($Cr(acac)_3$) was added to samples for ^{29}Si and ^{119}Sn NMR characterization as a shiftless relaxation agent.

^{1}H NMR (500 MHz, $CDCl_3$, 298 K): δ = 1.60-1.90 (vbr m, CH_2, cyclohexyl, 35 H), δ = 1.10-1.33 (vbr m, CH_2, cyclohexyl, 35 H), δ = 0.94 (s, CH_3, methyl, 35 H), δ = 0.65-0.81 (vbr m, C*H*, cyclohexyl, 7 H). ^{13}C NMR (125.7 MHz, $CDCl_3$, 298 K): δ = 27.70, 27.56, 27.18, 26.95, 26.73, 26.67 (s, *C*H_2, cyclohexyl); δ = 24.35, 23.44, 23.24 (s, 3:3:1 for *C*H, cyclohexyl); δ = -3.13 (s,*C*H_3, methyl). ^{29}Si NMR (79.4 MHz, $CDCl_3$, 298 K, 0.02 M $Cr(acac)_3$): δ = -65.01, -68.24, -69.55 (s, 3:1:3). ^{119}Sn NMR (149.1 MHz, $CDCl_3$, 298 K, 0.02 M $Cr(acac)_3$): δ = -247.60.

Reaction Procedures

Reactions of D-glucose (Sigma-Aldrich, anhydrous, ⩾99.5%) were conducted under anhydrous conditions in 10 mL thick-walled glass reactors (VWR) that were heated in a temperature-controlled oil bath placed on top of a digital stirring hot plate (Fisher Scientific). Both glucose and **2a** were separately dried under vacuum (<50 mTorr) for at least 12 hours prior to the addition of anhydrous DMSO and benzene solvents, respectively. Glass reactors (with their stir bars) were dried for at least 3 hours at 433 K, capped with Teflon

septa, and purged with argon while cooling. In a typical reaction, the dried reactors were charged with 6 mL of a 1:1 volumetric ratio of the catalyst and glucose stock solutions, resulting in a 2% (w/w) initial glucose solution, with a glucose:Sn molar ratio of 75. Reactors were placed in the oil bath at a predetermined temperature, and approximately 125 mg aliquots were extracted at regular time intervals. These reaction aliquots were mixed with 125 mg of a 2% (w/w) aqueous D-mannitol (Sigma-Aldrich, ⩾98%) solution, which was used as an internal standard for quantification. To ensure thorough catalyst removal from the aliquot solution prior to quantification, 0.3 mL of H_2O was added, and the solution was filtered using a 0.2 μm PTFE syringe filter.

Reaction aliquots were analyzed by high performance liquid chromatography (HPLC) using an Agilent 1200 system (Agilent) equipped with refractive index (RI) and evaporative light scattering (ELS) detectors. The glucose, fructose, mannose, and mannitol fractions were separated with a Hi-Plex Ca column (6.5 x 300 mm, 8 μm particle size, Agilent) held at 353 K. Ultrapure water was used as the mobile phase at a flow rate of 0.6 mL min^{-1}. Conversions and yields were calculated by:

$$X_{gluc} = \frac{n_{gluc}(t=0) - n_{gluc}(t)}{n_{gluc}(t=0)} x100[\%] \tag{3.1}$$

$$Y_i(t) = \frac{n_i(t)}{n_{gluc}(t=0)} x100[\%] \tag{3.2}$$

where $X_{gluc}(t)$ is the glucose conversion at time t, $Y_i(t)$ is the yield of product i at time t, $n_{gluc}(t=0)$ is the initial moles of glucose in the reactor, and $n_i(t)$ is the moles of product i at time t.

Reactions using singly- and doubly-labeled glucose at the C_1 position (1-^{13}C glucose, 98-

99%, Cambridge Isotope Laboratories; 2-^{2}H; 1-^{13}C glucose, 99% ^{13}C, 98% ^{2}H, Omicron Biochemicals) were performed utilizing the same conditions outlined for D-glucose, but were quenched in cold water after a set duration. To separate the catalyst from the reaction solution, approximately 6 mL of ultrapure water was added and the resultant biphasic solution was filtered. Solvent was removed from the catalyst-free fraction by rotary evaporation; the recovered solids were dissolved in D_2O and analyzed by ^{1}H and ^{13}C NMR. These NMR spectra were referenced to 3-(trimethylsilyl)-1-propanesulfonic acid sodium salt (DSS).

Computational Methods

Hybrid quantum mechanics/molecular mechanics (QM/MM) electronic structure calculations were used to examine the interactions between the sugars and the catalyst and also to compute various reaction pathways for glucose isomerization and epimerization. All 167 atoms of the catalyst/sugar complex were included in all of the calculations. Within the framework of the ONIOM approach to QM/MM calculations, the M062X functional was implemented to model the quantum mechanical domain of the system.[27–29] Specifically, the cyclohexyl ligands terminating the Si corners of **2a** were parameterized using the universal molecular mechanics force field (UFF). The complexing sugar, methyl substituent, and the silicon and oxygen atoms of the complex were modeled with the 6-31G(d,p) basis set, while the Sn atom was described using the LANL2DZ effective core basis set.[30] All calculations were performed in the gas phase using Gaussian 09 version A.09.[31]

3.3 Results and Discussion

Catalytic Behavior of 2a

Conversion and yield data for glucose reactions catalyzed by **2a** are given in Figure 3.2 and Figure 3.3, respectively. Reaction profiles were collected between 363 – 393 K at 10 K intervals. As with Sn-Beta-NH_3, **2a** converts glucose more selectively to mannose than fructose. Fructose is detected as a primary product. As the reaction temperature is increased, formation of by-products becomes increasingly significant, as indicated by the deterioration in carbon balance (Figure B.1). An initial investigation into identifying these products indicates that numerous retro-aldol and aldol products are formed. Retro-aldol and aldol reactions have been reported to be catalyzed by tin-containing molecular sieves, although under different reaction conditions, *e.g.*, at high temperatures (>433 K) and through the use of tandem catalysts.[32,33]

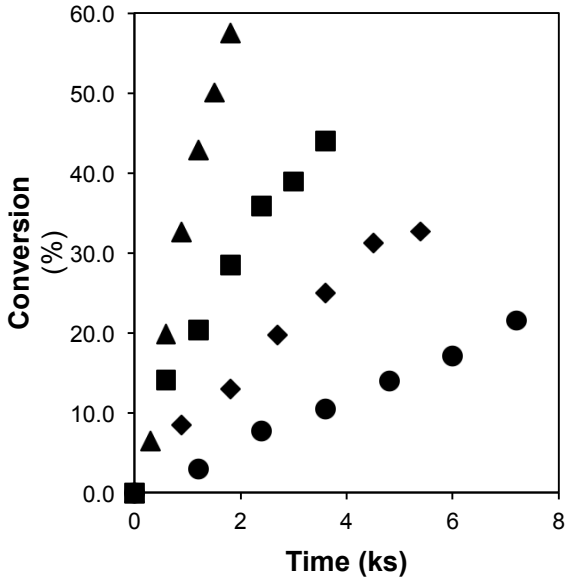

Figure 3.2: Glucose conversion as a function of time from the reaction of 2% (w/w) glucose in 1:1 DMSO:benzene solution with **2a** (1:75 Sn/glucose molar ratio) at 363 K (●), 373 K (♦), 383 K (■), 393 K (▲).

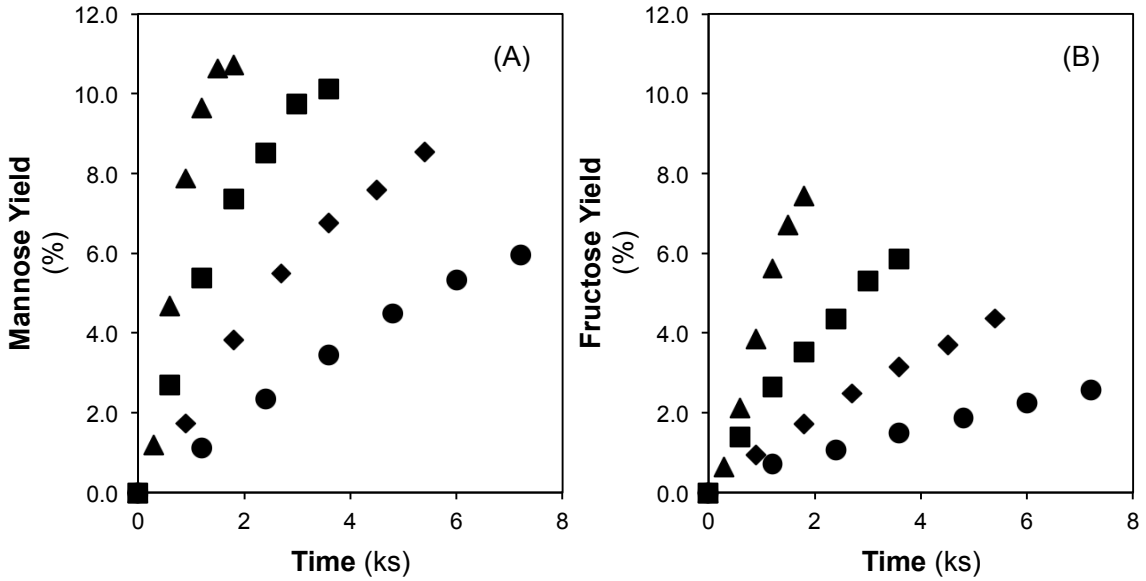

Figure 3.3: Mannose (A) and fructose (B) yields as a function of time from the reaction of 2% (w/w) glucose in 1:1 DMSO:benzene solution with **2a** (1:75 Sn/glucose molar ratio) at 363 K (●), 373 K (♦), 383 K (■), 393 K (▲).

Table 3.1 summarizes the initial rate data for as-made and modified Sn-Beta, **2a**, and for two other tin silsesquioxanes capable of binding glucose without necessarily protonating the Sn-O-Si bond.[24] These silsesquioxanes retain octahedrally coordinated tin sites with an adjacent siloxy group capped by either a proton (**1a**), analogous to the open site in Sn-Beta, or a trimethylsilyl substituent (**1b**), representative of sodium-exchanged zeolite Beta (Na-Sn-Beta) (structures for **1a** and **1b** are given in Figure 3.4).

From these data, **2a** and Sn-Beta-NH_3 have the lowest initial rates, approximately an order of magnitude slower than Sn-Beta. The decreased activity for Sn-Beta titrated with NH_3 (to effectively block the open framework site), in conjunction with that for **2a**, corroborates the hypothesis that reactions at closed sites are slow and selective to mannose. An alternative hypothesis consistent with the experimental data is that the "open" sites remain active for Sn-Beta-NH_3, while the modification reduces their activity and fructose selectivity. However,

Table 3.1: Initial rate data for as-made and modified Sn-Beta, as well as tin silsesquioxanes considered here and in other work.[15,24] All initial rate data were calculated from reactions performed at 353 K unless otherwise noted. All heterogeneous reactions were performed in methanol. [a]At 363K. [b]Initial rates at 353 K determined from activation energy data. Heterogeneous materials were normalized by total tin content, which may underestimate the actual initial rates at the open site in Sn-Beta.

	Catalytic Material						
Initial Rate, mol/(s-L-total mol Sn)	**1a**	**1b**	**2a**[a]	**2a**[b]	Sn-Beta	Na-Sn-Beta	Sn-Beta-NH_3
Glucose Conversion	1.42	8.23×10^{-1}	2.69×10^{-1}	1.02×10^{-1}	2.10	1.64	2.99×10^{-1}
Mannose Production	5.49×10^{-1}	3.80×10^{-1}	1.01×10^{-1}	4.43×10^{-2}	3.52×10^{-1}	1.04	1.89×10^{-1}
Fructose Production	7.56×10^{-1}	1.34×10^{-1}	6.28×10^{-2}	2.55×10^{-2}	9.30×10^{-1}	0	0

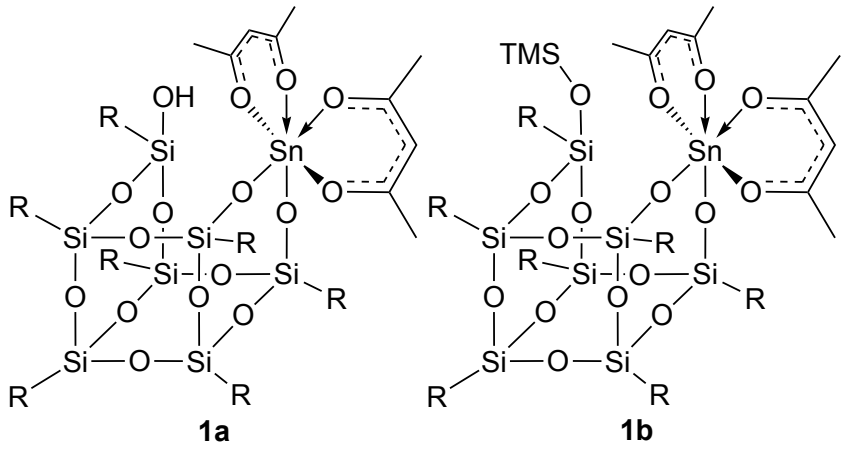

Figure 3.4: Schematic representation of the structures of **1a** and **1b**. "R" denotes a cyclohexyl ligand.

limited activity of the closed site is a simpler explanation: it does not require assuming the coincidence of two distinct modifications similarly affecting both rate and selectivity of the open site.

Apparent activation energies for the simultaneous production of mannose and fructose by **2a** are calculated from the data shown in Figure 3.5 (Arrhenius plots are given in Figures B.2 and B.3, and the calculated rate constants are listed in Table B.1). The concentrations of the mannose and fructose products were used to calculate the values of apparent first-order rate constants, *k*. High conversion values, wherein catalyst deactivation and equilibrium effects become significant, were ignored in the analysis. The epimerization of glucose to mannose has a calculated apparent activation energy of 87.91 kJ-mol^{-1}, while the isomerization of glucose to fructose has a modestly higher apparent activation energy of 96.08 kJ-mol^{-1}. For Sn-Beta, an experimentally determined apparent activation energy of 93 ± 15 kJ-mol^{-1} has been reported for fructose production in H_2O, and 70 ± 14 kJ-mol^{-1} for mannose production in CH_3OH.[13] The similarity of these activation energies, however, does not take

into account any variations in non-rate-limiting, pre-equilibrium step energies that may be responsible for the observed differences in activity between **2a** and Sn-Beta.

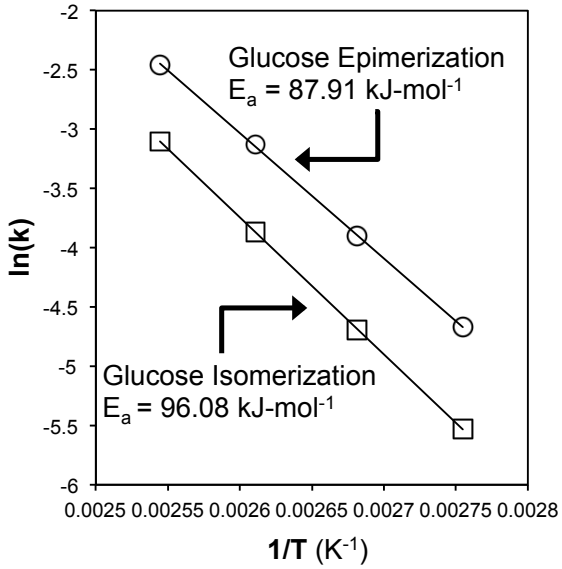

Figure 3.5: Arrhenius plot for the first-order epimerization and isomerization of glucose catalyzed by **2a**.

Glucose Reaction Pathways

Figure 3.6 depicts possible routes to fructose and mannose from glucose. A C_2 to C_1 hydride transfer converts glucose into fructose (F1), and a secondary hydride transfer from C_1 to A C_2 transforms fructose (F1) to mannose (M1). A 1,2-intramolecular carbon shift directly transforms glucose into mannose (M2). A subsequent hydride transfer also produces fructose (F2). The formation of these products may be distinguished through the use of isotopically labeled starting compounds.

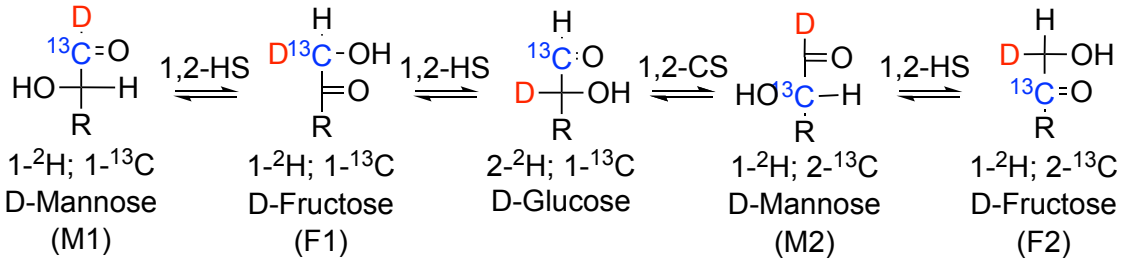

Figure 3.6: Possible reaction pathways involving hydride and carbon shifts at C_1 and C_2. Sugars are depicted using Fischer projections. Abbreviations F1, M1, M2, and F2 indicate location of ^{13}C on first or second carbon of sugar, when C_1 of glucose reactant is labeled. R = $C_4H_9O_4$.

^{13}C- and ^{2}H-labeling experiments

To investigate the reaction pathways promoted by **2a**, 10 %(w/w) glucose enriched with ^{13}C at the C_1 position (1-^{13}C glucose) or with ^{13}C at the C_1 position and ^{2}H at the C_2 position (2-^{2}H; 1-^{13}C glucose) solutions were reacted for 60 minutes at 373 K in 1:1 DMSO:benzene, maintaining a glucose:Sn molar ratio of 75. ^{13}C spectra (Figure 3.7 show strong resonances at δ = 98.7 and 94.8, corresponding to the β- and α-glucopyranose starting material labeled with ^{13}C at the C_1 position, respectively. Additionally, both spectra have resonances at δ = 74.0 and 73.5, corresponding to β- and α-mannopyranose labeled with ^{13}C at the C_2 position, respectively (M2 in Figure 3.6. These results, coupled with the reaction data, suggest that **2a** preferentially catalyzes the 1,2-intramolecular carbon shift of glucose to mannose, analogous to the Bílik reaction.[34]

In addition to the formation of mannose, fructose is produced in lower yields. For the singly labeled 1-^{13}C glucose experiment, two ^{13}C resonances at δ = 66.7 and 65.5 are observed, corresponding to the β and α forms of fructofuranose, respectively. These resonances are not observed in the spectra obtained from 2-^{2}H; 1-^{13}C glucose. This result is likely a consequence of a 1,2-intramolecular hydride shift that negates the nuclear Over-

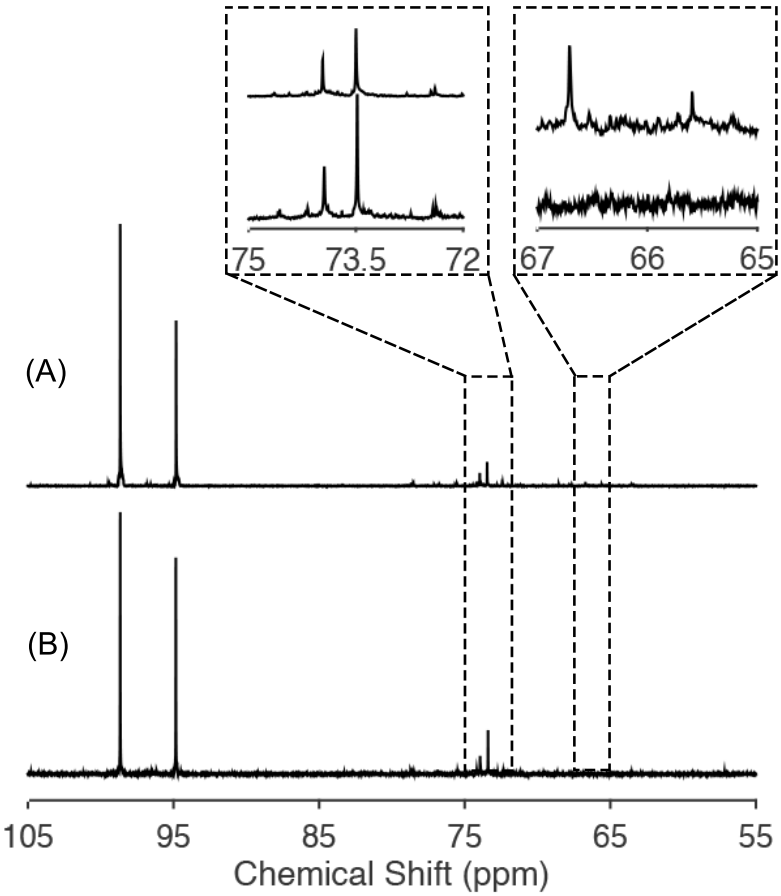

Figure 3.7: ^{13}C NMR spectra for reactant and products with **2a** (1:75 Sn/glucose molar ratio) in a 10% (w/w) at 373 K for 60 minutes with: (A) 1-^{13}C glucose and (B) 2-^{2}H; 1-^{13}C glucose in a 1:1 DMSO:benzene solvent system.

hauser enhancement (NOE), an effect that amplifies ^{13}C resonances for directly bonded ^{13}C-^{1}H pairs; no such amplification occurs for ^{13}C-^{2}H pairs, resulting in substantial attenuation of the ^{13}C resonances and the subsequent production of triplets from coupling to ^{2}H (spin 1). The low intensity triplets that would be expected in ^{13}C spectra for ^{13}C-^{2}H pairs are not observable in Figure 3.7, reflecting the low yield of fructose as a consequence of the kinetic isotope effect. The ^{1}H NMR spectra from the reaction of 2-^{2}H; 1-^{13}C glucose, shown in Figure 3.8, may also be used to confirm that the 1,2-intramolecular hydride shift is the prevailing fructose-forming mechanism. As discussed by Román-Leshkov *et al*., the

base-catalyzed conversion of 2-^{2}H glucose to fructose results in scrambling of the deuterons between the glucose and solvent system, resulting in unlabeled glucose exhibiting a peak corresponding to a proton in the C_2 position at δ = 3.2.[35] The spectra shown in Figure 3.8 do not demonstrate this behavior, indicating that the glucose remains deuterated at the C_2 position, further suggesting that the 1,2-intramolecular hydride shift mechanism occurs. Moreover, this spectrum exhibits no C_1 position mannose proton at δ = 5.17, indicating that the deuteron shifts from the C_2 to C_1 position during the intramolecular carbon shift reaction, and that the F1 to M1 hydride shift does not occur in significant yield. In general, the mannose to fructose hydride shift is not detectable under the reaction conditions utilized. These reaction pathways are analogous to what has been observed with Sn-Beta.[15,35]

Identification of Catalytic Species

Experiments were performed to confirm that the observed catalysis was due solely to **2a**, and not a consequence of starting reagents or leached tin species formed by degradation of the catalyst under reaction conditions. Control experiments were performed with **1** exposed to all synthesis procedures, but without the addition of CH_3SnCl_3. In this instance, no glucose conversion was observed. A solution of CH_3SnCl_3 in benzene catalyzed formation of fructose, but in yields lower than that observed with **2a**; no mannose formation was observed.

To examine the structural integrity of **2a** post reaction, the catalyst was separated from a reaction performed at 393 K for 1 hour, utilizing the same parameters and procedures outlined previously. These conditions were chosen to ensure a large excess of glucose relative to **2a**, so that statistically all Lewis acid sites should participate in the catalysis.

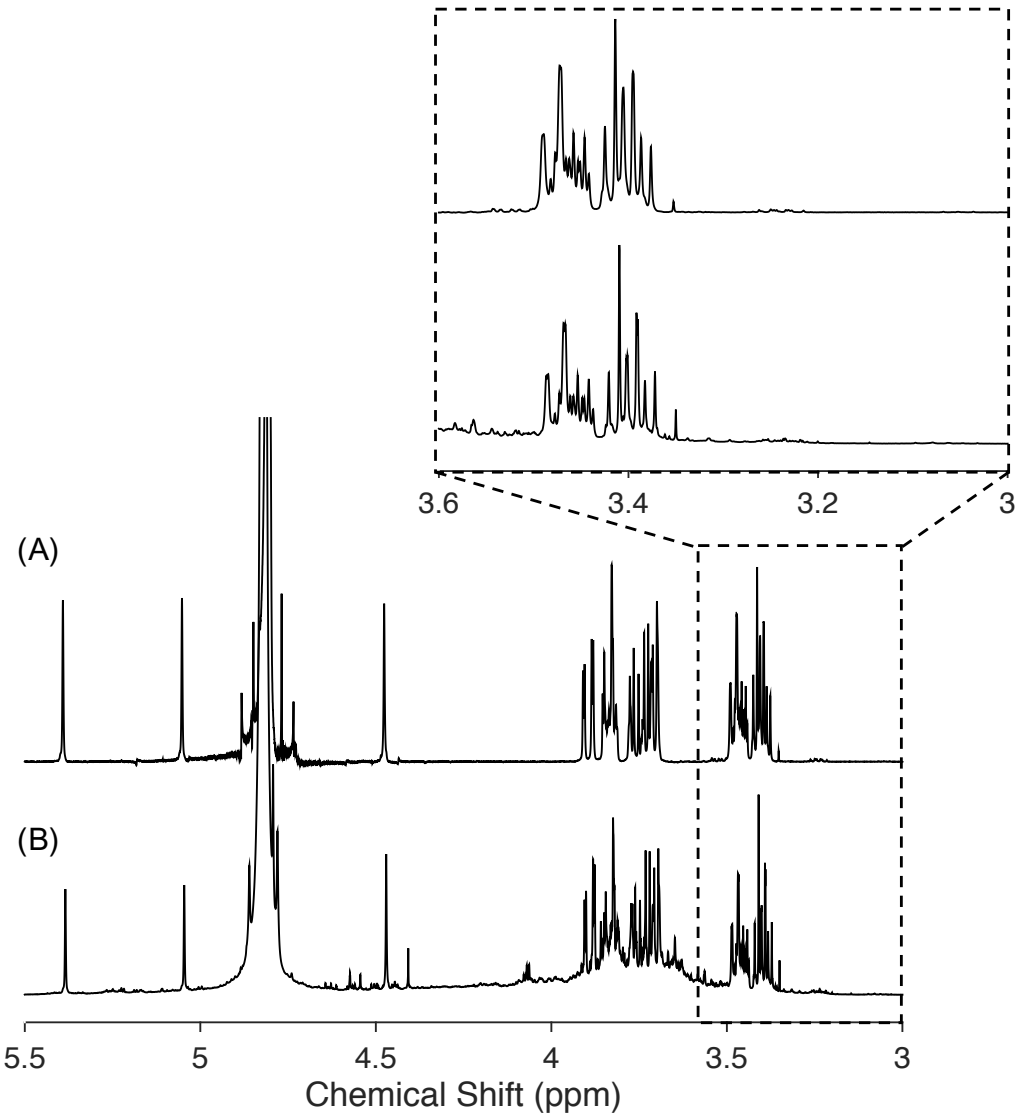

Figure 3.8: 1H NMR spectra for: (A) unreacted 2-^{2}H; 1-^{13}C glucose, and (B) reactant and products with **2a** (1:75 Sn/glucose molar ratio) in a 10% (w/w) at 373 K for 60 minutes with 2-^{2}H; 1-^{13}C glucose in a 1:1 DMSO:benzene solvent system.

In order to separate the catalyst from the crude reaction solution, an excess of hexane was added to the mixture while the reaction vessel was maintained at 393 K. This resulted in the formation of an immiscible two-phase system, consisting of the dense polar DMSO phase containing the carbohydrates and the less dense non-polar catalyst-containing phase. The two phases were separated, and the hexane solution was allowed to cool, then washed with

an excess of acetonitrile. The hexane phase was again separated, the volatiles were removed, and the resultant white powder was dried under vacuum for 12 hours. NMR analysis of this material (Figures B.4 - B.7) is in very good agreement with spectra obtained of the material prior to reaction, and data presented in the literature.[25] Taken together, these results suggest that the structure of **2a** likely remains intact over the course of the reaction, and is the origin of the catalytically active species.

Computational Chemistry

For Sn-Beta, the open site has been shown to be the active catalytic site, whereby a stannanol group facilitates the initial binding step of the glucose molecule to the Lewis acid site.[14,15,19–22,24,35] This reaction mechanism is not possible for **2a**, however, due to the absence of the stannanol.

In order for **2a** to catalyze the conversion of glucose, we hypothesize that the Sn-O-Si bridging bonds must be involved to allow the glucose C_1 hydroxy proton to transfer to one of the three Si-O-Sn bridging bonds, analogous to pathways proposed by Li *et al.* and Yang *et al.*[20,21] Beletskiy *et al.* provide evidence that this type of proton shift may occur for 2-propanol (adsorbed as 2-propoxide) on silica-immobilized tin silsesquioxane complexes.[36] Similar lattice protonation mechanisms have been proposed for metal-containing zeolites.[37] This proton transfer results in the formation of an adjacent silanol group to the tin site, as well as glucose bound to the tin site. *In situ* NMR spectroscopy characterization was attempted by exposing the catalyst to reaction conditions and collecting spectra at 373 K; unfortunately, no evidence for proton transfer to one of the Sn-O-Si bond was obtained. In order to garner further insight into the glucose reaction mechanisms for **2a**, a theoretical

approach was taken.

Figure 3.9 depicts the previously described proposed glucose ring-opening mechanism on **2a** and compares the relative gas-phase free energies. The calculations estimate that deprotonation and ring-opening are endothermic, with intrinsic free energy barriers of 41.3 and 66.6 kJ-mol^{-1}, respectively. Bermejo-Deval *et al.* report an activation energy of 37.3 kJ-mol^{-1} for ring-opening at an open site.[14] Work by Yang *et al.* also suggests that the initial glucose deprotonation step at the open site is thermodynamically more stable than at the closed site.[21] These data suggest that binding to and performing ring opening at a site without a hydroxyl moiety present (as with **2a** and the closed site in Sn-Beta) is less favorable. As considered by Li *et al.*, this variation and subsequent difference in energies is likely a function of geometric distortion and deviations in Lewis acidity between the two sites.[20]

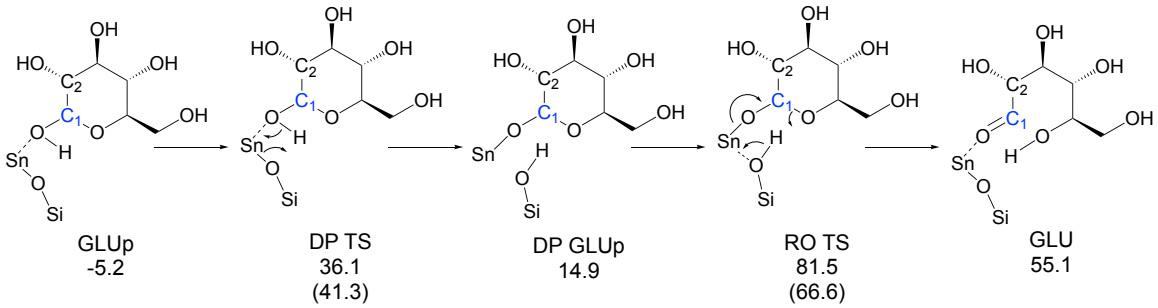

Figure 3.9: Glucose ring-opening mechanism. Gas-phase free energies (in kJ-mol^{-1}) at 373 K for intermediates and transition states are reported relative to isolated glucose and catalyst. Intrinsic barriers reported in parentheses. GLUp: glucopyranose; DP: deprotonation; RO: ring opening; GLU: open-chain glucose.

After ring-opening, hydride transfer or Bílik reactions convert glucose into fructose or mannose, respectively. Generally, there are three possible pathways in converting glucose, which we categorize as "O_1 Binding," "O_2 Binding," and "Bidentate," identified according

to whether the open glucose binds to the Sn Lewis acid site *via* the O_1 position, O_2 position, or both during the reaction. The mechanistic details and energetics of these pathways are compared in Figures 3.10 and 3.11.

The bidentate mechanism involves: 1) coordination of both O_1 and O_2 to the Sn center in an octahedral geometry, 2) deprotonation, forming a silanol and binding O_2 to the Sn, 3) a H/C-shift with a chelate-like transition state, and 4) reprotonation in sequential steps. For both isomerization and epimerization, the bidentate pathway is predicted to be the most favorable, with intrinsic free energy barriers of 79.6 kJ-mol^{-1} and 101.0 kJ-mol^{-1}, respectively.

The O_1 binding pathway begins by coordination of the aldehyde oxygen to the Sn, maintaining a hydrogen bonding interaction between O_2 and the Sn-O-Si bridge. The first step binds O_1 to the Sn during a concerted deprotonation of O_2 alongside the H/C-shift. Intrinsic barriers for the H/C-shift are 115.5 kJ-mol^{-1} and 110.9 kJ-mol^{-1}, respectively. Reprotonation of O_1 follows in a subsequent step.

The O_2 binding pathway starts with a deprotonation forming a silanol and binding O_2 to the Sn. This deprotonation is endothermic, with an intrinsic barrier of 50 kJ-mol^{-1} and a free energy of reaction of 26.9 kJ-mol^{-1}. O_1 then forms a hydrogen bond with the silanol formed in situ, which subsequently reprotonates the sugar during the concerted H/C-shift reaction. Intrinsic barriers for the H/C-shift are 61.1 kJ-mol^{-1} and 93.5 kJ-mol^{-1}, respectively.

To our knowledge, this is the first time a systematic approach has been considered for glucose isomerization and epimerization reaction mechanisms, which frequently consider only the bidentate, O_1 binding, or O_2 binding.[14,21–23,38,39]

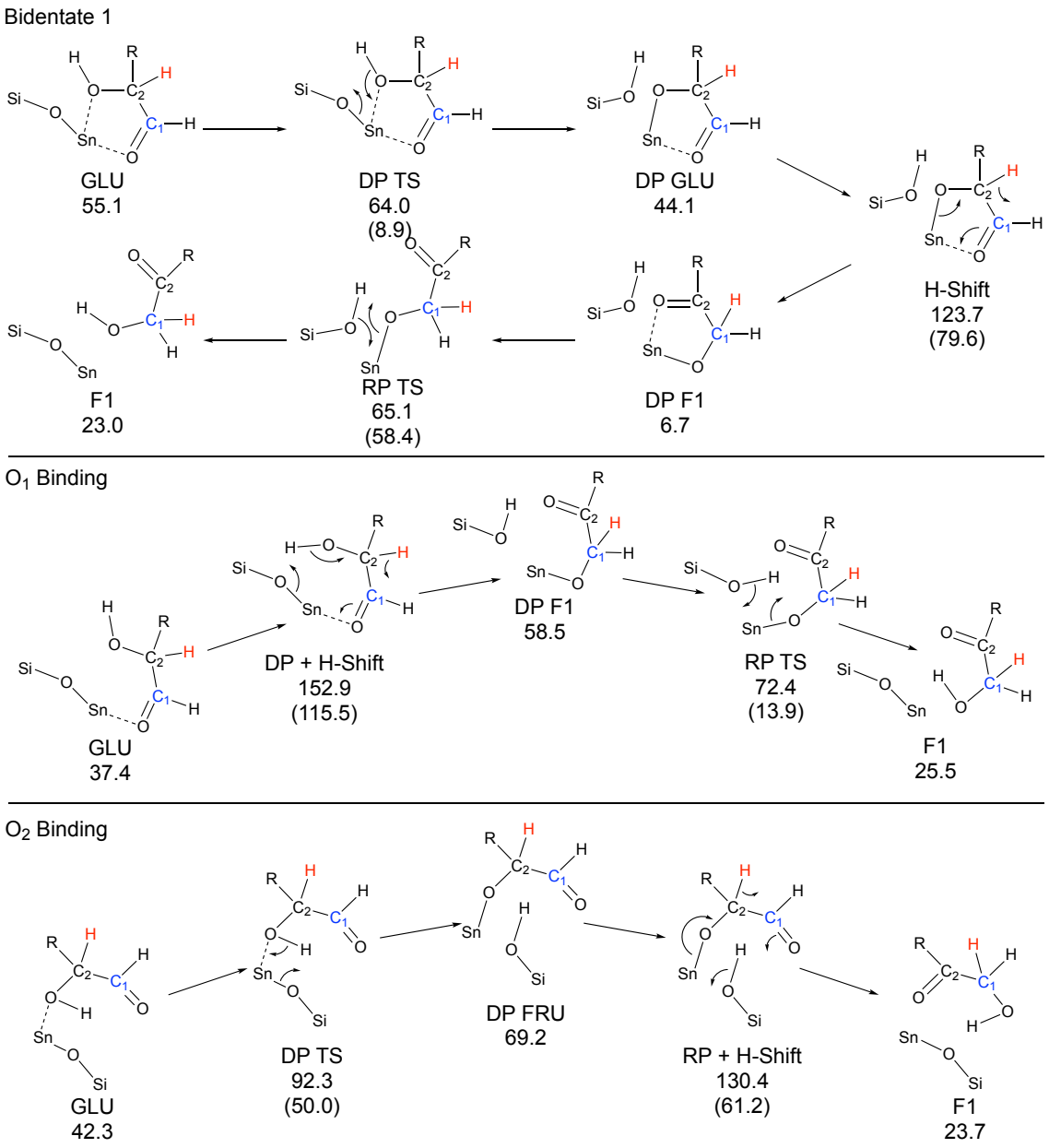

Figure 3.10: H-Shift Pathways. Three pathways are shown for transforming open-chain glucose (GLU) into open-chain fructose (F1), *via* deprotonation (DP), reprotonation (RP), and H-shift reactions. The bidentate transition state gives the lowest barrier for reaction, with a slightly more stable transition state than the O2 binding pathway. Gas-phase free energies (in kJ-mol^{-1}) at 373 K for intermediates and transition states are reported relative to isolated glucose and catalyst, with intrinsic barriers reported in parentheses.

To finish the catalytic cycle, the ring closing reactions of deprotonated fructose, open fructose, and open mannose were examined. Deprotonated open fructose ring-closes to

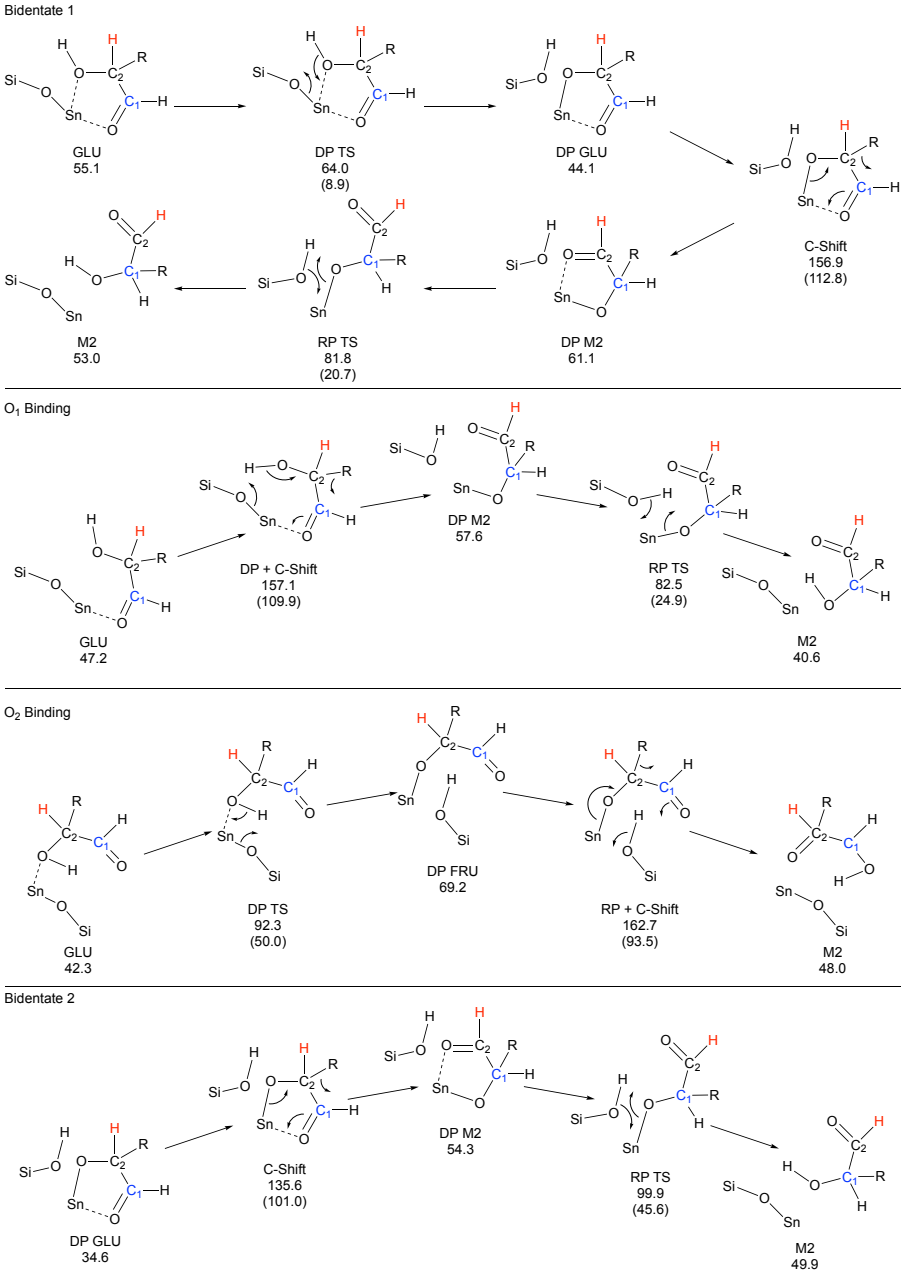

Figure 3.11: C-Shift Pathways. Open-chain glucose (GLU) transforms directly into open-chain mannose (M2) through deprotonation (DP), reprotonation (RP), and C-shift reactions. Four pathways are shown: three starting from the initial geometries of the H-shift reactions (bidentate, O_1 binding, and O_2 binding) and an additional bidentate pathway starting from a different geometry to facilitate O_3 hydroxyl interaction with **2a**. Gas-phase free energies (in kJ-mol^{-1}) at 373 K for intermediates and transition states are reported relative to isolated glucose and catalyst, with intrinsic barriers reported in parentheses.

produce O_1-deprotonated fructofuranose. A slightly different pathway for open fructose ring closing produces O_2-deprotonated fructofuranose. Subsequent reprotonation regenerates the catalyst and produces fructofuranose. Similarly, open mannose ring-closes to form O_1-deprotonated mannopyranose, and subsequent reprotonation regenerates the catalyst and produces mannopyranose. These pathways have relatively low barriers compared to H/C-shift reactions. The bidentate, O_1 binding, and O_2 binding pathways for interconverting fructose and mannose (F1 to M1), which have higher barriers than the competing fructose ring-closing pathways are depicted in Figures B.8-B.10. The energetics of the reported pathways are given in Table B.2. Products M1 and F2 are not observed because ring-closing is facile relative to additional H/C-shift reactions.

Selectivity Analysis

Selectivity trends were analyzed using the energy span model.[40] To quantitatively analyze the reaction pathways, the model must was first reduced. As shown, the bidentate, O_1 binding, and O_2 binding pathways all form the same products (F1 or M2). As such, the highest barrier pathways may be ignored, specifically the O_1 binding and O_2 binding modes for both the 1,2-intramolecular hydride and carbon shift reactions. Additionally, the subsequent H/C-shift reactions (producing F2 or M1) may be ignored as the ring-closing and reprotonation transition state barriers are significantly more favorable. For branched networks at steady state, the Curtin-Hammett principle can be used to estimate steady-state reaction selectivites using only the free energies of the bidentate H-shift transition state and the bidentate C-shift transition state to estimate the reaction selectivity, as defined by:[40,41]

$$\frac{[Man]}{[Fru]} = e^{G_{TS,FRU} - G_{TS,MAN}/RT} \tag{3.3}$$

The gas-phase transition state free energies for the mannose (135.6 kJ-mol^{-1}) and fructose (123.7 kJ-mol^{-1}) pathways are similar, although they favor fructose as the major product. In experiment, the difference in apparent activation energy is 8.2 kJ-mol^{-1} in favor of mannose production — a difference too small to be expected to be resolved by QM/MM calculations which do not take into account the complex solvation environment of the experiments.

Electronic Structure Analysis of H/C-Shift Reactions

The character of the H/C-shift reactions was also analyzed according to the Natural Bond Orbital (NBO) method (see Tables B.3 – B.8). In general, four overall mechanisms govern a hydride transfer: (a) electron-proton-electron pathway ($e^- - H^+ - e^-$) (b) electron-hydrogen atom transfer (c) hydrogen atom-electron transfer and (d) one-step hydride ion transfer.[42] Choudhary *et al*. analyzed the hydride transfer in the bidentate mechanism for xylose to xylulose on the Sn-Beta zeolite.[38] They proposed that the H-shift mechanism involves the rate-limiting transfer of a neutral hydrogen atom from C_2 to C_1, concerted with a rapid electron transfer from O_2 to O_1. Following a similar methodology, we conclude that the bidentate mechanism for the H-shift on **2a** follows the same mechanism: a neutral hydrogen atom transfers from C_2 to C_1 concertedly with an adiabatic electron transfer from O_2 to O_1, facilitated by a C_2-O_2 and C_1-O_1 anti-bonding π system at the transition state. The O_1-binding H-shift is a test case for observing the H-shift reaction without the prior deprotonation of O_2. Without deprotonation prior to the hydride transfer, the H-C_2 bond is less polarized and thus charge separation comes at a higher energy cost. Comparison

with the bidentate pathway shows how the sugar deprotonation step activates the C_2 donor fragment for the subsequent H-shift. The electronic structure of the bidentate C-shift was also analyzed. The results demonstrate that this pathway's electronic composition is remarkably analogous to that of the H-shift, including the C_2-O_2 and C_1-O_1 π system for transferring an electron and a neutral C_3 fragment as a transferring group. A detailed analysis may be found in Appendix B.

3.4 Conclusions

We have synthesized and tested methyl-ligated tin silsesquioxane as a catalyst for glucose reactivity to examine the activity and structure of tin species that are analogous to the closed tin site in Sn-Beta. The catalytic nature of **2a** suggests that there are glucose conversion pathways that involve the breaking of the Si-O-Sn linkage at some point in the reaction cycle and that such pathways may be possible from the closed sites in Sn-Beta. We have not conclusively proven this point here, and since the bond angles in **2a** are significantly different from Sn-Beta, these pathways may not occur in the latter. However, if they do, they participate in catalyzing the reaction of glucose at a rate significantly slower than the open site. Isotopic labeling experiments demonstrate that these reactions occur *via* 1,2-intramolecular carbon and hydrogen shift pathways for mannose and fructose, respectively, yielding products that are indistinguishable from those obtained by catalysis at the open site. The full catalytic cycle has been theoretically investigated considering three distinct pathways for the hydride- and carbon-shift reaction reactions. It has been calculated that the most favorable pathway to produce both fructose and mannose over **2a** is by glucose binding bidentately to the tin center, deprotonation to one of the Sn-O-Si bridges, and performing

either a hydride- or carbon-shift reaction. We propose that a similar mechanism occurs at the closed site in Sn-Beta.

3.5 Acknowledgments

Research was supported as part of the Catalysis Center for Energy Innovation, an Energy Frontier Research Center funded by the U.S. Department of Energy (DOE), Office of Science, Basic Energy Sciences (BES), under Award number DE-SC0001004. S.K.B. wishes to acknowledge funding from the National Science Foundation Graduate Research Fellowship Program under Grant No. DGE-1144469. T.R.J. also wishes to acknowledge funding from the National Science Foundation Graduate Research Fellowship Program under Grant No. 0750966, as well as the George W. Laird Merit Fellowship. Any opinions, findings, and conclusions or recommendations expressed in this material are those of the author(s) and do not necessarily reflect the views of the National Science Foundation. The authors would like to thank Marat Orazov and Jeff Christianson for numerous useful conversations.

3.6 References

(1) Román-Leshkov, Y.; Davis, M. E. Activation of Carbonyl-Containing Molecules with Solid Lewis Acids in Aqueous Media. *ACS Catalysis* **2011**, *1*, 1566–1580.

(2) Moliner, M. State of the art of Lewis acid-containing zeolites: lessons from fine chemistry to new biomass transformation processes. *Dalton transactions (Cambridge, England : 2003)* **2014**, *43*, 4197–208.

(3) Corma, A.; García, H. Lewis Acids as Catalysts in Oxidation Reactions: From Homogeneous to Heterogeneous Systems. *Chemical reviews* **2002**, *102*, 3837–92.

(4) Serrano-Ruiz, J. C.; Dumesic, J. A. Catalytic routes for the conversion of biomass into liquid hydrocarbon transportation fuels. *Energy & Environmental Science* **2011**, *4*, 83.

(5) Alonso, D. M.; Bond, J. Q.; Dumesic, J. A. Catalytic conversion of biomass to biofuels. *Green Chemistry* **2010**, *12*, 1493.

(6) Ragauskas, A. J.; Williams, C. K.; Davison, B. H.; Britovsek, G.; Cairney, J.; Eckert, C. A.; Frederick, W. J.; Hallett, J. P.; Leak, D. J.; Liotta, C. L.; Mielenz, J. R.; Murphy, R.; Templer, R.; Tschaplinski, T. The path forward for biofuels and biomaterials. *Science (New York, N.Y.)* **2006**, *311*, 484–489.

(7) Moliner, M.; Román-Leshkov, Y.; Davis, M. E. Tin-containing zeolites are highly active catalysts for the isomerization of glucose in water. *Proceedings of the National Academy of Sciences of the United States of America* **2010**, *107*, 6164–6168.

(8) Valencia, S.; Canos, A. Stannosilicate molecular sieves., US Patent 5,968,473, 1999.

(9) Corma, A.; Nemeth, L. T.; Renz, M.; Valencia, S. Sn-zeolite beta as a heterogeneous chemoselective catalyst for Baeyer-Villiger oxidations. *Nature* **2001**, *412*, 423–425.

(10) Renz, M.; Blasco, T.; Corma, A.; Fornés, V.; Jensen, R.; Nemeth, L. Selective and shape-selective Baeyer-Villiger oxidations of aromatic aldehydes and cyclic ketones with Sn-beta zeolites and H2O2. *Chemistry (Weinheim an der Bergstrasse, Germany)* **2002**, *8*, 4708–17.

(11) Corma, A.; Domine, M. E.; Valencia, S. Water-resistant solid Lewis acid catalysts: Meerwein-Ponndorf-Verley and Oppenauer reactions catalyzed by tin-beta zeolite. *Journal of Catalysis* **2003**, *215*, 294–304.

(12) Corma, A.; Domine, M. E.; Nemeth, L.; Valencia, S. Al-free Sn-Beta zeolite as a catalyst for the selective reduction of carbonyl compounds (Meerwein-Ponndorf-Verley Reaction). *Journal of the American Chemical Society* **2002**, *124*, 3194–3195.

(13) Bermejo-Deval, R.; Gounder, R.; Davis, M. E. Framework and Extraframework Tin Sites in Zeolite Beta React Glucose Differently. *ACS Catalysis* **2012**, *2*, 2705–2713.

(14) Bermejo-Deval, R.; Assary, R. S.; Nikolla, E.; Moliner, M.; Román-Leshkov, Y.; Hwang, S.-J.; Palsdottir, A.; Silverman, D.; Lobo, R. F.; Curtiss, L. A.; Davis, M. E. Metalloenzyme-like catalyzed isomerizations of sugars by Lewis acid zeolites. *Proceedings of the National Academy of Sciences of the United States of America* **2012**, *109*, 9727–32.

(15) Bermejo-Deval, R.; Orazov, M.; Gounder, R.; Hwang, S. J.; Davis, M. E. Active sites in Sn-beta for glucose isomerization to fructose and epimerization to mannose. *ACS Catalysis* **2014**.

(16) Corma, A.; Davis, M. E. Issues in the synthesis of crystalline molecular sieves: Towards the crystallization of low framework-density structures., 2004, DOI: 10.1002/cphc.200300997.

(17) Pacheco, J. J.; Davis, M. E. Synthesis of terephthalic acid via Diels-Alder reactions with ethylene and oxidized variants of 5-hydroxymethylfurfural. *Proceedings of the National Academy of Sciences of the United States of America* **2014**, *111*, 8363–7.

(18) Boronat, M.; Concepción, P.; Corma, A.; Renz, M.; Valencia, S. Determination of the catalytically active oxidation Lewis acid sites in Sn-beta zeolites, and their optimisation by the combination of theoretical and experimental studies. *Journal of Catalysis* **2005**, *234*, 111–118.

(19) Harris, J. W.; Cordon, M. J.; Di Iorio, J. R.; Vega-Vila, J. C.; Ribeiro, F. H.; Gounder, R. Titration and quantification of open and closed Lewis acid sites in Sn-Beta zeolites that catalyze glucose isomerization. *Journal of Catalysis* **2016**, *335*, 141–154.

(20) Li, Y.-P.; Head-Gordon, M.; Bell, A. T. Analysis of the Reaction Mechanism and Catalytic Activity of Metal-Substituted Beta Zeolite for the Isomerization of Glucose to Fructose. *ACS Catalysis* **2014**, *4*, 1537–1545.

(21) Yang, G.; Pidko, E. A.; Hensen, E. J. M. The mechanism of glucose isomerization to fructose over Sn-BEA zeolite: A periodic density functional theory study. *ChemSusChem* **2013**, *6*, 1688–1696.

(22) Rai, N.; Caratzoulas, S.; Vlachos, D. G. Role of Silanol Group in Sn-Beta Zeolite for Glucose Isomerization and Epimerization Reactions. *ACS Catalysis* **2013**, *3*, 2294–2298.

(23) Christianson, J. R.; Caratzoulas, S.; Vlachos, D. G. Computational Insight into the Effect of Sn-Beta Na Exchange and Solvent on Glucose Isomerization and Epimerization. *ACS Catalysis* **2015**, *1*.

(24) Brand, S. K.; Labinger, J. A.; Davis, M. E. Tin Silsesquioxanes as Models for the "Open" Site in Tin-Containing Zeolite Beta. *ChemCatChem* **2016**, *8*, 121–124.

(25) Feher, F. J.; Newman, D. A.; Walzer, J. F. Silsesquioxanes as models for silica surfaces. *Journal of the American Chemical Society* **1989**, *111*, 1741–1748.

(26) Liu, C.; Carraher, J. M.; Swedberg, J. L.; Herndon, C. R.; Fleitman, C. N.; Tessonnier, J.-P. Selective Base-Catalyzed Isomerization of Glucose to Fructose. *ACS Catalysis* **2014**, *4*, 4295–4298.

(27) Vreven, T.; Byun, K. S.; Komaromi, I.; Dapprich, S.; Montgomery Jr., J. A.; Morokuma, K.; Frisch, M. J. Combining Quantum Mechanics Methods with Molecular Mechanics Methods in ONIOM. *Journal of Chemical Theory and Computation* **2006**, *2*, 815–826.

(28) Dapprich, S.; Komáromi, I.; Byun, K. S.; Morokuma, K.; Frisch, M. J. A new ONIOM implementation in Gaussian98. Part I. The calculation of energies, gradients, vibrational frequencies and electric field derivatives. *Journal of Molecular Structure: THEOCHEM* **1999**, *461-462*, 1–21.

(29) Zhao, Y.; Truhlar, D. G. The M06 suite of density functionals for main group thermochemistry, thermochemical kinetics, noncovalent interactions, excited states, and transition elements: Two new functionals and systematic testing of four M06-class functionals and 12 other function. *Theoretical Chemistry Accounts* **2008**, *120*, 215–241.

(30) Wadt, W. R.; Hay, P. J. Ab initio effective core potentials for molecular calculations. Potentials for main group elements Na to Bi. *The Journal of Chemical Physics* **1985**, *82*, 284–298.
(31) Frisch, M. J. et al. Gaussian 09., Wallingford, 2009.
(32) Holm, M. S.; Saravanamurugan, S.; Taarning, E. Conversion of sugars to lactic acid derivatives using heterogeneous zeotype catalysts. *Science (New York, N.Y.)* **2010**, *328*, 602–605.
(33) Orazov, M.; Davis, M. E. Tandem catalysis for the production of alkyl lactates from ketohexoses at moderate temperatures. *Proceedings of the National Academy of Sciences* **2015**, *112*, 201516466.
(34) Hayes, M. L.; Pennings, N. J.; Serianni, A. S.; Barker, R. Epimerization of aldoses by molybdate involving a novel rearrangement of the carbon skeleton. *Journal of the American Chemical Society* **1982**, *104*, 6764–6769.
(35) Román-Leshkov, Y.; Moliner, M.; Labinger, J. A.; Davis, M. E. Mechanism of glucose isomerization using a solid Lewis acid catalyst in water. *Angewandte Chemie (International ed. in English)* **2010**, *49*, 8954–7.
(36) Beletskiy, E. V.; Hou, X.; Shen, Z.; Gallagher, J. R.; Miller, J. T.; Wu, Y.; Li, T.; Kung, M. C.; Kung, H. H. Supported Tetrahedral Oxo-Sn Catalyst: Single Site, Two Modes of Catalysis. *Journal of the American Chemical Society* **2016**, jacs.5b13436.
(37) Lewis, J. D.; Van De Vyver, S.; Román-Leshkov, Y. Acid-Base Pairs in Lewis Acidic Zeolites Promote Direct Aldol Reactions by Soft Enolization. *Angewandte Chemie - International Edition* **2015**, *54*, 9835–9838.
(38) Choudhary, V.; Caratzoulas, S.; Vlachos, D. G. Insights into the isomerization of xylose to xylulose and lyxose by a Lewis acid catalyst. *Carbohydrate Research* **2013**, *368*, 89–95.
(39) Assary, R. S.; Curtiss, L. A. Theoretical study of 1,2-hydride shift associated with the isomerization of glyceraldehyde to dihydroxy acetone by Lewis acid active site models. *Journal of Physical Chemistry A* **2011**, *115*, 8754–8760.
(40) Kozuch, S. Steady State Kinetics of Any Catalytic Network: Graph Theory, the Energy Span Model, the Analogy between Catalysis and Electrical Circuits, and the Meaning of "Mechanism". *ACS Catalysis* **2015**, *5*, 5242–5255.
(41) Curtin, D. Stereochemical Control of Organic Reaction Differences in Behavior of Diastereomers. *Rec. Chem. Prog.* **1954**, *15*, 111–128.
(42) Tapia, O.; Andres, J.; Aullo, J. M.; Bränden, C.-I. Electronic aspects of the hydride transfer mechanism. Ab initio analytical gradient studies of the cyclopropenyl-cation/lithium hydride model reactant system. *The Journal of Chemical Physics* **1985**, *83*, 4673.

Chapter 4

CONCLUSIONS AND FUTURE DIRECTIONS

4.1 Conclusions

Part I of this thesis has focused on developing well-defined metallosilsesquioxane-based homogeneous catalysts to model the multiplicity of potential catalytic sites that are present in tin-containing zeotype Beta. These structures were used to study the glucose isomerization and epimerization reactions at a fully characterized tin site, that is not possible using traditional heterogeneous molecular sieves. These compounds provide a unique and conclusive method for elucidating structure-activity relationships for glucose conversions within Sn-Beta.

The work presented in Chapter 2 was developed during a period of heightened interest in analyzing and characterizing the catalytic behavior of Sn-Beta. Almost all of these studies, however, focused on continued use of the heterogeneous material or theoretical computations.[1–3] The first report on this topic was published by Bermejo-Deval *et al*., which showed experimentally the importance of considering the silanol group adjacent to the the tin center as part of the catalytic site for the conversion of glucose.[3] It was demonstrated that titration of the silanol group resulted in a complete shift in catalytic activity to produce mannose. Moreover, this work also demonstrated that on the timescale of a reaction there is no open-closed site interchange. In a subsequent experimental study, Harris *et al*. have confirmed that the rate of reaction for the isomerization of glucose decreases as the open Sn sites are progressively titrated.[1]

Using materials **1a** and **1b** it was shown that, qualitatively, that the proximal silanol moiety is critical in directing how glucose is reacted and plays a direct role in the function of the catalytic site. In general, the presence of the silanol correlates directly with the 1,2-intramolecular hydride shift reaction (1,2-HS) to produce fructose, while materials lacking this functional group (*e.g.*, as a result of titration) correlate with 1,2-intramolecular carbon shift (1,2-CS) reactions. These results are consistent with existing studies reported in the literature.[1–3]

Chapter 3 focuses on the synthesis and characterization of a methyl-ligated tin silsesquioxane as a catalyst for glucose reactivity to examine the activity and structure of tin species that are analogous to the closed tin site in Sn-Beta. The results of this study suggest that glucose catalysis may occur at the closed site, but at a rate significantly slower than the open site. In addition to the experimental study, comprehensive theoretical computations were performed to determine the most favorable pathways for the production of mannose and fructose using **2a**. It was calculated that, thermodynamically, glucose preferably binds to the tin center bidentately, subsequently deprotonates to one of the Sn-O-Si bridges, and performs either a hydride- or carbon-shift reaction. Therefore, if reactions to do occur at tin sites that are fully coordinated to the molecular sieve framework, they likely do so *via* a mechanism similar to what we propose for **2a** and at a significantly lower rate than at the open site.

4.2 Future Directions

Sn-Beta is a capable catalyst for a host reactions that may be critical in the production of value-added chemicals from biomass, namely, Baeyer-Villiger oxidation, Meerwein-

Ponndorf-Verley, and aldol/retro-aldol reactions.[4–7] As the active catalytic site has been effectively established for glucose isomerization and epimerization reactions in Sn-Beta, workers should be motivated to investigate the possible participation of the proximal silanol in the aforementioned reactions. Previous computational studies have indicated that this moiety may act to shuttle protons to facilitate the 1,2-HS.[2] Similar to the isomerization reaction, the hypothesized mechanistic schemes for Baeyer-Villiger and aldol/retro-aldol reactions on carbohydrate substrates rely on proton abstraction and reallocation.[8] Data garnered from these investigations may ultimately lead to the design of a catalyst tailored to a given biomass conversion process to optimize selectivity and activity.

For certain systems, such as those stated above, metal-containing silsesquioxanes may readily provide significant insights to the catalytic mechanisms of heterogeneous materials. To date, few studies have been conducted implementing these materials, despite numerous proof-of-concept papers that demonstrate that silsesquioxanes estimate the electronic environment of a molecular sieve.[9–11] Moreover, work presented in this thesis is in agreement with previous studies indicating that complex carbohydrate reactions catalyzed by heterogeneous catalysts are able to be mimicked utilizing metallosilsesquioxanes. As such, the application of metallosilsesquioxanes to other catalytic systems of interest to the biomass catalysis community (among others) may prove exceptionally useful, and should be considered to develop stronger experimental structure-activity relationships and reaction mechanisms. In particular, **2a** has already demonstrated some capacity for performing the aldol/retro-aldol reaction when dihydroxyacetone and glcyeraldehyde are used as starting reagents. This reaction has gained interest in recent years after advances made in tandem catalytic systems proposed by Orazov and Davis.[4] However, minimal experimental

mechanistic studies for this type of catalytic system have been performed for microporous materials.

Heterogeneous catalysts are exceptionally interesting at an academic level and are an incredibly valuable commodity for the chemical industry. Therefore, fundamental principles garnered for a given reaction that are discovered using metallosilsesquioxanes (as well as other model systems) must be applied in the development of future heterogeneous catalysts to ensure that the most efficient, selective, and stable materials are utilized in any potential future biomass feedstock based industry.

4.3 References

(1) Harris, J. W.; Cordon, M. J.; Di Iorio, J. R.; Vega-Vila, J. C.; Ribeiro, F. H.; Gounder, R. Titration and quantification of open and closed Lewis acid sites in Sn-Beta zeolites that catalyze glucose isomerization. *Journal of Catalysis* **2016**, *335*, 141–154.

(2) Rai, N.; Caratzoulas, S.; Vlachos, D. G. Role of Silanol Group in Sn-Beta Zeolite for Glucose Isomerization and Epimerization Reactions. *ACS Catalysis* **2013**, *3*, 2294–2298.

(3) Bermejo-Deval, R.; Orazov, M.; Gounder, R.; Hwang, S. J.; Davis, M. E. Active sites in Sn-beta for glucose isomerization to fructose and epimerization to mannose. *ACS Catalysis* **2014**.

(4) Orazov, M.; Davis, M. E. Tandem catalysis for the production of alkyl lactates from ketohexoses at moderate temperatures. *Proceedings of the National Academy of Sciences* **2015**, *112*, 201516466.

(5) Boronat, M.; Corma, A.; Renz, M. Mechanism of the Meerwein-Ponndorf-Verley-Oppenauer (MPVO) redox equilibrium on Sn- and Zr-beta zeolite catalysts. *The journal of physical chemistry. B* **2006**, *110*, 21168–74.

(6) Boronat, M.; Concepción, P.; Corma, A.; Renz, M. Peculiarities of Sn-Beta and potential industrial applications. *Catalysis Today* **2007**, *121*, 39–44.

(7) Boronat, M.; Concepción, P.; Corma, A.; Renz, M.; Valencia, S. Determination of the catalytically active oxidation Lewis acid sites in Sn-beta zeolites, and their optimisation by the combination of theoretical and experimental studies. *Journal of Catalysis* **2005**, *234*, 111–118.

(8) Corma, A.; Nemeth, L. T.; Renz, M.; Valencia, S. Sn-zeolite beta as a heterogeneous chemoselective catalyst for Baeyer-Villiger oxidations. *Nature* **2001**, *412*, 423–425.

(9) Feher, F. J.; Newman, D. A.; Walzer, J. F. Silsesquioxanes as models for silica surfaces. *Journal of the American Chemical Society* **1989**, *111*, 1741–1748.

(10) Feher, F. J.; Budzichowski, T. A.; Weller, K. J. Polyhedral aluminosilsesquioxanes: soluble organic analogs of aluminosilicates. *Journal of the American Chemical Society* **1989**, *111*, 7288–7289.

(11) Feher, F. J.; Weller, K. J. Polyhedral Aluminosilsesquioxanes as Models for Aluminosilicates: Unique Synthesis of Anionic Al/Si/O Frameworks. *Organometallics* **1990**, *9*, 2638–2640.

Part II

Enantiomerically Enriched,

Polycrystalline Molecular Sieves

Chapter 5

INTRODUCTION TO PART II: CHIRAL MOLECULAR SIEVES

This beginning of this introduction provides an overview of the synthesis of molecular sieves. The notion of chirality is then discussed with regards to organic compounds and heterogeneous solids. The issues in obtaining and characterizing pure chiral solids are also discussed. Finally, a brief background of previous efforts to synthesize enantiopure molecular sieves is provided.

5.1 Introduction to Molecular Sieves and Their Synthesis

Molecular sieves are microporous materials that are broadly defined as crystalline solids with pores less than 2 nm. They are hierarchically formed from a three-dimensional network of TO_4 tetrahedra (T = tetrahedral atom, *e.g.*, Si, Al). Beyond microporous materials lies another class of materials known as mesoporous materials, that are defined to have pores between 2 to 50 nm. Mesoporous materials have been the subject of significant research efforts recently, as they serve as intriguing heterogeneous substrates to anchor highly-selective (and even enantiospecific) homogeneous catalysts.[1,2] However, they generally do not offer molecular sieving properties that have made microporous materials highly industrially relevant, and will not be considered in Part II of this thesis.

The well-defined crystalline structures of molecular sieves (and inclusion of a variety of heteroatoms, *vida infra*) has predicated their widespread implementation in a variety of applications, notably catalysis, ion exchange, separation, and adsorption.[3,4] Despite the diversity of molecular sieve structures, they are generally classified according to 1)

pore diameters and eccentricity, 2) internal cage sizes, and 3) dimensionality. Pore sizes are characterized by the the number of T-atoms that form the pore itself. The smallest accessible pore sizes are 8 membered-rings (MRs) (*i.e.*, 8 T-atoms circumscribe the pore). Almost all reported frameworks retain 8-12 MRs. While structures containing pores >12MR are known (*i.e.*, 14 and 18MRs), they are rare and usually unstable.[5,6] A few zeolites have also been synthesized with odd-membered rings (*i.e.*, 7 and 9 MRs).[7,8] Moreover, a given framework may have pores that lie in 1, 2, or 3 dimensions with variable sizes. Additionally, at the intersection of these pores, internal cages may form that are larger than the channels that lead to them. This consequently allows for the formation of reactive intermediates that cannot escape the framework. For instance, the methanol-to-olefin process utilizes an 8MR material with large cages (CHA framework, molecular sieve framework types are designated by three-letter codes that define the unique connectivity of the oxide tetrahedra).[9,10] It is believed that, in order for this process to be carried out with high selectivity to ethylene and propylene (while maintaining high conversion of methanol) the formation of (polymethyl)benzene in the cages occurs.[9] This reactive intermediate itself is too large to exit the cage, but the desired olefin products may. Frameworks without this specific structure (maintaining equivalent compositions) do not perform the reaction as selectively or actively.[11–13] This example can be extended to numerous other chemical processes, such as fluidized catalytic cracking and the reduction of NO_x.[14] It is estimated that the global demand of heterogeneous catalysts in 2015 (which are used in approximately 70% of all chemical processes) amounted to a $20 billion dollar industry.[15,16] There exists, therefore, significant motivation to develop and synthesize more efficient, selective, and stable molecular sieves for a diverse and extensive array of applications in the chemical industry.

Broadly, microporous materials form when oxide tetrahedra assemble into secondary building units, that then self-assemble into larger structural units. For microporous materials, this occurs in a regular, periodic fashion to form a crystalline material. This process is illustrated in Figure 5.1. Many variables, however, participate in determining the types of secondary building units that form and their subsequent crystallographic ordering.

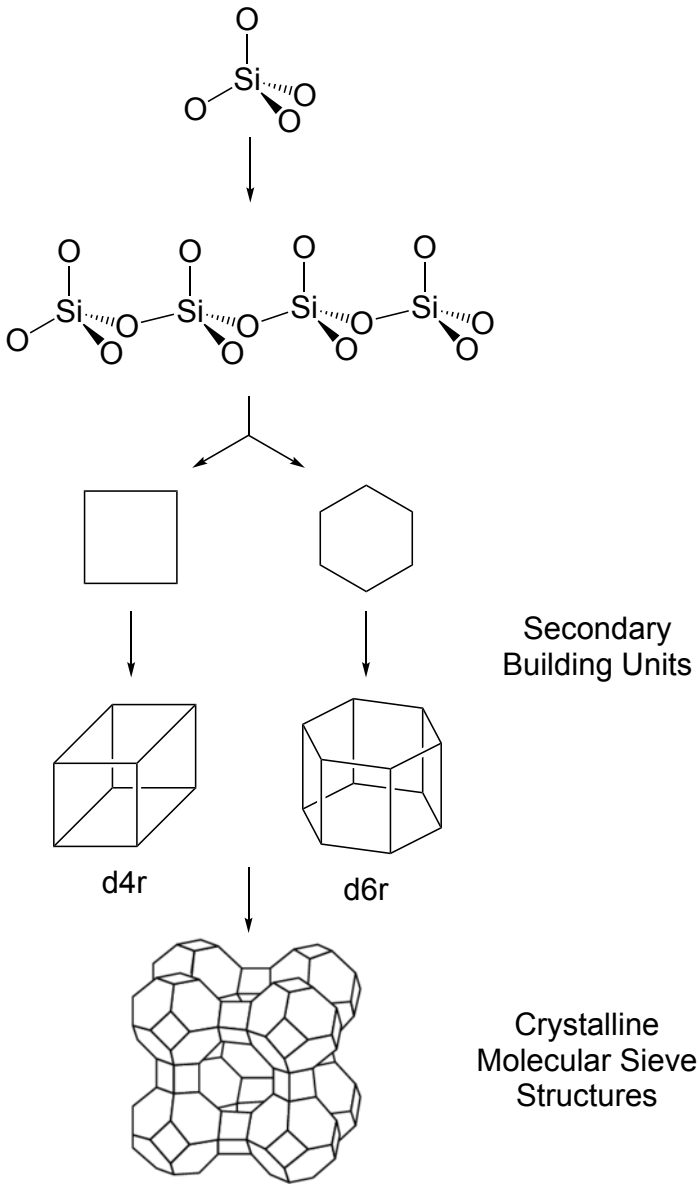

Figure 5.1: Illustration of the crystallization process for molecular sieves, beginning with polymerization of oxide tetrahedra that then form into secondary building units that self-assemble into three-dimensional crystalline materials.[10]

Microporous materials can occur as both natural minerals as well as synthetic materials. In general, naturally occurring minerals are aluminosilicates (a subclass of molecular sieves referred to as zeolites). Incorporation of aluminum into the framework structure imparts an overall net negative charge to the framework that must be balanced by cations. Specifically, each Al^{3+} atom within the framework requires a single extraframework charge-balancing cation. Typical cations in natural zeolites are alkali metals (*e.g.*, Na^{+}, K^{+}, ...) and alkaline earth (*e.g.*, Ca^{2+}, Ba^{2+}, ...). For comparison, a pure-silica structure is completely neutral, and does not require balancing counterions. Cation-containing zeolites serve specific applications in separations and ion exchanges industrially, but they are not catalytically active. An exchange of a cation with a proton, however, may impart Brønsted acid sites within the zeolite structure, forming a solid acid catalyst. Natural zeolites, however, are often phase impure, and may not retain properties that are desirable for a given chemical process. Synthetic analogues provide a means of "designing" and obtaining frameworks of desirable structures and compositional ranges. Currently, there are approximately 230 distinct and unique frameworks (a figure that has grown threefold in the past three decades) that are synthetically attainable out of hundreds of thousands hypothetical structures (around 40 of the structures are known to form naturally).[10,17] One critical difference between naturally occurring and synthetic molecular sieves is that the latter may be formed in the presence of an organic species. Charged organic species may also serve to balance framework charge. Synthetic materials may also include T-atoms beyond Al (*e.g.*, Sn, Ti, Zn,...). Materials that include heteroatoms other than aluminum are referred to as zeotypes or zeolite-like materials. Moreover, molecular sieves do not necessarily need to be formed exclusively from silica. For instance, aluminophosphates are constructed of $AlPO_4$ units, wherein Al^{3+}

is balanced by P^{5+} to form a net neutral framework. Similar to silica-based structures, catalytic activity may be imparted to these materials by manipulation of the framework charge and inclusion of extraframework counterions.

Synthetic molecular sieves are synthesized under hydrothermal conditions and require four primary components: 1) water, 2) inorganic elements (SiO_2, Al_2O_3, ...), 3) a mineralizing agent, such as hydroxide or fluoride, and in some cases 4) an organic molecule (typically an amine-based that is either charged or uncharged).[3,4,18–21] The mixture (often referred to as a gel) is then allowed to react between 100 - 200 °C until crystalline products are formed. As previously stated, however, the process by which crystallization occurs is a highly complex, multivariate system that is currently an active area of research.[22–26] Although the kinetics of crystallite formation are highly dependent on the concentrations and types of materials included in a given synthesis gel, a generic depiction of the process has been reasonably developed for a high-silica framework synthesized in the presence of an organic molecule.[22] Briefly: 1) silicates species in solution form a hydrophobic sphere of hydration around the organic species, 2) these spheres then begin to self-assemble and form aggregates on the order of 1-10 nm, and 3) the aggregates then spawn crystalline growth. In organic-containing syntheses, it is generally believed that the formation of crystallites are dominated by kinetics, despite all molecular sieves being metastable relative to quartz. Therefore, by maintaining equivalent (within statistical error) concentrations and types of inorganic materials, the kinetics of crystallization can be heavily influenced by the structure of the organic molecule included in the synthesis gel. In fact, the use of organics in the molecular sieve synthesis is often attributed with the aforementioned threefold increase in known frameworks in the past three decades.

The use of organics in the synthesis of molecular sieves falls into three broad functions: 1) space-filling species, 2) structure-directing, and 3) templating.[20,21] Organic species that act as space-filling agents lead to the formation of a given framework through weak interactions between the organic and inorganic framework. Typically, this produces frameworks that do not necessarily mimic the structure of the organic. For templating agents, however, there is a precise match between the structure of the organic and that of the resultant framework. Within these two extremes are organic structure-directing agents (OSDAs), which rely on stronger van der Waals interactions to direct formation of the framework, wherein there is a correlation between the geometry of the guest OSDA and resultant framework. OSDAs therefore enable a strategy for "rational design" of molecular sieves.

One difficulty, however, is developing molecular architectures that 1) direct to new frameworks previously unknown, 2) unlock compositions of structures that were not previously possible using other OSDAs, and 3) are not expensive. Zones *et al*. have proposed a number of guidelines for "designing" molecules to direct towards a general classes of framework structures.[27] Moreover, to balance counteracting hydrophobic and hydrophilic effects within the synthesis gel, it has been proposed and demonstrated that OSDAs of intermediate hydrophobicity (*e.g.*, C/N^+ = 11-15) ensure that the organic interacts approximately equally with all components in the system.[24] While it is possible to develop new organics based on these heuristics, it is tedious and inefficient. Recently, Pophale *et al.* have developed a computational method to rationally design OSDAs that direct to specified frameworks.[28] This computational method has proven highly effective in developing OSDAs to synthesize frameworks that previously formed under very narrow compositional ranges, or require very complex organics.[29]

It should be noted that in the context developing molecular sieves for industrial applications, the inclusion of organics often introduces an undesirable expense, particularly if they are not available commercially and require additional synthetic steps to produce. Many techniques have arisen to develop new structures, such as through assembly-disassembly-organization-reassembly (ADOR) from parent materials.[30] Often, however, such parent materials themselves require OSDAs to synthesize. Therefore, while OSDAs may prove prohibitively expensive with respect to industrial scale production economics, they are critical in the production of new molecular sieves frameworks and for synthesizing existing structures with new compositions. As with many technologies, however, the cost of production may decrease with time through improvements in synthesis techniques, reduction in OSDA complexity, or by varying inorganic parameters of the initial discovery.

5.2 Background and Motivation for Chiral Molecular Sieves

Chirality is defined as a system or object (macroscopic or microscopic) that cannot be superimposed onto its mirror image. Hands, for instance, are chiral. Achiral objects however (*i.e.*, objects or systems that do not retain chiral features) may be superimposed on their mirror images, such as a sphere. This example is illustrated in Figure 5.2

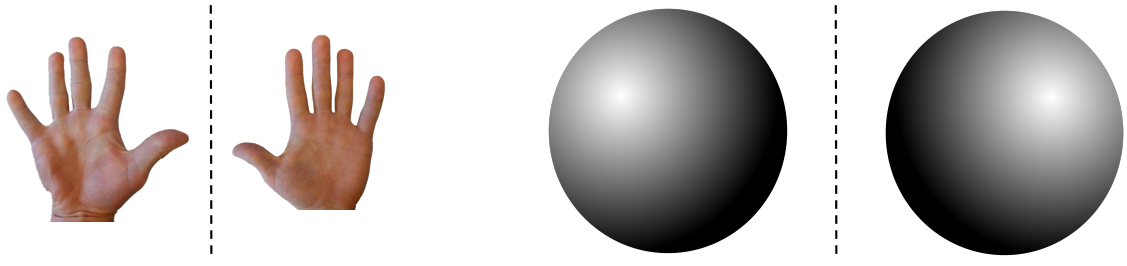

Figure 5.2: Demonstration of chiral, nonsuperimposable mirror images (left) and achiral, superimposable mirror images (right).

In the context of organic and inorganic chemistry, chirality provides a means of distinguishing between molecules that have equivalent chemical compositions, but with subtle differences in binding structures that results in the molecules being nonsuperimposable mirror images. These nonsuperimposable molecules are referred to as enantiomers. At a molecular level, chirality is induced as a consequence of a given atom (typically carbon) being bound to four different functional groups, as shown in Figure 5.3. The atom where this binding feature occurs is referred to as an asymmetric or chiral center. Asymmetric centers are typically denoted "*(R)*" or "*(S)*" based on the specific three-dimensional binding configuration of the unique and distinct functional groups. Bulk compounds that retain a singular enantiomer of a compound are referred to as enantiopure, while samples with equivalent molar concentrations of both enantiomers are known as racemic mixtures.

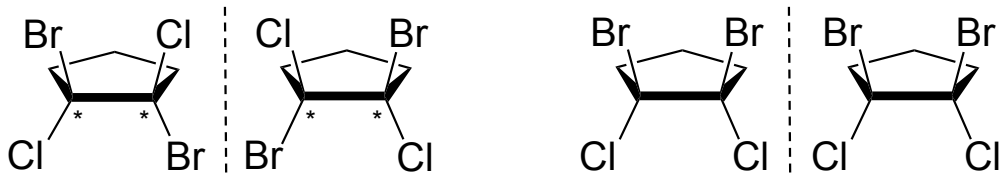

Figure 5.3: Representation of two distinct, chiral molecules (left) and an achiral molecule (right). The asymmetric centers for the chiral molecules are denoted by an asterisk.

Chirality and enantiopurity are ubiquitous in nature and the human body, yet achieving enantiopurity remains one of the great challenges of modern synthetic chemistry. The importance of enantiopurity is readily observed in pharmaceuticals, whereby one enantiomer of a drug may be a valuable product while the other is toxic. This is famously illustrated by naproxen (tradename Aleve) where the *(S)* enantiomer is a highly effective painkiller, while the *(R)* enantiomer is a potent liver toxin. Synthetic processes to produce naproxen industry therefore require costly separations.[31] While numerous other molecules mimic

this effect (particularly with regards to impact on the human physiology) other well-known examples may be found in penicillamine (an anti-arthritic), thalidomide (a treatment of morning sickness for in pregnant women) and L-DOPA (to ease the symptoms of Parkinson's disease). While nature produces many compounds as pure enantiomers, generally by relying upon enzymes, this has proven much harder to achieve synthetically. Enantioselective catalysts are known, but are generally homogeneous organometallic compounds that are limited by high cost, low stability and difficulty in separation from product streams. Due to these limitations, many enantiomeric separations are performed industrially using chiral salt resolutions (from naturally occurring enantiopure alkaloids) or chiral chromatography.[32] Heterogeneous catalysts overcome the separation challenge faced in homogeneous catalysis and are preferred industrially, accounting for 80% of achiral catalysts used.[15,16] Some success in heterogeneous chiral catalysis has been found by anchoring homogeneous catalysts to heterogeneous supports, making recovery easy.[33,34] However, these materials still often exhibit limited stability. A number of studies have focused on the synthesis of chiral metal-organic frameworks, and many have demonstrated capacity to perform asymmetric catalysis, but similarly suffer from stability issues.[35,36] Therefore, the demand for robust, heterogeneous catalysts capable of performing enantioselective reactions is high.

Chiral solids are not novel materials. Quartz crystals, for instance, retain a chiral morphology as well as many known molecular sieves frameworks, namely *BEA, CZP, GOO, -ITV, JRY, LTJ, OSO, SFS, and STW.[10,37–47] Unlike with organic and inorganic molecules, these crystalline structures do not retain asymmetric point chirality. Rather, these structures possess structural chiral features, such as a helical pore structure. As is shown in Figure 5.4, there are two distinct and nonsuperimposable forms of helices that

are that lead to two possible enantiomers for a given chiral molecular sieve. However, under typical hydrothermal synthesis conditions these materials are produced as racemic mixtures. This likely stems from the lack of control over the crystallization process and inability to manipulate the equivalent kinetics and thermodynamics of formation for either structural enantiomer.

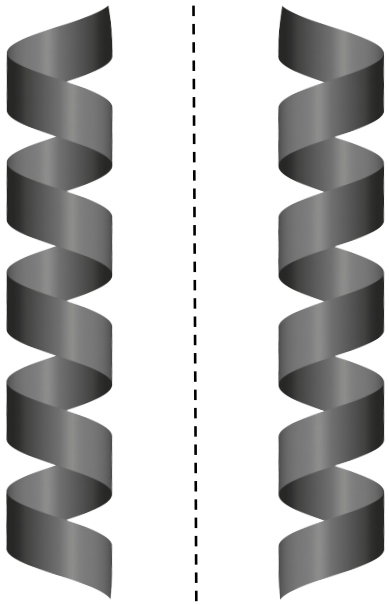

Figure 5.4: Representation of the nonsuperimposable helical pore structures associated with chiral molecular sieves.

It has been postulated by Lobo and Davis that OSDAs may act as an effective means of influencing the kinetics of formation to synthesize only one of the enantiomers for a chiral molecular sieve.[20] Specifically, it is suggested that the OSDA should itself be chiral, stable, and large enough to impart structural chirality. This hypothesis was tested using an undisclosed chiral OSDA in the synthesis of *BEA (an intergrowth of polymorph A (a helical, chiral pore structure) and polymorph B (achiral)). It was demonstrated that polymorph A was indeed enriched relative to traditional synthesis conditions, and that the material

was capable of yielding enantiomeric excess (ee) for adsorption and reactivity experiments (*ca.* 5% for each). Several other attempts have also been reported using *BEA.[48–52] Collectively, these studies indicate the viability of synthesizing an enantioenriched, chiral molecular sieve. However, given that *BEA forms as an intergrowth of polymorphs (and that enrichment of the chiral polymorph A domain does not necessarily guarantee enantioenrichment) has complicated the characterization of these materials and made it difficult to conclusively demonstrate enantiomerically enriched framework content. Lobo and Davis have suggested that synthesizing a microporous equivalent of quartz, whereby individual crystals are single enantiomorphs, would serve as the best platform to achieve and effectively characterize enantioenrichment.[20]

5.3 Overview of Part II

Chapter 6 of this thesis focuses on the synthesis, characterization, and exploration of the functionality of an enantioenriched, polycrystalline molecular sieve. This body of work provides the first instance of the controlled enantioenrichment of a bulk molecular sieve sample. Moreover, it is the first time that both enantiomers (and the racemic mixture) of a molecular sieve have been synthesized, allowing for robust controls to be performed for all characterizations and functionality examinations. It is demonstrated that a computationally "designed" chiral OSDA preferentially templates one enantiomer of the chiral STW framework structure. Enantioenrichment of the samples is subsequently demonstrated through new rotational HRTEM techniques that allow for the chiral space groups of either structural enantiomer to be distinguished. Finally, catalytic reactivity and adsorption studies were conducted to evaluate the capacity for these materials to perform enantioselective pro-

cesses. Chapter 7 discusses the future directions for studying and using chiral heterogeneous molecular sieves.

5.4 References

(1) Li, C. Chiral Synthesis on Catalysts Immobilized in Microporous and Mesoporous Materials. *Catalysis Reviews* **2004**, *46*, 419–492, DOI: 10.1081/CR-200036734.

(2) Che, S.; Liu, Z.; Ohsuna, T.; Sakamoto, K.; Terasaki, O.; Tatsumi, T. Synthesis and characterization of chiral mesoporous silica. *Nature* **2004**, *429*, 281–284.

(3) Čejka, J.; Corma, A.; Zones, S. I., *Zeolites and Catalysis: Synthesis, Reactions and Applications*; Wiley-VCH Verlag GmbH: 2010.

(4) Zones, S. Translating new materials discoveries in zeolite research to commercial manufacture. *Microporous and Mesoporous Materials* **2011**, *144*, 1–8, DOI: 10.1016/j.micromeso.2011.03.039.

(5) Davis, M. E.; Saldarriaga, C.; Montes, C.; Garces, J.; Crowdert, C. A molecular sieve with eighteen-membered rings. *Nature* **1988**, *331*, 698–699.

(6) Davis, M. E. The Quest For Extra-Large Pore, Crystalline Molecular Sieves. *Chemistry –A European Journal* **1997**, *3*, 1745–1750, DOI: 10.1002/chem.19970031104.

(7) Li, X.; Deem, M. W. Why Zeolites Have So Few Seven-Membered Rings. *The Journal of Physical Chemistry C* **2014**, *118*, 15835–15839.

(8) Camblor, M. A.; Diaz-Cabanas, M.-J.; Perez-Pariente, J.; Teat, S. J.; Clegg, W.; Shannon, I. J.; Lightfoot, P.; Wright, P. A.; Morris, R. E. SSZ-23: An Odd Zeolite with Pore Openings of Seven and Nine Tetrahedral Atoms. *Angewandte Chemie International Edition* **1998**, *37*, 2122–2126.

(9) Dahl, I. M.; Kolboe, S. On the reaction mechanism for propene formation in the MTO reaction over SAPO-34. *Catalysis Letters* **1993**, *20*, 329–336, DOI: 10.1007/BF00769305.

(10) McCuster, L. B.; Baerlocher, C. Database of Zeolite Structures., http://www.iza-structure.org/databases.

(11) Deimund, M. A.; Schmidt, J. E.; Davis, M. E. Effect of Pore and Cage Size on the Formation of Aromatic Intermediates During the Methanol-to-Olefins Reaction. *Topics in Catalysis* **2015**, *58*, 416–423, DOI: 10.1007/s11244-015-0384-y.

(12) Bhawe, Y.; Moliner-Marin, M.; Lunn, J. D.; Liu, Y.; Malek, A.; Davis, M. Effect of Cage Size on the Selective Conversion of Methanol to Light Olefins. *ACS Catalysis* **2012**, *2*, 2490–2495, DOI: 10.1021/cs300558x.

(13) Li, J.; Wei, Y.; Liu, G.; Qi, Y.; Tian, P.; Li, B.; He, Y.; Liu, Z. Comparative study of {MTO} conversion over SAPO-34, H-ZSM-5 and H-ZSM-22: Correlating catalytic performance and reaction mechanism to zeolite topology. *Catalysis Today* **2011**, *171*, 221–228, DOI: http://dx.doi.org/10.1016/j.cattod.2011.02.027.

(14) Corma, A. State of the art and future challenges of zeolites as catalysts. *Journal of Catalysis* **2003**, *216*, 40th Anniversary Commemorative Issue, 298–312, DOI: http://dx.doi.org/10.1016/S0021-9517(02)00132-X.

(15) Bravo-Suárez, J. J.; Kidder, M. K.; Schwartz, V., *Novel Materials for Catalysis and Fuels Processing*; J., B.-S. J., K., K. M., Viviane, S., Eds.; American Chemical Society: Washington, DC, 2013, DOI: 10.1021/bk-2013-1132.

(16) Bravo-Suárez, J. J.; Chaudhari, R. V.; Subramaniam, B. In *Novel Materials for Catalysis and Fuels Processing*; Chapter 1, pp 3–68, DOI: 10.1021/bk-2013-1132.ch001.

(17) Earl, D. J.; Deem, M. W. Toward a Database of Hypothetical Zeolite Structures. *Industrial & Engineering Chemistry Research* **2006**, *45*, 5449–5454, DOI: 10.1021/ie0510728.

(18) Li, J.; Corma, A.; Yu, J. Synthesis of new zeolite structures. *Chem. Soc. Rev.* **2015**, *44*, 7112–7127, DOI: 10.1039/C5CS00023H.

(19) Moliner, M.; Rey, F.; Corma, A. Towards the rational design of efficient organic structure-directing agents for zeolite synthesis., 2013, DOI: 10.1002/anie.201304713.

(20) Davis, M. E.; Lobo, R. F. Zeolite and molecular sieve synthesis. *Chemistry of Materials* **1992**, *4*, 756–768, DOI: 10.1021/cm00022a005.

(21) Wagner, P.; Davis, M. E. In *Supramolecular Organization and Materials Design:* Jones, W., Rao, C. N. R., Eds.; Cambridge University Press: Cambridge, 2001, pp 83–102, DOI: 10.1017/CBO9780511564987.004.

(22) De Moor, P.-P. E. A.; Beelen, T. P. M.; Komanschek, B. U.; Beck, L. W.; Wagner, P.; Davis, M. E.; van Santen, R. A. Imaging the Assembly Process of the Organic-Mediated Synthesis of a Zeolite. *Chemistry –A European Journal* **1999**, *5*, 2083–2088, DOI: 10.1002/(SICI)1521-3765(19990702)5:7<2083::AID-CHEM2083>3.0.CO;2-F.

(23) Davis, T. M.; Drews, T. O.; Ramanan, H.; He, C.; Dong, J.; Schnablegger, H.; Katsoulakis, M. A.; Kokkoli, E.; McCormick, A. V.; Penn, R. L.; Tsapatsis, M. Mechanistic principles of nanoparticle evolution to zeolite crystals. *Nat Mater* **2006**, *5*, 400–408.

(24) Cundy, C. S.; Cox, P. A. The hydrothermal synthesis of zeolites: Precursors, intermediates and reaction mechanism., 2005, DOI: 10.1016/j.micromeso.2005.02.016.

(25) Flanigen, E. M. In *Molecular Sieves*; American Chemical Society: 1973, pp 119–139, DOI: doi:10.1021/ba-1973-0121.ch010.

(26) Meier, W. M.; Uytterhoeven, J. B., *Molecular Sieves*; American Chemical Scoiety: 1973; Vol. 121, p 652, DOI: doi:10.1021/ba-1973-0121.

(27) Zones, S.; Lee, H.; Davis, M.; Casci, J.; Burton, A. In *Molecular Sieves: From Basic Research to Industrial ApplicationsProceedings of the 3rd International Zeolite Symposium (3rd FEZA)*, J. Čejka, N. Ž., Nachtigall, P., Eds.; Studies in Surface Science and Catalysis, Vol. 158, Part A; Elsevier: 2005, pp 1–10, DOI: http://dx.doi.org/10.1016/S0167-2991(05)80315-5.

(28) Pophale, R.; Daeyaert, F.; Deem, M. W. Computational prediction of chemically synthesizable organic structure directing agents for zeolites. *J. Mater. Chem. A* **2013**, *1*, 6750–6760, DOI: 10.1039/C3TA10626H.

(29) Schmidt, J. E.; Deem, M. W.; Davis, M. E. Synthesis of a specified, silica molecular sieve by using computationally predicted organic structure-directing agents. *Angewandte Chemie - International Edition* **2014**, *53*, 8372–8374.

(30) Roth, W. J.; Nachtigall, P.; Morris, R. E.; Wheatley, P. S.; Seymour, V. R.; Ashbrook, S. E.; Chlubná, P.; Grajciar, L.; Položij, M.; Zukal, A.; Shvets, O.; Čejka, J. A family

of zeolites with controlled pore size prepared using a top-down method. *Nat Chem* **2013**, *5*, 628–633.

(31) Yang, Y.; Su, B.; Yan, Q.; Ren, Q. Separation of naproxen enantiomers by supercritical/subcritical fluid chromatography. *Journal of Pharmaceutical and Biomedical Analysis* **2005**, *39*, 815–818, DOI: 10.1016/j.jpba.2005.05.008.

(32) Maier, N. M.; Franco, P.; Lindner, W. Separation of enantiomers: needs, challenges, perspectives. *Journal of Chromatography A* **2001**, *906*, 3–33, DOI: 10.1016/S0021-9673(00)00532-X.

(33) Corma, A.; Iglesias, M.; del Pino, C.; Sanchez, F. New Rhodium Complexes anchored on Modified USY Zeolites. A Remarkable Effect of the Support on the Enantioselectivity of Catalytic Hydrogenation of Prochiral Alkenes. *Journal of the American Chemical Society* **1991**, 1253–1255, DOI: 10.1039/c39910001253.

(34) Carmona, A.; Corma, A.; Iglesias, M.; Sánchez, F. Synthesis and characterisation of chiral Cu(I) complexes of substituted pyrrolidine ligands. Efficient catalysts for cyclopropanation reactions. *Inorganica Chimica Acta* **1996**, *244*, 239–245, DOI: 10.1016/0020-1693(95)04773-5.

(35) Xu, Z. X.; Ma, Y. L.; Zhang, J. Enantiopure anion templated synthesis of a zeolitic metal-organic framework. *Chem Commun (Camb)* **2015**, 1923–1925, DOI: 10.1039/c5cc09308b.

(36) Wang, C.; Zheng, M.; Lin, W. Asymmetric Catalysis with Chiral Porous Metal À Organic Frameworks : Critical Issues. **2011**, 1701–1709.

(37) Newsam, J. M.; Treacy, M. M. J.; Koetsier, W. T.; Gruyter, C. B. D. Structural Characterization of Zeolite Beta. *Proceedings of the Royal Society of London. A. Mathematical and Physical Sciences* **1988**, *420*, 375 LP –405, DOI: 10.1098/rspa.1988.0131.

(38) Higgins, J. B.; LaPierre, R. B.; Schlenker, J. L.; Rohrman, A. C.; Wood, J. D.; Kerr, G. T.; Rohrbaugh, W. J. The framework topology of zeolite beta. *Zeolites* **1988**, *8*, 446–452, DOI: 10.1016/S0144-2449(88)80219-7.

(39) Rajić, N.; Logar, N. Z.; Kaučič, V. A novel open framework zincophosphate: Synthesis and characterization. *Zeolites* **1995**, *15*, 672–678, DOI: 10.1016/0144-2449(95)00083-I.

(40) Rouse, R. C.; Rouse, R. C.; Peacor, D. R.; Peacor, D. R. Crystal structure of the zeolite mineral goosecreekite, CaAl2Si6O16 ·5H2O. *American Mineralogist* **1986**, *71*,

(41) Sun, J.; Bonneau, C.; Cantín, Á.; Corma, A.; Díaz-Cabañas, M. J.; Moliner, M.; Zhang, D.; Li, M.; Zou, X. The ITQ-37 mesoporous chiral zeolite. *Nature* **2009**, *458*, 1154–1157.

(42) Song, X.; Li, Y.; Gan, L.; Wang, Z.; Yu, J.; Xu, R. Heteroatom-stabilized chiral framework of aluminophosphate molecular sieves. *Angewandte Chemie - International Edition* **2009**, *48*, 314–317, DOI: 10.1002/anie.200803578.

(43) Broach, R. W.; Kirchner, R. M. Structures of the K+ and NH4+ forms of Linde J. *Microporous and Mesoporous Materials* **2011**, *143*, 398–400, DOI: 10.1016/j.micromeso.2011.03.025.

(44) Elomari, S.; Burton, A.; Medrud, R. C.; Grosse-Kunstleve, R. The synthesis, characterization, and structure solution of SSZ-56: An extreme example of isomer specificity

in the structure direction of zeolites. *Microporous and Mesoporous Materials* **2009**, *118*, 325–333, DOI: 10.1016/j.micromeso.2008.09.011.

(45) Tang, L.; Shi, L.; Bonneau, C.; Sun, J.; Yue, H.; Ojuva, A.; Lee, B.-L.; Kritikos, M.; Bell, R. G.; Bacsik, Z.; Mink, J.; Zou, X. A zeolite family with chiral and achiral structures built from the same building layer. *Nature Materials* **2008**, *7*, 381–385, DOI: 10.1038/nmat2169.

(46) Rojas, A.; Camblor, M. A. A pure silica chiral polymorph with helical pores. *Angewandte Chemie - International Edition* **2012**, *51*, 3854–3856.

(47) Rojas, A.; Arteaga, O.; Kahr, B.; Camblor, M. A. Synthesis, Structure, and Optical Activity of HPM-1, A Pure Silica Chiral Zeolite. *Journal of the American Chemical Society* **2013**, *135*, 11975–11984.

(48) Tong, M.; Zhang, D.; Fan, W.; Xu, J.; Zhu, L.; Guo, W.; Yan, W.; Yu, J.; Qiu, S.; Wang, J.; Deng, F.; Xu, R. Synthesis of chiral polymorph A-enriched zeolite Beta with an extremely concentrated fluoride route. *Scientific reports* **2015**, *5*, 11521, DOI: 10.1038/srep11521.

(49) Takagi, Y.; Komatsu, T.; Kitabata, Y. Crystallization of zeolite beta in the presence of chiral amine or rhodium complex. *Microporous and Mesoporous Materials* **2008**, *109*, 567–576, DOI: 10.1016/j.micromeso.2007.06.005.

(50) Taborda, F.; Willhammar, T.; Wang, Z.; Montes, C.; Zou, X. Synthesis and characterization of pure silica zeolite beta obtained by an aging-drying method. *Microporous and Mesoporous Materials* **2011**, *143*, 196–205, DOI: 10.1016/j.micromeso.2011.02.030.

(51) Camblor, M. A.; Corma, A.; Valencia, S. Spontaneous nucleation and growth of pure silica zeolite-B free of connectivity defects. *Chemical Communications* **1996**, 2365, DOI: 10.1039/cc9960002365.

(52) Zhang, R.-C.; Wang, J.-J.; Yuan, B.-Q.; Zhang, J.-C.; Zhou, L.; Wang, H.-B.; Zhang, D.-J.; An, Y.-L. Syntheses and Characterization of Chiral Zeolitic Silver Halides Based on 3-Rings. *Inorganic Chemistry* **2016**, *4*, 11593–11599, DOI: 10.1021/acs.inorgchem.6b02121.

Chapter 6

THE SYNTHESIS, CHARACTERIZATION, AND FUNCTIONALITY OF ENANTIOMERICALLY ENRICHED, POLYCRYSTALLINE MOLECULAR SIEVES

Information contained in Chapter 6 was originally published in:

(1) Brand, S. K.; Schmidt, J. E.; Deem, M. W.; Daeyaert, F.; Ma, Y.; Terasaki, O.; Orazov, M.; Davis, M. E. Enantiomerically Enriched, Polycrystalline Molecular Sieves. *Proceedings of the National Academy of Sciences* **2017**, DOI: 10.1073/pnas.1704638114,

6.1 Introduction

The synthesis of zeolites and zeolite-like molecular sieves has been accomplished using organic structure-directing agents (OSDAs).[1–4] This synthetic method utilizes an organic molecule (OSDA) to interact with and influence the assembly pathway of the inorganic components to create a crystalline, organic-inorganic composite material. Upon removal of the OSDA, the microporous void space that is created can be exploited in variety of applications, *i.e.*, catalysis, separations, ion exchange and adsorption.[5] These microporous, polycrystalline materials are three-dimensional networks of oxide tetrahedra (zeolites contain only silicon and aluminum, while zeolite-like molecular sieves can have a broader range of elements[1–5]) that create highly-ordered, hydrothermally-stable framework structures with pores of sizes less than 2 nm. Molecular sieves provide shape-selective properties and, coupled with the inclusion of catalytic active sites, are capable of innumerable, highly selective chemical reactions. Despite the abundance of chirality in nature, the discovery of a zeolite or zeolite-like microporous material with enantioselective properties has remained

elusive. Enantioenriched, chiral zeolitic materials are of particular interest for their potential to provide robust, new, enantiospecific, shape-selective catalytic pathways and separation processes.[6–13]

Several inherently chiral molecular sieves have been synthesized to date (although the bulk, polycrystalline samples are racemic), including *BEA, CZP, GOO, -ITV, JRY, LTJ, OSO, SFS, and STW (molecular sieve framework types are designated by three-letter codes that define the unique connectivity of the oxide tetrahedral).[14] In particular, several studies have reported polymorph A (that possesses a chiral helical pore) enriched *BEA. However, zeolite *BEA is limited in that the material crystallizes as highly faulted intergrowths of a racemic mixture of polymorphs A and polymorph B (achiral). In 1992, Lobo and Davis discussed the concept of synthesizing a chiral *BEA molecular sieve *via* the use of a chiral OSDA, and reported low enantioenrichment (ee) for both a chemical reaction and an adsorption experiment.[15] Recently, Tong *et al.* have reported a high-fluoride method of synthesizing polymorph A enriched *BEA using achiral OSDAs (although difficult to understand the origin of the proposed enantioenrichment), and reported low ee's from a chemical reaction.[16] Other authors have reported samples enriched in polymorph A with similar ambiguity in enantioenrichment.[17–20] These studies suggest the viability of synthesizing an enantioenriched, chiral molecular sieve. However, the inherent difficulty in controlling the synthesis of polymorphic domains, and the enantiomeric domains of only polymorph A in *BEA, has made it very problematic to conclusively prove that a bulk sample of a molecular sieve does in fact have an enantiomerically enriched framework content. Lobo and Davis discussed this issue and suggested that a preferred approach would be to design syntheses that target chiral molecular sieve structures where individual crystals

are single enantiomorphs (microporous analogs to quartz).[15] The STW framework is an example of this type of molecular sieve, since recent evidence shows that each individual crystal is a single enantiomorph (*i.e.*, there are no polymorph or opposite enantiomeric domains within a single crystal).[21]

A molecular sieve with the STW framework was initially synthesized as a germanosilicate (denoted, SU-32) in 2008,[22] and then as a hydrothermally stable pure-silica material in 2012.[22,23] The STW structure contains 10-membered rings (MRs: number of oxygen or tetrahedral atoms that make up the ring) that form chiral helical pores.[22] Past synthesis protocols that utilized achiral OSDAs resulted in bulk, polycrystalline samples that were racemic mixtures of the two structural enantiomers. STW, therefore, provides a good model for designing the synthesis of bulk, polycrystalline samples of either the "*R*" or "*S*" enantiomers of the framework. Here, we employ computational methods to aid in our design of chiral OSDAs for the synthesis of enantioenriched STW, and show for the first time, that a bulk sample of a polycrystalline, molecular sieve can be synthesized with significant enantiomeric enrichment. Our design (shown in Figure 6.1) provides for the synthesis of either the "*R*" or the "*S*" enantiomers of STW, thus yielding materials that enable appropriate control experiments when elucidating structures and functions.

6.2 Experimental Methods

Computational Details

We built the method of Pophale *et al.* to carry out the computations, here considering chirality of the OSDA.[24] The DREIDING forcefield was used in the GULP simulation program to carry out the calculations. The OSDA identified in Schmidt *et al.* was found to

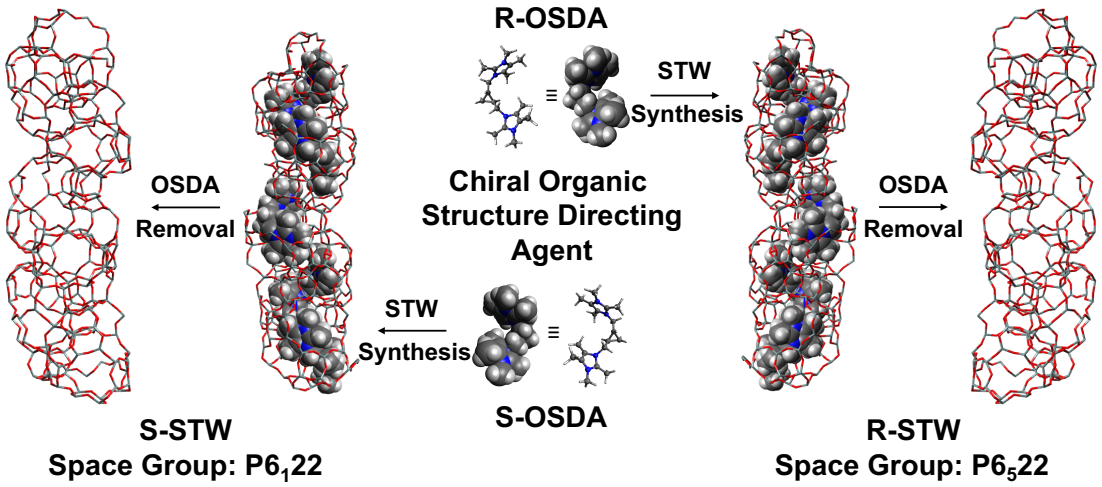

Figure 6.1: Illustration of the synthesis of enantioenriched STW samples using enantiopure, chiral OSDAs.

occupy the cages of STW at a loading of two per cage.[25] We carried out a combinatorial search of two OSDA monomers, linked by the Menshutkin reaction to a halogenated carbon chain. We obtained the linkers from the shelf and also extended the shelf by applying all zero-order reactions and brominating the resulting compounds having a OH group. We required the constructed molecules to contain two chiral centers, no more than 8 torsions, and between 2 and 4 quaternary amines. In all, we considered 644 linked diquats. The stabilization energies of all chiral enantiomorphs were calculated, and the energy gap between the most and second most stable form was computed. The stabilization energy was computed as in Pophale *et al.*, *via* geometric placement of the OSDAs in the zeolite, with four energy minimizations, followed by three increasingly longer molecular dynamics runs at 343 K.[24]

Sources of Chemicals

trans-2-Phenylcyclopropane-1-carboxylic acid (Sigma-Aldrich, 95%), quinine (Sigma-Aldrich, anhydrous, ≥98%), +-dehydroabietylamine (Sigma-Aldrich, 60%), toluene (EMD Millipore, ≥99.5%), glacial acetic acid (EMD Millipore, 99%), hexane (EMD Millipore, ≥95%), water (house still, ≥99.99%), sodium hydroxide (Alfa Aesar, 97%), diethyl ether (EMD Millipore, ≥99.0%), potassium carbonate (Sigma-Aldrich, anhydrous, 99.99% trace metals basis), methanol (EMD Millipore, ≥99.8%), sodium bicarbonate (Sigma-Aldrich, ≥99.7%), hydrochloric acid (Sigma-Aldrich, 37%), magnesium sulfate (Sigma-Aldrich, anhydrous, ≥99.5%), chloroform (EMD Millipore, ≥99.8%), ethyl acetate (EMD Millipore, ≥99.5%), hydrogen peroxide (EMD Millipore, 30% (w/w) in water), tetrahydrofuran (EMD Millipore, ≥99.5%), lithium aluminum hydride (Sigma-Aldrich, 95%), ammonium chloride (Sigma-Aldrich, 99.7%), bromine (Sigma-Aldrich, 99.5%), triphenylphosphine (Sigma-Aldrich, 99%), acetonitrile (Sigma-Aldrich, anhydrous, 99.8%), tetramethylimidazole (TCI Chemicals, 98%), Dowex Marathon A, hydroxide from (Sigma-Alrich), [Tetrabutylammonium] [(Λ,R)-(1,1'-binaphthalene-2,2'diolato) (bis (tetrachlor-1,2-benzenediolato) phosphat(V))] (Sigma-Aldrich, ≥95%), tetraethylorthosilicate (Sigma-Aldrich, 98%), hydrofluoric acid (Sigma-Aldrich, 48% (w/w) in water), aluminum isopropoxide (Sigma-Aldrich, ≥99.99% trace metals basis), and germanium oxide (Strem, 99.99%) were purchased and used as received.

Synthesis and NMR Characterization of the Chiral Organic Structure Directing Agent

A summary of the synthesis method implemented to develop both the *R*- and *S*-enantiomers of the organic structure directing agent used in this study is detailed in Figure 6.2 (chiral

separation) and Figure 6.3 (reaction pathway).

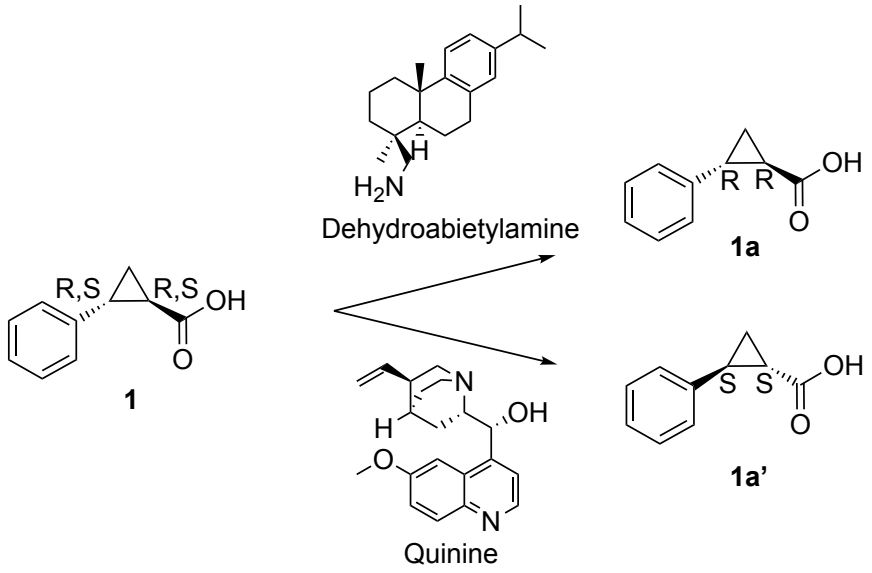

Figure 6.2: Chiral resolution scheme of trans-2-phenylcyclopropane-1-carboxylic acid using dehydroabietylamine or quinine to yield **1a** or **1a'**, respectively.[26,27]

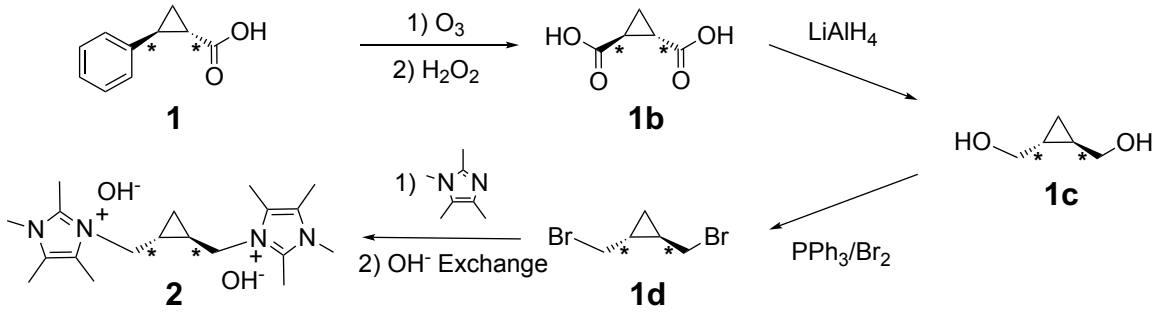

Figure 6.3: Scheme for the synthesis of the racemic OSDA **2** from **1**. Note that the same synthesis procedure can be applied to **1a** or **1a'** to yield *R*-**2** or *S*-**2**, respectively.

Separation of the Enantiomers of 1

Several methods have been described to separate what are denoted the (-)-*R* (**1a**) and (+)-*S* (**1a'**) enantiomers of trans-2-phenylcyclopropanecarboxylic acid (**1**) using either quinine

and brucine or dehydroabietylamine, respectively.[26,27] In this work, brucine was avoided due to the toxicity of this compound.

Chiral Resolution of (1*R*,2*R*)-2-Phenylcyclopropane-1-carboxylic acid (1a)

The purification of dehydroabietylamine was conducted by the method reported by Gottstein.[28] 900 g of dehydroabietylamine was dissolved in 1.5 liters of toluene. Then a solution of 210 g of glacial acetic acid in 500 mL of toluene was added. The solution was then refrigerated overnight and the product was collected *via* filtration and washed with cold toluene. The product was recrystallized one time from toluene and washed with hexane and dried under vacuum to yield 490 g of purified dehydroabietylamine acetate.

Dehydroabietylamine acetate (490 g) was dissolved in 630 mL of boiling water. Then 500 mL of 10% NaOH solution were added. After the mixture was chilled it was extracted several times with diethyl ether, the combined extracts were washed with water and dried over anhydrous potassium carbonate. The ether was then removed using rotary evaporation to yield 357 g of a yellow oil that slowly solidified.

The enantiopurification was performed according to the method of Cheng *et al*.[27] 150 g of **1** (racemic mixture from Aldrich, MW = 162.19, 925 mmol) was dissolved in 940 mL of warm methanol. Then 263 g of purified dehydroabietylamine (925 mmol) was dissolved separately in 750 mL of warm methanol. The two solutions were slowly combined and, after sitting at room temperature overnight, the resultant solid salt of dehydroabietylamine and **1a** was recovered using filtration and was then recrystallized from 90% aqueous methanol six times to yield a solid with a rotation of $[\alpha]_D^{20}$ −81° (c 0.42, MeOH) (literature: $[\alpha]_D^{20}$ −80.8° (c 0.61, MeOH)) .[27] The total mass of recovered solids was 78.5 g.

The free acid was isolated by adding the salt dehydroabietylamine and **1a** to a saturated solution of $NaHCO_3$ and then extracting with diethyl ether. The aqueous fraction was then acidified with 37% hydrochloric acid followed by successive extractions with diethyl ether. The organic extractions were combined, dried over anhydrous magnesium sulfate, and then the solvent removed using rotary evaporation to yield 18.1 g of enantiopure **1a**. The rotation of **1a** in chloroform was found to be $[\alpha]_D^{20}$ −375.6° (c 1.07, $CHCl_3$) (literature: $[\alpha]_D^{20}$ −401° (c 0.88, $CHCl_3$)).[27]

Chiral Resolution of (1*S*,2*S*)-2-Phenylcyclopropane-1-carboxylic acid (1a')

Following the method of Cheng *et al*. and Overberger *et al*., 125 g of **1** (racemic mixture from Aldrich, MW=162.19, 771 mmol) were added to 250 g of quinine (Aldrich, MW=324.42, 771 mmol) in 4 L of ethyl acetate at reflux.[26,27] The mixture was then allowed to cool to room temperature and allowed to sit at room temperature for 1 week, over which time large white crystals of the salt of quinine and **1a'** precipitated from the solution. The crystals were recovered by filtration, and the filtrate was then recrystallized an additional 5 times from ethyl acetate to yield a white product with a rotation of $[\alpha]_D^{20}$ −10.0° (c 1.0, EtOH) (literature: $[\alpha]_D^{20}$ −10.2° (c 1.0, EtOH)).[27] The total yield of the salt at was 95.1 g.

The free-acid product was recovered by dissolving 46.6 g of the salt of quinine and **1a'** in 500 mL of 1 M HCl at room temperature. **1a'** was then recovered by extraction with diethyl ether to yield 15.0 g. The rotation of **1a'** in chloroform was found to be $[\alpha]_D^{20}$ +370.8° (c 1.07, $CHCl_3$) (literature: $[\alpha]_D^{20}$ +406° (c 1.0, $CHCl_3$)).[27]

For both **1a** and **1a'**, further crystallization steps did not alter the polarimetry experiments. Additionally, the ^1H NMR of both compounds was identical to the starting material ($CDCl_3$,

500 MHz): δ = 7.0-7.2 (m, 5H, Ph), 2.52 (m, 1H), 1.83 (m, 1H), 1.59 (m, 1H), 1.33 (m, 1H).

The synthesis procedures detailed below are written from the perspective of using a racemic starting material. However, the exact same procedures can be applied for the enantiopure starting materials **1a** and **1a'** to obtain *R*-**2** and *S*-**2**, respectively.

Trans-2-phenylcyclopropane carboxylic acid (1) to trans-1,2-cyclopropane carboxylic acid (1b)

1b was prepared by ozonolysis of **1** (either enantiomer, or the racemic mixture) in acetic acid according to the procedure reported by Inouye *et al*.[29] In a typical synthesis 11.6 g of **1a** (MW = 162.19) was dissolved in 200 mL of glacial acetic acid. A stream of ozone was bubbled through the mixture with stirring (125 mL/minute of 6.7% ozone in O_2) at 50°C. The mixture was allowed to react for 36 hours. The reaction was cooled, and 50 mL of 30% aqueous H_2O_2 was added and stirred overnight. All liquid was then removed using vacuum distillation. Then, an additional 50 mL of 30% aqueous H_2O_2 was added, stirred for several hours, and the liquid again removed using vacuum distillation. This was repeated a total of 4 times, and the recovered solids were dried under vacuum. A total of 7.49 g of solid 1b was recovered (MW=130.10). ^{1}H NMR (D_2O, 500 MHz): δ = 2.04 (m, 2H), 1.39 (m, 2H). ^{13}C NMR (D_2O, 500 MHz): 175.7, 22.1, 15.3.

Trans-1,2-cyclopropane carboxylic acid (1b) to trans-1,2-cyclopropane diol (1c)

The procedure for the reduction of **1b** to **1c** was adapted from Taylor *et al*. 200 mL of THF in a 1 L round-bottom flask (RBF) were cooled in an ice bath under a nitrogen atmosphere.[30]

Then 14.95 g of $LiAlH_4$ was slowly added and stirred for 1 hour. 25 g of **1b** was dissolved in THF and the slowly added to the $LiAlH_4$ suspension using a dropping funnel. After the addition was complete the mixture was stirred at 0 °C for 2 hours. Then, the RBF was removed from the ice bath and slowly allowed to warm up to room temperature and stirred for 2 hours. Finally, the reaction was heated to reflux and stirred overnight. The mixture was then cooled in an ice bath and 60 g of saturated ammonium chloride solution was slowly added, followed by 100 mL of ethyl acetate. The suspension was stirred for 4 hours and then filtered. The retentate was resuspended in additional ethyl acetate, stirred an additional 4 hours, and then filtered once again. The liquid filtrate was combined and dried over magnesium sulfate. After removing the magnesium sulfate by filtration, the solvent was removed using rotary evaporation to yield a yellow oil. The yield of **1c** was 9.54 g (93.4 mmol, 70%) and was used without further purification. ^{1}H NMR ($CDCl_3$, 500 MHz): δ = 5.05 (s, 2H), 3.76 (m, 2H), 3.07 (m, 2H), 1.01 (m, 2H), 0.43 (m, 2H). ^{13}C NMR ($CDCl_3$, 500 MHz): δ = 65.8, 19.8, 7.2.

Trans-1,2-cyclopropane diol (1c) to trans-1,2-dibromocyclopropane (1d)

1d was prepared following a method reported by de la Fuente *et al*.[31] In a typical reaction, 16.04 g of bromine was added to a solution of 26.32 g triphenylphosphine in dry acetonitrile (200 mL) at 273 K. A solution of 5 g of **1c** in dry acetonitrile (100 mL) was added to the reaction mixture, which was then stirred under an argon purge overnight at room temperature. Remaining acetonitrile was subsequently evaporated to yield a clear oil as well as a white triphenylphosphine oxide solid. This crude mixture was finely dispersed in hexane (2 x 250 mL) and filtered to remove the triphenylphosphine oxide. The hexane

solution was evaporated under vacuum to give 4.0 g of **1d**. If necessary, **1d** was purified using column chromatography on silica gel with hexane/ethyl ether (95:5) as the eluent. ^{1}H NMR ($CDCl_3$, 500 MHz): δ = 3.35 (m, 4H), 1.33 (m, 2H), 0.86 (m, 2H). ^{13}C NMR ($CDCl_3$, 500 MHz): δ = 37.0, 24.4, 17.3.

Trans-1,2-dibromocyclopropane (1d) to Final OSDA Product (2)

Compound **1d** was dissolved in chloroform and then a 10% excess of tetramethylimidazole was added and the solution was refluxed overnight. After the reaction was complete, the reaction mixture was cooled to room temperature and then the diquaternary product was extracted using water (3 times). The water was removed using rotary evaporation and the resulting solid was then dried under vacuum overnight. Finally, the product was recrystallized from chloroform to yield a white product in quantitative yield. ^{1}H NMR ($CDCl_3$, 500 MHz): δ = 4.80 (m, 1H), 4.04 (m, 1H), 3.74 (s, 3H), 2.99 (s, 3H), 2.31 (s, 3H), 2.24 (s, 3H), 1.73 (m, 1H), 0.85 (t, 2H). ^{13}C NMR ($CDCl_3$, 500 MHz): δ = 143.2, 125.8, 125.1, 48.2, 32.8, 17.4, 12.4, 10.6, 9.5, 9.1.

Prior to use in inorganic syntheses, **2** was ion exchanged to hydroxide form using Dowex Marathon A exchange resin and the final product concentration was determined using a Mettler-Toledo DL22 autotitrator using 0.01 M HCl as the titrant.

Characterization of the Enantiopurity of 2

A survey of the literature finds that the enantiodiscrimination of quaternary (and diquaternary) ammonium compounds can be challenging. One method that has seen published success for this is the chiral shift reagent, Tetrabutylammonium][(Λ,R)-(1,1'-binaphthalene-

2,2'diolato)(bis(tetrachlor-1,2-benzenediolato)phosphat(V)) (BINPHAT).[32–35] In a typical NMR experiment, BINPHAT was mixed in equimolar amounts (according to charge) with **2** in boiling $CDCl_3$ and the product was studied using ^{1}H NMR.

Enantiomers of **2** are denoted *R*-**2** and *S*-**2**

Synthesis and Characterization of STW

Synthesis of germanosilicate STW using OSDA 2

STW was synthesized by methods adopted from those previously reported.[23,25] Conditions under which germanosilicate STW was found to crystallize most successfully were found to stem from starting gel compositions of 1 SiO_2 : 0.5 GeO_2 : 4 H_2O : 0.5 HF : 0.5 **2** (enantiopure or racemic). For a typical reaction, the desired quantity of germanium oxide and OSDA were mixed, and the solids were allowed to homogenize over the period of an hour. Next, a quantity of tetraethylorthosilicate was added, and the mixture was allowed to hydrolyze over the period of 12 hours. Ethanol produced as a consequence of the hydrolysis was then allowed to evaporate at room temperature, in addition to a quantity of water to attain the desired H_2O/SiO_2 ratio. After allowing the gel to age at its final composition for 24 hours, as-synthesized, racemic, pure-silica STW (particle size *ca*. 1 μm) was added as seed material (10% (w/w) of SiO_2 in the gel) to this gel and mixed. The final gel was transferred to a Teflon-lined stainless steel autoclave and heated at 433 K in a rotating oven until crystallization products formed. The recovered solids were centrifuged, washed extensively with water and acetone, then dried in an oven at 343 K. To remove the organic occluded within the structure, the sample was placed into a tube furnace maintained at 423 K through which ozone was passed (125 mL/minute of 6.7% ozone in O_2). For materials

with less germanium content, the solids were calcined in flowing air (100 mL min^{-1}, Airgas, breathing grade) at 853 K (after a ramp of 1 K min^{-1}) for 6 hours after maintaining 423 K for 3 hours.

Synthesis of aluminogermanosilicate STW using OSDA 2

Aluminogermanosilicate STW was synthesized using a similar procedure outlined *vide supra* for germanosilicate STW. However, to the initial combination of germanium oxide and OSDA, a quantity of aluminum isopropoxide was added and allowed to homogenize and hydrolyze. The final gel composition of samples used in catalytic function testing were 1 SiO_2 : 0.5 GeO_2 : 0.01 Al_2O_3 : 5 H_2O : 0.5 HF : 0.5 **2** (enantiopure or racemic). Similar procedures were also followed to remove the organic content.

A summary of STW syntheses using **2** is provided in Appendix D, in addition to NMR, XRD, TGA, SEM and, EDS characterizations (Tables D.1-D.4 and Figures D.1-D.6).

Reaction and Analysis Procedures

After addition of 20 mg of Al-containing STW (Si/Al = 30 ± 10), 20 mmol of epoxide substrate, and 5 g of methanol (with pre-dissolved naphthalene as internal standard) were added to a 10 mL thick-walled glass reactor (VWR) containing a stir bar. The reactor was crimp-sealed and placed in a temperature-controlled oil bath at the desired reaction temperature. At predetermined times, aliquots of (100 μL) were extracted and analyzed.

Quantitative GC/FID analysis was performed on an Agilent 7890B GC system equipped with a flame ionization detector and an Agilent Cyclosil-B column. Liquid ^{1}H and ^{13}C NMR spectra were recorded with a Varian INOVA 500 MHz spectrometer equipped with

an auto-x pfg broad band probe. All liquid NMR analysis was performed in deuterated methanol.

Adsorption Procedures

Adsorption isotherms were collected on a Quantachrome Autosorb iQ with varying methods depending upon the adsorbate.

HRTEM Sample Preparation

The powdered sample was crushed and dispersed into ethanol using ultrasonic processing. Several drops of the dispersion were dropped onto a carbon-film supported TEM grid. Gold particles were deposited onto the sample through sputter coating.

Electron diffraction patterns and HRTEM images were obtained using a 200 kV using JEOL JEM-2100F (Cs = 0.5 mm, Cc = 1.1 mm). Each projection image was reconstructed from a through-focus series of 20 HRTEM images acquired with a constant focus step of 53 Å. The structure projection reconstruction was done using software *Qfocus*.[36]

6.3 Results and Discussion

Directed Computational Design of a Chiral OSDA for STW

Schmidt *et al.* reported on the synthesis of STW utilizing a computationally predicted OSDA.[25] This work demonstrated the feasibility of *a priori* predicting chemically synthesizable monoquaternary, imidazolium OSDAs to create a specified, fluoride-mediated, pure-silica framework. Additionally, STW has been reported to form using diquaternary imidazolium-based OSDAs that are of sufficient size to conform to 10MR channel structure, implying more rigid, chiral analogues may be included in the framework of STW,

and may potentially impart structural chirality.[25,37–44] Here, we implemented the previously published computational method implemented by Schmidt *et al*., and utilized the molecular design constraints suggested by Lobo and Davis.[15,24] The computational method was modified such that a given enantiomer of each potential OSDA molecule was simulated in both enantiomers of STW, with successful candidates producing a strong stabilization in only a single enantiomer. Based on our previous work with STW, we believed that a computed stabilization energy larger than -15 kJ-(mol Si)$^{-1}$ would be needed in order to form STW. Ultimately, a single OSDA candidate was selected (Table 6.1). Relative to the other predicted OSDAs for STW, **2** has the largest energy difference between enantiomers, making it the most suitable target for experimental evaluation. Coupled with energy predictions, this molecule was also selected after ensuring that the both enantiomers were synthetically attainable.[25]

Synthesis and Characterization of Enantiopure OSDA 2

Chiral resolution of the starting compound (trans-2-phenylcyclopropane-1-carboxylic acid, **1**) was performed by successive crystallizations with either dehydroabietylamine (DHBA) or quinine as chiral derivatization agents to obtain the *R* (**1a**) or *S* (**1a'**) forms of the starting material (Figure 6.2). Polarimetry measurements were taken for the salt and free-acid forms of **1a** and **1a'** to confirm enantiopurity, after the separation was complete. (Λ,R)-BINPHAT tetrabutylammonium salt was used as a chiral shift reagent to detect the enantiopurity of **2** after executing the reactions outlined in Figure 6.3. As shown in Figure 6.4, the neat product ^{1}H NMR resonances at 4.80 and 4.04 ppm are singular and distinct multiplets. Addition of BINPHAT to a racemic sample of **2** results in a twofold spectral change: (1) a

Table 6.1: Potential chiral OSDAs including **2**, that was used to prepare enantioenriched STW, and their associated stabilization energies of both enantiomers in the STW framework (stabilization energies in kJ-(mol Si)$^{-1}$)

Proposed OSDA	$E_{enantiomer\ 1}$ (i.e. P6$_1$22)	$E_{enantiomer\ 2}$ (i.e. P6$_5$22)
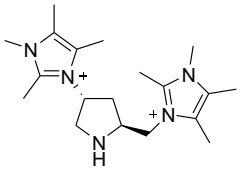	-16.32	-14.60
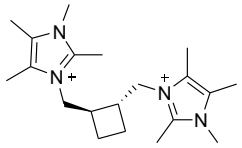	-14.65	-1.37
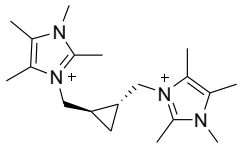	-15.27	-1.58
Selected Molecule: OSDA **2**		

distinct shift upfield of only the aforementioned peaks from their initial position, and (2) an observed peak split. Integration of the split peaks indicates that they maintain a 1:1 ratio, expected for a racemic compound. However, the two enantiomers of **2** show only a single peak. This method confirms the enantiopurity of **2**, and demonstrates that no racemization occurs throughout the organic synthesis scheme.

Synthesis and Characterization of Enantioenriched STW

Syntheses of STW were conducted with enantiopure samples of the *R* and *S* enantiomers of **2**, as well as the racemic mixture of the two. These syntheses were performed at temperatures and H_2O/SiO_2 ratios that are typical for silica-enriched, fluoride-mediated syntheses. As STW is composed of approximately 80% double 4-tetrahedral atom rings that are known to be stabilized by inclusion of germanium, addition of varying quantities

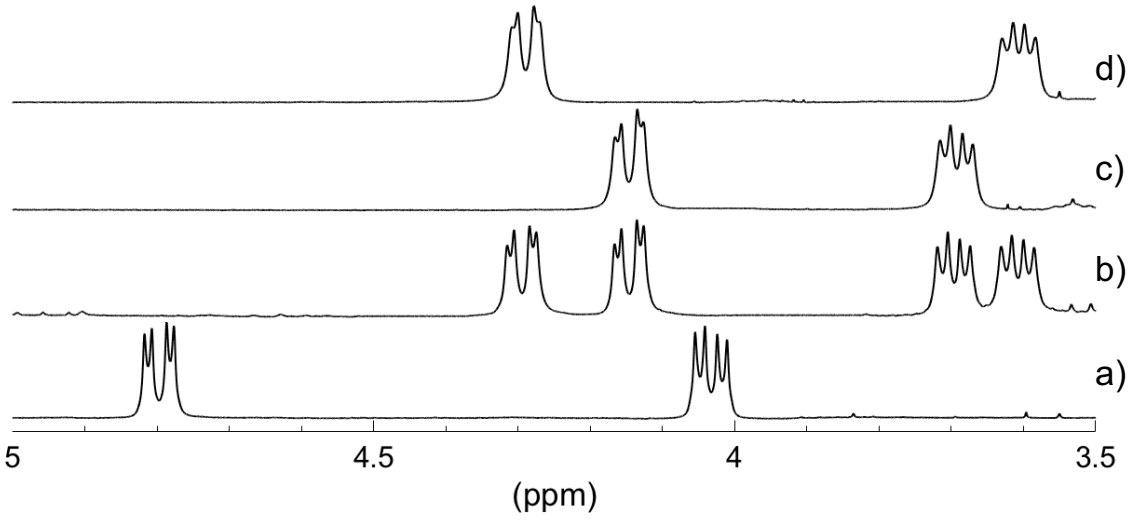

Figure 6.4: ^{1}H NMR chiral shift experiments to analyze the enantiopurity of **2**: a) neat racemic **2**, b) racemic **2** with BINPHAT, c) *R*-**2** with BINPHAT, and d) *S*-**2** with BINPHAT. An imidazole methyl resonance in a) has been suppressed at 3.74 ppm for clarity.

of germanium to the synthesis gels was explored.[45,46] Following the work of Schmidt *et al*., reagent molar ratios that lead to the synthesis of STW in the shortest times were: 1 SiO_2 : x GeO_2 : 5 H_2O: 0.5 HF : 0.5 **2** at 160 °C (where x is a varying from 0.05 to 0.5) using 10% (w/w) seeds produced from an achiral diquaternary OSDA with crystal sizes on the order of 1 μm.[25] Aluminum-containing samples were also synthesized (in the presence of Ge) using aluminum isopropoxide. In these syntheses, initial gel Si/Al ratios were maintained above 50, otherwise RTH impurities were observed in the resultant products.[38,39] Aging the synthesis gels over the course of 24 hours was found to reduce crystallization times. A complete summary of the synthesis results is provided (Tables D.1-D.3) along with representative powder X-ray diffraction (PXRD) patterns (Figure D.1). Additionally, ^{19}F, ^{29}Si and ^{27}Al solid-state NMR (SS NMR) spectra, a representative thermogravimetric analysis (TGA) and a selection of scanning electron micrographs (SEMs) are listed as supporting characterizations (Figures D.2-D.6). In general, the concentrations of germanium

and aluminum were found to increase in the product materials relative to the synthesis gel. Representative results from energy-dispersive X-ray spectroscopy (EDS) are given in Table D.4 for products from germanosilicate and aluminogermanosilicate synthesis gels. In addition to STW, numerous other phases were produced without significant variation in synthesis conditions, including LTA, RTH, IWV, CSV, as well as several phases that could not be identified or consisted of layered organosilicate materials. Synthesis of these microporous materials is not unexpected, as they have all been shown to be derived from similarly shaped imidazole-based OSDAs under crystallization conditions similar to those reported here.[37–44,47]

As-made STW crystals obtained utilizing **2** were analyzed by ^{13}C CP-MAS solid-state NMR to evaluate whether the OSDA remains intact and directs the formation of STW. Figure 6.5 compares the neat OSDA liquid ^{13}C NMR spectrum (Figure 6.5a) with those obtained from analyzing the occluded organic (from solid-state ^{13}C NMR, Figure 6.5b) and the organic recovered by dissolution of the framework structure (liquid ^{13}C NMR, Figure 6.5c). Agreement between all spectra indicates that **2** is occluded intact within the STW framework, and is the structure directing agent. As such, STW is not formed from an organic decomposition product or as a consequence of spontaneous, directed crystallization from the seed crystals. Efforts to perform chiral shift experiments on recovered OSDA **2** collected from dissolution of the STW framework by hydrofluoric acid were not successful due to solubility issues (**2**, chiral shift reagent, and solvent combinations).

Although it has been speculated that chiral OSDAs (when directed towards a chiral structure) should necessarily lead to an enrichment in the chirality of framework, this concept has never been conclusively proven. In order to do so, the chirality of the organic

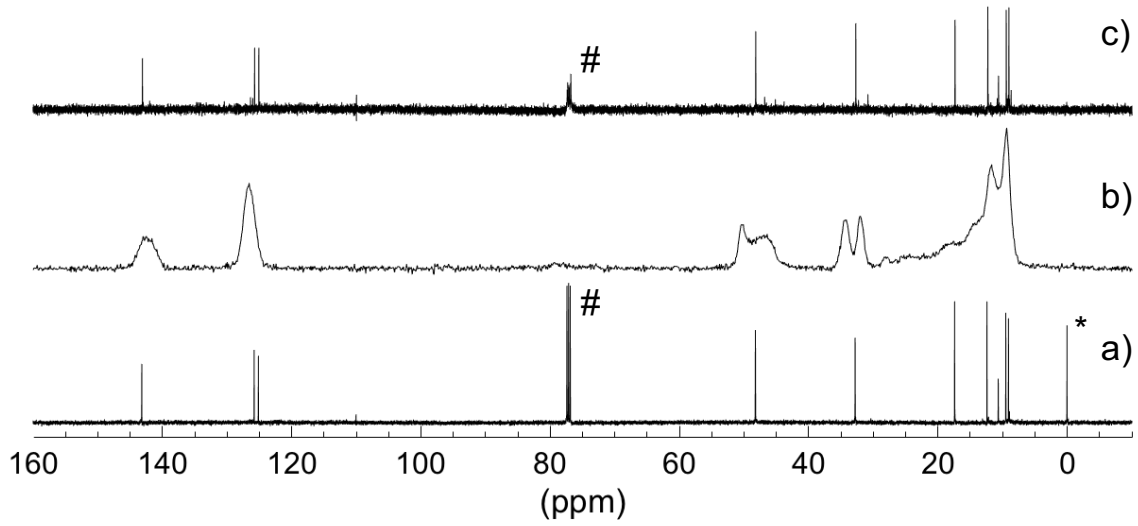

Figure 6.5: Comparison of the ^{13}C NMR collected for a) the neat organic, b) the occluded organic within an enantioenriched STW sample, and c) the OSDA recovered dissolving the framework with hydrofluoric acid and extracting the organic. Peaks marked with a # or * denote the $CDCl_3$ solvent and TMS standard, respectively.

occluded within the STW structure must be known, as must the chirality of the framework structure for a bulk, polycrystalline sample. Circular dichroism (CD) provides an effective method of accomplishing the former for as-made STW samples. The results for *R*-, *S*-, and racemic STW samples are given in Figure 6.6. As demonstrated, the molecules occluded within *R*- and *S*-STW absorb light at 242 nm with equal and opposite polarities. No measured rotation of light is observed for the racemic sample as, statistically, any polarization effects are negated for a sample containing equivalent quantities of chiral crystals. These data collectively demonstrate that **2** remains chiral and enantiopure within the STW framework. While it may be possible to analyze the structural chirality of a calcined STW structure, no adsorption in the 200-300 nm range was detected from our germanosilicate samples. Incorporation of UV-active heteroatoms beyond those that have been used in this work may provide a pathway for future investigation *via* CD studies.

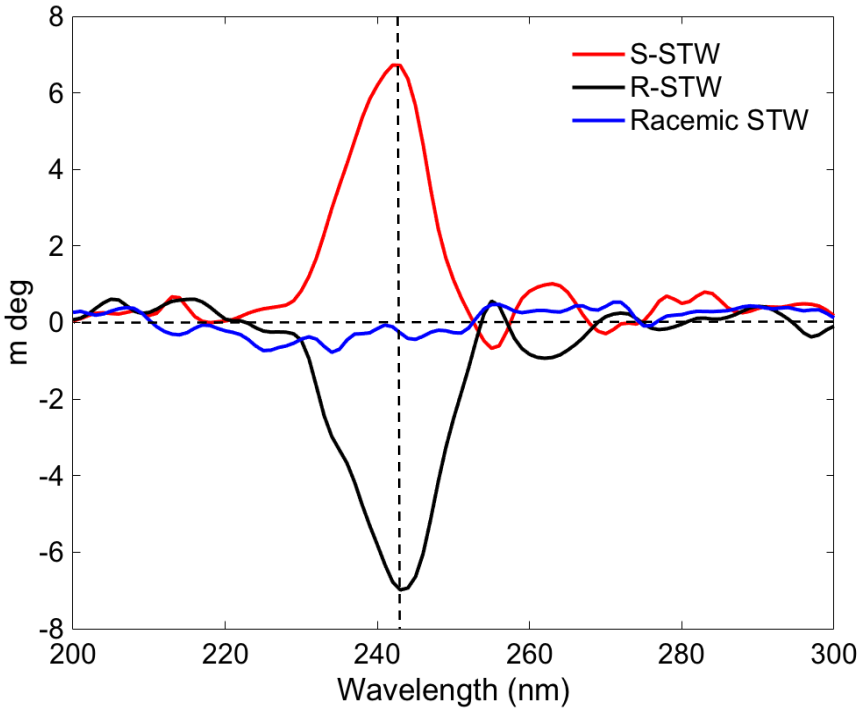

Figure 6.6: Circular dichroism spectra for as-made samples of STW using *R*-, *S*-, and racemic OSDA **2**.

In previous reports involving the enrichment of polymorph A in *BEA (which does not guarantee enantioenrichment), characterization of any true structural enrichment of polymorph A has been limited to transmission electron microscopy (TEM) analysis (PXRD analyses are fraught with problems) of the polymorph domains, and demonstration of enantioenrichment by measuring some function, *e.g.*, catalysis or adsorption.[15,16] A distinct issue with this methodology, however, is that the synthesis of these materials lacks proper controls with regards to the enantiomorphs obtained in the product materials, and therefore it is not possible to perform appropriate analytical and experimental controls to confirm chirality. The methods we have developed and used here are not subject to these problems. We are able to control the synthesis of a chiral OSDA (and obtain the *R*-, *S*-, and racemic forms thereof) to yield bulk, polycrystalline STW samples composed of individual crystals

of a single chirality. As such, characterization and functional results that are capable of probing the bulk chirality of the two enantioenriched samples of opposing direction must demonstrate enantiomeric excess (ee) that is approximately equal and opposite, with the racemic preparation revealing no ee. The CD experiments for the *R*-, *S*-, and racemic STW samples provide the first illustration of how these types of controls can be exploited to derive meaningful conclusions.

Characterization of the structural chirality of STW is complicated. An examination of the literature yields few methods for effectively determining this property for siliceous microporous materials beyond the demonstration of enantiomeric excesses derived from reactions or adsorption experiments. Analytical difficulty partially stems from the small crystal sizes (as is the case for STW synthesized with OSDAs used here) that prohibit the use of single crystal XRD. Rojas *et al*. point towards the possibility of examining the optical activity to quantity enantiomeric excess within a bulk, polycrystalline sample.[45] Scanning and high-resolution transmission electron microscopy (SEM and HRTEM, respectively) have proven to be highly advantageous methods for analyzing crystallite morphologies. HRTEM has been used previously to analyze the polymorph domains in *BEA.[16,20] However, specific chiral space groups (*i.e.*, structural enantiomers) within the detected polymorph A domains were not able to be determined. Fundamentally, the difficulty in unequivocally distinguishing between the space groups of a chiral material using traditional TEM techniques arises from properties inherent to both structural chirality and experimental limitations. Specifically, on a given two-dimensional plane (as is observed in a typical TEM experiment), the structures of the two enantiomers are superimposable and indistinguishable. A method was therefore developed to perform three-dimensional HRTEM experiments by Ma *et al*. in

order to effectively characterize chiral space groups.[21] The projection of STW-framework shifts after rotating along the screw axis as schematically illustrated in Figure 6.7a. Of note is that the rotation direction can be either clockwise (to the right) or count-clockwise (to the left) viewed along *c* to reach at least two zone axes. A zeolite crystal (that has been deposited with gold nanoparticles (diameter 5 nm) that serve as reference points with the microporous structure) is first aligned to $[2\overline{1}\overline{1}0]$ zone axis and a through-focus series of HRTEM images are taken from a thin area. The crystal is then tilted continuously to the right or to the left by 30° about the screw axis as schematically illustrated in Figure 6.7a. Based on simulated results, the crystal is right-handed if the shift direction is downwards when the crystal is tilted to the right (Figure 6.7b and c). Upon rotation, the $[1\overline{1}00]$ or $[10\overline{1}0]$ zone axes are observed if the tilting direction is to the right or left, respectively. A series of through-focus images are then taken again along either zone axis. Two images along $[2\overline{1}\overline{1}0]$ and $[1\overline{1}00]$ are obtained by structure projection reconstructions using the through-focus series of HRTEM images and are aligned based on the positions of gold nanoparticles (Figure 6.7d-g and Figures D.7-D.9 in Appendix D). By comparing the aligned images from the two zone axes, there is an observable shift between the two projections from which the space group of the crystal can be assigned.

The results collected from using this method to analyze STW crystals selected from bulk, polycrystalline samples synthesized using the *R*-, *S*- and racemic versions of **2** are given in Table 6.2. Out of the six crystals analyzed for both the *R*- and *S*-OSDA derived samples, five were determined to possess the $P6_122$ and $P6_522$ space groups, respectively, demonstrating (within this data set) notable enantioenrichment. Moreover, these experimental results are consistent with computational predictions whereby *R*-OSDA **2** is expected to yield crystals

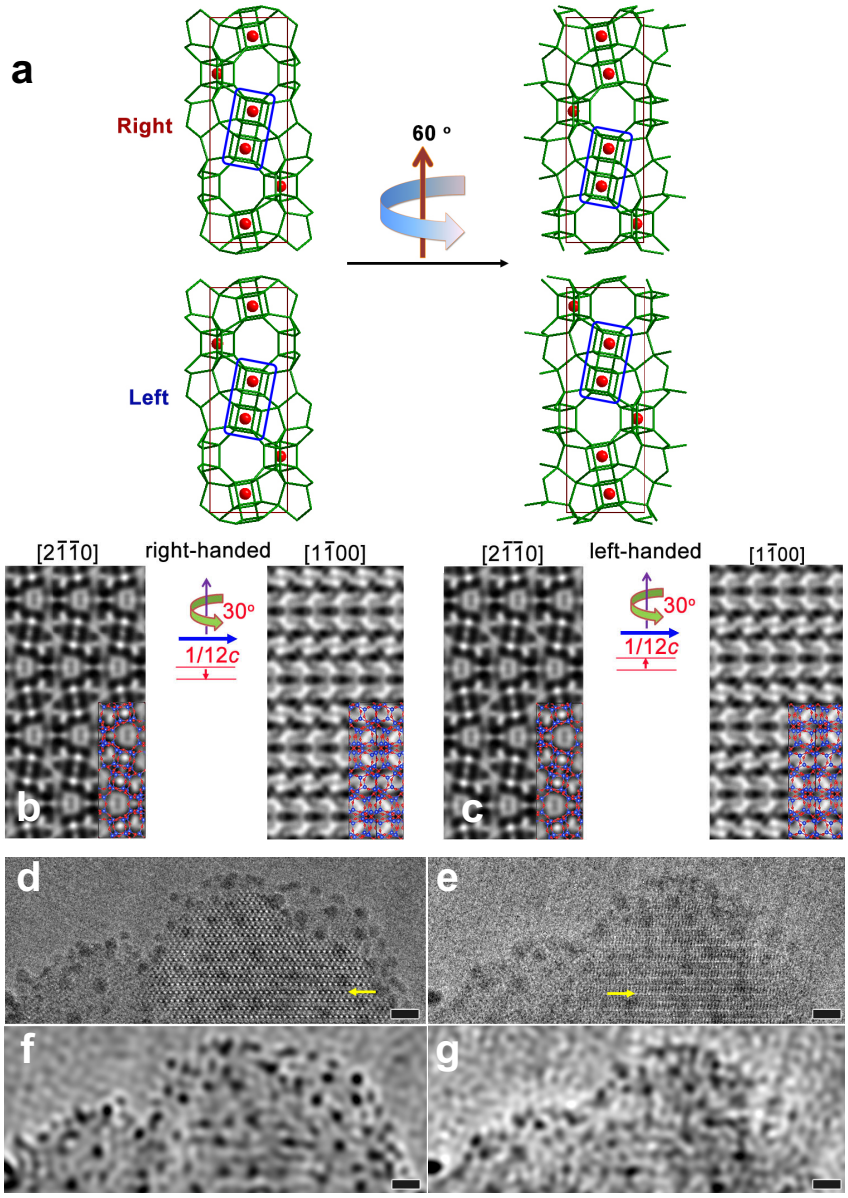

Figure 6.7: a) Schematic representation of a six-fold rotation of STW frameworks with different handedness. b-c) Simulated HRTEM images of the zeolite with right- and left-handedness, respectively. The atomic structure models, where blue and red balls represent Si and O atoms, were overlaid on top of the simulated images. The shift between two images for right-handed and left-handed STW frameworks has the same length but reverse directions. d-e) Comparison of two HRTEM images with gold nanoparticles as markers. A crystal was tilted from [$2\bar{1}\bar{1}0$] (d) to [$10\bar{1}0$] (e) and a shift-down was observed, which indicates a space group of $P6_522$. f-g) The processed images of (f) and (g) after Fourier filtering that only includes spatial frequencies within a particular range to enhance the contrasts of gold nanoparticles. Scale bars are 5 nm.

with $P6_122$ space group and, similarly, *S*-OSDA **2** is anticipated to result in crystals with the $P6_522$ space group (Table 6.1). Analysis of the racemic sample resulted in an equal number of crystals from each space group, as expected.

Table 6.2: Summary of the results obtained from rotational HRTEM analysis for STW crystals synthesized from the *R*-, *S*- and racemic OSDA **2**.

OSDA Used	Number of Crystals Analyzed	$P6_122$	$P6_522$
R-**2**	6	5	1
S-**2**	6	1	5
Racemic **2**	6	3	3

Ideally, for a given sample synthesized using a chiral OSDA, HRTEM analysis would subsequently demonstrate only crystals from the expected space group. However, as shown in Table 6.2, a crystal from both chiral OSDA derived samples was determined to be from the unexpected space group (*e.g.*, $P6_522$ from the *R*-OSDA). Possible reasons for incomplete purity include (1) the crystal of the opposite space group was a seed crystal, (2) there was OSDA degradation that occurred that yielded a racemic portion of the polycrystalline sample, and (3) the inherent nature of the crystallization process does not synthesize an enantiopure, but only an enantioenriched, polycrystalline sample. Further studies are underway to test for these possibilities in hopes of eliminating any of these complications. While currently the number of crystals that have been analyzed is not sufficient to draw a statistically conclusive picture of the bulk chirality of the samples, these HRTEM data (coupled with the distinct differences detected between *R*- and *S*-OSDA synthesized materials) are useful to demonstrate, for the first time, enantioenrichment of a bulk, polycrystalline sample of a molecular sieve. Work is ongoing to analyze a larger number of crystals and subse-

quently improve the statistics for quantifying enantioenrichment of STW samples prepared without seed crystals.

CD and HRTEM characterizations demonstrate that a given enantiomer of OSDA **2** maintains its respective chirality in the occluded state, and is capable of producing an enantioenriched, molecular sieve framework. While there may exist crystallization processes wherein achiral molecules lead to enantioenrichment of product solids, such as by spontaneous chiral symmetry breaking by self-catalyzed crystallization,[48] such systems would not allow for the directed synthesis of specific enantiomers of crystals, as we are able to demonstrate in this work. Thus, it follows that the initial hypothesis by Lobo and Davis that any bulk, polycrystalline sample having enantioenrichment (not obtained solely from chiral seeds) must be derived from a chiral OSDA with a particular set of properties, appears valid.[15] Additionally, this synthesis methodology ensures that all forms (*R*-, *S*-, and racemic) are attainable, thus allowing for appropriate controls to be performed.

Adsorption and Catalysis with Enantioenriched STW

The chirality in STW is defined over the specific distance within the helical STW pore structure (Figure 6.1).[49] As a consequence, adsorption and catalysis that show ee's will involve molecules that are of sufficient size to effectively experience the chirality of the structure, yet still be able to pass through the limited size of the pores. As such, we expect that any measured ee's will be greatly dependent on the selection of molecules used to test for a function. Moreover, the external surfaces of the crystallites may behave nonspecifically, resulting in diminishing ee's.

To examine whether the enantioenriched STW samples are capable of performing enan-

tioselective functions, catalysis and adsorption experiments were conducted. Epoxide ring-opening reactions on 1,2-epoxyalkanes were selected for catalysis, as they have been shown to take place within molecular sieves at relatively low temperatures.[50–52] Such low-temperature probe reactions are particularly desirable because symmetry-breaking dispersive interactions with the catalyst surface are expected to be relatively larger contributors to the transition state free energies compared to high-temperature scenarios. The results from these reactions are reported in Table 6.3. For epoxides shorter than C_8, enantiomeric excesses that are not significantly different than experimental error are observed. However, as the chain length is further extended (to approximate the size of OSDA **2**) the magnitude of the ee's become significantly different from experimental error. Of importance is that results that approximately the same magnitude of the ee's are obtained, but in opposite directions, from the *R*-STW and the *S*-STW, as should be. *Trans*-stilbene oxide was also used as a substrate and minimal ring opening was observed. As this substrate is too large to enter the pores of STW, this control experiment demonstrates that the rate of reaction outside the pore structure (*i.e.*, on the surface of the crystals) is negligible, and that any measured ee's do not occur as a consequence of surface or solvent effects.

Vaporsorption experiments were performed utilizing the pure *R*-, *S*- and racemic solutions of 2-butanol. Previous computational studies suggested that germanosilicate STW is capable of selectively adsorbing *R*- and *S*-glycidol into the helices of the respective enantiomers of the framework, with increasing discrimination between enantiomers from a racemic mixture with decreasing system temperatures.[53] Experiments were therefore performed at 278 K (which allows for a vapor pressure great enough to collect sufficient adsorption data). Figure 6.8 illustrates the adsorption isotherms obtained for *R*-, *S*- and racemic 2-butanol

Table 6.3: Summary of enantiomeric excess from the ring opening of 1,2-epoxyalkanes with methanol using aluminum-containing racemic, *R*-, and *S*-STW as catalysts. Product **a** is the less substituted 1-methoxyalkan-2-ol product, while product **b** is the more substituted 2-methoxyalkan-1-ol product. The reaction solutions were analyzed after 48 hours.

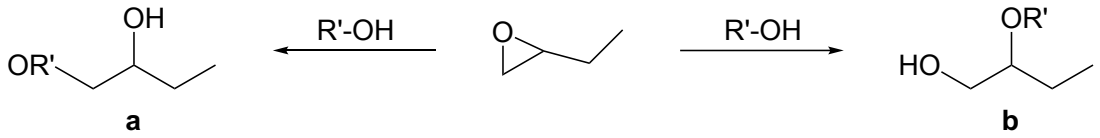

a **b**

Substrate	**Enantiomeric Excess of Products Using Enantioenriched STW**					
	R-STW		Racemic STW		S-STW	
	a, %	**b**, %	**a**, %	**b**, %	**a**, %	**b**, %
1,2-epoxybutane	-0.14	2.31	0.05	0.06	0.02	-2.26
1,2-epoxyhexane	1.29	2.83	0.20	-0.92	-1.96	-3.46
1,2-epoxyoctane	4.13	9.85	1.14	-0.86	-4.41	-10.65

in germanosilicate *R*- and *S*-STW. For *R*-STW, *R*-2-butanol is selectively adsorbed relative to *S*-2-butanol. The racemic 2-butanol isotherm lies at the approximate average of the isotherms from the enantiomerically enriched sample 2-butanol isotherms. An equivalent, but inverse, result is observed from *S*-STW.

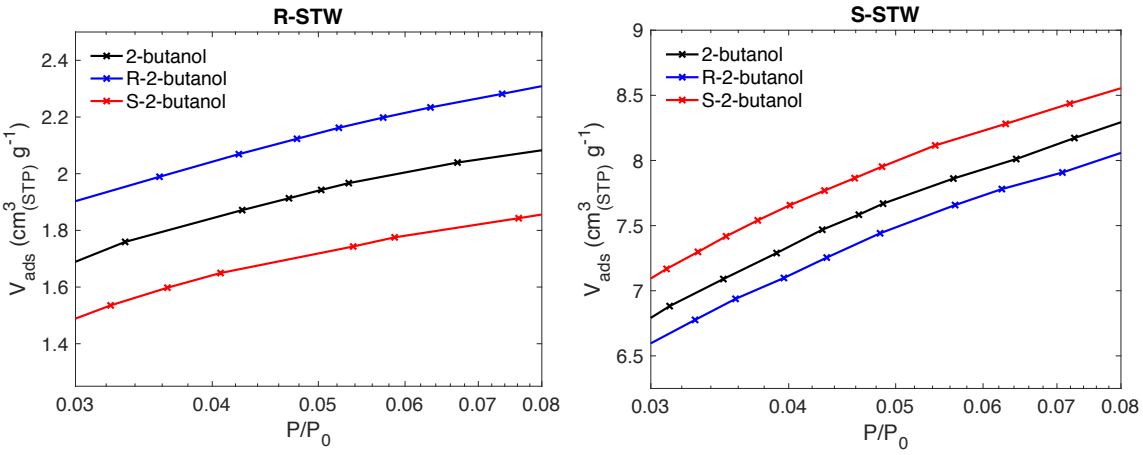

Figure 6.8: 2-butanol adsorption isotherms at 278 K for germanosilicate *R*- and *S*-STW. Differences in uptake are a result of variations in sample crystallinity.

6.4 Conclusion

We have computationally designed a large, rigid, and stable chiral OSDAs to synthesize the two polycrystalline, enantiomorphs of STW (enantiomerically enriched) following the synthesis heuristics specified by Lobo and Davis for chiral molecular sieves.[15] Under typical silica-enriched, fluoride-mediated inorganic reaction conditions the chiral OSDA directs towards the formation of the STW framework. Solid-state NMR and circular dichroism characterizations demonstrate that the occluded OSDA remains intact within the STW pores and retains enantiopurity. Newly developed three-dimensional HRTEM techniques are applied to determine the chirality of individual crystals. These data show that the samples synthesized using a chiral OSDA are enantioenriched with the space group of STW that is *a priori* computationally predicted based on the OSDA's chirality, while the racemic OSDA leads to a racemic mixture of crystals. We believe that this is the first reported and confirmed instance of a rational and controlled synthesis of bulk, polycrystalline molecular sieve with enantioenrichment. Additionally, we find that the enantioenriched materials are capable of yielding enantioenrichment for reaction and adsorption experiments.

The initial discovery of transition-metal-catalyzed asymmetric reactions by Noyori and co-workers gave preliminary ee's up to 10% for the copper-catalyzed cyclopropanations of olefins.[54] Improvements over time of this catalytic system have to led to industrial applications of asymmetric hydrogenation catalysts.[55] We hope that our initial demonstration of molecular sieve asymmetric catalysis may follow a similar pathway.

6.5 Acknowledgments

The authors would like to thank Chevron Energy and Technology Company for proving funding for this work, Dr. Sonjong Hwang (Caltech) for his assistance with solid state NMR data collection, Dr. Jay Winkler (Caltech) for assistance with the solid state circular dichroism experiments, and Dr. Stacey I. Zones (Chevron) and Peter Oleynikov (ShanghaiTech) for many useful discussions.

6.6 References

(1) Moliner, M.; Rey, F.; Corma, A. Towards the rational design of efficient organic structure-directing agents for zeolite synthesis., 2013, DOI: 10.1002/anie.201304713.

(2) Zones, S. Translating new materials discoveries in zeolite research to commercial manufacture. *Microporous and Mesoporous Materials* **2011**, *144*, 1–8, DOI: 10.1016/j.micromeso.2011.03.039.

(3) Li, J.; Corma, A.; Yu, J. Synthesis of new zeolite structures. *Chem. Soc. Rev.* **2015**, *44*, 7112–7127, DOI: 10.1039/C5CS00023H.

(4) Wang, Z.; Yu, J.; Xu, R. Needs and trends in rational synthesis of zeolitic materials. *Chem. Soc. Rev.* **2012**, *41*, 1729–1741, DOI: 10.1039/C1CS15150A.

(5) Čejka, J.; Corma, A.; Zones, S. I., *Zeolites and Catalysis: Synthesis, Reactions and Applications*; Wiley-VCH Verlag GmbH: 2010.

(6) Bravo-Suárez, J. J.; Chaudhari, R. V.; Subramaniam, B. In *Novel Materials for Catalysis and Fuels Processing*, Bravo-Suárez, J. J., Kidder, M. K., Schwartz, V., Eds.; ACS Symposium Series, Vol. 1132; American Chemical Society: Washington, 2013, pp 3–68, DOI: 10.1021/bk-2013-1132.

(7) Corma, A.; Iglesias, M.; del Pino, C.; Sanchez, F. New Rhodium Complexes anchored on Modified USY Zeolites. A Remarkable Effect of the Support on the Enantioselectivity of Catalytic Hydrogenation of Prochiral Alkenes. *Journal of the American Chemical Society* **1991**, 1253–1255, DOI: 10.1039/c39910001253.

(8) Carmona, A.; Corma, A.; Iglesias, M.; Sánchez, F. Synthesis and characterisation of chiral Cu(I) complexes of substituted pyrrolidine ligands. Efficient catalysts for cyclopropanation reactions. *Inorganica Chimica Acta* **1996**, *244*, 239–245, DOI: 10.1016/0020-1693(95)04773-5.

(9) Xu, Z. X.; Ma, Y. L.; Zhang, J. Enantiopure anion templated synthesis of a zeolitic metal-organic framework. *Chem Commun (Camb)* **2015**, 1923–1925, DOI: 10.1039/c5cc09308b.

(10) Wang, C.; Zheng, M.; Lin, W. Asymmetric Catalysis with Chiral Porous Metal À Organic Frameworks : Critical Issues. **2011**, 1701–1709.

(11) Coronas, J. Present and future synthesis challenges for zeolites. *Chemical Engineering Journal* **2010**, *156*, 236–242, DOI: 10.1016/j.cej.2009.11.006.

(12) Yu, J.; Xu, R. Chiral zeolitic materials: structural insights and synthetic challenges. *Journal of Materials Chemistry* **2008**, *18*, 4021, DOI: 10.1039/b804136a.

(13) Maier, N. M.; Franco, P.; Lindner, W. Separation of enantiomers: needs, challenges, perspectives. *Journal of Chromatography A* **2001**, *906*, 3–33, DOI: 10.1016/S0021-9673(00)00532-X.

(14) McCuster, L. B.; Baerlocher, C. Database of Zeolite Structures., http://www.iza-structure.org/databases.

(15) Davis, M. E.; Lobo, R. F. Zeolite and molecular sieve synthesis. *Chemistry of Materials* **1992**, *4*, 756–768, DOI: 10.1021/cm00022a005.

(16) Tong, M.; Zhang, D.; Fan, W.; Xu, J.; Zhu, L.; Guo, W.; Yan, W.; Yu, J.; Qiu, S.; Wang, J.; Deng, F.; Xu, R. Synthesis of chiral polymorph A-enriched zeolite Beta

with an extremely concentrated fluoride route. *Scientific reports* **2015**, *5*, 11521, DOI: 10.1038/srep11521.

(17) Takagi, Y.; Komatsu, T.; Kitabata, Y. Crystallization of zeolite beta in the presence of chiral amine or rhodium complex. *Microporous and Mesoporous Materials* **2008**, *109*, 567–576, DOI: 10.1016/j.micromeso.2007.06.005.

(18) Taborda, F.; Willhammar, T.; Wang, Z.; Montes, C.; Zou, X. Synthesis and characterization of pure silica zeolite beta obtained by an aging-drying method. *Microporous and Mesoporous Materials* **2011**, *143*, 196–205, DOI: 10.1016/j.micromeso.2011.02.030.

(19) Camblor, M. A.; Corma, A.; Valencia, S. Spontaneous nucleation and growth of pure silica zeolite-B free of connectivity defects. *Chemical Communications* **1996**, 2365, DOI: 10.1039/cc9960002365.

(20) Zhang, R.-C.; Wang, J.-J.; Yuan, B.-Q.; Zhang, J.-C.; Zhou, L.; Wang, H.-B.; Zhang, D.-J.; An, Y.-L. Syntheses and Characterization of Chiral Zeolitic Silver Halides Based on 3-Rings. *Inorganic Chemistry* **2016**, *4*, 11593–11599, DOI: 10.1021/acs.inorgchem.6b02121.

(21) Ma, Y.; Oleynikov, P.; Terasaki, O. Electron crystallography for determining the handedness of a chiral zeolite nanocrystal. *Nature Materials* **2017**, DOI: 10.1038/nmat4890.

(22) Tang, L.; Shi, L.; Bonneau, C.; Sun, J.; Yue, H.; Ojuva, A.; Lee, B.-L.; Kritikos, M.; Bell, R. G.; Bacsik, Z.; Mink, J.; Zou, X. A zeolite family with chiral and achiral structures built from the same building layer. *Nature Materials* **2008**, *7*, 381–385, DOI: 10.1038/nmat2169.

(23) Rojas, A.; Camblor, M. A. A pure silica chiral polymorph with helical pores. *Angewandte Chemie - International Edition* **2012**, *51*, 3854–3856.

(24) Pophale, R.; Daeyaert, F.; Deem, M. W. Computational prediction of chemically synthesizable organic structure directing agents for zeolites. *Journal of Materials Chemistry A* **2013**, *1*, 6750–6760, DOI: 10.1039/c3ta10626h.

(25) Schmidt, J. E.; Deem, M. W.; Davis, M. E. Synthesis of a specified, silica molecular sieve by using computationally predicted organic structure-directing agents. *Angewandte Chemie - International Edition* **2014**, *53*, 8372–8374.

(26) Overberger, C. G.; Okamoto, Y.; Bulacovschi, V. Synthesis and Optical Properties of Asymmetric Polyamides Derived from Optically Active Dicarboxylic Acids and Spirodiamine. *Macromolecules* **1975**, *8*, 31–36.

(27) Cheng, K.; Lee, Y. S.; Rothman, R. B.; Dersch, C. M.; Bittman, R. W.; Jacobson, A. E.; Rice, K. C. Probes for Narcotic Receptor Mediated Phenomena. 41. Unusual Inverse μ-Agonists and Potent μ-Opioid Antagonists by Modification of the N-Substituent in Enantiomeric 5-(3-Hydroxyphenyl)morphans. *Journal of Medicinal Chemistry* **2011**, *54*, 957–969.

(28) Gottstein, W. J. US Patent 3,454,626. **1969**.

(29) Inouye, Y.; Sugita, T.; Walborsky, H. M. Cyclopropanes—XVII: The absolute configurations of trans-1,2-cyclopropanedicarboxylic acid and trans-2-phenylcyclopropanecarboxylic acid. *Tetrahedron* **1964**, *20*, 1695–1699.

(30) Taylor, R. J. K.; Campbell, L.; McAllister, G. D., *Organic Syntheses*, en; John Wiley & Sons, Inc.: Hoboken, NJ, USA, 2003, pp 15–26, DOI: 10.1002/0471264229.os085.03.

(31) De la Fuente, V.; Waugh, M.; Eastham, G. R.; Iggo, J. A.; Castillón, S.; Claver, C. Phosphine ligands in the palladium-catalysed methoxycarbonylation of ethene: insights into the catalytic cycle through an HP NMR spectroscopic study. *Chemistry (Weinheim an der Bergstrasse, Germany)* **2010**, *16*, 6919–32, DOI: 10.1002/chem.200903158.

(32) Pasquini, C.; Desvergnes-Breuil, V.; Jodry, J. J.; Dalla Cort, A.; Lacour, J. Chiral anion-mediated asymmetric induction onto chiral diquats. *Tetrahedron Letters* **2002**, *43*, 423–426.

(33) Lacour, J.; Vial, L.; Herse, C. Efficient NMR Enantiodifferentiation of Chiral Quats with BINPHAT Anion. *Organic Letters* **2002**, *4*, 1351–1354.

(34) Lacour, J.; Londez, a.; Goujon-Ginglinger, C.; Buss, V.; Bernardinelli, G. Configurational ordering of cationic chiral dyes using a novel C(2)-symmetric hexacoordinated phosphate anion. *Organic letters* **2000**, *2*, 4185–8.

(35) Herse, C.; Bas, D.; Krebs, F. C.; Bürgi, T.; Weber, J.; Wesolowski, T.; Laursen, B. W.; Lacour, J. A highly configurationally stable [4]heterohelicenium cation. *Angewandte Chemie - International Edition* **2003**, *42*, 3162–3166, DOI: 10.1002/anie.200351443.

(36) Wan, W.; Hovmöller, S.; Zou, X. Structure projection reconstruction from through-focus series of high-resolution transmission electron microscopy images. *Ultramicroscopy* **2012**, *115*, 50–60, DOI: http://dx.doi.org/10.1016/j.ultramic.2012.01.013.

(37) Schmidt, J. E.; Zones, S. I.; Xie, D.; Davis, M. E. The synthesis of aluminophosphate and germanosilicate LTA using a triquaternary structure directing agent. *Microporous and Mesoporous Materials* **2014**, *200*, 132–139, DOI: 10.1016/j.micromeso.2014.08.051.

(38) Schmidt, J. E.; Deimund, M. A.; Davis, M. E. Facile Preparation of Aluminosilicate RTH across a Wide Composition Range Using a New Organic Structure-Directing Agent. *Chemistry of Materials* **2014**, *26*, 7099–7105, DOI: 10.1021/cm503625u.

(39) Schmidt, J. E.; Deimund, M. A.; Xie, D.; Davis, M. E. Synthesis of RTH-type zeolites using a diverse library of imidazolium cations. *Chemistry of Materials* **2015**, *27*, 3756–3762, DOI: 10.1021/acs.chemmater.5b01003.

(40) Schmidt, J. E.; Xie, D.; Davis, M. E. Synthesis of the RTH-type layer: the first small-pore, two dimensional layered zeolite precursor. *Chem. Sci.* **2015**, *6*, 5955–5963, DOI: 10.1039/C5SC02325D.

(41) Schmidt, J. E.; Xie, D.; Rea, T.; Davis, M. E. CIT-7, a crystalline, molecular sieve with pores bounded by 8 and 10-membered rings. *Chem. Sci.* **2015**, *6*, 1728–1734, DOI: 10.1039/C4SC03935A.

(42) Boal, B.; Schmidt, J.; Deimund, M.; Deem, M.; Henling, L.; Brand, S.; Zones, S.; Davis, M. Facile Synthesis and Catalysis of Pure-Silica and Heteroatom LTA. *Chemistry of Materials* **2015**, *27*, 7774–7779.

(43) Schmidt, J. E.; Xie, D.; Davis, M. E. High-silica, heulandite-type zeolites prepared by direct synthesis and topotactic condensation. *J. Mater. Chem. A* **2015**, *3*, 12890–12897, DOI: 10.1039/C5TA02354H.

(44) Schmidt, J. E.; Chen, C. Y.; Brand, S. K.; Zones, S. I.; Davis, M. E. Facile Synthesis, Characterization, and Catalytic Behavior of a Large-Pore Zeolite with the IWV Framework. *Chemistry - A European Journal* **2016**, *22*, 4022–4029, DOI: 10.1002/chem.201504717.

(45) Rojas, A.; Arteaga, O.; Kahr, B.; Camblor, M. A. Synthesis, Structure, and Optical Activity of HPM-1, A Pure Silica Chiral Zeolite. *Journal of the American Chemical Society* **2013**, *135*, 11975–11984.

(46) Sastre, G.; Pulido, A.; Corma, A. An attempt to predict and rationalize relative stabilities and preferential germanium location in Si/Ge zeolites. *Microporous and Mesoporous Materials* **2005**, *82*, 159–163, DOI: 10.1016/j.micromeso.2005.01.021.

(47) Boal, B. W.; Deem, M. W.; Xie, D.; Kang, J. H.; Davis, M. E.; Zones, S. I. Synthesis of Germanosilicate Molecular Sieves from Mono- and Di-Quaternary Ammonium OSDAs Constructed from Benzyl Imidazolium Derivatives: Stabilization of Large Micropore Volumes Including New Molecular Sieve CIT-13. *Chemistry of Materials* **2016**, *28*, 2158–2164, DOI: 10.1021/acs.chemmater.6b00031.

(48) Kondepudi, D. K.; Kaufman, R. J.; Singh, N. Chiral symmetry breaking in sodium chlorate crystallizaton. *Science (New York, N.Y.)* **1990**, *250*, 975–976, DOI: 10.1126/science.250.4983.975.

(49) Dryzun, C.; Mastai, Y.; Shvalb, A.; Avnir, D. Chiral silicate zeolites. *Journal of Materials Chemistry* **2009**, *19*, 2062, DOI: 10.1039/b817497k.

(50) Onaka, M.; Kawai, M.; Izumi, Y. Zeolite-Catalyzed Ring-Opening of Epoxides with Amines., en *Chemistry Letters* **1985**, *14*, 779–782, DOI: 10.1246/cl.1985.779.

(51) Ogawa, H.; Miyamoto, Y.; Fujigaki, T.; Chihara, T. Ring-opening of 1,2-epoxyalkane with alcohols over H-ZSM-5 in liquid phase. *Catalysis Letters* **1996**, *40*, 253–255, DOI: 10.1007/BF00815291.

(52) Tang, B.; Dai, W.; Wu, G.; Guan, N.; Li, L.; Hunger, M. Improved Postsynthesis Strategy to Sn-Beta Zeolites as Lewis Acid Catalysts for the Ring-Opening Hydration of Epoxides. *ACS Catalysis* **2014**, *4*, 2801–2810, DOI: 10.1021/cs500891s.

(53) Zhang, L.; Jiang, J. Enantioselective adsorption and diffusion of S-/R-glycidol in homochiral zeolites: A molecular simulation study. *Journal of Membrane Science* **2011**, *367*, 63–70.

(54) Nozaki, H.; Moriuti, S.; Takaya, H.; Noyori, R. Asymmetric induction in carbenoid reaction by means of a dissymmetric copper chelate. *Tetrahedron Letters* **1966**, *7*, 5239–5244, DOI: 10.1016/S0040-4039(01)89263-7.

(55) Noyori, R. Asymmetric catalysis: Science and opportunities (nobel lecture). *Angew. Chem. Int. Ed.* **2002**, *41*, 2008–2022, DOI: 10.1002/1521-3773(20020617)41:12<2008::AID-ANIE2008>3.0.CO;2-4.

Chapter 7

CONCLUSIONS AND FUTURE DIRECTIONS

7.1 Conclusions

The work presented in Chapter 6 describes the controlled synthesis of the two enantiomers of the STW framework using a computationally designed, large, rigid, and stable chiral organic structure directing agent as was initially specified by Lobo and Davis in 1992.[1] Characterizations of the OSDA and inorganic framework structure (liquid and solid-state NMR, powder XRD, CD, HRTEM) demonstrate that the chiral OSDA produces enantioenriched STW samples. Crucially, samples that are synthesized with the chiral OSDA yield crystals with the *a priori* computationally predicted space group (as confirmed by novel 3-dimensional HRTEM techniques). A racemic mixture of the OSDA similarly results in a racemic crystalline samples. At the time of writing, this is the first reported and confirmed instance of a rational and controlled synthesis of bulk, polycrystalline molecular sieve with enantioenrichment. Moreover, preliminary adsorption and reactivity experiments indicate that these materials are capable of performing enantioselective processes.

Most importantly, the system presented in Chapter 6 provides a means of performing rigorous controls to demonstrate true enantioenrichment for the synthesized STW crystals and any subsequent function. Specifically, the TEM, catalysis, and adsorption experiments performed with *R*- and *S*-STW samples demonstrates relative enantioenrichment of equivalent (and opposite) magnitudes. Moreover, as expected, similar experiments performed with racemic STW samples resulted in no measurable enantioenrichment. Interestingly,

the largest ee's obtained from catalysis are *ca*. 10%. A similar ee was reported for the first asymmetric catalysis for an organometallic compound in 1966.[2] Given the current efficacy of organometallic compounds in performing enantioselective catalysis (ee ≥99%), it is possible that further optimization of the heterogeneous STW system may yield similar results.

7.2 Future Directions

The work presented in the second part of this thesis presents a preliminary, proof-of-concept for the bulk and controlled synthesis of an enantioenriched molecular sieve. As such, there exists a multitude of opportunities to improve upon the reported system, namely:

1) the computational design of the OSDA can be improved to reduce synthetic complexity, as well as improve the stability energetics within the STW framework (and readily allowing for the production of pure-silica, seedless syntheses),

2) a higher throughput method of determining the space group of individual crystals should be developed in order to garner greater statistical confidence for enantioenrichment (perhaps by exploiting the optical activity of the crystals, as examined by Rojas *et al*.)[3], and

3) a large scale investigation into the types of chiral reactions (by incorporation of a variety of heteroatoms) and separations possible by STW, as well as determination of how substrate size influences enantioselectivities.

Optimization of these parameters may provide a means of developing a viable heterogeneous chiral catalyst. In particular, successfully developing the latter point is critical in order for enantioenriched STW to garner further academic and industrial interest. As was discussed in the introduction to Part II, the production of enantiopure compounds is

critical in the pharmaceutical industry (among others). At the industrial scale, production of enantiopure compounds typically requires significant capital investment in equipment to perform the requisite reactions and associated enantiomeric separations. Using a heterogeneous, enantioenriched molecular sieve, one can imagine the possibility of combining these steps into a single step process. This would likely result in significant reduction in capital as well as operational costs (*e.g.*, through the use of fewer solvents and chiral derivatization agents). Similar reductions in process complexity may also be imagined in a variety of other chemical industries, such as those focused on pesticides and fragrances.

In addition to the optimization of existing catalytic and separation processes, metal-containing enantioenriched STW may provide means to perform novel and desirable enantioselective catalysis. The upgrading of biomass-derived substrates to value-added products is one area that shows significant potential for this application, as discussed in part I of this thesis. For instance, the production of lactic acid (as a monomer for the production of poly(lactic acid), a biodegradable and environmentally benign plastic used in a growing number of consumer and medical applications) relies heavily on enzymatic fermentation that: 1) may only be conducted under a narrow range of conditions, 2) produces large quantities of waste, 3) is energy intensive, and 4) cost inefficient.[4–9] The subsequent products may contain varying content of either the D- or L- enantiomer depending on the enzymatic process selected. However, synthesis of solely the D-enantiomer of lactic acid is difficult.[10] The properties of poly(lactic acid (PLA), which is formed through a controlled ring-opening polymerization, are heavily influenced by the content of the D- or L- enantiomers along in the polymer chain (*e.g.*, crystallinity, glass transition temperature, and melting temperature).[5,6] Using renewable sources of carbohydrates and enantioenriched STW, it may be

possible to synthesize either enantiomer of lactic acid (or their derivatives) selectively under a wide range of conditions, providing a means of readily producing biodegradable plastics with tunable properties.[11–13] A variety of other relevant systems are imaginable across a host of industries.

7.3 References

(1) Davis, M. E.; Lobo, R. F. Zeolite and molecular sieve synthesis. *Chemistry of Materials* **1992**, *4*, 756–768, DOI: 10.1021/cm00022a005.

(2) Nozaki, H.; Moriuti, S.; Takaya, H.; Noyori, R. Asymmetric induction in carbenoid reaction by means of a dissymmetric copper chelate. *Tetrahedron Letters* **1966**, *7*, 5239–5244, DOI: http://dx.doi.org/10.1016/S0040-4039(01)89263-7.

(3) Rojas, A.; Arteaga, O.; Kahr, B.; Camblor, M. A. Synthesis, Structure, and Optical Activity of HPM-1, A Pure Silica Chiral Zeolite. *Journal of the American Chemical Society* **2013**, *135*, 11975–11984.

(4) Martin, O.; Avérous, L. Poly(lactic acid): plasticization and properties of biodegradable multiphase systems. *Polymer* **2001**, *42*, 6209–6219, DOI: http://dx.doi.org/10.1016/S0032-3861(01)00086-6.

(5) Jamshidian, M.; Tehrany, E. A.; Imran, M.; Jacquot, M.; Desobry, S. Poly-Lactic Acid: Production, Applications, Nanocomposites, and Release Studies. *Comprehensive Reviews in Food Science and Food Safety* **2010**, *9*, 552–571, DOI: 10.1111/j.1541-4337.2010.00126.x.

(6) Shen, L.; Worrell, E.; Patel, M. Present and future development in plastics from biomass. *Biofuels, Bioproducts and Biorefining* **2010**, *4*, 25–40, DOI: 10.1002/bbb.189.

(7) Tuck, C. O.; Pérez, E.; Horváth, I. T.; Sheldon, R. A.; Poliakoff, M. Valorization of Biomass: Deriving More Value from Waste. *Science* **2012**, *337*, 695–699, DOI: 10.1126/science.1218930.

(8) Vink, E. T.; Rábago, K. R.; Glassner, D. A.; Gruber, P. R. Applications of life cycle assessment to NatureWorks™ polylactide (PLA) production. *Polymer Degradation and Stability* **2003**, *80*, 403–419, DOI: http://dx.doi.org/10.1016/S0141-3910(02)00372-5.

(9) Dusselier, M.; Van Wouwe, P.; Dewaele, A.; Jacobs, P. A.; Sels, B. F. Shape-selective zeolite catalysis for bioplastics production. *Science* **2015**, *349*, 78–80, DOI: 10.1126/science.aaa7169.

(10) Okano, K.; Zhang, Q.; Shinkawa, S.; Yoshida, S.; Tanaka, T.; Fukuda, H.; Kondo, A. Efficient Production of Optically Pure d-Lactic Acid from Raw Corn Starch by Using a Genetically Modified l-Lactate Dehydrogenase Gene-Deficient and Amylase-Secreting Lactobacillus plantarum Strain. *Applied and Environmental Microbiology* **2009**, *75*, 462–467.

(11) Holm, M. S.; Saravanamurugan, S.; Taarning, E. Conversion of sugars to lactic acid derivatives using heterogeneous zeotype catalysts. *Science (New York, N.Y.)* **2010**, *328*, 602–605.

(12) Sharninghausen, L. S.; Campos, J.; Manas, M. G.; Crabtree, R. H. Efficient selective and atom economic catalytic conversion of glycerol to lactic acid. *Nature Communications* **2014**, *5*,

(13) Dusselier, M.; Van Wouwe, P.; Dewaele, A.; Makshina, E.; Sels, B. F. Lactic acid as a platform chemical in the biobased economy: the role of chemocatalysis. *Energy Environ. Sci.* **2013**, *6*, 1415–1442, DOI: 10.1039/C3EE00069A.

Appendix A

SUPPLEMENTARY INFORMATION FOR CHAPTER 2

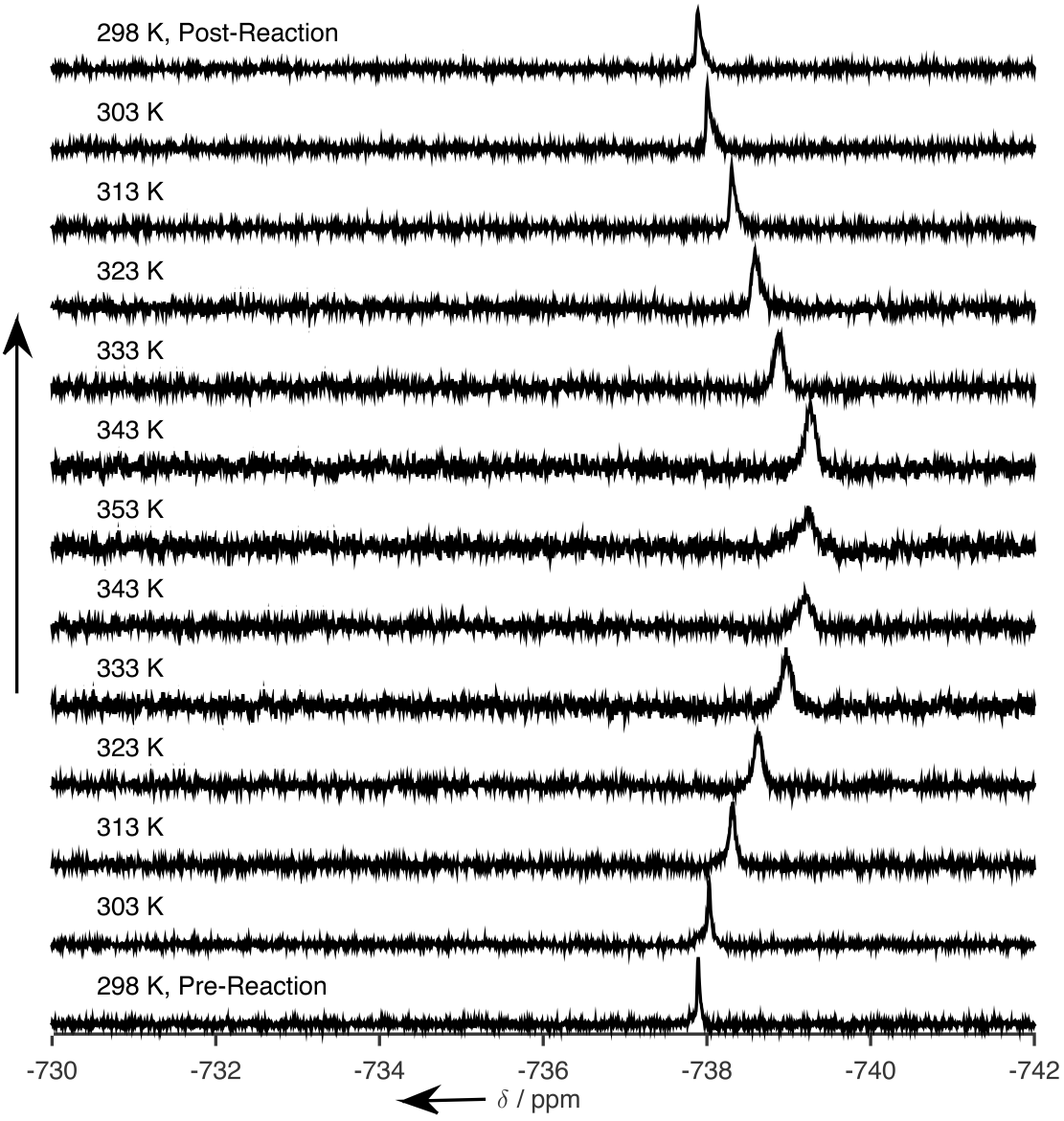

Figure A.1: Variable-temperature ^{119}Sn NMR spectra for **1b** collected between 298 K and 353 K in 10 K increments.

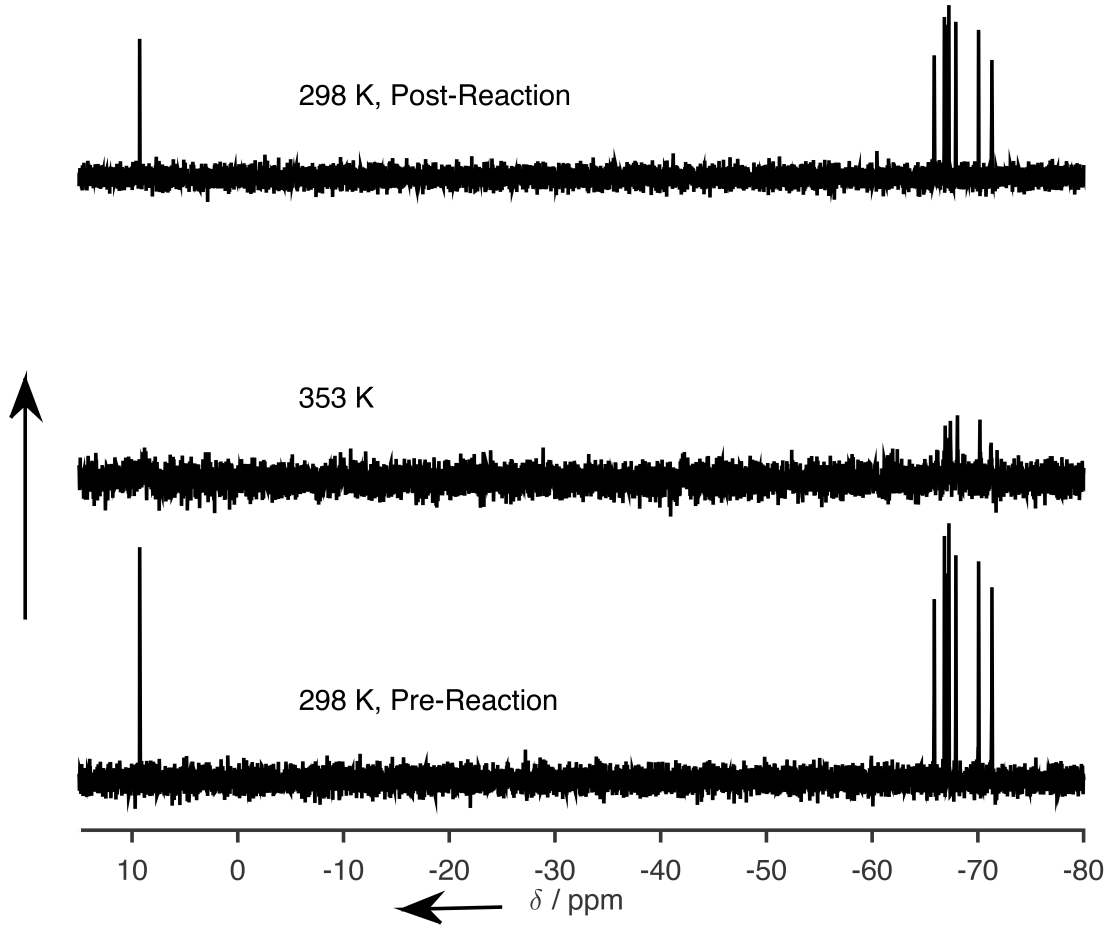

Figure A.2: Variable-temperature ^{29}Si NMR spectra for **1b** collected at 298 K prior to heating, at 353 K, then again at 298 K after cooling the sample.

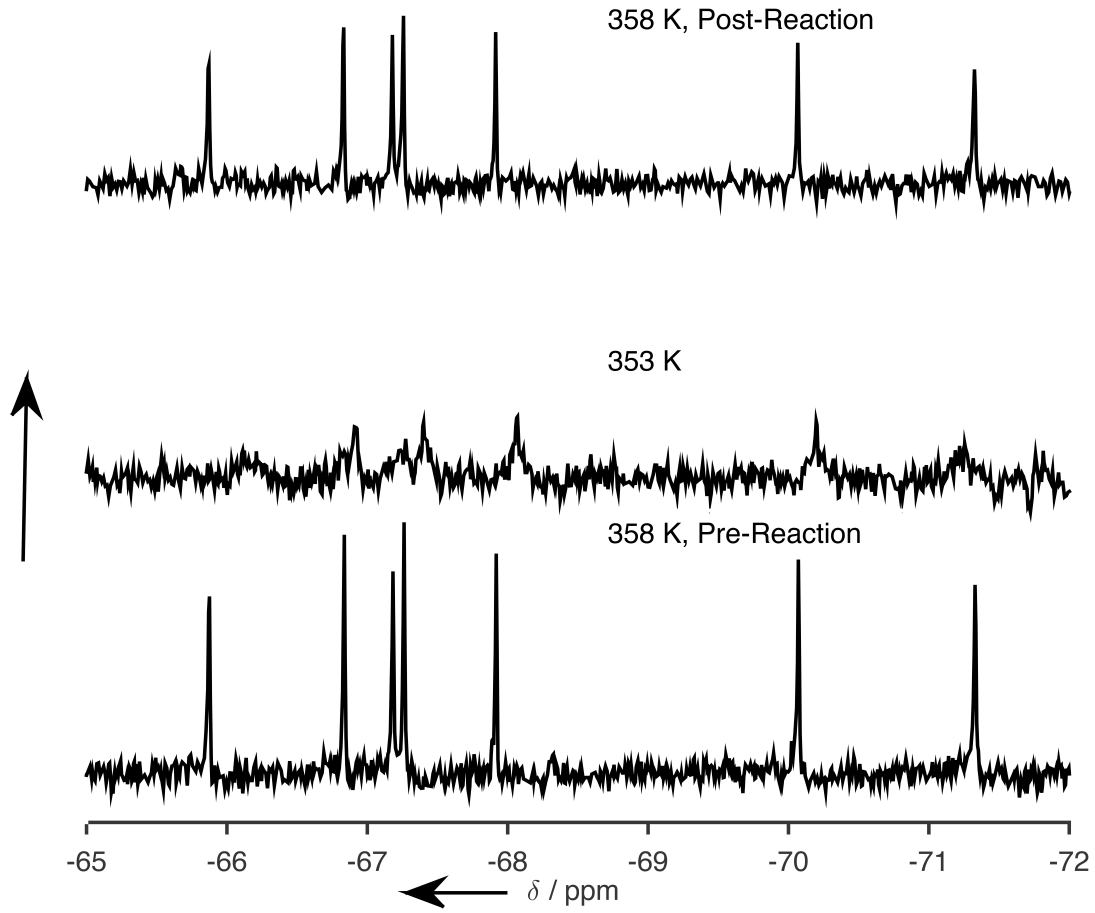

Figure A.3: Enhanced view of the variable-temperature ^{29}Si NMR spectra for **1b** collected at 298 K prior to heating, at 353 K, then again at 298 K after cooling the sample.

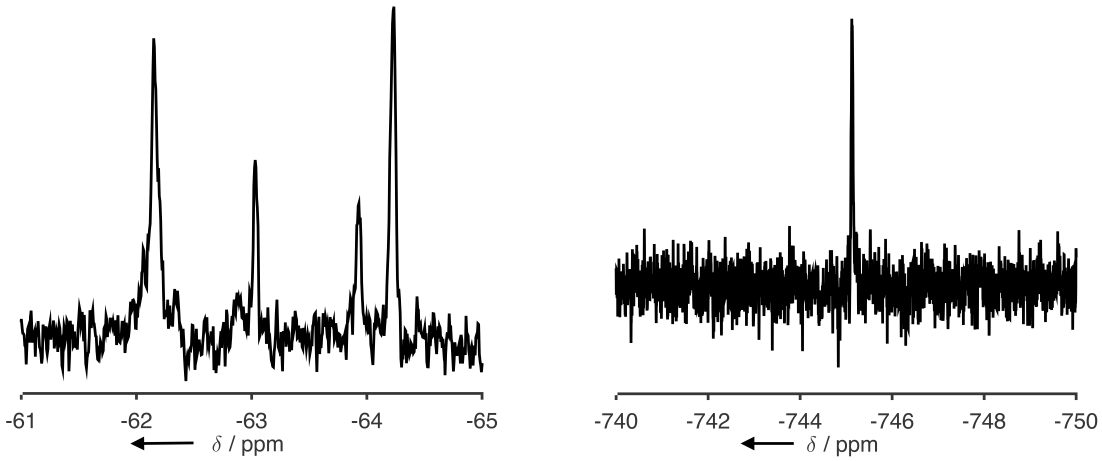

Figure A.4: ^{29}Si NMR spectrum obtained at 298 K post-reaction (left) and ^{119}Sn (right) at 353 K of **1a** under reaction conditions.

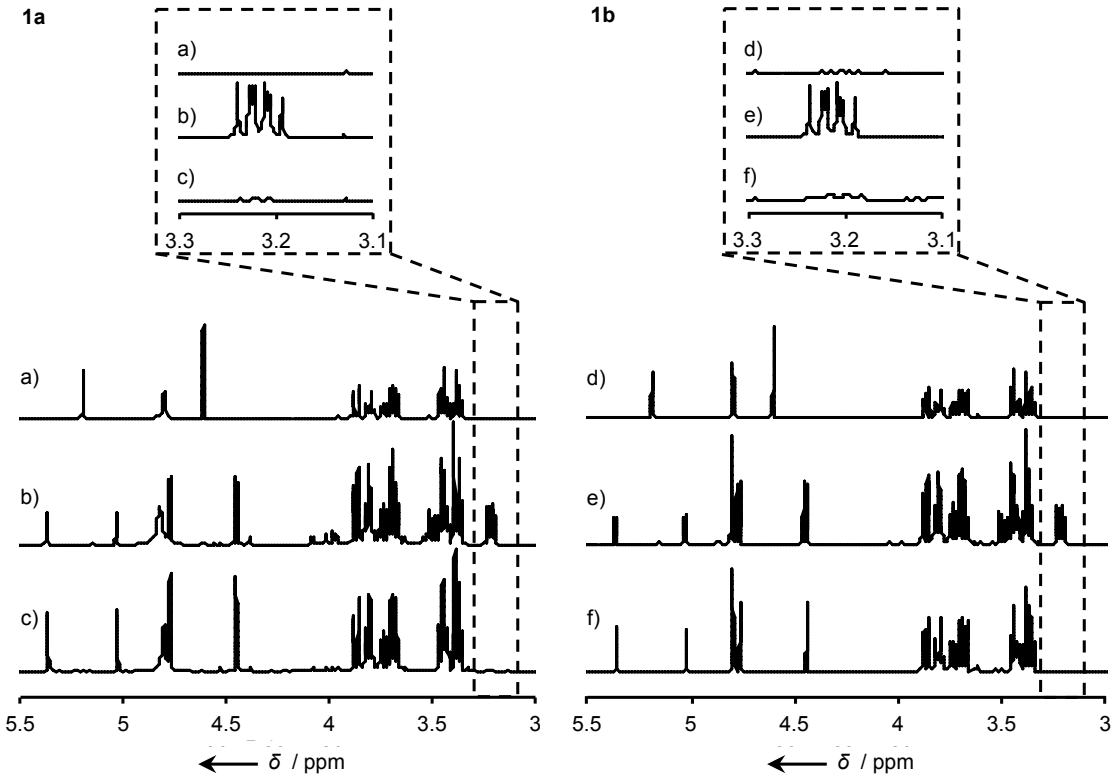

Figure A.5: ^{1}H NMR spectra of the reactant and product solutions in D_2O obtained after reacting a) 2-^{2}H glucose, b) 1-^{13}C glucose, and c) 2-^{2}H; 1-^{13}C glucose with **1a**; d) 2-^{2}H glucose, e) 1-^{13}C glucose, and f) 2-^{2}H; 1-^{13}C glucose with **1b**.

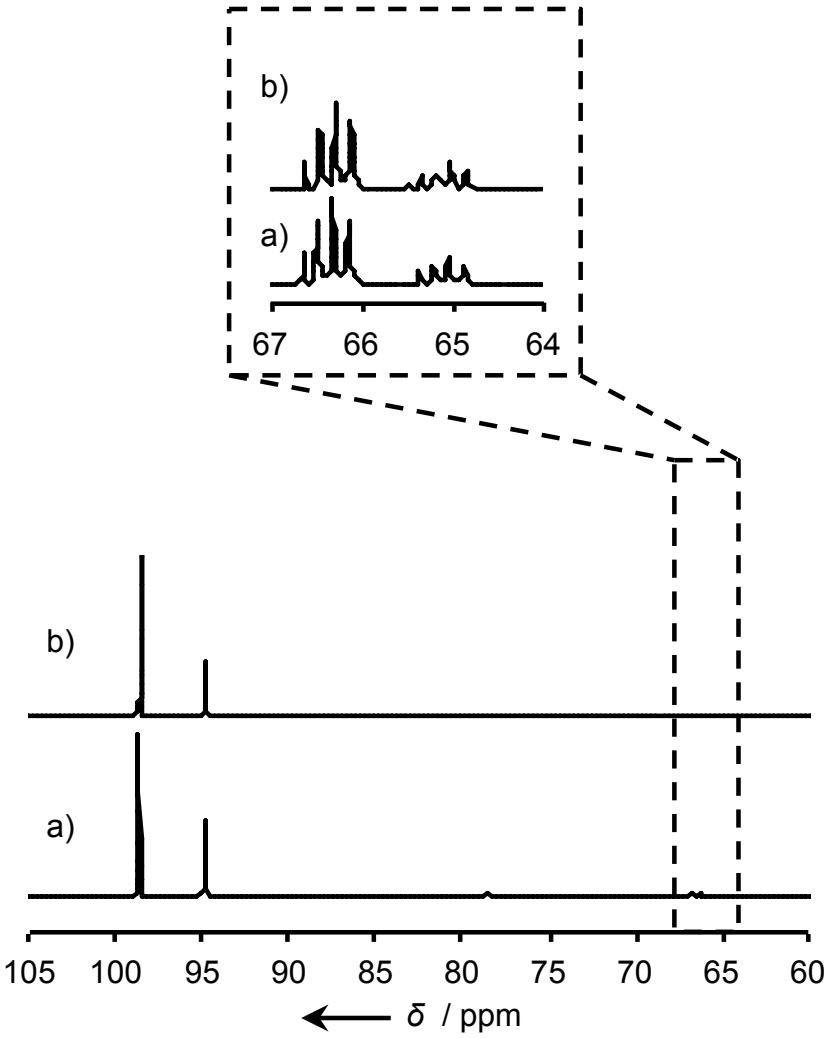

Figure A.6: ^{13}C NMR spectra of the reactant and product solutions in D_2O obtained after reaction with a 10% (w/w) 2-^{2}H;1-^{13}C glucose with Sn-Beta in a) H_2O and b) D_2O after 1 hour at 353 K.

Appendix B

SUPPLEMENTARY INFORMATION FOR CHAPTER 3

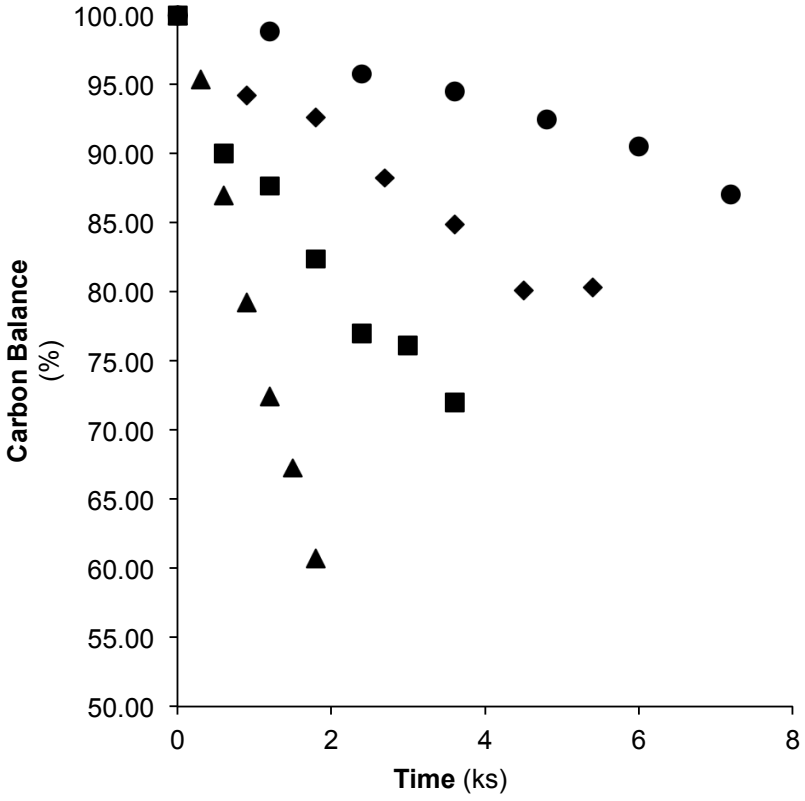

Figure B.1: Carbon balance for reaction testing carried out using 2% (w/w) glucose in an equivolumetric DMSO:benzene solution with **2a** (1:75 Sn/glucose molar ratio) at 363 K (●), 373 K (♦), 383 K (■), 393 K (▲).

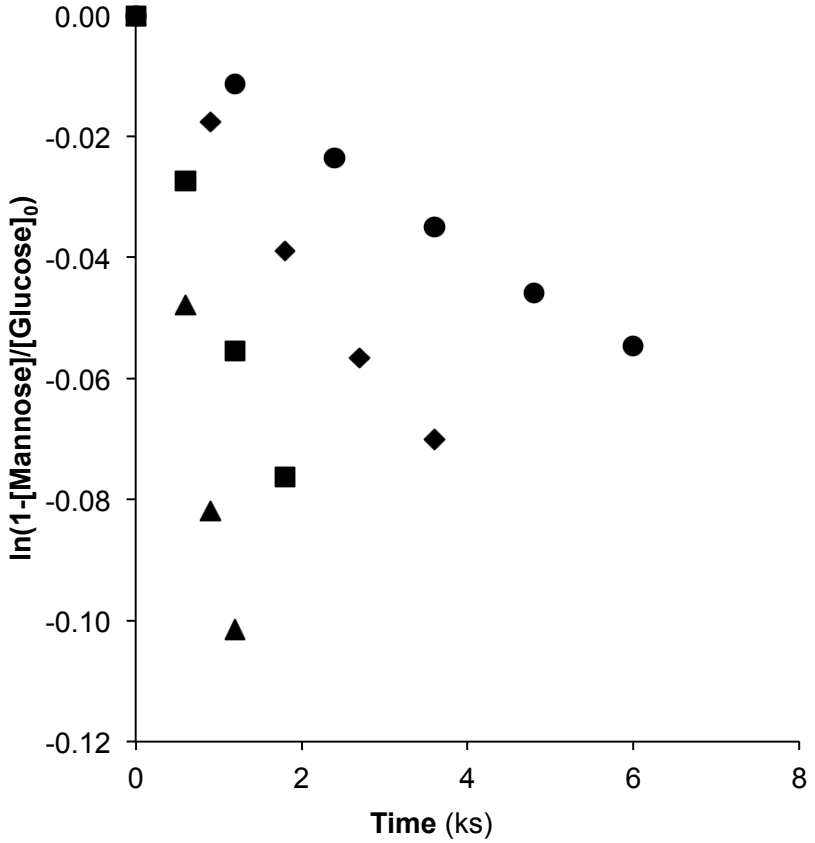

Figure B.2: First order epimerization reaction of glucose to mannose. Reaction testing was carried out using 2% (w/w) glucose in an equivolumetric DMSO:benzene solution with **2a** (1:75 Sn/glucose molar ratio) at 363 K (●), 373 K (♦), 383 K (■), 393 K (▲).

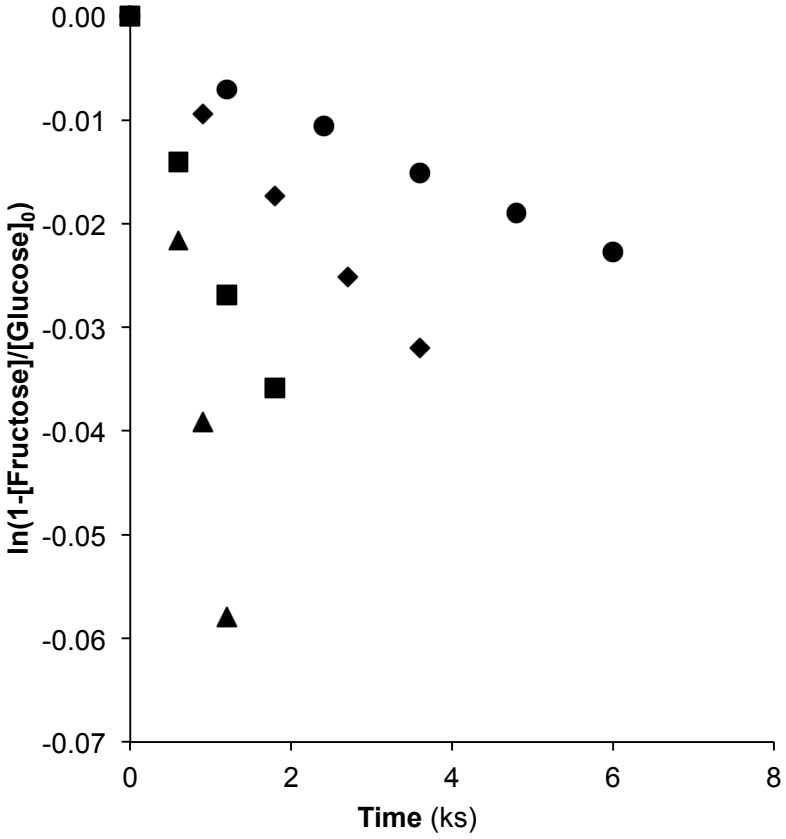

Figure B.3: First order isomerization reaction of glucose to fructose. Reaction testing was carried out using 2% (w/w) glucose in an equivolumetric DMSO:benzene solution with **2a** (1:75 Sn/glucose molar ratio) at 363 K (●), 373 K (♦), 383 K (■), 393 K (▲).

Table B.1: Kinetic rate constants for the production of mannose (*via* epimerization) and glucose (*via* isomerization) from glucose. Reaction testing was carried out using 2% (w/w) glucose in an equivolumetric DMSO:benzene solution with **2a** (1:75 Sn/glucose molar ratio).

Temperature	Mannose k (s^{-1},10^3)	Fructose k (s^{-1},10^3)
363	9.398	3.985
373	20.189	9.165
383	43.713	20.876
393	85.902	45.073

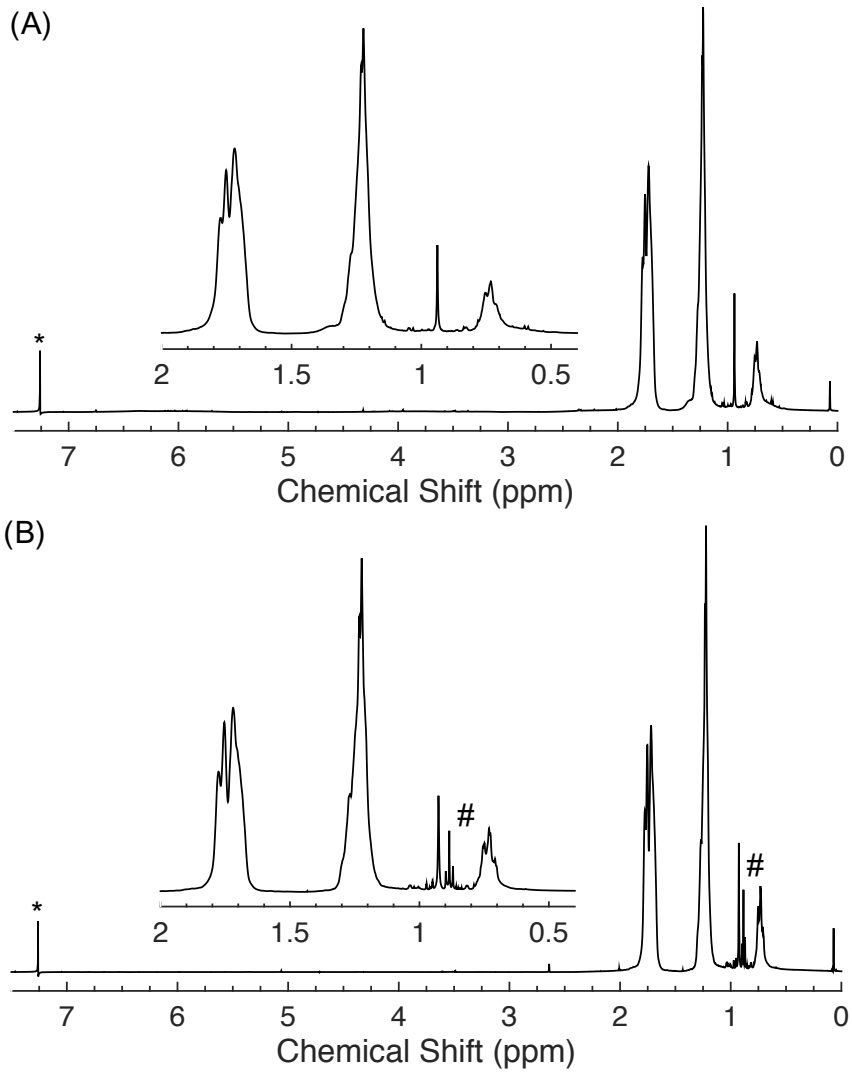

Figure B.4: ^{1}H NMR spectral comparison of as-synthesized **2a** catalyst (A) with **2a** separated (B) from a 2% (w/w) glucose in an equivolumetric DMSO:Benzene solution at 393 K after 1 hour using a 1:75 Sn/glucose molar ratio. The * denotes the chloroform solvent peak, while the # designates a residual hexane peak.

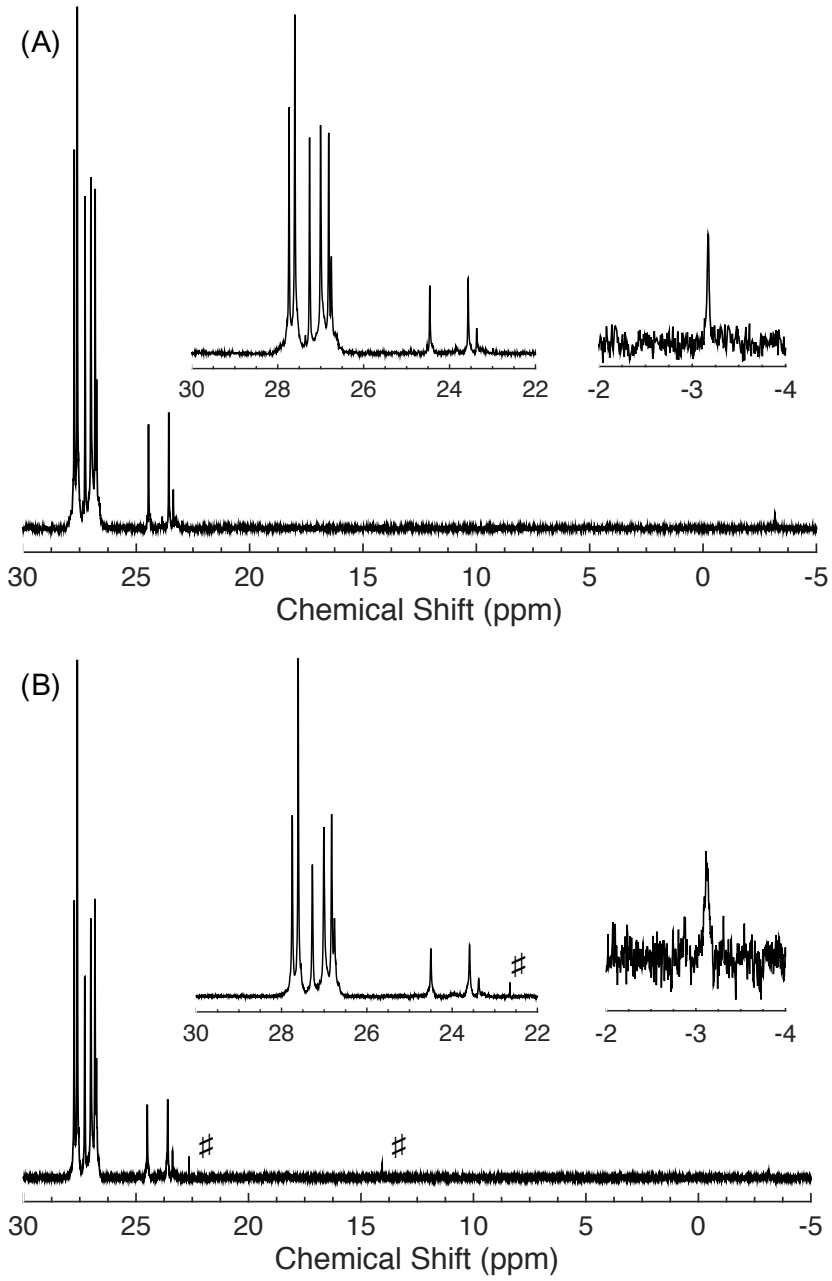

Figure B.5: ^{13}C NMR spectral comparison of as-synthesized **2a** catalyst (A) with **2a** separated (B) from a 2% (w/w) glucose in an equivolumetric DMSO:Benzene solution at 393 K after 1 hour using a 1:75 Sn/glucose molar ratio. The # denote a residual hexane peak.

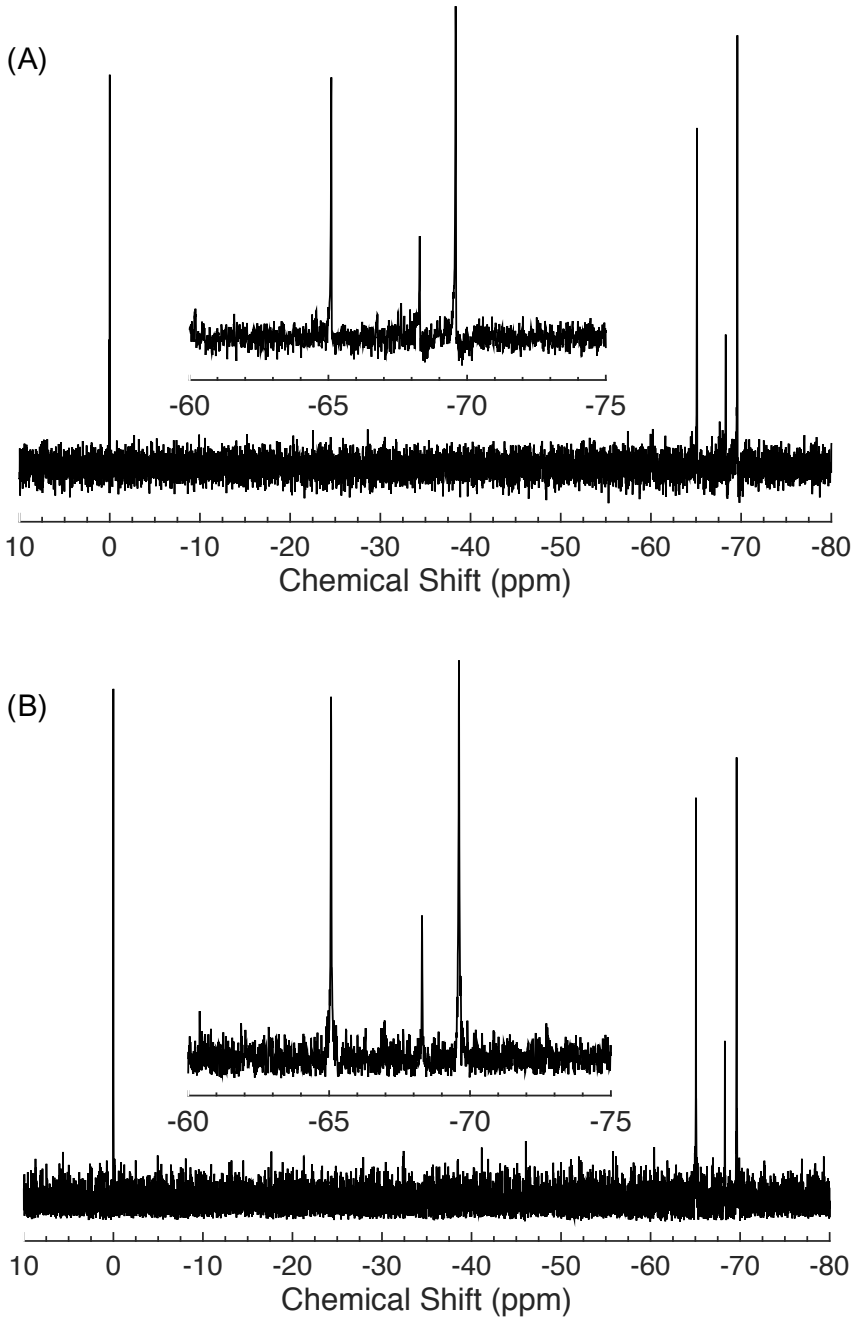

Figure B.6: ^{29}Si NMR spectral comparison of as-synthesized **2a** catalyst (A) with **2a** separated (B) from a 2% (w/w) glucose in an equivolumetric DMSO:Benzene solution at 393 K after 1 hour using a 1:75 Sn/glucose molar ratio.

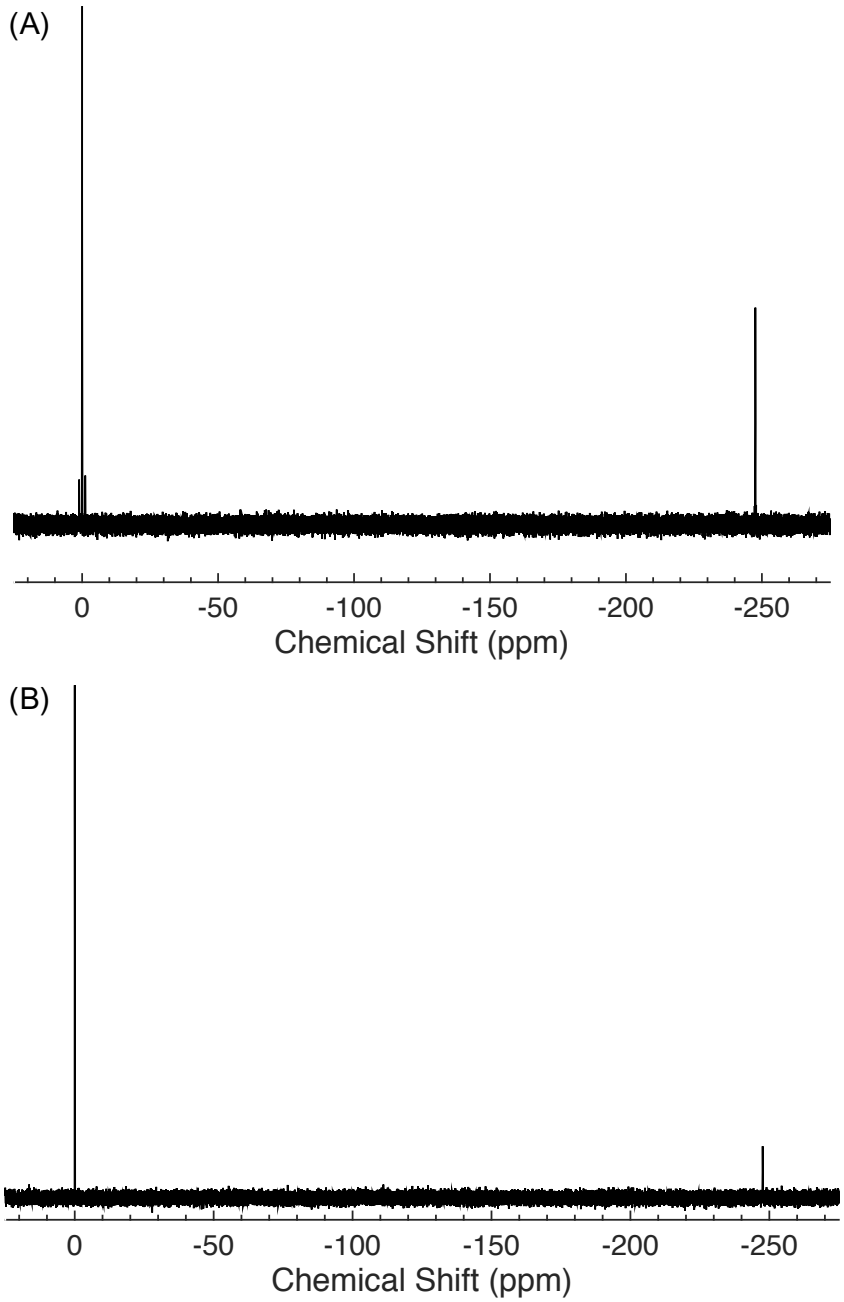

Figure B.7: ^{119}Si NMR spectral comparison of as-synthesized **2a** catalyst (A) with **2a** separated (B) from a 2% (w/w) glucose in an equivolumetric DMSO:Benzene solution at 393 K after 1 hour using a 1:75 Sn/glucose molar ratio.

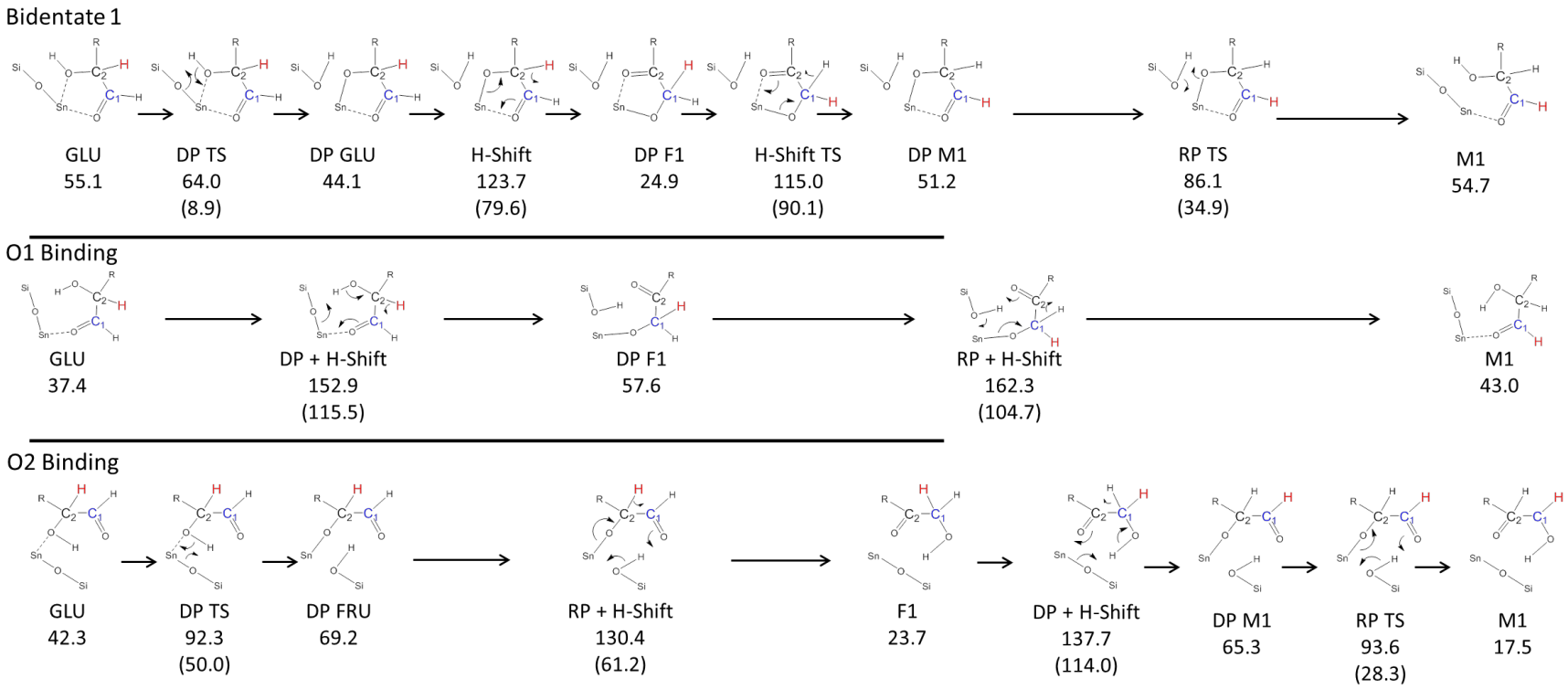

Figure B.8: Reaction scheme for H-shift pathways from glucose to fructose and subsequent H-shift pathways from fructose to mannose. R is C_3-C_6 fragment of glucose. DP and RP correspond to sugar deprotonation and reprotonation reactions, respectively. Gas-phase free energies (in kJ-mol^{-1}) at 373 K for intermediates and transition states are reported relative to isolated glucose and catalyst, with intrinsic barriers reported in parentheses.

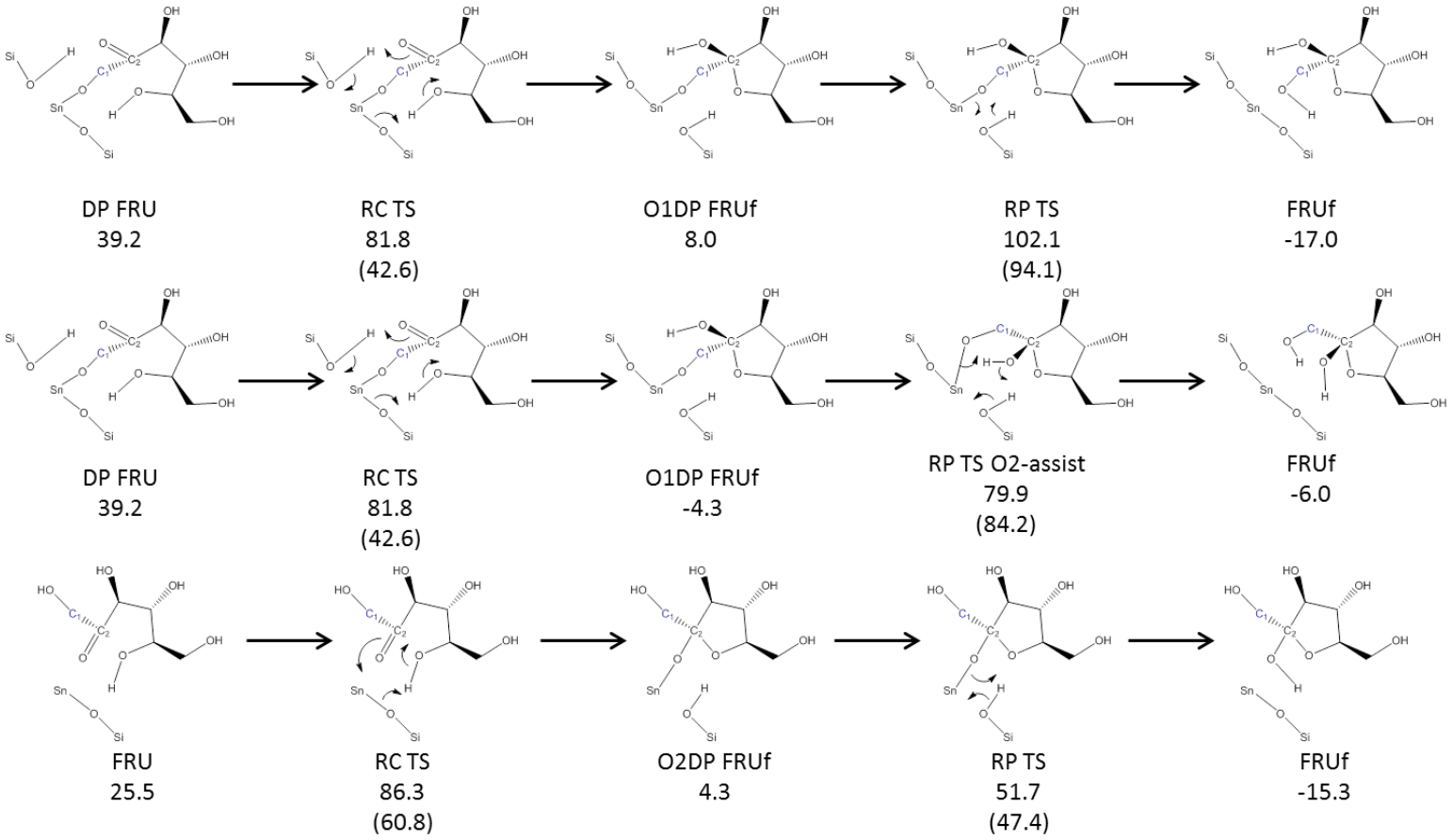

Figure B.9: Fructose ring-closing pathways. From deprotonated open fructose (FRU), a concerted ring-closing reaction will produce fructofuranose with O_1 deprotonated (O_1DP FRUf). Notably, two different Sn-O-Si bridges participate in this reaction. Reprotonation of O_1 directly has a higher barrier than reprotonating the O_2 hydroxyl, which transfers its hydrogen to O_1. Alternatively, open fructose can be formed after reprotonating DP FRU. From this sugar, the ring-closing and reprotonation are more analogous to the glucose and mannose ring-opening/closing, in which the anomeric oxygen is deprotonated in the intermediate. Gas-phase free energies (in kJ-mol^{-1}) at 373 K for intermediates and transition states are reported relative to isolated glucose and catalyst, with intrinsic barriers reported in parentheses.

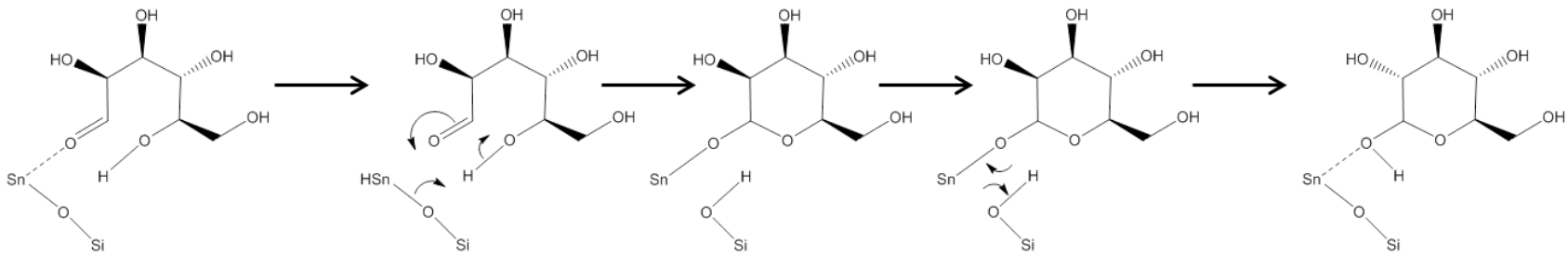

Figure B.10: Mannose ring-closing pathway. During ring closing of open mannose (MAN), the O_5 hydroxyl is transferred to the catalyst while O_1 binds to the Sn, and a silanol is formed. The silanol subsequently transfers H to O_1 to form mannopyranose (MANp) and regenerate the catalyst. Gas-phase free energies (in kJ-mol^{-1}) at 373 K for intermediates and transition states are reported relative to isolated glucose and catalyst, with intrinsic barriers reported in parentheses.

Table B.2: Energetics of reported pathways.

Ring-Opening Energetics

All energies in kJ/mol	Electronic Energy	Zero-Point Corrected Energy	Enthalpy	Gibbs Free Energy (298 K)	Gibbs Free Energy (373 K)
Adsorbed GLU	-94.96	-86.44	-87.17	-21.64	-5.15
Adsorbed GLU	-94.96	-86.44	-87.17	-21.64	-5.15
Deprotonation TS	-45.66	-49.14	-51.42	18.47	36.06
Deprotonated GLU	-67.17	-61.81	-61.70	-0.54	14.85
Ring Opening TS	-20.24	-18.33	-23.77	60.34	81.51
Open-Chain GLU	-42.17	-35.72	-36.68	36.67	55.13

Bidentate H-Shift Energetics

All energies in kJ/mol	Electronic Energy	Zero-Point Corrected Energy	Enthalpy	Gibbs Free Energy (298 K)	Gibbs Free Energy (373 K)
Open-Chain GLU	-42.17	-35.72	-36.68	36.67	55.13
Deprotonation TS	0.33	-9.95	-10.17	49.06	63.97
Deprotonated GLU	-35.04	-33.66	-33.03	28.59	44.09
H-Shift TS	53.87	44.22	44.65	107.77	123.66
Deprotonated FRU	-85.71	-81.71	-81.81	-11.14	6.65
Reprotonation TS	-32.33	-34.99	-38.53	44.28	65.12
Open-Chain FRU	-69.08	-61.86	-61.32	6.02	22.97

O_1 Binding H-Shift Energetics

All energies in kJ/mol	Electronic Energy	Zero-Point Corrected Energy	Enthalpy	Gibbs Free Energy (298 K)	Gibbs Free Energy (373 K)
Open-Chain GLU	-55.55	-48.49	-48.56	20.07	37.35
DP+H-Shift TS	71.47	63.78	61.67	134.52	152.86
Deprotonated FRU	-26.91	-22.53	-23.15	42.07	58.49
Reprotonation TS	-3.01	-10.10	-11.28	55.58	72.41
Open-Chain FRU	-55.83	-52.01	-50.78	10.14	25.47

O_2 Binding H-Shift Energetics

All energies in kJ/mol	Electronic Energy	Zero-Point Corrected Energy	Enthalpy	Gibbs Free Energy (298 K)	Gibbs Free Energy (373 K)
Open-Chain GLU	-38.64	-35.13	-34.21	26.95	42.34
Deprotonation TS	13.87	10.81	10.16	75.78	92.30
Deprotonated GLU	-12.39	-13.34	-12.95	52.68	69.20
RP+H-Shift TS	66.38	53.87	53.21	114.90	130.43
Open-Chain FRU	-64.90	-53.51	-51.54	8.57	23.70

Bidentate 1 C-Shift Energetics

All energies in kJ/mol	Electronic Energy	Zero-Point Corrected Energy	Enthalpy	Gibbs Free Energy (298 K)	Gibbs Free Energy (373 K)
Open-Chain GLU	-42.17	-35.72	-36.68	36.67	55.13
Deprotonation TS	0.33	-9.95	-10.17	49.06	63.97
Deprotonated GLU	-35.04	-33.66	-33.03	28.59	44.09
C-Shift TS	80.11	77.20	76.81	140.80	156.91
Deprotonated MAN	-18.97	-17.84	-17.49	45.30	61.10
Reprotonation TS	20.75	9.69	10.29	67.38	81.75
Open-Chain MAN	-17.59	-16.51	-14.06	39.54	53.03

Bidentate 2 C-Shift Energetics

All energies in kJ/mol	Electronic Energy	Zero-Point Corrected Energy	Enthalpy	Gibbs Free Energy (298 K)	Gibbs Free Energy (373 K)
Deprotonated GLU	-50.51	-48.51	-48.14	17.97	34.60
C-Shift TS	49.04	46.18	44.08	117.21	135.62
Deprotonated MAN	-35.45	-33.01	-34.23	36.50	54.30
Reprotonation TS	12.94	7.55	3.96	80.62	99.92
Open-Chain MAN	-44.10	-37.53	-38.99	32.04	49.92

O_1 Binding C-Shift Energetics

All energies in kJ/mol	Electronic Energy	Zero-Point Corrected Energy	Enthalpy	Gibbs Free Energy (298 K)	Gibbs Free Energy (373 K)
Open-Chain GLU	-30.43	-27.65	-25.85	32.51	47.20
DP+C-Shift TS	84.63	80.64	80.17	141.61	157.08
Deprotonated MAN	-27.47	-25.44	-25.06	40.99	57.62
Reprotonation TS	12.97	2.81	3.07	66.51	82.47
Open-Chain MAN	-41.30	-38.61	-36.90	25.01	40.59

O_2 Binding C-Shift Energetics

All energies in kJ/mol	Electronic Energy	Zero-Point Corrected Energy	Enthalpy	Gibbs Free Energy (298 K)	Gibbs Free Energy (373 K)
Open-Chain GLU	-38.64	-35.13	-34.21	26.95	42.34
Deprotonation TS	13.87	10.81	10.16	75.78	92.30
Deprotonated GLU	-12.39	-13.34	-12.95	52.68	69.20
RP+C-Shift TS	89.80	87.49	87.62	147.57	162.65
Open-Chain MAN	-31.12	-28.54	-26.30	33.08	48.03

Direct Ring-Closing of Deprotonated FRU

All energies in kJ/mol	Electronic Energy	Zero-Point Corrected Energy	Enthalpy	Gibbs Free Energy (298 K)	Gibbs Free Energy (373 K)
Deprotonated FRU	-47.08	-44.88	-45.03	22.29	39.24
Ring-Closing TS	-10.16	-14.44	-18.35	61.65	81.79
O_1 Deprotonated FRUf	-88.26	-83.95	-87.87	-11.26	8.02
Reprotonation TS	34.29	25.73	24.53	86.46	102.05
FRUf	-96.89	-91.25	-91.19	-31.89	-16.96

Direct Ring-Closing of Deprotonated FRU; O2-Assisted Reprotonation

All energies in kJ/mol	Electronic Energy	Zero-Point Corrected Energy	Enthalpy	Gibbs Free Energy (298 K)	Gibbs Free Energy (373 K)
Deprotonated FRU	-47.08	-44.88	-45.03	22.29	39.24
Ring-Closing TS	-10.16	-14.44	-18.35	61.65	81.79
O1 Deprotonated FRUf	-88.75	-83.76	-85.94	-20.68	-4.25
O2-Assisted RP TS	2.05	-8.49	-13.00	61.25	79.94
FRUf	-94.42	-87.81	-90.35	-22.94	-5.98

Ring-Closing of Open-Chain Fructose

All energies in kJ/mol	Electronic Energy	Zero-Point Corrected Energy	Enthalpy	Gibbs Free Energy (298 K)	Gibbs Free Energy (373 K)
Deprotonated FRU	-26.91	-22.53	-23.15	42.07	58.49
Reprotonation TS	-3.01	-10.10	-11.28	55.58	72.41
Open-Chain FRU	-55.83	-52.01	-50.78	10.14	25.47
Ring-Closing TS	-10.90	-11.13	-14.64	66.03	86.34
O2 Deprotonated FRUf	-81.72	-80.46	-81.15	-12.89	4.29
Reprotonation TS	-35.38	-39.39	-42.77	32.71	51.70
FRUf	-115.12	-108.65	-112.23	-34.78	-15.29

Mannose Ring-Closing Energetics

All energies in kJ/mol	Electronic Energy	Zero-Point Corrected Energy	Enthalpy	Gibbs Free Energy (298 K)	Gibbs Free Energy (373 K)
Open-Chain MAN	-28.30	-26.88	-24.40	29.44	42.99
Ring-Closing TS	-5.60	1.52	-6.38	87.43	111.03
Deprotonated MANp	-59.38	-48.44	-52.18	22.83	41.71
Reprotonation TS	-26.75	-28.57	-32.40	42.84	61.77
MANp	-88.04	-79.95	-80.26	-18.28	-2.69

Electronic Structure Analysis of H/C-Shift Reactions

Bidentate H-Shift

Following the treatment of Choudhary *et al*., we examine the donor:hydride:acceptor charge distribution, treating the C_2-C_6 fragment (including oxygen and hydrogen atoms) as the donor and the C_1, O_1, HC_1 fragment as the acceptor. The donor:hydride:acceptor charge distribution shifts from -0.937:0.252:0.075 on the reactant, to -0.543:0.282:-0.351 at the transition state, to 0.005:0.258:-0.850 on the product. The shift in charge from the donor fragment to the acceptor fragment clearly indicates the net transfer of charge that accompanies the H-shift. NBO analysis indicates a lone pair orbital on the transferring H with an occupancy of 0.714, with no bond between the transferring H and C_1 or C_2. At the transition state, O_1, and O_2 are both bonded to Sn, as well, with σ(Sn-O_1) and σ(Sn-O_2) bonding orbital occupancies of 1.904 and 1.901, respectively, and both O_1 and O_2 have partial double bonds with C_1 and C_2: the π(C_1-O_1) and π(C_2-O_2) orbitals have occupancies are 1.989 and 1.982, respectively, while the anti-bonding π*(C_1-O_1) and π*(C_2-O_2) orbitals have high occupancies, at 0.570 and 0.712, respectively. Therefore, the NBO analysis shows the formation of the C_2-O_2 double bond and the weakening of the C_1-O_1 double bond, corresponding to the transformation of the aldose into a ketose. At the transition state, the transferring hydrogen is slightly positively charged.

Which mechanism for the H-shift is most tenable? The significant positive charge on the transferring H rules out the hydride ion mechanism (d). Mechanisms (a) and (b) involve a fast electron transfer prior to the rate-limiting transfer of a proton or a neutral hydrogen, and would produce an intermediate with two electrons of opposite spin on different atoms.[1]

We performed unrestricted calculations, which converged to the restricted solution, ruling out these mechanisms. That leaves mechanism (c), a rate-limiting neutral H atom shift, followed by an electron transfer. In our case, the H atom (partial charge of 0.282 and lone pair occupancy of 0.714) is transferred during an adiabatic e^- transfer from donor to acceptor through the conjugated π system between C_2-O_2 and C_1-O_1, in agreement with Choudhary *et al*.

This can also be observed by examining the change in electron density of the complex over the course of the reaction (Figure B.11). In the deprotonated glucose, O_2 has higher electron density than O_1, but at the H-shift transition state, the electron density is diminishing at O_2 while increasing at O_1. This shift in electron density is also reflected in the NBO partial charges; the O_1 and O_2 partial charges are -0.613 and -0.965, respectively, in the deprotonated glucose reactant, -0.793 and -0.853 at the transition state, and -0.931 and -0.656 in the deprotonated fructose product. Likewise, the partial charges on C_1 and C_2 shift from 0.472 and -0.019, respectively in deprotonated glucose, to 0.182 and 0.239 at the transition state, to -0.178 and 0.599 in the product. The net charge transfer between the donor and acceptor fragments (0.932 electrons) is completely accounted for among these four atoms.

Bidentate C-shift

The charge distribution on the C-shift reaction can be examined in an analogous way, treating the C_1, O_1, HC_1 fragment as the acceptor, the C_2, O_2, HO_2 fragment as the donor, and the C_3-C_6 (including oxygens and hydrogens) as the transferring group. The donor:C_3 group:acceptor charge distribution shifts from -0.710:0.017:0.050 on the reactant

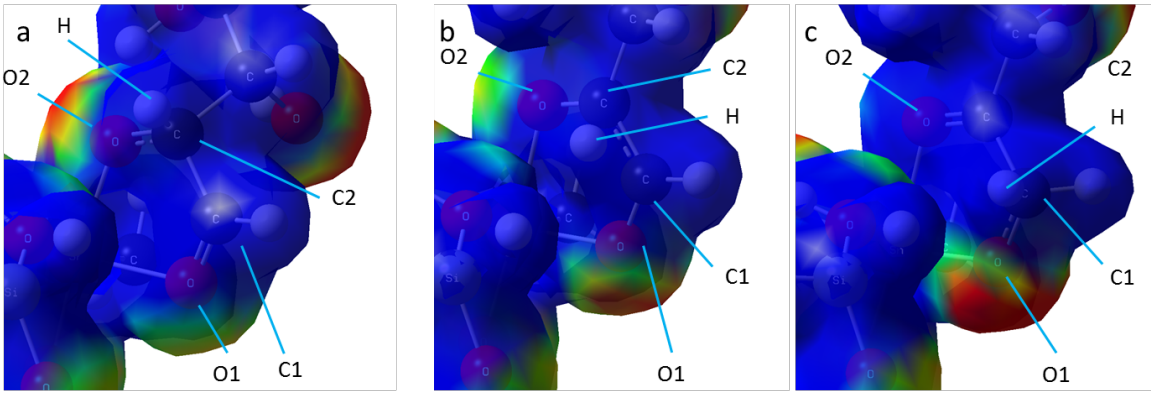

Figure B.11: Transfer of electron density during bidentate H-shift, shown by electrostatic potential mapping at 0.02 $e^{-}/Å^{3}$. Red corresponds to high electron density and blue corresponds to low electron density. From deprotonated glucose, H on C_2 (a) is transferred (b) to C_1, forming deprotonated fructose (c).

to -0.396:0.144:-0.395 at the transition state, to 0.0.067:0.004:-0.710 on the product. As in the H-shift, the donor is transferring electron density to the acceptor. The C-shift transition state shares many features with the H-shift transition state. O_1 and O_2 are both formally bonded to Sn; σ(Sn-O_1) and σ(Sn-O_2) have occupancies of 1.899 and 1.933. O_1 and O_2 also have partially formed/broken double bonds; π(C_1-O_1) and π(C_2-O_2) have occupancies of 1.986 and 1.980, and π*(C_1-O_1) and π*(C_2-O_2) have occupancies of 0.579 and 0.611. While the H-shift has a lone pair on the transferring H at the transition state, the C-shift has a lone pair on the transferring C_3 (occupancy 0.914) and no bond with C_1 or C_2.

What mechanism for the C-shift best agrees with these results? The C_3 atom as well as the C_3 fragment is slightly positively charged over the course of the C-shift reaction, ruling out a C- mechanism. Unrestricted calculations converged to the restricted solution, ruling out the C-shift analogs to mechanisms (a) and (b), assuming the C-shift step is slower than the e^{-} transfer. Therefore, we conclude that the C-shift mechanism, like the H-shift, is a rate-limiting neutral C fragment transfer accompanied by an adiabatic e^{-} transfer from O_2

to O_1 through the conjugated π system. Electron density maps (Figure B.12) also show the transfer of electron density from O_2 to O_1 over the course of the reaction, as corroborated by the partial charges, as well (Table B.4).

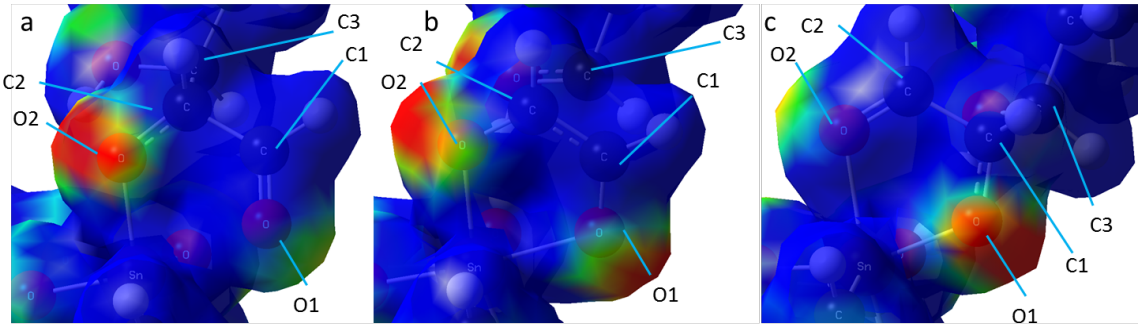

Figure B.12: Transfer of electron density during bidentate C-shift, shown by electrostatic potential mapping at 0.02 $e^-/Å^3$. Red corresponds to high electron density and blue corresponds to low electron density. From deprotonated glucose (a), C_3 is transferred (b) to C_1, forming deprotonated mannose (c).

O_1 Binding H-shift

The O_2 binding and O_1 binding pathways are generally similar, in that both involve a hydride transfer concerted with a proton transfer. The O_1 binding H-shift begins with open-chain glucose with O_1 coordinated to the Sn site, and O_2 hydroxyl H-bonded to a Sn-O-Si bridge. The concerted H-shift reaction involves the same H transfer from the C_2 fragment to the C_1 fragment as seen in the bidentate mechanism, so the same donor:hydrogen:acceptor relationship applies. However, the concerted reaction also involves an H-transfer from O_2 to the complex. This H-transfer is a proton transfer, as supported by a high partial charge on H (>0.5) throughout the reaction, and a very small change in charge on the complex fragment (only 0.171 electrons), so only a small amount of electron density is being transferred along this route.

The C_2-C_1 H-shift is formally a hydride transfer. It follows the same mechanism as the bidentate (H + e^-) due to the positive charge on H and no evidence of electron transfer prior to H-shift, according to unrestricted calculations. As in the bidentate transition state, the transferring H has a partially occupied lone pair (occupancy of 0.702) and no formal bonds with C_1 or C_2, and both O_1 and O_2 have weak double bonds with high occupancies of $\pi^*(C_1\text{-}O_1)$ and $\pi^*(C_2\text{-}O_2)$ of 0.781 and 0.563. O_1 is formally bonded to the Sn, but in contrast to the bidentate transition state, O_2 is formally bonded to the transferring proton ($\sigma(O_2\text{-H})$ and $\sigma^*(O_2\text{-H})$ occupancies of 1.980 and 0.116), which has not yet formed a bond with the bridge O. This O_2-H bond is weaker than in the reactant (σ^*(O2-H) = 0.037), because electron density from the bridge O lone pairs is delocalized by the σ^*(O2-H), according to second order perturbation delocalization. By examining geometries along the intrinsic reaction coordinate between the transition state and the product, this σ^*(O2-H) actually reaches an occupancy of 0.203 before the proton is finally transferred to the bridge oxygen.

Overall, the C_1 fragment decreases in charge by -0.96, the C_2 fragment increases in charge by 0.72, and the catalyst structure increases in charge by 0.171. Therefore, the C_2 fragment is still transferring around 1 e^- to the C_1 fragment during the formal hydride transfer, but it receives a small amount of charge from **2a** during the proton transfer to the catalyst, offsetting the charge transfer.

The O_1 binding C-shift is structurally similar to that for the O_1 binding H-shift.

Table B.3: NBO partial charges of the sugar molecule during chelate H-shift reaction. Points a-d are select points along the intrinsic reaction coordinate, with relative electronic energies provided for reference. The donor fragment consists of C_2-C_6, O_2-O_6, HC_3-HC_6, and HO_3-HO_6, the acceptor fragment consists of C_1, O_1, and HC_1, and **2a** consists of all the atoms present in the catalyst prior to interaction with the sugar. During this reaction, HO_2 is located on **2a** as a silanol.

	Reactant	a	b	TS	c	d	Product
E (kcal/mol)	0.00	9.26	12.49	19.02	11.34	4.02	-2.97
C_1	0.4722	0.4633	0.4310	0.1822	-0.1246	-0.1723	-0.1777
C_2	-0.0189	-0.0279	-0.0049	0.2392	0.5647	0.6329	0.5991
C_3	0.0456	0.0544	0.0527	0.0306	-0.0021	-0.0132	-0.0072
C_4	0.0395	0.0396	0.0399	0.0378	0.0340	0.0338	0.0403
C_5	0.0558	0.0535	0.0531	0.0531	0.0531	0.0530	0.0556
C_6	-0.1344	-0.1351	-0.1347	-0.1348	-0.1349	-0.1350	-0.1340
O_1	-0.6125	-0.6516	-0.6859	-0.7933	-0.8845	-0.9182	-0.9314
O_2	-0.9652	-0.9409	-0.9223	-0.8536	-0.7441	-0.6936	-0.6561
O_3	-0.7924	-0.7752	-0.7743	-0.7660	-0.7561	-0.7557	-0.7636
O_4	-0.8120	-0.8057	-0.8066	-0.8046	-0.8019	-0.8012	-0.8109
O_5	-0.7859	-0.7855	-0.7854	-0.7849	-0.7837	-0.7832	-0.7814
O_6	-0.8036	-0.8046	-0.8045	-0.8045	-0.8047	-0.8048	-0.8071
HC_1	0.2154	0.2217	0.2303	0.2600	0.2677	0.2598	0.2590
HC_2	0.2521	0.2627	0.2754	0.2817	0.2568	0.2399	0.2479
HC_3	0.2598	0.2566	0.2581	0.2663	0.2739	0.2736	0.2721
HC_4	0.2332	0.2232	0.2261	0.2323	0.2369	0.2391	0.2378
HC_5	0.2473	0.2492	0.2494	0.2502	0.2509	0.2511	0.2534
$HC_{6,1}$	0.2145	0.2154	0.2155	0.2168	0.2185	0.2188	0.2186
$HC_{6,2}$	0.2325	0.2318	0.2320	0.2322	0.2321	0.2320	0.2333
HO_2	0.5620	0.5647	0.5655	0.5627	0.5574	0.5561	0.5427
HO_3	0.5079	0.5053	0.5056	0.5071	0.5086	0.5090	0.5101
HO_4	0.5300	0.5273	0.5290	0.5281	0.5248	0.5245	0.5330
HO_5	0.5037	0.5032	0.5032	0.5044	0.5057	0.5059	0.5021
HO_6	0.5055	0.5064	0.5063	0.5073	0.5086	0.5088	0.5095
HC_2 donor	-0.9371	-0.9090	-0.8618	-0.5429	-0.1157	-0.0042	0.0046
HC_2	0.2521	0.2627	0.2754	0.2817	0.2568	0.2399	0.2479
HC_2 acceptor	0.0750	0.0334	-0.0246	-0.3511	-0.7413	-0.8308	-0.8502
HO_2	0.5620	0.5647	0.5655	0.5627	0.5574	0.5561	0.5427
2a	0.0481	0.0482	0.0455	0.0495	0.0429	0.0391	0.0550

Table B.4: NBO partial charges of the sugar molecule during chelate C-shift reaction. Points a-d are select points along the intrinsic reaction coordinate, with relative electronic energies provided for reference. The donor fragment consists of C_2, O_2, and HO_2, the acceptor fragment consists of C_1, O_1, and HC_1, and the C_3 fragment consists of C_3-C_6, O_3-O_6, HO_3-HO_6, and HC_3-HC_6. **2a** consists of all the atoms present in the catalyst prior to interaction with the sugar. During this reaction, HO_2 is located on **2a** as a silanol.

	Reactant	a	b	TS	c	d	Product
E (kcal/mol)	0.00	6.41	10.74	22.77	10.57	4.10	2.05
C_1	0.4456	0.4437	0.4330	0.1901	-0.0033	-0.0102	-0.0110
C_2	-0.0289	-0.0171	-0.0078	0.1722	0.4488	0.4673	0.4630
C_3	0.0555	0.0570	0.0612	0.1176	0.0489	0.0522	0.0538
C_4	0.0323	0.0359	0.0330	0.0062	0.0289	0.0310	0.0296
C_5	0.0412	0.0436	0.0440	0.0465	0.0425	0.0415	0.0430
C_6	-0.1447	-0.1429	-0.1426	-0.1447	-0.1424	-0.1427	-0.1430
O_1	-0.5962	-0.6147	-0.6474	-0.8236	-0.9295	-0.9499	-0.9538
O_2	-0.9602	-0.9484	-0.9349	-0.8391	-0.6753	-0.6424	-0.6373
O_3	-0.8132	-0.8039	-0.8114	-0.7939	-0.8469	-0.8566	-0.8499
O_4	-0.8059	-0.7961	-0.8008	-0.8005	-0.8110	-0.8187	-0.8155
O_5	-0.7798	-0.7795	-0.7801	-0.7757	-0.7774	-0.7785	-0.7786
O_6	-0.8113	-0.8114	-0.8146	-0.8080	-0.8073	-0.8129	-0.8138
HC_1	0.2009	0.2063	0.2153	0.2388	0.2546	0.2540	0.2547
HC_2	0.2788	0.2727	0.2752	0.2714	0.2485	0.2398	0.2413
HC_3	0.2335	0.2230	0.2207	0.2458	0.2490	0.2467	0.2437
HC_4	0.2379	0.2377	0.2400	0.2526	0.2478	0.2501	0.2489
HC_5	0.2392	0.2345	0.2353	0.2399	0.2396	0.2399	0.2389
$HC_{6,1}$	0.2414	0.2392	0.2395	0.2432	0.2410	0.2405	0.2407
$HC_{6,2}$	0.2196	0.2150	0.2167	0.2166	0.2169	0.2177	0.2150
HO_2	0.5621	0.5716	0.5716	0.5726	0.5757	0.5751	0.5735
HO_3	0.5323	0.5368	0.5447	0.5538	0.5446	0.5460	0.5474
HO_4	0.5186	0.5175	0.5193	0.5217	0.5211	0.5201	0.5205
HO_5	0.4990	0.5010	0.5009	0.5014	0.4985	0.4980	0.4990
HO_6	0.5217	0.5220	0.5248	0.5218	0.5203	0.5239	0.5247
C_3 donor	-0.7103	-0.6928	-0.6674	-0.3955	0.0220	0.0647	0.0670
C_3 fragment	0.0171	0.0291	0.0306	0.1441	0.0141	-0.0019	0.0042
C_3 acceptor	0.0504	0.0352	0.0009	-0.3947	-0.6782	-0.7062	-0.7101
HO_2	0.5621	0.5716	0.5716	0.5726	0.5757	0.5751	0.5735
2a	0.0807	0.0569	0.0643	0.0735	0.0664	0.0682	0.0654

Table B.5: NBO partial charges of the sugar molecule during Concerted 1 H-shift reaction. Points a-d are select points along the intrinsic reaction coordinate, with relative electronic energies provided for reference. The donor fragment consists of C_2-C_6, O_2-O_6, HC_3-HC_6, and HO_3-HO_6, the acceptor fragment consists of C_1, O_1, and HC_1, and **2a** consists of all the atoms present in the catalyst prior to interaction with the sugar. During this reaction, HO_2 is transferred from O_2 to a bridge on **2a**.

	Reactant	a	b	TS	c	d	Product
E (kcal/mol)	0.00	10.00	18.86	28.27	19.09	11.83	7.51
C_1	0.4907	0.4977	0.4238	0.0410	-0.1888	-0.1961	-0.1948
C_2	-0.0285	-0.0474	0.0095	0.3917	0.6272	0.6209	0.6005
C_3	0.0576	0.0655	0.0639	0.0260	-0.0064	-0.0102	-0.0115
C_4	0.0501	0.0436	0.0455	0.0482	0.0504	0.0471	0.0471
C_5	0.0453	0.0402	0.0405	0.0402	0.0407	0.0422	0.0432
C_6	-0.1324	-0.1334	-0.1340	-0.1341	-0.1338	-0.1340	-0.1344
O_1	-0.6537	-0.6993	-0.7579	-0.8751	-0.9375	-0.9558	-0.9676
O_2	-0.7978	-0.8098	-0.7961	-0.7323	-0.6593	-0.6397	-0.6250
O_3	-0.7956	-0.8029	-0.7987	-0.7903	-0.7875	-0.7921	-0.7951
O_4	-0.7935	-0.8026	-0.8011	-0.7981	-0.7988	-0.8020	-0.8032
O_5	-0.7820	-0.8019	-0.8000	-0.7948	-0.7904	-0.7902	-0.7903
O_6	-0.7879	-0.7979	-0.7972	-0.7959	-0.7959	-0.7969	-0.7974
HC_1	0.2022	0.2407	0.2572	0.2913	0.2806	0.2642	0.2401
HC_2	0.2466	0.2662	0.2875	0.2937	0.2737	0.2625	0.2759
HC_3	0.2212	0.2341	0.2390	0.2562	0.2580	0.2502	0.2485
HC_4	0.2156	0.2226	0.2246	0.2308	0.2337	0.2303	0.2263
HC_5	0.2369	0.2308	0.2323	0.2344	0.2320	0.2295	0.2266
$HC_{6,1}$	0.2362	0.2365	0.2374	0.2395	0.2393	0.2373	0.2361
$HC_{6,2}$	0.2336	0.2319	0.2321	0.2313	0.2296	0.2287	0.2299
HO_2	0.5429	0.5470	0.5531	0.5697	0.5750	0.5751	0.5770
HO_3	0.5251	0.5301	0.5319	0.5297	0.5257	0.5233	0.5243
HO_4	0.5211	0.5294	0.5292	0.5292	0.5280	0.5269	0.5276
HO_5	0.5164	0.5143	0.5142	0.5143	0.5112	0.5080	0.5071
HO_6	0.5032	0.5135	0.5131	0.5123	0.5114	0.5113	0.5118
HC_2 donor	-0.7552	-0.8032	-0.7139	-0.2617	0.0150	-0.0091	-0.0279
HC_2	0.2466	0.2662	0.2875	0.2937	0.2737	0.2625	0.2759
HC_2 acceptor	0.0392	0.0391	-0.0769	-0.5429	-0.8457	-0.8876	-0.9223
HO_2	0.5429	0.5470	0.5531	0.5697	0.5750	0.5751	0.5770
2a	-0.0735	-0.0491	-0.0498	-0.0590	-0.0180	0.0592	0.0973

Table B.6: NBO partial charges of the sugar molecule during Concerted 1 C-shift reaction. Points a-d are select points along the intrinsic reaction coordinate, with relative electronic energies provided for reference. The donor fragment consists of C_2, O_2, and HO_2, the acceptor fragment consists of C_1, O_1, and HC_1, and the C_3 fragment consists of C_3-C_6, O_3-O_6, HO_3-HO_6, and HC_3-HC_6. **2a** consists of all the atoms present in the catalyst prior to interaction with the sugar. During this reaction, HO_2 is transferred from O_2 to a bridge on **2a**.

	Reactant	a	b	TS	c	d	Product
E (kcal/mol)	0.00	12.33	17.66	26.56	17.00	12.24	1.18
C_1	0.4821	0.4713	0.4422	0.1689	0.0003	-0.0185	-0.0221
C_2	-0.0482	-0.0150	0.0037	0.2493	0.4315	0.4326	0.4491
C_3	0.0539	0.0631	0.0677	0.1013	0.0563	0.0649	0.0554
C_4	0.0435	0.0425	0.0403	0.0227	0.0412	0.0474	0.0540
C_5	0.0550	0.0508	0.0508	0.0530	0.0535	0.0534	0.0541
C_6	-0.1325	-0.1355	-0.1360	-0.1363	-0.1358	-0.1358	-0.1347
O_1	-0.6325	-0.7180	-0.7590	-0.8837	-0.9559	-0.9735	-0.9876
O_2	-0.8103	-0.8017	-0.7992	-0.7357	-0.6412	-0.6082	-0.5827
O_3	-0.7947	-0.7811	-0.7745	-0.7543	-0.7781	-0.7941	-0.8044
O_4	-0.7918	-0.7863	-0.7836	-0.7760	-0.7871	-0.7890	-0.7889
O_5	-0.7956	-0.8033	-0.8022	-0.8004	-0.8004	-0.8003	-0.7999
O_6	-0.8015	-0.8030	-0.8036	-0.8042	-0.8039	-0.8039	-0.8032
HC_1	0.1878	0.2347	0.2466	0.2688	0.2690	0.2722	0.2711
HC_2	0.2951	0.2707	0.2742	0.2589	0.2143	0.2051	0.1865
HC_3	0.2334	0.2412	0.2561	0.2852	0.2650	0.2440	0.2325
HC_4	0.2303	0.2285	0.2314	0.2274	0.2125	0.2175	0.2217
HC_5	0.2352	0.2467	0.2470	0.2467	0.2426	0.2413	0.2411
$HC_{6,1}$	0.2117	0.2169	0.2180	0.2193	0.2147	0.2133	0.2137
$HC_{6,2}$	0.2364	0.2357	0.2370	0.2396	0.2394	0.2403	0.2394
HO_2	0.5367	0.5391	0.5404	0.5555	0.5632	0.5572	0.5698
HO_3	0.5147	0.5213	0.5219	0.5157	0.4981	0.5065	0.5174
HO_4	0.5132	0.5137	0.5131	0.5115	0.5127	0.5166	0.5142
HO_5	0.5125	0.5136	0.5147	0.5159	0.5121	0.5109	0.5103
HO_6	0.5067	0.5090	0.5099	0.5116	0.5091	0.5082	0.5072
C_3 donor	-0.5635	-0.5460	-0.5214	-0.2276	0.0046	0.0295	0.0530
C_3 fragment	0.0303	0.0739	0.1080	0.1785	0.0519	0.0411	0.0298
C_3 acceptor	0.0374	-0.0120	-0.0703	-0.4460	-0.6867	-0.7198	-0.7385
HO_2	0.5367	0.5391	0.5404	0.5555	0.5632	0.5572	0.5698
2a	-0.0409	-0.0549	-0.0568	-0.0605	0.0669	0.0919	0.0859

Table B.7: NBO partial charges of the sugar molecule during Concerted 2 H-shift reaction. Points a-d are select points along the intrinsic reaction coordinate, with relative electronic energies provided for reference. The donor fragment consists of C_2-C_6, O_2-O_6, HC_3-HC_6, and HO_3-HO_6, the acceptor fragment consists of C_1, O_1, and HC_1, and **2a** consists of all the atoms present in the catalyst prior to interaction with the sugar. During this reaction, HO_2 is transferred from a silanol on **2a** to O_1, regenerating the Sn-O-Si bridge.

	Reactant	a	b	TS	c	d	Product
E (kcal/mol)	0.00	9.83	12.06	15.05	7.09	-2.92	-8.22
C_1	0.4467	0.4730	0.4575	0.2556	-0.1274	-0.1975	-0.1925
C_2	-0.0342	-0.0571	-0.0407	0.1450	0.5441	0.6552	0.6350
C_3	0.0544	0.0628	0.0630	0.0463	0.0039	-0.0169	-0.0200
C_4	0.0402	0.0364	0.0352	0.0352	0.0383	0.0387	0.0438
C_5	0.0415	0.0416	0.0415	0.041	0.0405	0.0396	0.0390
C_6	-0.1343	-0.1350	-0.1354	-0.1356	-0.1355	-0.1350	-0.1346
O_1	-0.5786	-0.6119	-0.6251	-0.6864	-0.7584	-0.7804	-0.7730
O_2	-0.9719	-0.9579	-0.9367	-0.8892	-0.7827	-0.7139	-0.6626
O_3	-0.7963	-0.8034	-0.8016	-0.7967	-0.7887	-0.7857	-0.7874
O_4	-0.8003	-0.7979	-0.7965	-0.7945	-0.7917	-0.7908	-0.7877
O_5	-0.7817	-0.7790	-0.7788	-0.7789	-0.7796	-0.7804	-0.7813
O_6	-0.7953	-0.7938	-0.7932	-0.7927	-0.7921	-0.7919	-0.7915
HC_1	0.1865	0.2069	0.2330	0.2577	0.2686	0.2517	0.2461
HC_2	0.2614	0.3119	0.3397	0.3613	0.3277	0.2822	0.2462
HC_3	0.2366	0.2467	0.2529	0.2629	0.2750	0.2769	0.2747
HC_4	0.2266	0.2274	0.2267	0.2305	0.2389	0.2427	0.2343
HC_5	0.2451	0.2499	0.2508	0.2508	0.2495	0.2482	0.2482
$HC_{6,1}$	0.2336	0.2353	0.2367	0.2376	0.2383	0.2380	0.2362
$HC_{6,2}$	0.2196	0.2179	0.2192	0.2199	0.2203	0.2201	0.2245
HO_2	0.5716	0.5625	0.5611	0.5537	0.5360	0.5266	0.5190
HO_3	0.5185	0.5181	0.5211	0.5219	0.5178	0.5164	0.5142
HO_4	0.5164	0.5120	0.5144	0.5155	0.5142	0.5137	0.5078
HO_5	0.4928	0.4928	0.4937	0.4951	0.4967	0.4972	0.4974
HO_6	0.5062	0.5045	0.5044	0.5048	0.5059	0.5060	0.5029
HC_2 donor	-0.9825	-0.9787	-0.9234	-0.6808	-0.1869	-0.0218	-0.0070
HC_2	0.2614	0.3119	0.3397	0.3613	0.3277	0.2822	0.2462
HC_2 acceptor	0.0546	0.0680	0.0653	-0.1731	-0.6172	-0.7262	-0.7194
HO_2	0.5716	0.5625	0.5611	0.5537	0.5360	0.5266	0.5190
2a	0.0949	0.0363	-0.0428	-0.0611	-0.0597	-0.0607	-0.0389

Table B.8: NBO partial charges of the sugar molecule during Concerted 1 C-shift reaction. Points a-d are select points along the intrinsic reaction coordinate, with relative electronic energies provided for reference. The donor fragment consists of C_2, O_2, and HO_2, the acceptor fragment consists of C_1, O_1, and HC_1, and the C_3 fragment consists of C_3-C_6, O_3-O_6, HO_3-HO_6, and HC_3-HC_6. **2a** consists of all the atoms present in the catalyst prior to interaction with the sugar. During this reaction, HO_2 is transferred from the silanol on **2a** to O_1, regenerating the Sn-O-Si bridge.

	Reactant	a	b	TS	c	d	Product
E (kcal/mol)	0.00	8.60	11.17	21.77	9.19	2.69	-4.75
C_1	0.4506	0.4496	0.4530	0.1947	-0.0282	-0.0200	-0.0213
C_2	-0.0288	-0.0125	-0.0061	0.1977	0.5154	0.5089	0.4690
C_3	0.0576	0.0654	0.0650	0.1530	0.0491	0.0427	0.0476
C_4	0.0401	0.0385	0.0363	0.0143	0.0386	0.0380	0.0401
C_5	0.0427	0.0414	0.0408	0.0449	0.0408	0.0390	0.0358
C_6	-0.1355	-0.1379	-0.1375	-0.1374	-0.1366	-0.1350	-0.1334
O_1	-0.5692	-0.6021	-0.6113	-0.7197	-0.7765	-0.7755	-0.7840
O_2	-0.9614	-0.9736	-0.9673	-0.8698	-0.7111	-0.6624	-0.6268
O_3	-0.7997	-0.7906	-0.7876	-0.7534	-0.8066	-0.8117	-0.8075
O_4	-0.8023	-0.7886	-0.7877	-0.7797	-0.7835	-0.7842	-0.7743
O_5	-0.7899	-0.7840	-0.7840	-0.7813	-0.7846	-0.7879	-0.7982
O_6	-0.7947	-0.7907	-0.7895	-0.7895	-0.7915	-0.7899	-0.7896
HC_1	0.1981	0.2117	0.2175	0.2655	0.2670	0.2651	0.2751
HC_2	0.2282	0.2456	0.2444	0.2418	0.2137	0.2029	0.2054
HC_3	0.2396	0.2512	0.2490	0.2564	0.2674	0.2629	0.2430
HC_4	0.2127	0.2169	0.2215	0.2422	0.2380	0.2386	0.2392
HC_5	0.2374	0.2469	0.2466	0.2435	0.2411	0.2302	0.2277
$HC_{6,1}$	0.2332	0.2358	0.2358	0.2389	0.2358	0.2356	0.2357
$HC_{6,2}$	0.2241	0.2273	0.2265	0.2270	0.2265	0.2280	0.2296
HO_2	0.5685	0.5510	0.5550	0.5435	0.5232	0.5202	0.5209
HO_3	0.5320	0.5157	0.5150	0.5309	0.5193	0.5217	0.5175
HO_4	0.5206	0.5042	0.5022	0.5025	0.5016	0.5006	0.4931
HO_5	0.4963	0.5019	0.5018	0.5061	0.5045	0.5060	0.5103
HO_6	0.5065	0.4989	0.4984	0.5026	0.5024	0.5018	0.5030
C_3 donor	-0.7619	-0.7404	-0.7291	-0.4303	0.0179	0.0493	0.0476
C_3 fragment	0.0208	0.0521	0.0526	0.2209	0.0623	0.0364	0.0195
C_3 acceptor	0.0796	0.0592	0.0593	-0.2594	-0.5376	-0.5305	-0.5301
HO_2	0.5685	0.5510	0.5550	0.5435	0.5232	0.5202	0.5209
2a	0.0931	0.0781	0.0622	-0.0747	-0.0659	-0.0755	-0.0579

B.1 References

(1) Choudhary, V.; Caratzoulas, S.; Vlachos, D. G. Insights into the isomerization of xylose to xylulose and lyxose by a Lewis acid catalyst. *Carbohydrate Research* **2013**, *368*, 89–95.

Appendix C

A COMPUTATIONAL EXAMINATION OF THE HYDRIDE AND CARBON SHIFT REACTIONS ON TIN SILSESQUIOXANES

Information contained in this Appendix was originally published in:

(1) Josephson, T. R.; Brand, S. K.; Caratzoulas, S.; Vlachos, D. G. 1,2-H- versus 1,2-C-Shift on Sn-Silsesquioxanes. *ACS Catalysis* **2017**, *7*, 25–33, DOI: 10.1021/acscatal.6b03128,

T.R.J. provided computational data presented.

C.1 Introduction

Utilization of lignocellulosic biomass as a renewable chemical feedstock is a promising path to a more sustainable chemical industry.[1–5] Lewis-acidic zeolites, Sn-Beta in particular, have emerged as useful catalysts for a wide range of transformations in biomass conversion, including Baeyer-Villiger oxidation of ketones to lactones, the Meerwein-Ponndorf-Verley (MPV) reduction of carbonyls, the 1,2-intramolecular hydride shift (1,2-HS) of glucose and xylose, retro-aldol and esterification of sugars to lactates, the 1,2-intramolecular carbon shift (1,2-CS) of glucose and arabinose, and dehydration reactions in the production of renewable aromatics from furans.[6–13]

The isomerization of glucose to fructose is of particular interest due to the abundance of cellulose as a glucose feedstock and the value of fructose for production of 5-hydroxymethylfurfural (HMF) and lactic acid.[14–16] ^{119}Sn NMR and acetonitrile adsorption and spectroscopy have identified two types of Sn sites in Sn-Beta: a "closed" framework Sn site, $Sn(OSi)_4$, and a hydrolyzed "open" site, $Sn(OSi)_3OH$ with a neighboring SiOH.[17]

Open sites are stronger Lewis acids than closed sites and more active for glucose isomerization.[17–19] Figure C.1 shows a reaction scheme for different glucose transformation reactions catalyzed by Sn-Beta. Sn-Beta selectively produces fructose F1 *via* a 1,2-HS reaction from glucose, and mannose M1 as a side product *via* a subsequent 1,2-HS reaction from fructose.[18] Modification of the open site by Na^+ titration or with borate salts shifts selectivity from fructose to mannose, but this mannose is produced *via* a 1,2-CS (M2), or Bílik reaction.[12,18,20] Moreover, different synthesis methods produce catalysts with different ratios of open and closed sites.[17,19] Understanding these structure-activity and structure-selectivity relationships is important for optimizing Sn-Beta synthesis and deployment in future biorefineries.

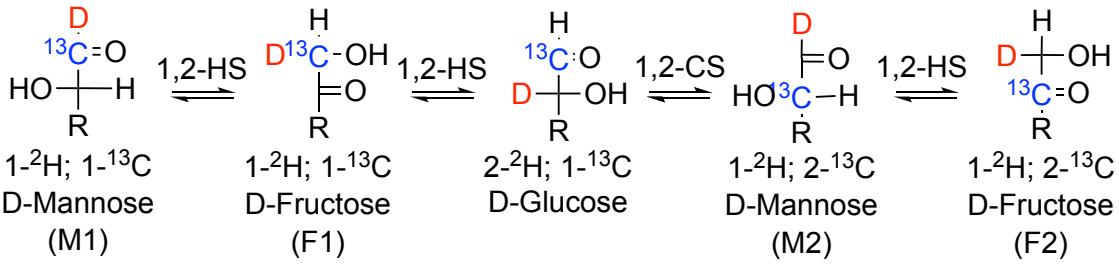

Figure C.1: Possible reaction pathways involving hydride and carbon shifts at C_1 and C_2. Sugars are depicted using Fischer projections. Abbreviations F1, M1, M2, and F2 indicate location of ^{13}C on first or second carbon of sugar, when C_1 of glucose reactant is labeled. R = $C_4H_9O_4$.

Beginning with Assary and Curtiss' examination of glyceraldehyde isomerization to dihydroxyacetone on open and closed sites of Sn-Beta, several computational studies have investigated the glucose isomerization mechanism on the Sn-Beta zeolite.[21–27] These have found that the open site is more active than the closed site, whether examined as a 5T (five tetrahedral atoms) cluster, or an extended 208T QM/MM model, implicating the stronger Brønsted basicity of SnOH relative to SnOSi. However, a study using periodic DFT

found little difference between closed and open sites.[21,22,26] Using a 9T open site cluster, Rai *et al*. found that glucose in a bidentate coordination to the Sn favored the 1,2-CS reaction, while glucose coordinated to the Sn and neighboring SiOH favored the 1,2-HS reaction, suggesting the neighboring SiOH enabling fructose selectivity by participating in a concerted reaction.[25] However, a more complete analysis of this 9T cluster with and without Na-exchange identified a more favorable bidentate binding geometry that favored the H-shift without SiOH participation, instead finding that Na^+ provides electrostatic stabilization of the C-shift transition state (TS) more than the H-shift TS.[27] A larger, less flexible zeolite cluster favored a concerted, rather than bidentate, mechanism for both Sn-Beta and Na-Sn-Beta, and observed the same electrostatic effect on the H/C-shift transition states.

These studies highlight several challenges associated with modeling Sn-Beta. In addition, there is no experimental consensus for the crystallographic location of the Sn atom. Consequently, computational studies have used either the T2 substitution, as it is most thermodynamically stable closed site, or the T9 substitution, in agreement with acetonitrile adsorption and spectroscopic evidence.[17,24–29] The T5/T6 sites exhibited similar agreement with acetonitrile adsoprtion, and have also been proposed on account of EXAFS experiments, but have not been examined computationally.[17,30]

Silsesquioxanes have been useful for reducing the heterogeneous-homogeneous gap in catalysis by providing single-site molecular analogues for evaluating structure-property relationships.[31] Recently, several Sn silsesquioxanes have been synthesized and tested to evaluate the active sites in Sn-Beta.[32–35] Beletskiy *et al*., synthesized a tetrahedral Sn-silisesquioxane, grafted it onto silica, and demonstrated its activity for epoxide ring-opening

and MPV reduction, comparable to Sn-Beta.[32,33] This catalyst was also active for glucose isomerization to fructose, but formed significant side products, possibly due to surface silanol groups. Brand *et al*. have synthesized and tested three tin silsesquioxanes (Figure C.2) with structural differences designed to model the open (**1a**), Na-exchanged (**1b**), and closed (**2a**) sites in Sn-Beta.[34,35] All catalysts are active for glucose isomerization and epimerization. Analysis of initial rate data for these three tin silsesquioxanes and Sn-Beta, Na-Sn-Beta, and NH_3-Sn-Beta reveals several structure-property correlations among the catalysts.[35] Sn-Beta and **1a** are most active, and selective towards fructose (although mannose formed from Sn-Beta is from a 1,2-HS from fructose, while **1a** forms mannose through the 1,2-CS of glucose). Na-Sn-Beta and **1b**, each of which have had the neighboring SiOH replaced, showed reduced activity in glucose conversion and a shift in product selectivity to mannose formed by 1,2-CS of glucose, implicating the SiOH as an important feature for promoting selectivity to fructose. NH_3-Sn-Beta, CH_3-Sn-Beta, and **2a** exhibited an order of magnitude reduction in activity relative to Sn-Beta, with mannose as major product, providing evidence for some residual activity on closed Sn sites. Taken together, these silsesquioxane experiments have decoupled the functions of the open, closed, and Na-exchanged sites, which cannot be done explicitly in the heterogeneous case due to challenges in synthesizing zeolites with exclusively one kind of Sn site.

In our previous paper, we calculated several pathways for glucose ring-opening, conversion to fructose and mannose, and product ring-closing on **2a**.[35] In this work, we report glucose transformation mechanisms for **1a** and **1b**, focusing on the rate-determining steps of the 1,2-HS and 1,2-CS.

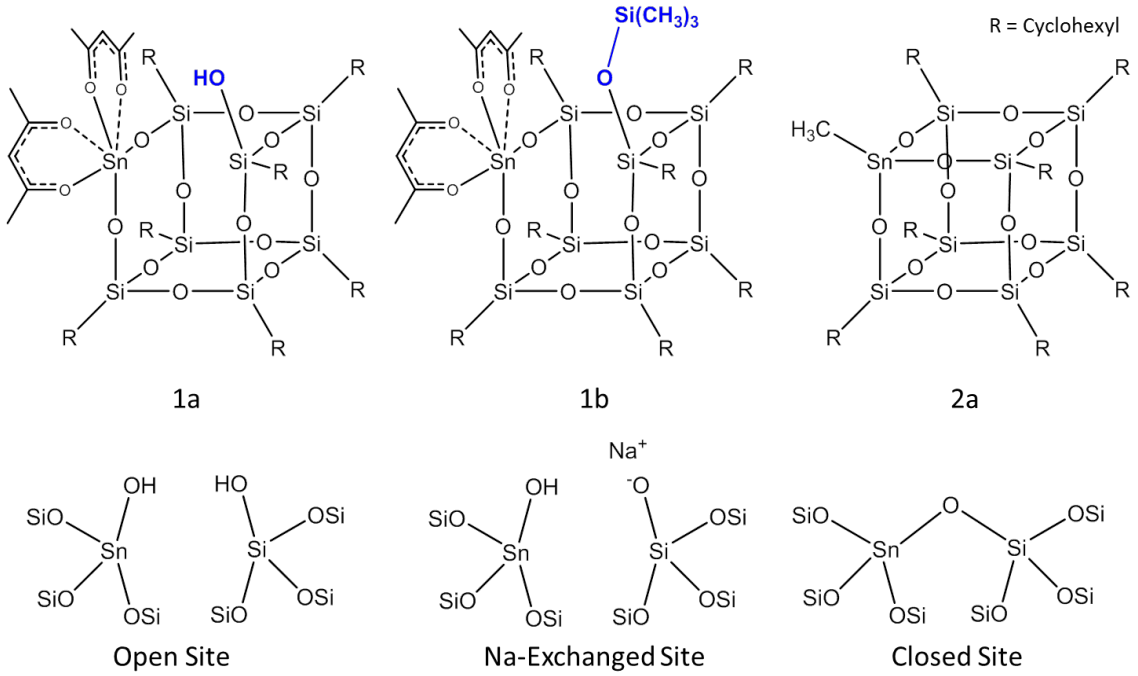

Figure C.2: Tin-silsesquioxanes synthesized and tested for glucose isomerization by Brand *et al*. **1a** and **1b** contain an octahedral Sn site, coordinated by two acetylacetonate ligands, and **2a** contains a tetrahedral Sn site ligated by a methyl group.[34,35] These are structural models of the Sn-Beta open, Na-exchanged, and closed sites.

C.2 Computational Methods

Electronic structure calculations were performed using density functional theory to calculate reaction pathways and examine catalyst/substrate interactions. Geometry optimizations and frequency calculations were performed using the M062X functional with the LANL2DZ effective core basis set for the Si and Sn atoms, 3-21G for the cyclohexyl ligands, and 6-31G(d,p) basis set for the sugar, acac ligands, framework O atoms, and the H or CH_3 groups on the SiOH (**1a**) or SiOTMS (**1b**) moieties (basis set A).[36,37] After geometry optimization, single-point electronic energy calculations with larger basis sets were performed to refine the calculated electronic energies, using LANL2DZ for Si and Sn, 6-31G(d,p) for the cyclohexyl ligands, and 6-31G(2df,pd) for the sugars, acac ligands, framework O atoms,

and H/TMS (basis set B). Transition states were verified by identifying a single imaginary frequency, and reactants and products were connected to transition states by following the intrinsic reaction coordinate. Calculations were performed in the gas phase using Gaussian 09 version A.09; Natural Bond Orbital (NBO) analysis was performed with NBO version 6.0; and analysis using Bader's Atoms-In-Molecules theory (QTAIM) was performed using Critic2.[38–41]

C.3 Results and Discussion

Catalyst Structure

To investigate the stability of the Sn-O interactions with the acac ligands, we examined several possible conformations of **1a** and **1b** (Figure C.3). Both **1a** and **1b** were most stable with both acac ligands in the cis orientation; significant energy penalties (>20 kcal-mol^{-1}) are incurred by pulling one or both ligands into the trans orientation. Several alternative conformations for **1a** were considered by deprotonating the SiOH to a ligand and forming a third Sn-O-Si bridge. When the proton was transferred to C_3 of the acac (forming a diketone) or to an acac O (forming an enol), the resulting structures were significantly less stable than the original structure, because the SiOH is not strongly acidic and the acac ligand is not a strong proton acceptor (*vide infra*). An additional configuration was 3.7 kcal-mol^{-1} less stable than the original structure. In this, the SiOH coordinates to the Sn and H-bonds to the displaced cis acac ligand. The dominant Lewis structure of the Sn site in the most stable configuration according to NBO analysis is presented in Figure C.10.

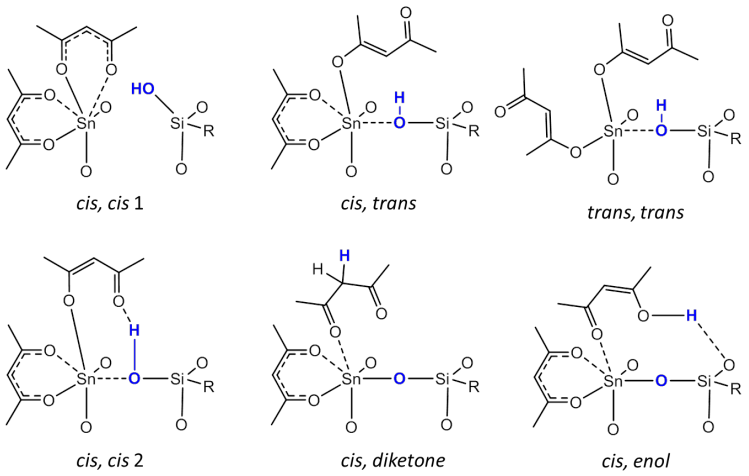

Conformation	1a	1b
cis, cis 1	0.0	0.0
cis, trans	25.2	24.7
trans, trans	54.9	49.9
cis, cis 2	8.44	N/A
cis, diketone	24.9	N/A
cis, enol	8.78	N/A

Figure C.3: Different orientations of acac ligands on Sn in **1a** and **1b**, with relative free energies at 353 K reported in kcal-mol^{-1}.

Proton Affinities

Both the 1,2-HS and 1,2-CS reactions are activated by an initial deprotonation of the substrate.[23] In addition, the Brønsted basicity of the SnOH in Lewis-acidic zeolites has been proposed as a descriptor for the 1,2-HS barrier.[26] To probe the relative strength of candidate Brønsted bases, proton affinities were calculated for several sites on the catalyst (Figure C.4). The Sn-O-Si bridge oxygens bound the proton most strongly, with proton affinities of 242 kcal-mol^{-1} for both **1a** and **1b**. In **1a**, a proton placed on the SiOH migrated to the Sn-O-Si bridge during optimization, while in **1b**, a proton placed on the SiOTMS was shared with a ligand oxygen. The proton affinities of the ligand oxygens (O_4-O_7) were considerably less favorable — ranging from 217.0 to 222.3 kcal-mol^{-1} — and in several cases, the proton migrated away from the ligand O to another O during optimization. The third carbon of each acac ligand also had weaker proton affinities (ranging from 217.7 to 229.7 kcal-mol^{-1}). We therefore rule out the acac ligands as proton acceptors in sugar deprotonation.

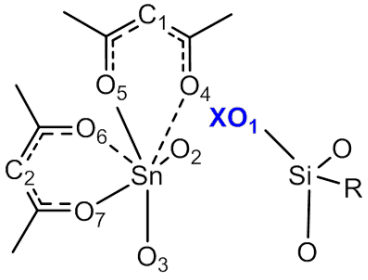

Protonation Site	1a Proton Affinity (kcal/mol)	1b Proton Affinity (kcal/mol)
$O_{1\,c}$	239.8 [a]	237.2 [c]
O_2	240.2	241.9
O_3	235.3	239.5
O_4	242.0 [a]	220.3
O_5	219.9	217.6
O_6	217.0	222.3
$O_{7\,b}$	239.0 [b]	238.4 [b]
C_1	217.7	220.5
C_2	224.7	229.7

Figure C.4: Proton affinities of candidate Brønsted bases in **1a** (X=H) and **1b** (X=Si$(CH_3)_3$). [a]Proton migrated to bridge O_2 during optimization; shared with SiOH. [b]Proton migrated to Si-O-Si bridge; shared with ligand O_7 [c]Proton on OTMS; shared with ligand O_7.

Reaction Pathways

To reduce configurational complexity, accelerate calculations, and focus on the salient features of the reaction mechanism, we approximated glucose as glyceraldehyde (GLY), the smallest aldose which allows for comparison of the 1,2-HS and 1,2-CS reactions, producing dihydroxyacetone (DHA) and GLY with opposite chirality to the reactant, respectively.

The 1,2 hydride/carbon shift reaction on a bifunctional Lewis acid/Brønsted base active site can be generalized to three possible mechanisms, depending on the binding geometry to the site.[35] The "bidentate binding" pathway, so-named for the bidentate coordination of the sugar at the transition state, involves three steps: 1) deprotonation of O_2 to the Brønsted base and binding of O_2 to the Lewis acid, 2) the H/C-shift reaction in a chelate-like transition state, and 3) reprotonation of O_1. The "O_1 binding" pathway is two steps: concerted deprotonation with the H/C-shift, followed by reprotonation. The "O_2 binding" pathway is also two steps: deprotonation of O_2 to the Brønsted base and subsequent H/C-

shift concerted with reprotonation. Only 6 pathways are needed to examine a catalyst with a single Lewis-acid/Brønsted base site, the methyl-tin silsesquioxane **2a**, with only the Sn-O-Si bridge moiety. While **1b** has only Sn-O-Si bridges as Brønsted bases, allowing for 6 distinct pathways, **1a** has Sn-O-Si bridges as well as a SiOH, which may facilitate proton transfers to the Sn-O-Si bridges or to the acac ligands, as has been proposed for Sn-Beta.[25,27]

Reaction Pathways on Sn-O-Si Bridges

Figure C.5 depicts the pathways on the Sn-O-Si bridges, and Table C.2 and Figures C.11-C.13 contain the energetics for these pathways on **1a** and **1b**. For a 1,2-HS reaction, the product is DHA, and R_1 and R_2 designate H and CH_2OH, respectively. For a 1,2-CS reaction, the product is GLY of opposite chirality, and R_1 and R_2 designate CH_2OH and H, respectively.

The bidentate binding pathway begins by deprotonating GLY to a Sn-O-Si bridge, binding O_2 of GLY to the Sn and forming a new silanol. At intermediate B-3, **1a** has two SiOH groups, while **1b** has this new SiOH and the original SiOTMS. Because GLY cannot coordinate both O_1 and O_2 to the Sn prior to the deprotonation, it must adopt the chelate geometry B-4 in a separate step. Likewise, the intermediate B-6 did not retain the bidentate binding mode prior to the reprotonation step. We did not identify transition states between B-3 and B-4 or B-6 and B-7, although on **1b**, optimization of the product from the B-5 transition state bypassed B-6 and converged directly to B-7. The highest free energy state in these pathways was B-5, with the H-shift being favored over the C-shift on both **1a** (TS free energies of 28.3 and 32.8 kcal-mol^{-1}, respectively) and **1b** (27.5 and 38.1 kcal-mol^{-1}).

The higher barrier for the C-shift is likely due to greater steric hindrance by the acac ligands on the transferring CH_2OH group compared to the H. Christianson *et al.*, also found the bidentate-binding C-shift TS to be less stable than that for the H-shift on Sn-Beta.[27]

The bidentate binding pathways contain configurations unique to this work in their unusually crowded 7-coordinated Sn. In Sn-Beta, both closed and open sites are tetrahedral when all water ligands have been removed, 5-coordinated with NH_3 adsorbed, and octahedral when water is adsorbed.[18] In aqueous solution, the coordination of Sn (IV) is 6, as $[Sn(OH_2)_6]^{4+}$, but higher coordination has not been observed.[42] Furthermore, while bidentate binding is possible in relatively flexible zeolite clusters, it is unfavorable in larger, less flexible clusters and periodic zeolite models in which the open site is formed by hydrolyzing a Sn-O-Si.[22,25–27] For these reasons, we were not expecting to find a favorable bidentate binding mode in **1a** and **1b**, yet it is not only possible, but most favorable for H-shift pathways. In order to accommodate the sugar oxygens at the TS, the ligand and framework oxygens are displaced, and the average Sn-O(acac) distance increases from 2.052 Å in isolated **1a** to 2.122 Å at the bidentate H-shift TS on **1a**. An octahedral Sn ideally contains O-Sn-O angles of 90°, and **1a** and **1b** have angles ranging from 84.5° between oxygens on the same ligand, and 101.2° between a framework and ligand O. However, in the bidentate H-shift TS, for example, the coordinated oxygens form a pentagonal bipyramid with O-Sn-O angles ranging from 70.7° to 76.4° in the plane of the pentagon, near the ideal value of 72°. While the bidentate H-shift is the most stable H-shift pathway, the bidentate C-shift is unfavorable due to its bulkier transition state; the steric hindrance imposed by the acac ligands results in more favorable monodentate binding for the C-shift.

The O_1-binding pathway begins by coordinating O_1 to the Sn and the O_2 hydroxyl into

an H-bond with a Sn-O-Si bridge. This either requires bringing Sn into a 7-coordinated arrangement (O_1 H/C-shift on **1a**, and O_1 H-shift on **1b**) or displacing an O of the acac ligand (O_1 C-shift on **1b**). O_2 is then deprotonated to form a silanol in a concerted reaction with the H/C-shift. The final step is reprotonation of O_1 from the newly formed silanol. On **1a**, both the H-shift and C-shift TS were considerably less stable than in the bidentate binding mode (16 and 9 kcal-mol^{-1} higher energy, respectively), but on **1b**, the O_1-binding C-shift TS was more stable than the bidentate binding TS by 10 kcal-mol^{-1}. This stabilization occurs due to reduced crowding around the Sn site and interactions between the O_3 hydroxyl and acac ligand oxygens.

The O_2-binding pathway begins as the bidentate binding pathway, by deprotonating the O_2 hydroxyl to a Sn-O-Si bridge. The aldehyde O_1 forms an H-bond with the newly-formed silanol, and in the next step, the silanol transfers its proton to O_1 in a concerted step with the H/C-shift, forming the final product. As in the O_1 binding pathways, the O_2 binding H/C-shift on **1a** and H-shift on **1b** are less stable the bidentate pathways, while the C-shift on **1b** is comparable to the bidentate C-shift, though less stable than the O_1-binding TS.

The Sn-O-Si bridge pathways comprise the possible pathways on **1b**, and we can identify an important effect of the SiOH replacement with SiOTMS. On **1a**, the bidentate H-shift is favored over the C-shift by 4.5 kcal-mol^{-1}, while on **1b**, the H-shift is even more favored, by 7.6 kcal-mol^{-1}; in this case, the bulky TMS crowds the ligands, which cannot displace as much to accommodate the bulky C-shift TS. On the other hand, the O_1-binding pathway on **1b** significantly stabilizes the C-shift, while it does not on **1a**. This brings the difference between the most favorable pathways on **1b**, the bidentate H-shift and the O_1 binding C-shift, to less than 1 kcal-mol^{-1}, within typical DFT errors.

It is helpful to highlight the unity in these mechanisms – states B-1, B-2, and B-3 are comparable to O_2-1, O_2-2, and O_2-3, while states B-7, B-8, and B-9 are comparable to O_2-3, O_2-4, and O_2-5, although specific geometries may vary.

Reaction Pathways Unique to 1a

The silanol function on **1a** enables additional reaction pathways by facilitating proton transfers during the H/C-shift steps and by permitting the cis,cis 2 configuration of **1a**, allowing participation of a ligand oxygen. We identified O_1 and O_2 binding pathways with the SiOH acting as the proton acceptor/donor, facilitating a proton transfer with either a Sn-O-Si bridge or with a ligand O, as well as a pathway in which a displaced acac ligand stabilizes the H/C-shift transition state by interacting with the transferring moiety. These pathways are shown in Figure C.6 and C.7; energetics are reported in Table C.3 and Figures C.14 and C.15.

In the O_{1sb} and O_{2sb} pathways, GLY approaches the Sn site on the same side as the SiOH, and the SiOH participates by shuttling a proton to a Sn-O-Si bridge. In the O_{1sb} pathways, the SiOH donates an H-bond across a face of the silicate cube to an opposite Sn-O-Si bridge, and when the GLY undergoes a concerted H-shift and deprotonation, the SiOH acts as a proton "wire," receiving the O_2 hydroxyl proton and passing its own proton to the Sn-O-Si bridge. In the O_{2sb} pathways, GLY deprotonates to a Sn-O-Si bridge and binds to the Sn as in the O_2 pathways, but the subsequent concerted H-shift/reprotonation uses the SiOH to shuttle the proton to O_1. TS energies for all of these pathways were unfavorable, being over 10 kcal-mol^{-1} greater than H/C-shift TS energies for the bidentate binding mode on **1a**.

Two variations on these pathways were also explored. In these pathways, catalyst **1a**

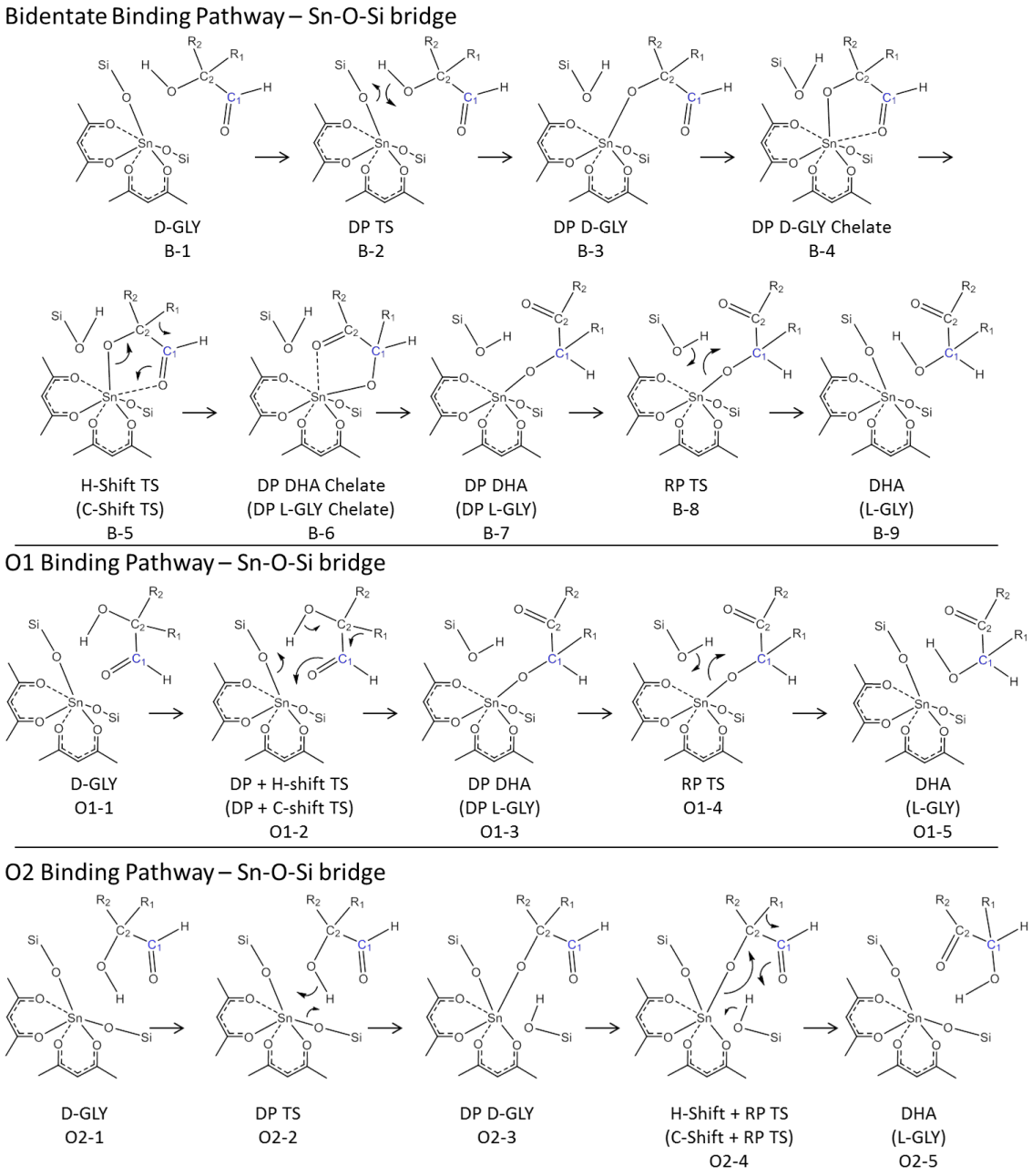

Figure C.5: Reaction pathways for H/C-shift on Sn-O-Si bridge in **1a** and **1b**. GLY = glyceraldehyde, DHA = dihydroxyacetone, DP = deprotonation, RP = reprotonation. When R_1 = H, R_2 = CH_2OH, the rate-determining step contains a H-shift, and the product is DHA. When R_1 = CH_2OH, R_2 = H, the rate-determining step contains a C-shift, and the product is glyceraldehyde of opposite chirality to the reactant.

first rearranges to the cis,cis 2 configuration (see Figure C.3). When the sugar binds, the displaced acac ligand O interacts with the O_3 hydroxyl of GLY, and HC_2, which will undergo

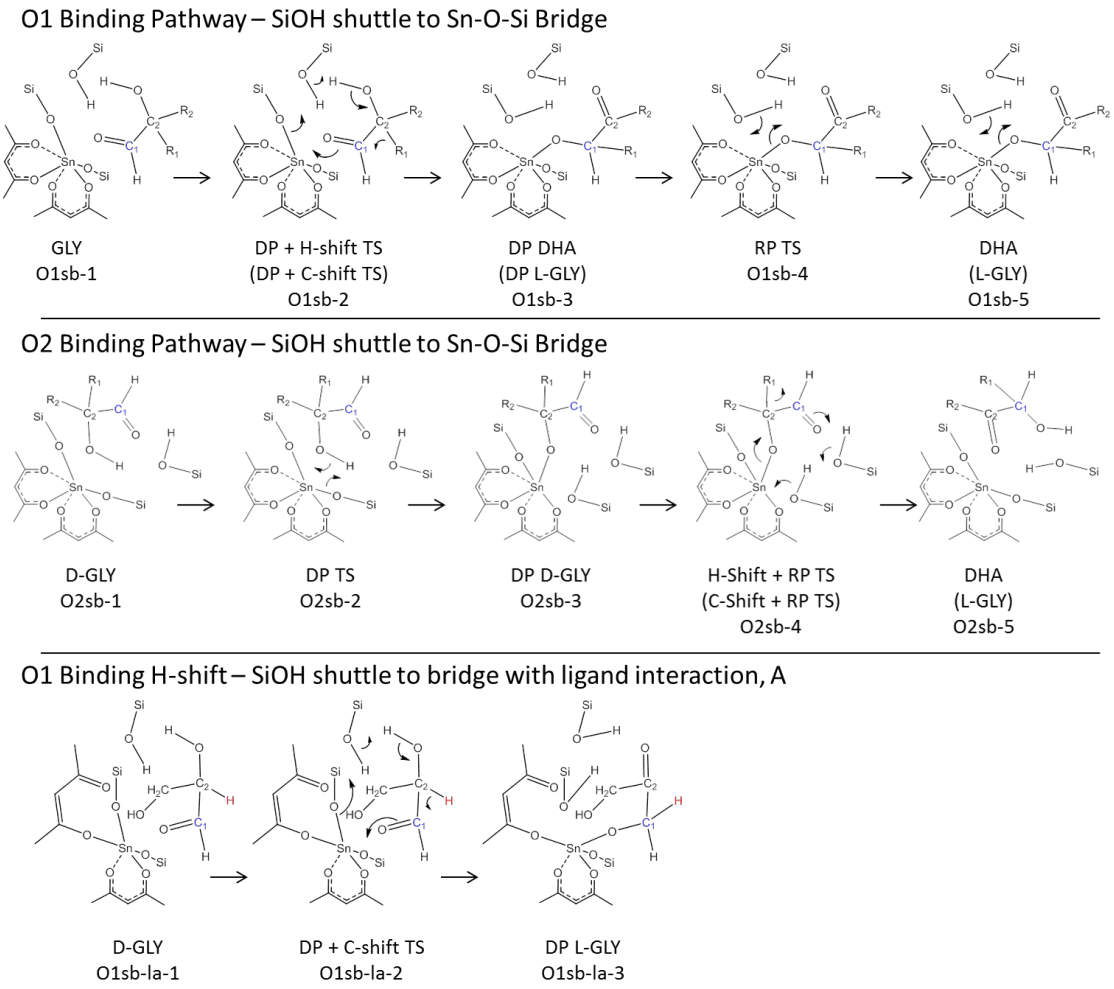

Figure C.6: Pathways unique to **1a**, invoking the SiOH in proton transfer to a Sn-O-Si bridge. GLY = glyceraldehyde, DHA = dihydroxyacetone, DP = deprotonation, RP = reprotonation. When R_1 = H, R_2 = CH_2OH, the rate-determining step contains a H-shift, and the product is DHA. When R_1 = CH_2OH, R_2 = H, the rate-determining step contains a C-shift, and the product is glyceraldehyde of opposite chirality to the reactant.

the H-shift, is either far from (O_{1sb-la}) or near to (O_{1sb-lb}) the acac O. The H-shift proceeds in a concerted reaction with the SiOH shuttling a proton from O_2 to the Sn-O-Si bridge, but the ligand interaction reduces the barrier. In O_{1sb-la}, the ligand oxygen is H-bonded to O_3 at the TS, bringing the TS free energy to 38.8 kcal-mol^{-1}, and in O_{1sb-lb}, the ligand oxygen is coordinated to the transferring H atom, reducing the transition state free energy to 32.7 kcal-mol^{-1}. Having a ligand O stabilizing the transferring H does reduce the barrier,

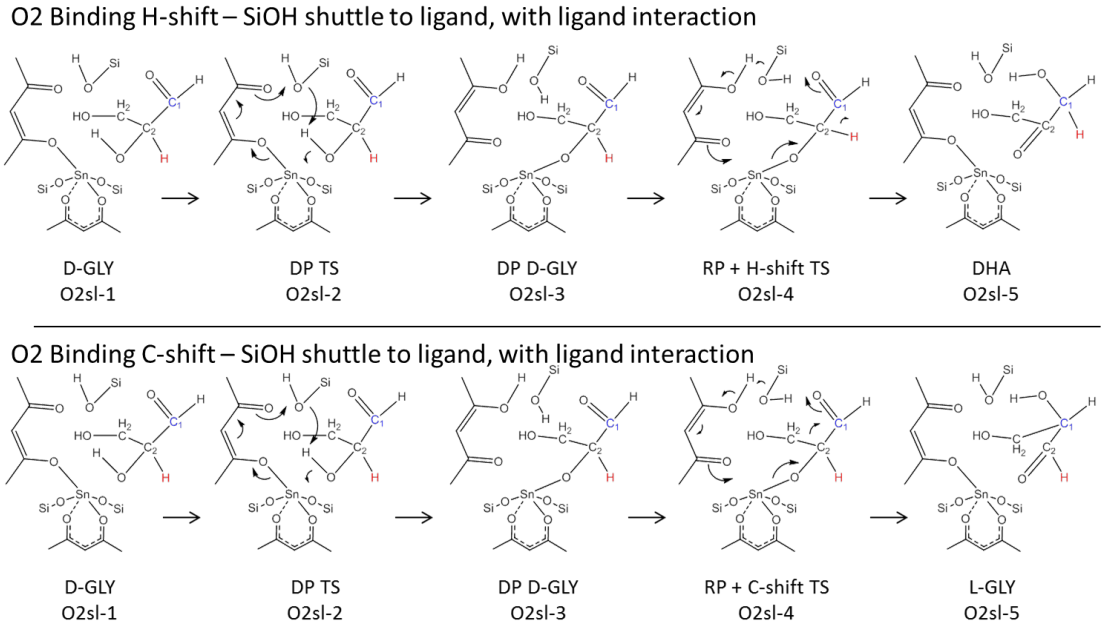

Figure C.7: Pathways unique to **1a**, continued, invoking the SiOH in proton transfer to an acac ligand O. GLY = glyceraldehyde, DHA = dihydroxyacetone, DP = deprotonation, RP = reprotonation.

but the bidentate pathway, with a TS energy of 28.3 kcal-mol^{-1}) remains favored by 4.4 kcal-mol^{-1}.

We also identified pathways involving the SiOH shuttling a proton to an acac ligand oxygen. These also begin with the catalyst in the cis,cis 2 configuration, except when the sugar binds, the displaced acac ligand oxygen retains its H-bond with the SiOH. In these pathways, the sugar undergoes an O_1-binding pathway, a concerted C-shift with deprotonation to the SiOH, which passes its proton to the ligand O, forming an enol. Reversing this proton shuttle back to the O_1 oxygen completes the cycle to produce the product sugar. In both the H- and C-shift reactions, the O_3 hydroxyl is interacting with the ligand acac (or enol at O_{2sl-3}), which dramatically reduces the C-shift TS free energy to 28.2 kcal/mol. This is the most favorable C-shift pathway on **1a**, which is comparable in

energy to the H-shift, although varying significantly in structure.

Overall, the most favorable H-shift TS for both **1a** and **1b** is the bidentate binding mode, with transition state free energies of 28.3 and 27.5 kcal-mol^{-1}, respectively. Figure C.9 shows images of these geometries. We find that, while the SiOH permits numerous additional pathways on **1a**, none of these are more energetically favorable than the bidentate binding mode, which both **1a** and **1b** can accommodate. Likewise, the most favorable C-shift TS for both **1a** and **1b** have remarkably similar free energies, 28.2 and 28.3 kcal-mol^{-1}, respectively, even though **1a** involves a concerted proton shuttle from O_2 to SiOH to an acac ligand, while **1b** involves a concerted proton transfer to a Sn-O-Si bridge. The common feature in both of these pathways is a strong interaction between acac ligand oxygen(s) and the O_3 hydroxyl at the transition state. Despite the structural diversity among these reaction pathways, the transition state energies are indistinguishable, within typical DFT errors. These maximum transition state free energy results for all pathways are summarized in Figure C.8.

One common feature among the most favorable C-shift reactions is an H-bonding interaction between the C_3 hydroxyl and an oxygen atom of the catalyst. To examine this more closely, we analyzed several H/C-shift transition states using Bader's Atoms In Molecules (QTAIM) theory.[40] Table C.4 in the Supporting Information provides key information about the (3, -1) bond critical points (BCPs) involved in the H/C-shift elementary steps.

The key interaction identified in the Bader analysis for the C-shift is the contraction of the C_3-O_3 bond at the transition state, which is accompanied by an increase in electron density and charge concentration as the single bond takes on more double-bond character. The lowest-barrier C-shift TS exhibits the most dramatic contraction of the C_3-O_3 bond,

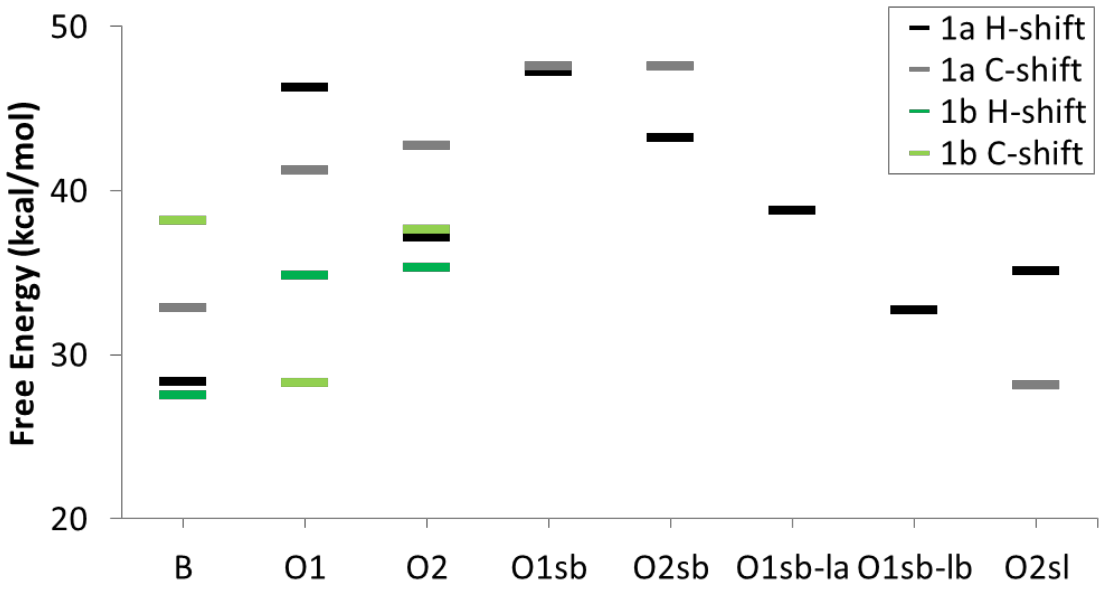

Figure C.8: Maximum transition state free energy of all reaction pathways. Free energies calculated at 353 K, with electronic energies calculated using basis set B (see computational methods) and zero-point corrections and entropic contributions calculated using basis set A. Full reaction profiles are reported in Tables C.2 and C.3 and in Figures C.11-C.15 in the Supporting Information. Free and transition state energies calculated using basis set A are also reported in Tables C.5 and C.6 and Figure C.16

from 1.403 Å in gas phase to 1.333 Å at the O_{2sl-4} C-shift TS, while the highest-barrier C-shift exhibits less contraction, with a C_3-O_3 bond length of 1.361 Å at the C-shift TS. This contraction is accompanied by an increase in charge density ρ, an increase in local charge concentration (marked by a sign change in $\nabla 2(\rho)$), and an increase in bond ellipticity — all signatures of increased double-bond character. This is facilitated by H-bond interactions between the O_3 hydroxyl and SiOH, SiOSi, or ligand O in the catalyst, depending on the pathway. In the most favorable C-shift on both **1a** and **1b**, the O_3 hydroxyl is interacting with two ligand oxygens, which stabilize a weakened O_3-H bond and a strengthened C_3-O_3 bond. The activity for both of these catalysts for the C-shift pathway is therefore a consequence of the acac ligands.

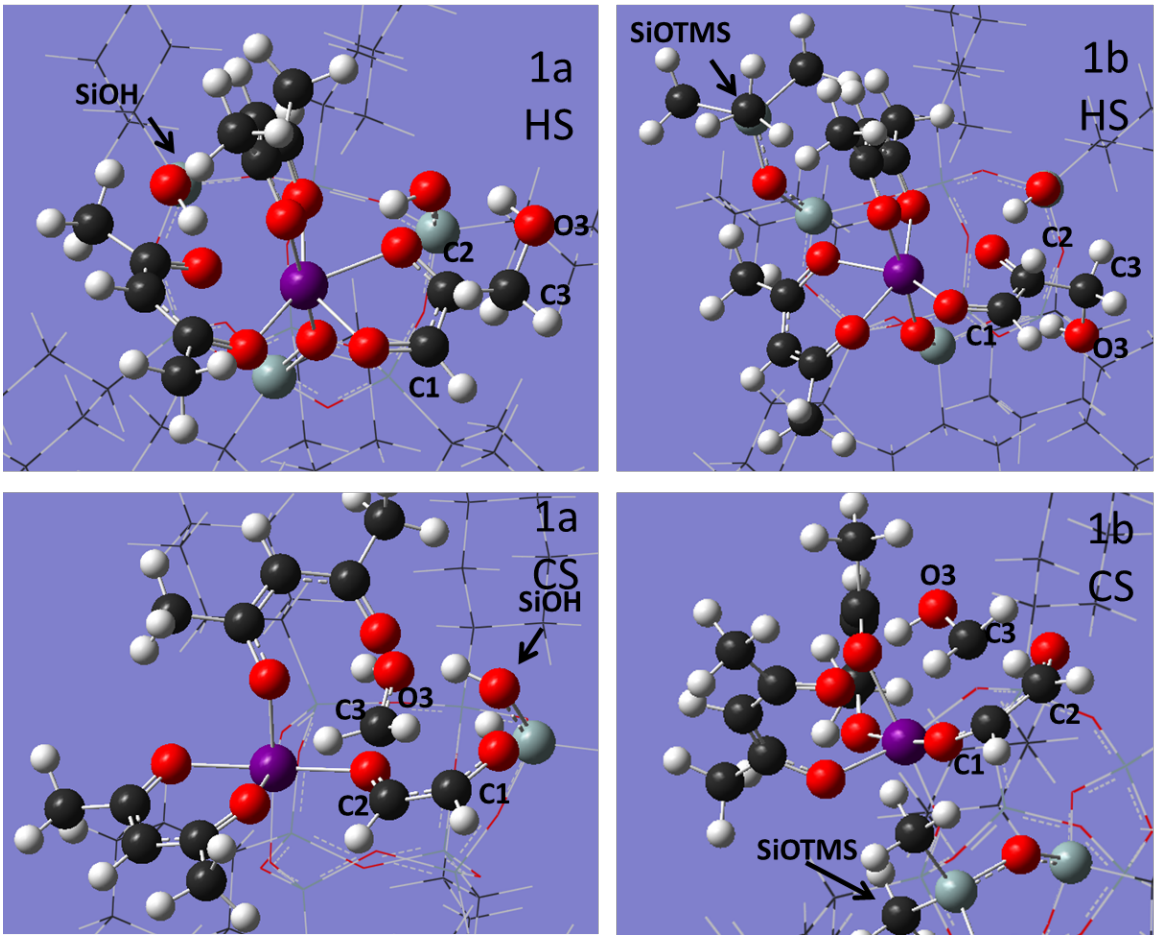

Figure C.9: Lowest-barrier transition state geometries for the H/C-shift reaction on 1a and 1b. The sugar, acac ligands, Sn-O-Si bridge atoms, and SiOH/SiOTMS are shown as ball and stick to clarify the active site geometry and to highlight the sugar/catalyst interactions. Coordinates may be found in the Supporting Information as OH_H_B-5, OH_C_O_{2sl-4}, TMS_H_B-5, and TMS_C_O_{1-2}.

According to the Energy Span Model and the Curtin-Hammett Principle, the selectivity of a simple reaction network with measured turn-over frequencies (TOF) to two products can be expressed as

$$S = \frac{TOF_A}{TOF_B} \approx e^{\Delta G_{TS}} = e^{\frac{G_{TS,B} - G_{TS,A}}{RT}} \tag{C.1}$$

where ΔGTS is the difference in Gibbs free energy of the selectivity-determining TS for products A and B.[43,44] From the experimental data at 353 K, with **1a**, $G_{TS,MAN} - G_{TS,FRU}$

= 0.22 kcal-mol^{-1}, while with **1b**, $G_{TS,MAN} - G_{TS,FRU}$ = -0.73 kcal-mol^{-1} (see Table C.1). Both of these free energy differences are less than typical DFT error of 2 kcal-mol^{-1}.

Table C.1: Experimental initial rate data on **1a** and **1b** from Brand *et al*. and the Gibbs free energy differences between the TOF-determining transition states for fructose and mannose formation assuming constant pre-exponential terms.[34,35]

	1a	**1b**
Fructose TOF (mol/(s-L-mol Sn))	0.756	0.134
Mannose TOF (mol/(s-L-mol Sn))	0.549	0.380
TOF_{Fru}/TOF_{Man}	1.38	0.353
ΔG_{TS}	0.320	-1.04
$G_{TS,Man}$-$G_{TS,Fru}$ at 353 K (kcal/mol)	0.224	-0.731

Although our DFT calculations do not (and could not, with an error of 2 kcal-mol^{-1}) characterize the effect of the TMS substitution, they are consistent with experiment in identifying H-shift and C-shift pathways of comparable barriers on each catalyst. Nevertheless, within this level of accuracy, we can rule out the hypothesis that SiOH participation in the rate-determining step is critical for fructose selectivity, because H-shift pathways involving SiOH participation (O_{1sb}, O_{2sb}, O_{1sb-la}, O_{1sb-l}, and O_{2sl}) consistently gave higher barriers than the bidentate H-shift pathway (4.4 kcal-mol^{-1} higher for O_{1sb}-lb and > 6.9 kcal-mol^{-1} higher for the others). We also identify the importance of ligand O interactions with O_3 for stabilizing the C-shift transition state; pathways without this ligand interaction gave higher barriers (4.7 kcal-mol^{-1} higher for bidentate on **1a** and >9 kcal-mol^{-1} higher for the others).

1a and **1b** are therefore limited models of the open sites of Sn-Beta and Na-Sn-Beta, in particular due to the presence of the acac ligands, which stabilizes the C-shift transition state whether or not a SiOH is present. Sn-Beta is so selective to H-shift reactions that mannose from C-shift is undetected; mannose is instead produced *via* a double H-shift. Consequently, the activation of the C-shift pathway by Na-Sn-Beta is a dramatic change.

Because **1a** is already active for the C-shift, the shift in selectivity to mannose with the TMS substitution is more incremental. We have identified why this is the case: the acac ligands can stabilize the C-shift transition so that it has comparable barriers to the H-shift on both **1a** and **1b**.

C.4 Conclusions

Several pathways were investigated for H-shift and C-shift pathways on the tin-silsesquioxanes **1a** and **1b**. The H-shift proceeds through a bidentate binding pathway on both **1a** and **1b**, and the C-shift proceeds through concerted pathways that invoke the acac ligand. The most favorable H/C-shift pathways on **1a** and **1b** have comparable barriers, consistent with both fructose (from H-shift) and mannose (from C-shift) produced in significant quantities on both catalysts. Although the experimentally observed shift in selectivity is too subtle to capture the effect of TMS substitution within the DFT framework, we demonstrate that SiOH need not participate in the TOF-determining transition state, and that the acac ligands are responsible for activating the C-shift pathways on **1a** and **1b**.

C.5 Acknowledgments

Research was supported as part of the Catalysis Center for Energy Innovation, an Energy Frontier Research Center funded by the U.S. Department of Energy (DOE), Office of Science, Basic Energy Sciences (BES), under Award number DE-SC0001004. This research used resources of the National Energy Research Scientific Computing Center, a DOE Office of Science User Facility supported by the Office of Science of the U.S. Department of Energy under Contract No. DE-AC02-05CH11231. T.R.J. wishes to acknowledge funding

from the National Science Foundation Graduate Research Fellowship Program under Grant No. 0750966, as well as the George W. Laird Merit Fellowship. S.K.B. wishes to acknowledge funding from the National Science Foundation Graduate Research Fellowship Program under Grant No. DGE-1144469. Any opinions, findings, and conclusions or recommendations expressed in this material are those of the author(s) and do not necessarily reflect the views of the National Science Foundation. The authors would like to thank Professor Mark E. Davis and Dr. Jeff Christianson for numerous useful conversations.

C.6 References

(1) Werpy, T.; Petersen, G. Top Value Added Chemicals from Biomass. *U.S. Department of Energy* **2004**, *1*, 76, DOI: 10.2172/926125.

(2) Ragauskas, A. J.; Williams, C. K.; Davison, B. H.; Britovsek, G.; Cairney, J.; Eckert, C. A.; Frederick, W. J.; Hallett, J. P.; Leak, D. J.; Liotta, C. L.; Mielenz, J. R.; Murphy, R.; Templer, R.; Tschaplinski, T. The path forward for biofuels and biomaterials. *Science (New York, N.Y.)* **2006**, *311*, 484–489.

(3) Tilman, D.; Socolow, R.; Foley, J. J. A.; Hill, J.; Larson, E.; Lynd, L.; Pacala, S.; Reilly, J.; Searchinger, T.; Somerville, C.; Williams, R. Beneficial biofuels—the food, energy, and environment trilemma. *Science* **2009**, *325*, 270–271, DOI: 10.1126/science.1177970.

(4) Perlack, R. D. R.; Stokes, B. B. J.; Eaton, L. M.; Turnhollow, A. F. U.S. Billion-Ton Update: Biomass Supply for a Bioenergy and Bioproducts Industry. *Renewable Energy* **2011**, 1–229.

(5) Bruijnincx, P. C. A.; Weckhuysen, B. M. Shale gas revolution: An opportunity for the production of biobased chemicals? *Angewandte Chemie - International Edition* **2013**, *52*, 11980–11987, DOI: 10.1002/anie.201305058.

(6) Corma, A.; Nemeth, L. T.; Renz, M.; Valencia, S. Sn-zeolite beta as a heterogeneous chemoselective catalyst for Baeyer-Villiger oxidations. *Nature* **2001**, *412*, 423–425.

(7) Corma, A.; García, H. Lewis Acids as Catalysts in Oxidation Reactions: From Homogeneous to Heterogeneous Systems. *Chemical reviews* **2002**, *102*, 3837–92.

(8) Moliner, M.; Román-Leshkov, Y.; Davis, M. E. Tin-containing zeolites are highly active catalysts for the isomerization of glucose in water. *Proceedings of the National Academy of Sciences of the United States of America* **2010**, *107*, 6164–6168.

(9) Choudhary, V.; Pinar, A. B.; Sandler, S. I.; Vlachos, D. G.; Lobo, R. F. Xylose isomerization to xylulose and its dehydration to furfural in aqueous media. *ACS Catalysis* **2011**, *1*, 1724–1728, DOI: 10.1021/cs200461t.

(10) Holm, M. S.; Saravanamurugan, S.; Taarning, E. Conversion of sugars to lactic acid derivatives using heterogeneous zeotype catalysts. *Science (New York, N.Y.)* **2010**, *328*, 602–605.

(11) Bermejo-Deval, R.; Gounder, R.; Davis, M. E. Framework and Extraframework Tin Sites in Zeolite Beta React Glucose Differently. *ACS Catalysis* **2012**, *2*, 2705–2713.

(12) Gunther, W. R.; Wang, Y.; Ji, Y.; Michaelis, V. K.; Hunt, S. T.; Griffin, R. G.; Román-Leshkov, Y. Sn-Beta zeolites with borate salts catalyse the epimerization of carbohydrates via an intramolecular carbon shift. *Nature communications* **2012**, *3*, 1109.

(13) Williams, C. L.; Chang, C.-C.; Do, P.; Nikbin, N.; Caratzoulas, S.; Vlachos, D. G.; Lobo, R. F.; Fan, W.; Dauenhauer, P. J. Cycloaddition of Biomass-Derived Furans for Catalytic Production of Renewablep-Xylene. *ACS Catalysis* **2012**, *2*, 935–939, DOI: 10.1021/cs300011a.

(14) Van Putten, R.-J.; van der Waal, J. C.; de Jong, E.; Rasrendra, C. B.; Heeres, H. J.; de Vries, J. G. Hydroxymethylfurfural, a versatile platform chemical made from renewable resources. *Chemical reviews* **2013**, *113*, 1499–597.

(15) Orazov, M.; Davis, M. E. Tandem catalysis for the production of alkyl lactates from ketohexoses at moderate temperatures. *Proceedings of the National Academy of Sciences* **2015**, *112*, 201516466.

(16) Dusselier, M.; Van Wouwe, P.; Dewaele, A.; Makshina, E.; Sels, B. F. Lactic acid as a platform chemical in the biobased economy: the role of chemocatalysis. *Energy & Environmental Science* **2013**, *6*, 1415, DOI: 10.1039/c3ee00069a.

(17) Boronat, M.; Concepción, P.; Corma, A.; Renz, M.; Valencia, S. Determination of the catalytically active oxidation Lewis acid sites in Sn-beta zeolites, and their optimisation by the combination of theoretical and experimental studies. *Journal of Catalysis* **2005**, *234*, 111–118.

(18) Bermejo-Deval, R.; Orazov, M.; Gounder, R.; Hwang, S. J.; Davis, M. E. Active sites in Sn-beta for glucose isomerization to fructose and epimerization to mannose. *ACS Catalysis* **2014**.

(19) Harris, J. W.; Cordon, M. J.; Di Iorio, J. R.; Vega-Vila, J. C.; Ribeiro, F. H.; Gounder, R. Titration and quantification of open and closed Lewis acid sites in Sn-Beta zeolites that catalyze glucose isomerization. *Journal of Catalysis* **2016**, *335*, 141–154.

(20) Hayes, M. L.; Pennings, N. J.; Serianni, A. S.; Barker, R. Epimerization of aldoses by molybdate involving a novel rearrangement of the carbon skeleton. *Journal of the American Chemical Society* **1982**, *104*, 6764–6769.

(21) Assary, R. S.; Curtiss, L. A. Theoretical study of 1,2-hydride shift associated with the isomerization of glyceraldehyde to dihydroxy acetone by Lewis acid active site models. *Journal of Physical Chemistry A* **2011**, *115*, 8754–8760.

(22) Bermejo-Deval, R.; Assary, R. S.; Nikolla, E.; Moliner, M.; Román-Leshkov, Y.; Hwang, S.-J.; Palsdottir, A.; Silverman, D.; Lobo, R. F.; Curtiss, L. A.; Davis, M. E. Metalloenzyme-like catalyzed isomerizations of sugars by Lewis acid zeolites. *Proceedings of the National Academy of Sciences of the United States of America* **2012**, *109*, 9727–32.

(23) Choudhary, V.; Caratzoulas, S.; Vlachos, D. G. Insights into the isomerization of xylose to xylulose and lyxose by a Lewis acid catalyst. *Carbohydrate Research* **2013**, *368*, 89–95.

(24) Yang, G.; Pidko, E. A.; Hensen, E. J. M. The mechanism of glucose isomerization to fructose over Sn-BEA zeolite: A periodic density functional theory study. *ChemSusChem* **2013**, *6*, 1688–1696.

(25) Rai, N.; Caratzoulas, S.; Vlachos, D. G. Role of Silanol Group in Sn-Beta Zeolite for Glucose Isomerization and Epimerization Reactions. *ACS Catalysis* **2013**, *3*, 2294–2298.

(26) Li, Y.-P.; Head-Gordon, M.; Bell, A. T. Analysis of the Reaction Mechanism and Catalytic Activity of Metal-Substituted Beta Zeolite for the Isomerization of Glucose to Fructose. *ACS Catalysis* **2014**, *4*, 1537–1545.

(27) Christianson, J. R.; Caratzoulas, S.; Vlachos, D. G. Computational Insight into the Effect of Sn-Beta Na Exchange and Solvent on Glucose Isomerization and Epimerization. *ACS Catalysis* **2015**, *1*.

(28) Shetty, S.; Pal, S.; Kanhere, D. G.; Goursot, A. Structural, electronic, and bonding properties of zeolite Sn-beta: A periodic density functional theory study. *Chemistry - A European Journal* **2005**, *12*, 518–523, DOI: 10.1002/chem.200500487.

(29) Boronat, M.; Concepción, P.; Corma, A.; Navarro, M. T.; Renz, M.; Valencia, S. Reactivity in the confined spaces of zeolites: the interplay between spectroscopy and theory to develop structure-activity relationships for catalysis. *Physical chemistry chemical physics : PCCP* **2009**, *11*, 2876–2884.

(30) Bare, S. R.; Kelly, S. D.; Sinkler, W.; Low, J. J.; Valencia, S.; Corma, A.; Nemeth, L. T.; Modica, F. S.; Valencia, S.; Corma, A.; Nemeth, L. T. Uniform catalytic site in Sn-β-zeolite determined using X-ray absorption fine structure. *J. Am. Chem. Soc.* **2005**, *127*, 12924–12932, DOI: 10.1021/ja052543k.

(31) Quadrelli, E. A.; Basset, J. M. On silsesquioxanes' accuracy as molecular models for silica-grafted complexes in heterogeneous catalysis. *Coordination Chemistry Reviews* **2010**, *254*, 707–728.

(32) Beletskiy, E. V.; Shen, Z.; Riofski, M. V.; Hou, X.; Gallagher, J. R.; Miller, J. T.; Wu, Y.; Kung, H. H.; Kung, M. C. Tetrahedral Sn-silsesquioxane: Synthesis, characterization and catalysis. *Chemical Communications* **2014**, *50*, 15699–15701, DOI: 10.1039/c4cc07897g.

(33) Beletskiy, E. V.; Hou, X.; Shen, Z.; Gallagher, J. R.; Miller, J. T.; Wu, Y.; Li, T.; Kung, M. C.; Kung, H. H. Supported Tetrahedral Oxo-Sn Catalyst: Single Site, Two Modes of Catalysis. *Journal of the American Chemical Society* **2016**, jacs.5b13436.

(34) Brand, S. K.; Labinger, J. A.; Davis, M. E. Tin Silsesquioxanes as Models for the "Open" Site in Tin-Containing Zeolite Beta. *ChemCatChem* **2016**, *8*, 121–124.

(35) Brand, S. K.; Josephson, T. R.; Labinger, J. A.; Caratzoulas, S.; Vlachos, D. G.; Davis, M. E. Methyl-Ligated Tin Silsesquioxane Catalyzed Reactions of Glucose. *Journal of Catalysis* **2016**, Just Accepted.

(36) Zhao, Y.; Truhlar, D. G. The M06 suite of density functionals for main group thermochemistry, thermochemical kinetics, noncovalent interactions, excited states, and transition elements: Two new functionals and systematic testing of four M06-class

functionals and 12 other function. *Theoretical Chemistry Accounts* **2008**, *120*, 215–241.

(37) Wadt, W. R.; Hay, P. J. Ab initio effective core potentials for molecular calculations. Potentials for main group elements Na to Bi. *The Journal of Chemical Physics* **1985**, *82*, 284–298.

(38) Frisch, M. J. et al. Gaussian 09., Wallingford, 2009.

(39) Glendening, E. D.; Landis, C. R.; Weinhold, F. NBO 6.0: Natural bond orbital analysis program. *Journal of Computational Chemistry* **2013**, *34*, 1429–1437, DOI: 10.1002/jcc.23266.

(40) Bader, R. F. W. Atoms in Molecules: A Quantum Theory, International Series of Monographs on Chemistry 22. *Oxford University Press, Oxford Henkelman G, Arnaldsson A, Jónsson H (2006) A fast and robust algorithm for Bader decomposition of charge density. Comput Mater Sci* **1990**, *36*, 354–360.

(41) Otero-De-La-Roza, A.; Johnson, E. R.; Lua??a, V. Critic2: A program for real-space analysis of quantum chemical interactions in solids. *Computer Physics Communications* **2014**, *185*, 1007–1018, DOI: 10.1016/j.cpc.2013.10.026.

(42) Taylor, M. J.; Coddington, J. M. The constitution of aqueous tin(IV) chloride and bromide solutions and solvent extracts studied by 119Sn NMR and vibrational spectroscopy. *Polyhedron* **1992**, *11*, 1531–1544, DOI: 10.1016/S0277-5387(00)83148-4.

(43) Kozuch, S. Steady State Kinetics of Any Catalytic Network: Graph Theory, the Energy Span Model, the Analogy between Catalysis and Electrical Circuits, and the Meaning of "Mechanism". *ACS Catalysis* **2015**, *5*, 5242–5255.

(44) Curtin, D. Stereochemical Control of Organic Reaction Differences in Behavior of Diastereomers. *Rec. Chem. Prog.* **1954**, *15*, 111–128.

C.7 Supplementary Information

Lewis structures from NBO analysis of catalysts **1a** and **1b**.

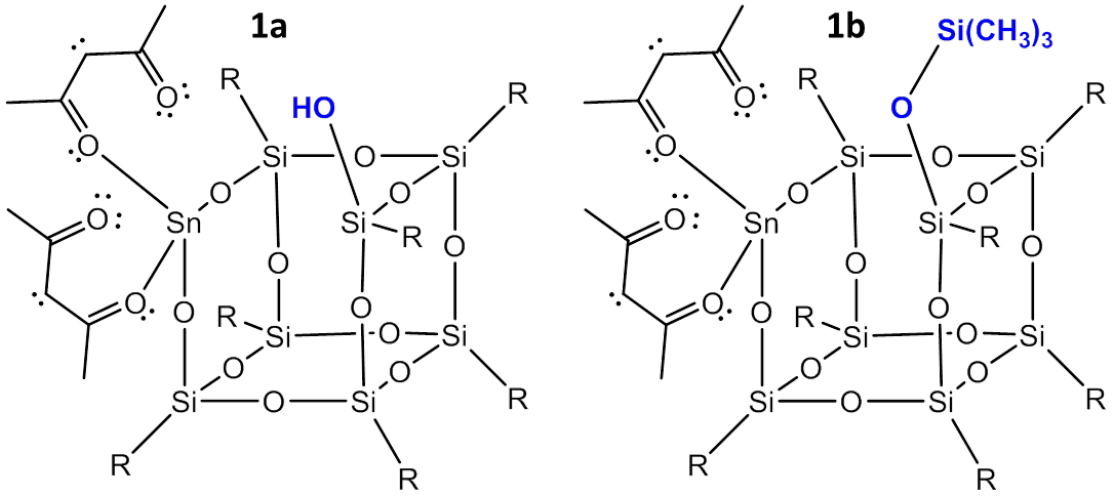

Figure C.10: The most stable resonance structures of **1a** and **1b** are characterized by four covalent Sn-O bonds. Each acac ligand has one bond to Sn, two C=O, a lone pair on C_3, and only one lone pair on the O bonded to Sn.

Table C.2: Free energies at 353 K for H-shift and C-shift reactions on Sn-O-Si bridges on **1a** and **1b**. Electronic energies were calculated using basis set B (see computational methods), and zero-point corrections and entropic contributions were calculated using basis set A. Free energies are reported with respect to isolated glyceraldehyde and catalyst.

Sn-O-Si Bridge Mechanisms		B-1	B-2 TS	B-3	B-4	B-5 TS	B-6	B-7	B-8 TS	B-9
1a	H-shift	12.48	24.47	5.57	7.51	28.30	11.18	11.85	21.55	17.99
	C-shift	12.48	24.47	5.57	12.01	32.83	9.73	18.53	26.86	22.96
1b	H-shift	2.89	25.61	2.81	4.27	27.52		-1.41	8.59	6.16
	C-shift	2.89	25.61	2.81	9.64	38.13		1.42	16.26	0.32

		O_{1-1}	O_{1-2} TS	O_{1-3}	O_{1-4} TS	O_{1-5}
1a	H-shift	19.40	46.27	7.90	21.82	3.13
	C-shift	20.45	41.19	16.93	26.86	22.96
1b	H-shift	8.45	34.79	0.27	8.59	6.16
	C-shift	13.42	28.27	13.50	20.93	9.47

		O_{2-1}	O_{2-2} TS	O_{2-3}	O_{2-4} TS	O_{2-5}
1a	H-shift	13.64	19.06	5.25	37.15	-0.55
	C-shift	13.64	19.06	7.90	42.70	20.75
1b	H-shift	9.61	13.86	0.59	35.27	9.38
	C-shift	9.61	13.86	0.76	37.58	1.82

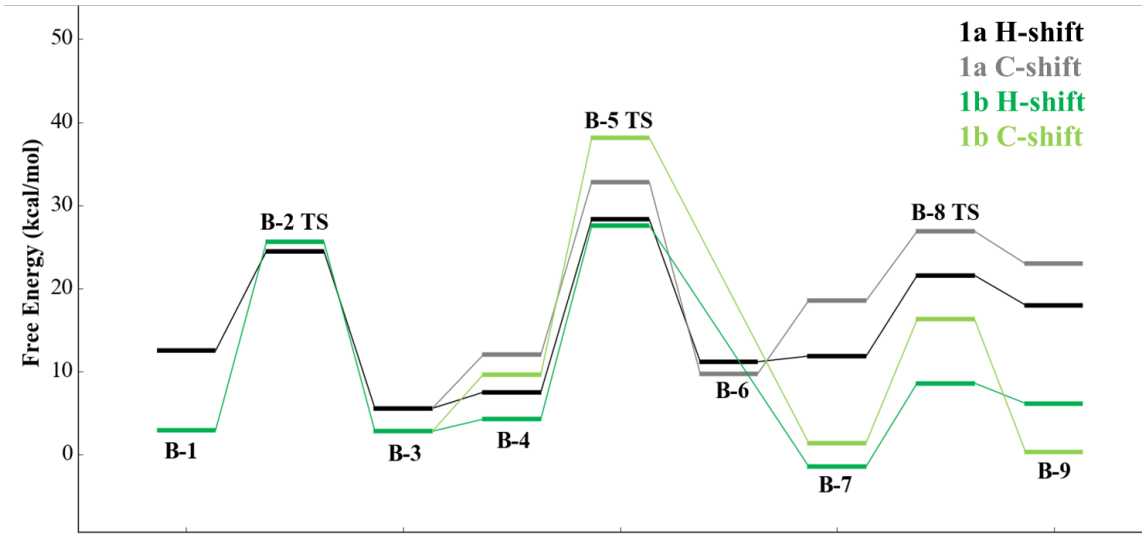

Figure C.11: Free energy profiles of H/C-shift on **1a** and **1b** through the bidentate pathway.

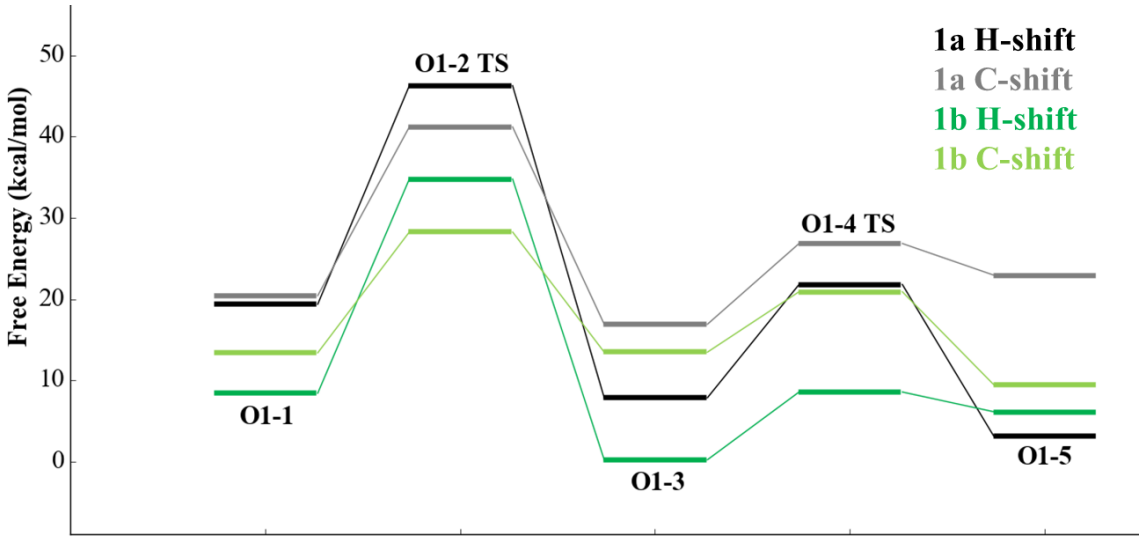

Figure C.12: Free energy profiles of H/C-shift on **1a** and **1b** through the O_1 binding pathway.

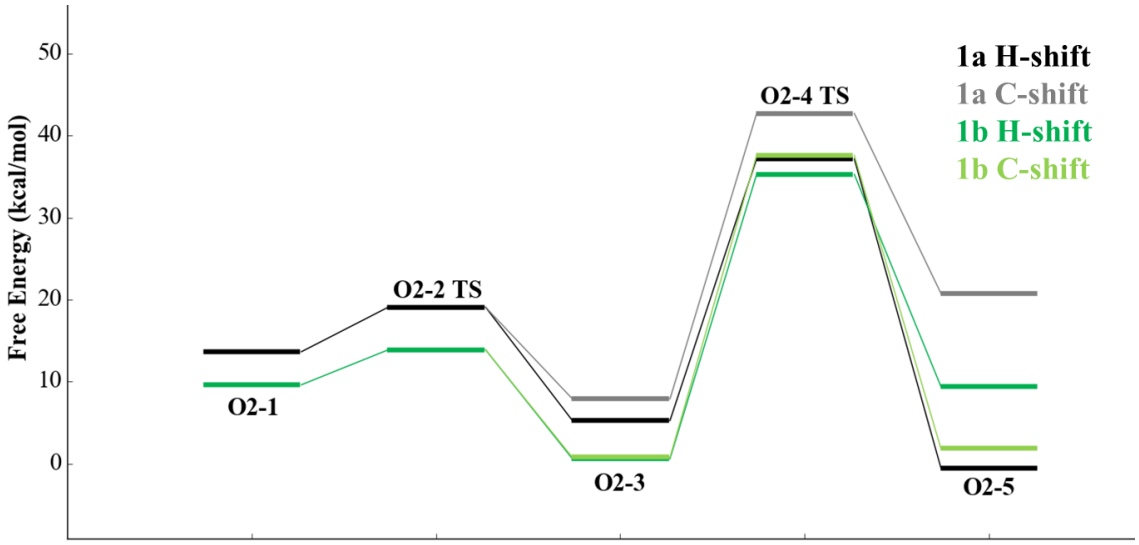

Figure C.13: Free energy profiles of H/C-shift on **1a** and **1b** through the O_2 binding pathway.

Table C.3: Free energies at 353 K for H-shift and C-shift reactions using the SiOH moiety in **1a**. Electronic energies were calculated using basis set B (see computational methods), and zero-point corrections and entropic contributions were calculated using basis set A. "sb" indicates a pathway in which the silanol transfers protons to a Sn-O-Si bridge, "la" indicates an acac ligand interacting with O_3 of the sugar, "lb" indicates an acac ligand assisting the H-shift through an interaction with the transferring H, and "sl" indicates a proton transfer between the silanol and a ligand O. Free energies are reported with respect to isolated glyceraldehyde and catalyst.

Mechanisms Unique to **1a**		O_{1sb-1}	O_{1sb-2} TS	O_{1sb-3}	O_{1sb-4} TS	O_{1sb-5}
1a	H-shift	23.00	47.20	11.85	21.55	17.99
	C-shift	14.36	47.59	18.34	18.24	10.43

		O_{2sb-1}	O_{2sb-2} TS	O_{2sb-3}	O_{2sb-4} TS	O_{2sb-5}
1a	H-shift	10.43	18.24	20.40	43.20	18.61
	C-shift	10.43	18.24	18.34	47.59	14.36

		$O_{1sb-la-1}$	$O_{1sb-la-2}$ TS	$O_{1sb-la-3}$
1a	H-shift	16.74	38.77	13.20

		$O_{1sb-lb-1}$	$O_{1sb-lb-2}$ TS	$O_{1sb-lb-3}$
1a	H-shift	16.32	32.72	16.72

		O_{2sl-1}	O_{2sl-2} TS	O_{2sl-3}	O_{2sl-4} TS	O_{2sl-5}
1a	H-shift	13.80		12.74	35.09	13.97
	C-shift	13.80		13.80	28.15	18.98

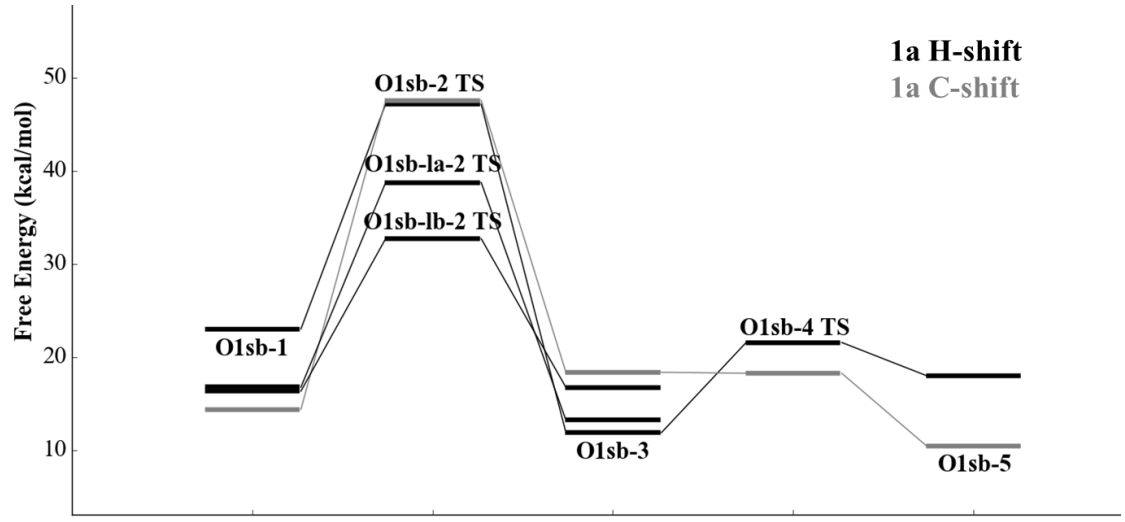

Figure C.14: Free energy profiles of H/C-shift on **1a** through the O_{1sb}, O_{1sb-la}, and O_{1sb-lb} pathways.

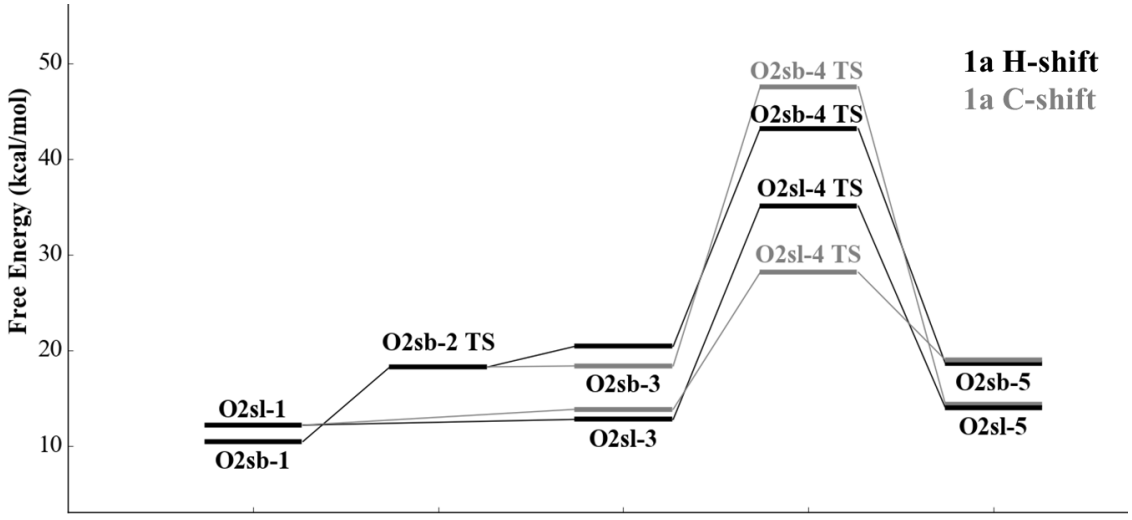

Figure C.15: Free energy profiles of H/C-shift on **1a** through the O_{2sb} and O_{2sl} pathways.

Bader Analysis of H/C-shift Transition States on 1a

During the bidentate H-shift reaction, the C_2-H bond is stretched from 1.10 to 1.36 at the transition state. The electron density ρ at the BCP decreases from 0.168 to 0.121, indicating a weakening of the bond, and the Laplacian $\nabla^2(\rho)$ changes sign, from -0.139 to

0.102, indicating a switch from a region of local charge concentration to charge depletion. The ellipticity of the C_2-H BCP increases from 3.12 x 10^{-4} to 3.74, further indicating a dramatic weakening of the bond. At the H-shift TS, the transferring H does not yet have a bond with C_1, even though the C_1-H distance is only 1.38 ; no C_1-H BCP is observed, nor is there a (3,+1) ring critical point (RCP) present in the C_1-C_2-H triangle.

Likewise, in the bidentate C-shift reaction, the C_2-C_3 bond is stretched from the reactant to the C-shift transition state, which is accompanied by a decrease in ρ (from 0.173 to 0.078), an increase in $\nabla^2(\rho)$ (from 0.072 to 0.161), and an increase in ellipticity (from 3.90 x 10^{-3} to 1.06), indicating severe weakening in the C-C bond. The BCP is between C_1 and C_3 at the TS, but there is no BCP between C_2 and C_3, nor a RCP in the C_1-C_2-C_3 triangle. The C_3-O_3 distance contracts slightly, from 1.41 to 1.36 , and this is accompanied by an increase in ρ at the BCP from 0.237 to 0.258, a sign change in $\nabla^2(\rho)$ from 0.092 to -0.026, and an increase in ellipticity from 4.89 x 10^{-3} to 1.70 x 10^{-2}, all signatures of increased π character in the C_3-O_3 bond. While the C_3-O_3 bond is strengthened, the O_3-H bond is weakened slightly, with a small decrease in ρ from 0.241 to 0.238, a small increase in $\nabla^2(\rho)$ from -0.528 to -0.484, and a slight increase in ellipticity from 4.88 x 10^{-3} to 6.20 x 10^{-3}.

The bidentate C-shift reaction has a transition state energy of 32.8 kcal-mol^{-1}, the O_{2sl} pathway has a TS energy of 28.2 kcal-mol^{-1}, and the O_{1sb} pathway has a TS energy of 47.6 kcal-mol^{-1}. The stability of each TS is correlated to the ρ, $\nabla^2(\rho)$, and ϵ of the C_3-O_3 bond, reinforcing the importance of stabilizing the C_3 moiety at the C-shift transition state.

Table C.4: Bader Analysis of Select Bond Critical Points (BCPs) for gas-phase glyceraldehyde (GLY) and various intermediate and transition states.

Gas-phase GLY	ρ	$\nabla^2(\rho)$	ϵ (ellipticity)
C_2-C_3	1.74 x 10^{-1}	6.79 x 10^{-2}	2.33 x 10^{-3}
C_2-H	1.68E x 10^{-1}	-1.39 x 10^{-1}	2.08 x 10^{-3}
C_3-O_3	2.38E x 10^{-1}	8.77 x 10^{-2}	9.09 x 10^{-3}
O_3-H	2.42E x 10^{-1}	-5.41 x 10^{-1}	5.56 x 10^{-3}
HO_3-O_1	2.57E x 10^{-2}	7.34 x 10^{-2}	6.57 x 10^{-1}

OH_H_B-4 DP GLY	ρ	$\nabla^2(\rho)$	ϵ (ellipticity)
C_2-C_3	1.73 x 10^{-1}	7.02 x 10^{-2}	3.90 x 10^{-3}
C_2-H	1.68 x 10^{-1}	-1.39 x 10^{-1}	3.19 x 10^{-4}
C_3-O_3	2.37 x 10^{-1}	9.24 x 10^{-2}	4.89 x 10^{-3}
O_3-H	2.41 x 10^{-1}	-5.28 x 10^{-2}	4.88 x 10^{-3}
HO_3-OHSi	3.46 x 10^{-2}	9.04 x 10^{-2}	1.68 x 10^{-1}

OH_H_B-5 Bidentate H-Shift TS	ρ	$\nabla^2(\rho)$	ϵ (ellipticity)
C_2-C_3	1.80 x 10^{-1}	4.84 x 10^{-2}	1.28 x 10^{-2}
C_2-H	1.21 x 10^{-1}	1.02 x 10^{-1}	3.47
C_3-O_3	2.41 x 10^{-1}	7.41 x 10^{-2}	8.45 x 10^{-3}
O_3-H	2.38 x 10^{-1}	-4.94 x 10^{-1}	5.52 x 10^{-3}
HO_3-OHSi	3.56 x 10^{-2}	9.27 x 10^{-2}	6.78 x 10^{-3}

OH_C_B-5 Bidentate C-shift TS	ρ	$\nabla^2(\rho)$	ϵ (ellipticity)
C_1-C_3	7.83 x 10^{-2}	1.61 x 10^{-1}	1.06
C_2-H	1.71 x 10^{-1}	-1.62 x 10^{-1}	7.63 x 10^{-3}
C_3-O_3	2.58 x 10^{-1}	-2.59 x 10^{-2}	1.70 x 10^{-2}
O_3-H	2.38 x 10^{-1}	-4.84 x 10^{-1}	6.20 x 10^{-3}
HO_3-OHSi	3.40 x 10^{-2}	8.88 x 10^{-2}	3.61 x 10^{-2}

OH_C_O_{2sl-4} Ligand-Assist C-Shift TS	ρ	$\nabla^2(\rho)$	ϵ (ellipticity)
C_2-C_3	8.00 x 10^{-2}	1.63 x 10^{-1}	7.94 x 10^{-1}
C_2-H	1.71 x 10^{-1}	-1.56 x 10^{-1}	1.06 x 10^{-2}
C_3-O_3	2.68 x 10^{-1}	-7.71 x 10^{-2}	1.42 x 10^{-2}
O_3-H	2.35 x 10^{-1}	-4.54 x 10^{-1}	5.54 x 10^{-3}
HO_3-ligand O_1	2.97 x 10^{-2}	8.22 x 10^{-2}	6.97 x 10^{-2}
HO_3-ligand O_2	2.80 x 10^{-2}	7.62 x 10^{-2}	6.81 x 10^{-2}

OH_C_O_{1sb-2} O_1 C-shift TS	ρ	$\nabla^2(\rho)$	ϵ (ellipticity)
C_1-C_2	2.15 x 10^{-1}	-7.01 x 10^{-2}	7.47 x 10^{-3}
C_1-C_3	8.98 x 10^{-2}	1.67 x 10^{-1}	3.44 x 10^{-1}
C_2-H	1.71 x 10^{-1}	-1.58 x 10^{-1}	8.51 x 10^{-3}
C_3-O_3	2.56 x 10^{-1}	-1.48 x 10^{-2}	1.59 x 10^{-2}
O_3-H	2.37 x 10^{-1}	-4.77 x 10^{-1}	5.11 x 10^{-3}
HO_3-O_{Ligand}	3.58 x 10^{-2}	9.45 x 10^{-2}	9.13 x 10^{-3}

Table C.5: Free energies calculated using small basis set (basis set A in computational methods) for the Sn-O-Si bridge mechanisms.

Sn-O-Si Bridge Mechanisms		B-1	B-2 TS	B-3	B-4	B-5 TS	B-6	B-7	B-8 TS	B-9
1a	H-shift	7.64	21.01	4.13	5.20	25.71	7.65	9.49	17.16	13.10
	C-shift	7.64	21.01	4.13	10.42	30.64	7.98	17.87	23.75	19.38
1b	H-shift	-1.28	20.34	2.20	1.63	25.46		-4.59	0.02	-2.63
	C-shift	-1.28	20.34	2.20	6.28	34.95		-1.47	10.96	-5.44

		O_{1-1}	O_{1-2} TS	O_{1-3}	O_{1-4} TS	O_{1-5}
1a	H-shift	13.85	41.38	3.55	15.45	-2.4355
	C-shift	16.99	38.08	14.33	23.75	19.38
1b	H-shift	0.51	26.48	-5.84	0.02	-2.63
	C-shift	8.39	24.70	8.89	15.81	3.31

		O_{2-1}	O_{2-2} TS	O_{2-3}	O_{2-4} TS	O_{2-5}
1a	H-shift	9.05	14.13	2.51	31.77	-4.50
	C-shift	9.05	14.13	5.62	36.67	15.37
1b	H-shift	1.49	6.60	-3.64	27.63	2.52
	C-shift	1.49	6.60	-3.74	30.88	-5.70

Table C.6: Free energies calculated using small basis set (basis set A in computational methods) for the mechanisms unique to **1a**.

Mechanisms Unique to **1a**		O_{1sb-1}	O_{1sb-2} TS	O_{1sb-3}	O_{1sb-4} TS	O_{1sb-5}
1a	H-shift	16.50	41.97	9.49	17.16	13.10
	C-shift	12.31	43.20	14.44	15.38	8.24

		O_{2sb-1}	O_{2sb-2} TS	O_{2sb-3}	O_{2sb-4} TS	O_{2sb-5}
1a	H-shift	8.24	15.38	14.33	37.51	12.49
	C-shift	8.24	15.38	14.44	43.20	12.31

		$O_{1sb-la-1}$	$O_{1sb-la-2}$ TS	$O_{1sb-la-3}$
1a	H-shift	14.84	37.61	11.40

		$O_{1sb-lb-1}$	$O_{1sb-lb-2}$ TS	$O_{1sb-lb-3}$
1a	H-shift	14.79	32.12	14.91

		O_{2sl-1}	O_{2sl-2} TS	O_{2sl-3}	O_{2sl-4} TS	O_{2sl-5}
1a	H-shift	10.29	9.69	33.82	12.39	
	C-shift	10.29	11.46	28.65	18.22	

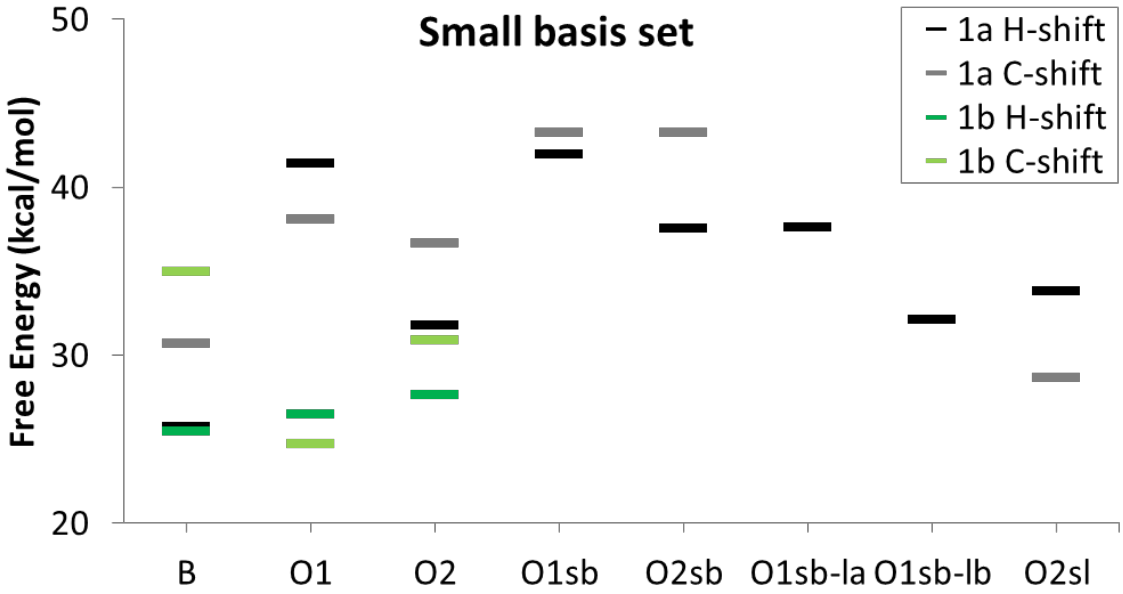

Figure C.16: Maximum TS free energy of all reaction pathways. Free energies calculated at 353 K, with electronic energies calculated using basis set A (see computational methods) and zero-point corrections and entropic contributions calculated using basis set A.

Appendix D

SUPPLEMENTARY INFORMATION FOR CHAPTER 6

Table D.1: Summary of STW syntheses using racemic **2**. A = amorphous, U = unknown, synthesis time is reported in days. [1]A mixture of **2** and pentamethylimidazolium (P) in a ratio of **2**/P = 9 was used as the OSDA. [2]**2**/P = 4, [3]**2**/P = 2.3.

Si/Ge	Si/Al	H_2O/TO_2	Temp. (°C)	Seeds	Time	Results
2	∞	5	175	None	6	STW + dense
9	∞	5	175	None	16	STW + U
∞	∞	5	175	None	23	BEA + dense
2	∞	<3	175	None	4	IWV
9	∞	<3	175	None	4	IWV
∞	∞	<3	175	None	20	Si-RTH layered
2	∞	4	175	None	4	IWV + STW
2	∞	5	175	None	4	IWV + STW
2	∞	7	175	None	4	IWV + STW
10	∞	4	175	None	4	IWV + CIT-7
10	∞	5	175	None	4	IWV
10	∞	7	175	None	4	IWV
2	∞	5	175	Si-STW	4	STW
10	∞	5	175	Si-STW	4	IWV + STW
2	∞	5	160	Si-STW	3	STW + U
∞	∞	4	175	None	13	Si-RTH layered
∞	∞	5	175	None	13	Si-RTH layered
∞	∞	7	175	None	36	Dense
10	∞	5	160	Si-STW	8	STW
∞	∞	5	160	Si-STW	11	Si-RTH layered
∞	∞	5	175	Si-STW	11	Si-RTH layered
10	∞	5	160	Si-STW	23	STW
15	∞	5	160	Si-STW	16	STW
20	∞	5	160	Si-STW	16	MTW
20	∞	5	160	Si-STW	16	MTW
10	∞	5	160	Si-STW	13	STW + IWV
15	∞	5	160	Si-STW	13	STW + IWV
20	∞	5	160	Si-STW	7	STW
20	∞	5	160	Si-STW	18	STW + IWV
20	∞	5	160	Si-STW	18	STW + IWV
30	∞	5	160	Si-STW	7	IWV
30	∞	5	160	Si-STW	7	IWV
50	∞	5	160	Si-STW	18	STW + IWV
50	∞	5	160	Si-STW	18	IWV
10	∞	4	160	Si-STW	20	STW
10	∞	7	160	Si-STW	5	IWV + STW
10	∞	7	160	Si-STW	5	IWV + STW
20	∞	4	160	Si-STW	20	STW
20	∞	7	160	Si-STW	5	IWV + STW

Si/Ge	Si/Al	H_2O/TO_2	Temp. (°C)	Seeds	Time	Results
20	∞	10	160	Si-STW	5	IWV
30	∞	4	160	Si-STW	20	STW + A
30	∞	7	160	Si-STW	12	IWV
30	∞	10	160	Si-STW	20	IWV
∞	∞	4	160	Si-STW	37	STW + layered[1]
∞	∞	4	160	Si-STW	37	STW[2]
∞	∞	4	160	Si-STW	20	STW[3]
∞	∞	2	160	None	14	MTW + STW
∞	∞	2	160	None	14	MTW + STW
∞	∞	3	160	None	14	MTW + STW
∞	∞	3	160	None	19	MTW + STW
4	∞	5	160	None	7	LTA
8	∞	5	160	None	7	LTA
20	∞	5	160	Si-STW	7	LTA + U
100	∞	5	160	Si-STW	30	A
20	∞	5	160	Si-STW	8	U
8	∞	4	160	Si-STW	10	U
10	∞	4	160	Si-STW	24	U
12	∞	4	160	Si-STW	10	U + A
14	∞	4	160	Si-STW	10	U + A
10	∞	4	160	Si-STW	13	IWV + LTA
2	∞	5	160	Si-STW	10	STW
2	∞	5	160	Si-STW	10	LTA + A
4	∞	5	160	Si-STW	10	LTA + U
4	∞	5	160	Si-STW	10	LTA + U
4	∞	5	160	Si-STW	13	STW + U
4	∞	5	160	Si-STW	13	STW + U
6	∞	5	160	Si-STW	13	STW + U
6	∞	5	160	Si-STW	13	STW + U
8	∞	5	160	Si-STW	29	LTA + U
8	∞	5	160	Si-STW	29	LTA + U
10	∞	5	160	Si-STW	29	LTA + U
10	∞	5	160	Si-STW	29	LTA + U
8	∞	5	160	Si-STW	11	LTA
8	∞	5	160	Si-STW	11	LTA
2	100	5	160	Si-STW	13	STW + LTA
2	100	5	160	Si-STW	13	STW
12	∞	5	160	Si-STW	11	LTA
12	∞	5	160	Si-STW	11	LTA

Table D.2: Summary of STW syntheses using *R*-**2**. A = amorphous, U = unknown, synthesis time is reported in days.

Si/Ge	Si/Al	H_2O/TO_2	Temp. (°C)	Seeds	Time	Results
20	∞	4	160	Si-STW	16	STW
20	∞	4	160	Si-STW	16	RTH
20	∞	4	160	Si-STW	16	RTH + IWV + STW
20	∞	4	160	Si-STW	16	RTH
30	∞	4	160	Si-STW	16	RTH
2	100	4	160	Si-STW	10	STW
2	100	4	160	Si-STW	10	STW + LTA
2	100	4	160	Si-STW	10	STW + LTA + U
2	100	4	160	Si-STW	10	STW + LTA

Table D.3: Summary of STW syntheses using *S*-**2**. A = amorphous, U = unknown, synthesis time is reported in days.

Si/Ge	Si/Al	H_2O/TO_2	Temp. (°C)	Seeds	Time	Results
20	∞	5	160	None	10	IWV + STW
20	∞	5	160	Si-STW	5	IWV + STW
5	∞	5	160	None	5	STW + tiny IWV
5	∞	5	175	Si-STW	5	IWV + STW
∞	∞	5	160	Si-STW	8	MTW + STW
∞	∞	5	160	None	8	MTW + STW
20	∞	4	160	Si-STW	13	STW
20	∞	4	160	Si-STW	13	STW
20	∞	4	160	Si-STW	25	A
20	∞	4	160	Si-STW	25	A
10	∞	4	160	Si-STW	24	LTA + U
10	∞	4	160	Si-STW	24	LTA + U
2	∞	5	160	Si-STW	12	STW + LTA
2	∞	5	160	Si-STW	12	STW + LTA
2	∞	5	160	Si-STW	12	STW
2	∞	5	160	None	12	STW + LTA
2	∞	5	160	None	12	LTA + U
2	100	5	160	Si-STW	13	STW
2	100	5	160	Si-STW	12	STW
2	100	5	160	Si-STW	13	STW + LTA
2	100	5	160	Si-STW	20	STW + LTA

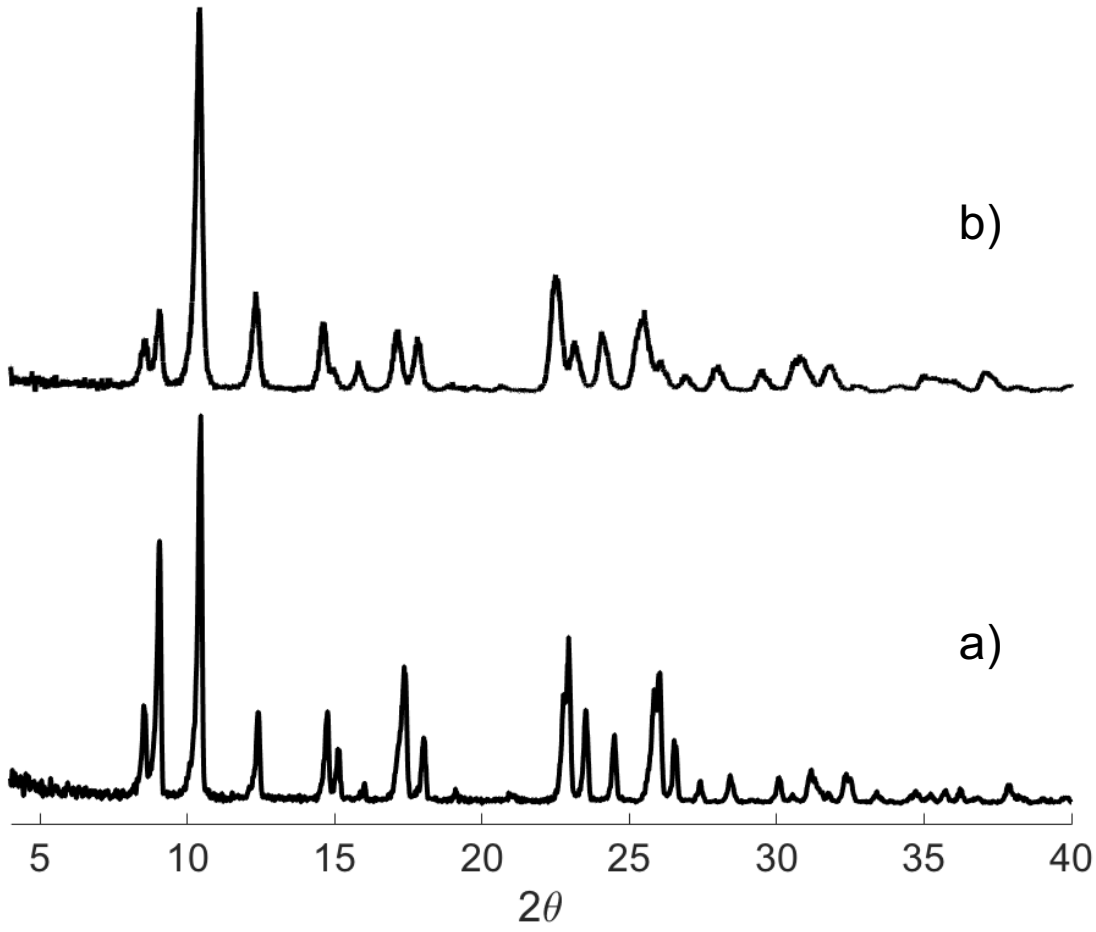

Figure D.1: Representative PXRD diffraction patterns for a) pure-silica racemic STW and b) germanosilicate enantrioenriched S-STW. The d-spacings in the enantioenriched sample are shifted as a consequence of the germanium content.

^{13}C, ^{19}F, ^{27}Al and ^{29}Si solid-state NMR were performed using a Bruker DSX-500 spectrometer (11.7 T) and a Bruker 4mm MAS probe. The spectral operating frequencies were 500.2 MHz, 125.721 MHz, 130.287 MHz and 99.325 MHz for ^{1}H, ^{13}C, ^{19}F, ^{27}Al and ^{29}Si nuclei, respectively. Spectra were referenced to external standards as follows: tetramethylsilane (TMS) for ^{1}H and ^{29}Si, $CFCl_3$ for ^{19}F, adamantane for ^{13}C as a secondary external standard relative to tetramethylsilane and 1.0 M $Al(NO_3)_3$ aqueous solution for ^{27}Al. Samples were spun at 14 kHz for ^{1}H and ^{27}Al MAS NMR and 8 kHz for ^{13}C and ^{29}Si

MAS and CPMAS NMR experiments. ^{19}F MAS NMR were collected at both 13 and 15 kHz to assign spinning sidebands. For detection of ^{27}Al signal, a short 0.5s - μ/18 pulse was used before FID was recorded in order to make quantitative comparison among resonances.

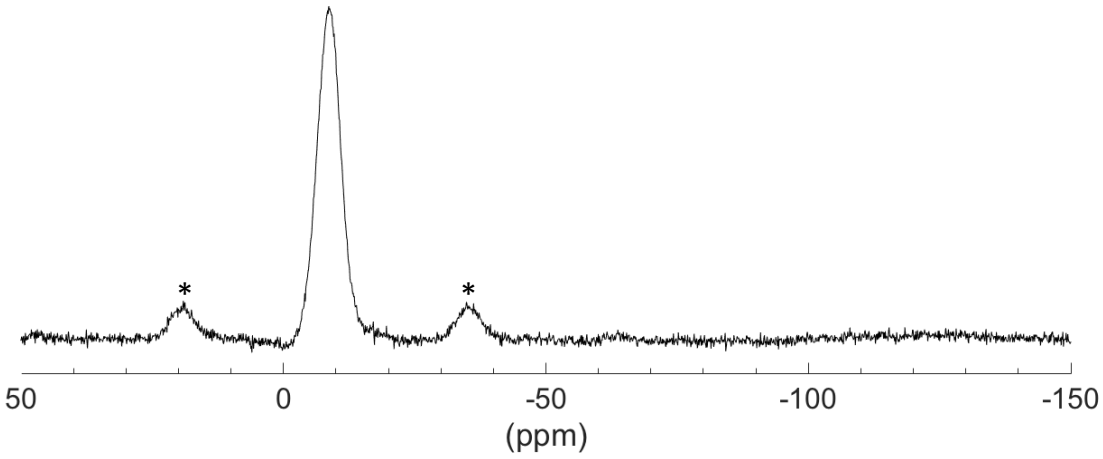

Figure D.2: ^{19}F NMR spectrum for an enantioenriched *S*-STW germanosilicate sample. Peaks labeled with a * correspond to spinning side bands.

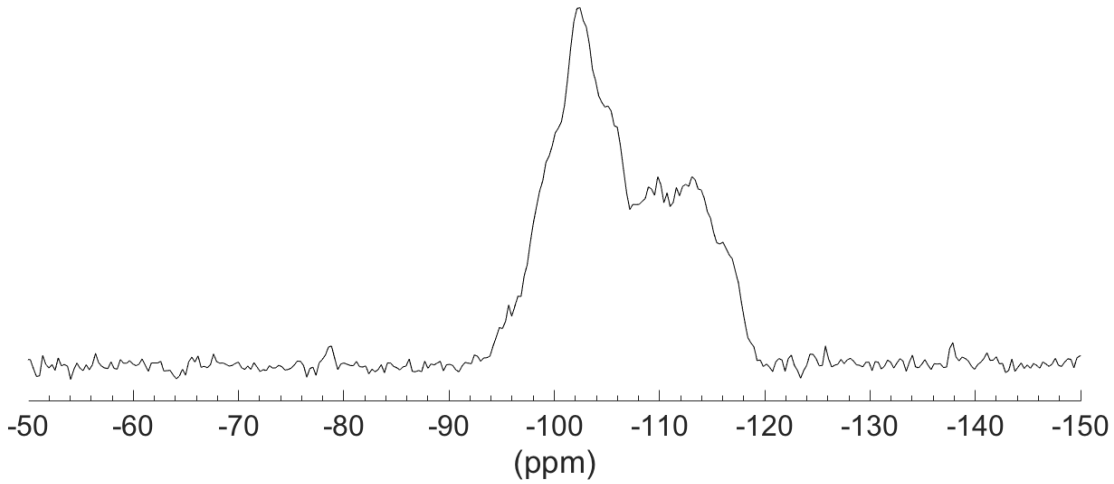

Figure D.3: ^{29}Si NMR spectrum for an enantioenriched *S*-STW germanosilicate sample.

Thermogravimetric analysis (TGA) measurements were performed on Perkin Elmer STA 6000. Samples (0.01-0.06 g) were placed in an alumina crucible and heated at 1 K/min in a flowing stream (0.667 cm^3/s) of air.

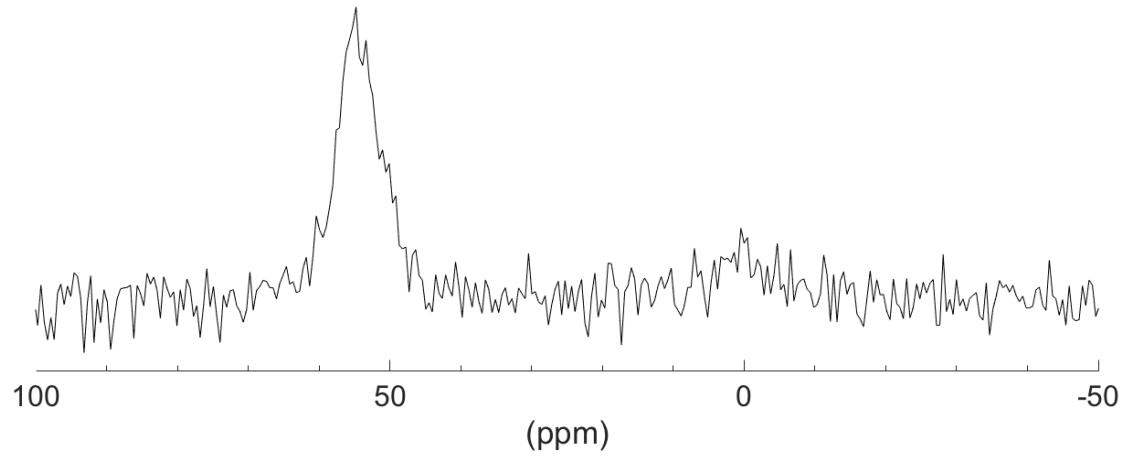

Figure D.4: ^{27}Al NMR spectrum for an enantioenriched *S*-STW aluminogermanosilicate sample.

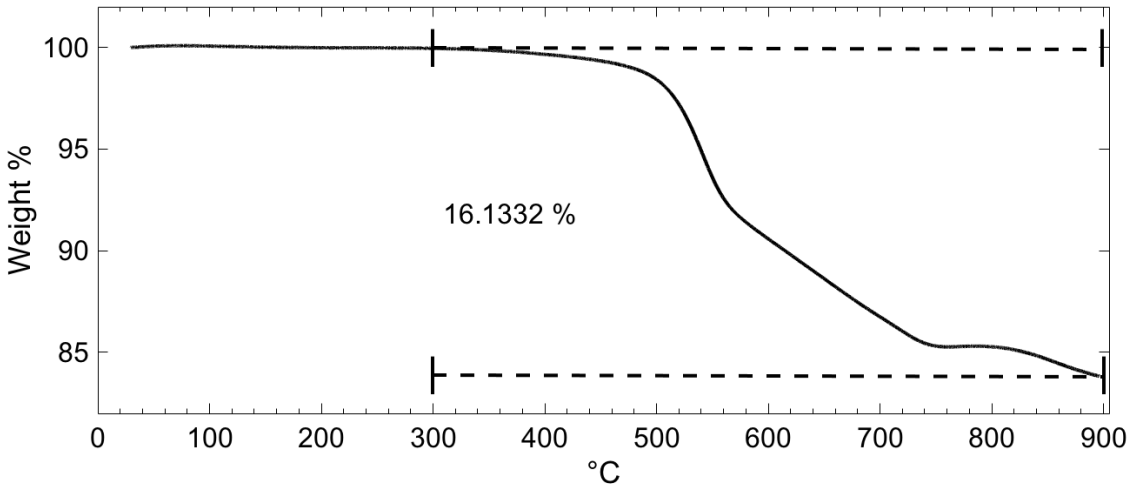

Figure D.5: A representative TGA profile for enantioenriched germanosilicate *S*-STW.

EDS spectra were acquired with an Oxford X-Max SDD X-ray Energy Dispersive Spectrometer system on a ZEISS 1550 VP FESEM, equipped with in-lens SE.

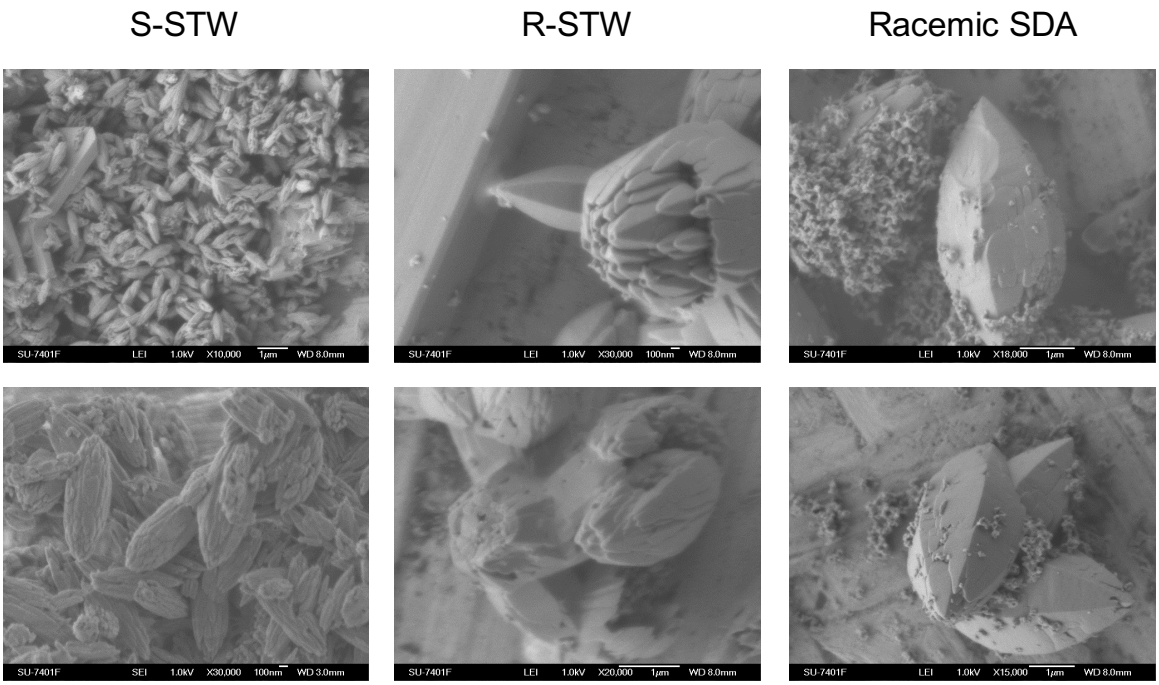

Figure D.6: Select SEM images for *S*-, *R*- and racemic STW.

Table D.4: Representative energy-dispersive X-Ray spectroscopy results for products obtained using *S*-**2** in germanosilicate and aluminogermanosilicate synthesis gels.

Starting Gel	Si/Ge	Si/Al
Germanosilicate, Si/Ge = 2	0.806 ± 0.047	-
Aluminogermanosilicate, Si/Ge = 2; Si/Al = 100	0.861 ± 0.045	30.15 ± 11.96

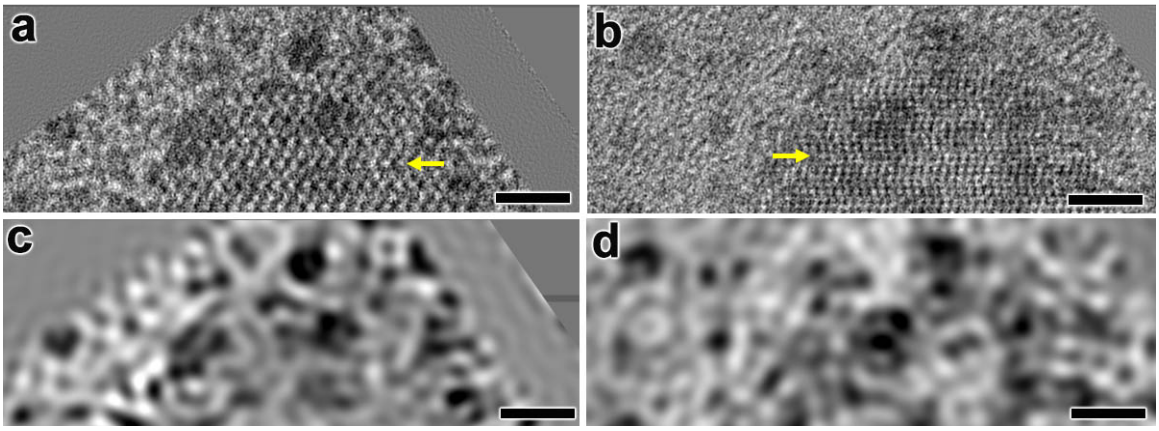

Figure D.7: Comparison of two HRTEM images with gold nanoparticles as markers. **a,b**, A crystal was tilted from $[2\bar{1}\bar{1}0]$ (**a**) to $[1\bar{1}00]$ (**b**) and a shift-up was observed, which indicates a space group of $P6_522$. **c,d**, The processed images of (**a**) and (**b**) after Fourier filtering that only includes spatial frequencies within a particular range to enhance the contrasts of gold nanoparticles.

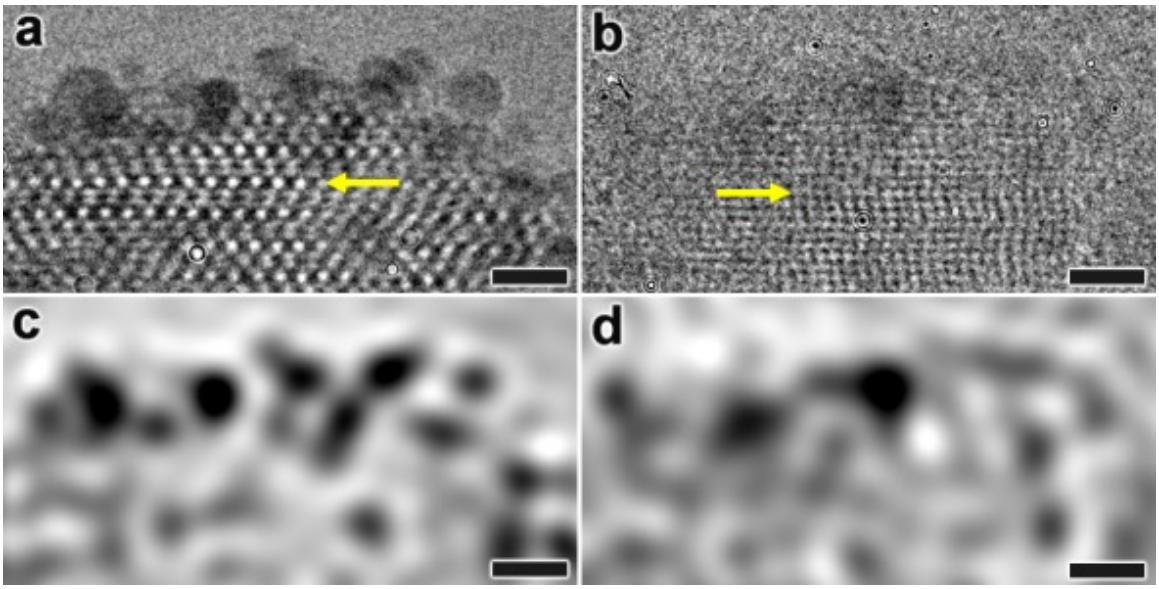

Figure D.8: Comparison of two HRTEM images with gold nanoparticles as markers. **a,b**, A crystal was tilted from $[2\bar{1}\bar{1}0]$ (**a**) to $[1\bar{1}00]$ (**b**) and a shift-down was observed, which indicates a space group of $P6_122$. **c,d**, The processed images of (**a**) and (**b**) after Fourier filtering that only includes spatial frequencies within a particular range to enhance the contrasts of gold nanoparticles.

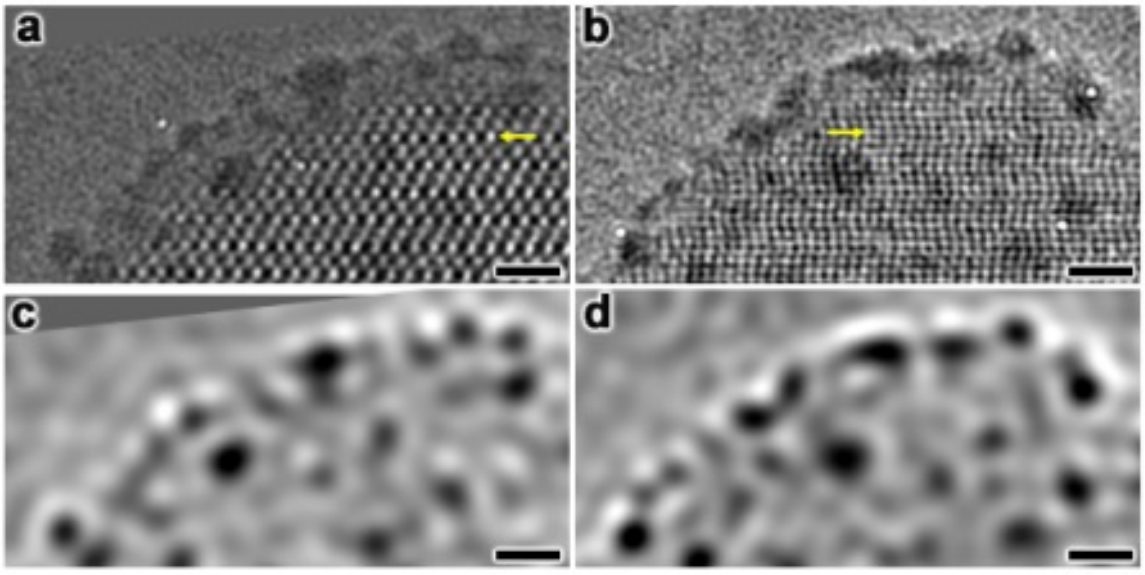

Figure D.9: Comparison of two HRTEM images with gold nanoparticles as markers. **a,b**, A crystal was tilted from $[2\overline{1}\overline{1}0]$ (**a**) to $[10\bar{1}0]$ (**b**) and a shift-up was observed, which indicates a space group of $P6_122$. **c,d**, The processed images of (**a**) and (**b**) after Fourier filtering that only includes spatial frequencies within a particular range to enhance the contrasts of gold nanoparticles.